UNIVERSITY OF CALIFORNIA, SAN DIEGO

The Dynamics of Fluid Flow and Associated Chemical Fluxes at Active Continental Margins

A dissertation submitted in partial satisfaction of the degree
requirements for the degree Doctor of Philosophy
in
Earth Sciences

by

Evan Alan Solomon

Committee in charge:

Dr. Miriam Kastner, Chair
Dr. Neal Driscoll
Dr. Joris Gieskes
Dr. James Hawkins
Dr. Hans Jannasch
Dr. Julie D. Morris
Dr. Mark Thiemens

2007

The dissertation of Evan Alan Solomon is approved, and it is acceptable in quality and form for publication on microfilm:

_____

_____

_____

_____

_____

_____

_____

Chair

University of California, San Diego

2007

This thesis is dedicated to all of my primary, middle, and high school teachers who sparked my interest in science at an early age, and my college professors for their constant support, for their strong commitment to teaching, and for encouraging me to pursue a career in the Earth Sciences.

TABLE OF CONTENTS

LIST OF FIGURES

LIST OF TABLES

ACKNOWLEDGEMENTS

As with any large pursuit in life, this dissertation could not have been accomplished without the outstanding support of a great number of colleagues and friends. First and foremost, I give many thanks to my thesis advisor, Professor Miriam Kastner, for her constant support throughout my tenure as a graduate student at SIO. Miriam has been a great inspiration through the years, and has unquestionably taught me how to be a thoughtful, independent, and thorough earth scientist. Miriam enabled me to be very independent during graduate school, provided me the opportunity to participate in 10 research expeditions (three of which were on the Drillship *JOIDES Resolution*), and furnished me with the finances not only for my salary support, but also for numerous scientific meetings both in the U.S. and abroad. Miriam will continue to amaze me with her creativity and vision.

Many thanks also go to the members of my thesis committee. Joris Gieskes has always given me jovial and critical guidance, taught me how to interpret pore fluid profiles, and has provided me with a wealth of knowledge with regards to chemical analyses. Jim Hawkins has provided valuable feedback on ideas contained within this dissertation, and has been an excellent educator teaching a variety of courses ranging from the geology of subduction zones to the geology of the Basin and Range. I will never forget the Great Trek North field trip that Jim led through the eastern Sierras in the Fall of 2001. Some of the people I met during that field trip continue to be great friends and colleagues to this day. I thank Neal Driscoll for his great scientific insight and creativity, and his general zeal for science. He will continue to be a great

inspiration in the future. I thank Julie Morris for being a fantastic co-chief scientist during ODP Leg 205, which was one of my first research expeditions. I thank her for believing in me during that cruise, when many of the analytical techniques and scientific background were new to me; I can say that it was a "shotgun" lesson in marine geochemistry. I thank both Julie and Mark Thiemens for taking the time out of their busy schedules to serve on my thesis committee.

Much of my research has been interdisciplinary, thus I have many collaborators to thank. Hans Jannasch's amazing engineering and forward thinking provided the framework for the field instrumentation for both the Costa Rica and Gulf of Mexico projects. Hans helped me design the MOSQUITO during my first year at SIO, and I am indebted to Hans for all of his help with instrumentation and for his generosity during my many trips up to MBARI. I also thank Yishai Weinstein for his help with the Gulf of Mexico project. I thank Geoff Wheat for his help with the Costa Rica monitoring, he brought years of experience in downhole sampling at ODP sites to the project. I thank Ian MacDonald for is generous assistance before, during, and after the Gulf of Mexico research expeditions. I thank Pat Castillo for assistance with the Sr isotopic analyses. Many thanks go to Dave Valentine for letting me use his laboratory for hydrocarbon analyses, and Frank Kinnaman for his assistance with the hydrocarbon analyses and for providing me with housing during my many trips up to Santa Barbara. I thank Adina Paytan for her help with the barite concentration analyses. I am grateful for the camaraderie and help of Professor Art Spivack during the NGHP India Ocean gas hydrates project. I am indebted to Chris Mann for teaching me how to operate the ICP-MS.

Andrew Aubrey has been a fantastic friend and great colleague during my time at SIO. I have immensely enjoyed his company during our hourly work breaks the past six years, and I am indebted to him for his invaluable assistance in building the MOSQUITOs and assisting with their recovery. I thank Tabitha Hensley for her help with four of our research expeditions, and staying positive during the Gulf of Mexico hurricane even though everyone was very seasick. Many special thanks go to the SIO Analytical Facility for the constant support and maintenance of the equipment, without the facility this thesis would never have been completed. In particular, I thank Annette Dehyle, Bruce Deck, and Evelyn York.

I cannot thank our laboratory manager, Gretchen Robertson (a.k.a. "Super-tech") enough. Not only has she taught me everything I know with respect to chemical and isotopic analyses, she also has single-handedly prepared everything for the 10 research expeditions completed during my tenure at SIO. Gretchen is a meticulous and careful chemist, and she has contributed a lot to the work presented in this thesis. I also thank my fellow laboratory mate, Wei Wei, for her friendship and guidance.

To me, graduate school is more than just education and research, it is also a place where friendships are made. I thank my friends for making this important time exciting, worthwhile, and fun. I am especially thankful of my friends for helping me find the great pubs in San Diego, music venues, and coffee shops. Many special thanks go to Dan Deeds and Brian Hopkinson, both of whom I met during prospective student's week, for their friendship and attending the plethora of concerts I dragged them to the past six years. I thank Roman de Jesus for all the great times we had brewing quality ales, attending brewing festivals, and going to shows. I thank Melissa

Headly for being the best roommate one could hope for. I thank Mike Vardaro, Travis Meador, Wendy Strangman, Andrew King, Roberta Hansman, Heather Graven, Mario and Melissa Soldevia, Genevieve Boisvert, Ryan Rykaczewski, Steven Smriga, Rachel Borgatti, Patrick Rafter, Julie Robidart, Katherine Maloney, Natalie Rodriguez, and Lynne Folwick for all the great times here in San Diego. A special thanks to Kristen Marhaver for always making me laugh, and being a great friend during the last year of graduate school.

Last but not least, I thank my family. In particular I thank my parents Tod Solomon and Victoria McClure for their financial and emotional support during college and graduate school, without their support this thesis would not be possible. I also thank my stepparents Kathleen Solomon and Derek McClure for their support and friendship.

Financial support has been provided by the National Science Foundation, the U.S. Department of Energy, and the Joint Oceanographic Institutions-U.S. Scientific Support Program and Ocean Drilling Program.

Chapter 2, in full, is the material in preparation for submission to Earth and Planetary Science Letters, Solomon, E.A., Kastner, M., Wheat, C.G., Jannasch, H., Robertson, G., Morris, J.D., in prep. Hydrogeochemical transience along the décollement and subducting igneous basement at the Costa Rica margin. The dissertation author is the primary investigator and author of the manuscript.

Chapter 3, in part, has been submitted for publication as it appears in Solomon, E.A., Kastner, M, and Robertson, G, 2006. Barium cycling at the Costa Rica convergent margin. *In* J.D. Morris, H.W. Villinger, and A. Klaus (Eds.), *Proc. ODP Sci. Results*, 205, 1-22. The dissertation author is the primary investigator and author of the manuscript.

Chapter 4, in full, is the material as submitted to Earth and Planetary Science Letters: Solomon, E.A., Kastner, M., Jannasch, H., Robertson, G., and Weinstein, Y., 2007. Dynamic fluid flow and chemical fluxes associated with a seafloor gas hydrate deposit on the northern Gulf of Mexico slope. The dissertation author is the primary investigator and author of the manuscript.

Chapter 5, in full, is the material as submitted to Nature: Solomon, E.A., Kastner, M., and MacDonald, I.R., 2007. Methane flux to the atmosphere from perennial hydrocarbon plumes in the Gulf of Mexico. The dissertation author is the primary investigator and author of the manuscript.

VITA

2001	B.S., Geology, Summa Cum Laude, University of Nevada, Reno
2003 – 2007	Teaching Assistant, University of California, San Diego
2001 – 2007	Graduate Student, Scripps Institution of Oceanography, University of California, San Diego
2007	Ph.D., Earth Sciences, Scripps Institution of Oceanography, University of California, San Diego

PUBLICATIONS

Solomon, E.A., Kastner, M., Wheat, G., Jannasch, H.W., Robertson, G., and Morris, J.D. Hydrogeochemical transience along the décollement and subducting igneous basement at the Costa Rica margin. *In prep. for submission to Earth Planet. Sci Lett. in Dec. 2007.*

Solomon, E.A., Kastner, M., and MacDonald, I.R. Methane fluxes from perennial hydrocarbon plumes in the northern Gulf of Mexico. *Nature, submitted.*

Solomon, E.A., Kastner, M., Jannasch, H., Robertson, G., and Weinstien, Y. Dynamic fluid flow and chemical fluxes associated with a seafloor gas hydrate deposit on the northern Gulf of Mexico slope. *Earth Planet. Sci. Lett., submitted.*

Newman, K.R., Cormier, M-H., Weissel, J.K., Driscoll, N.W., Kastner, M., Solomon, E.A., Robinson, G.A., Hill, J.C., Singh, H., Camilli, R., Eustice, R. Active methane venting observed at giant seafloor pockmarks along the U.S. mid-Atlantic shelf break. *Earth Planet. Sci. Lett., submitted.*

Solomon, E.A., Kastner, M., Wheat, G., Jannasch, H., Davis, E., Villinger, H., Morris, J.D., Robertson, G., 2007. Hydrogeochemical transience along the décollement and subducting igneous basement at the Costa Rica margin, *NSF-Margins* Workshop to Integrate Subduction Factory and Seismogenic Zone Studies in Central America, Heredia, Costa Rica, available at : www.nsf-margins.org/CostaRica2007/all_abstracts.pdf.

Solomon, E.A., Kastner, M., and Robertson, G., 2006. Barium cycling at the Costa Rica convergent margin, in Morris J., Villinger H., and Klaus A. (Eds.), Proc. ODP, Sci. Res. Leg 205: College Station, TX (Ocean Drilling Program), 1–22. doi:10.2973/odp.proc.sr.205.210.2006

Kastner, M., Becker, K., Davis, E., Fisher, A.T., Jannasch, H.W., Solomon, E.A., Wheat, G., 2006. New insights into the hydrogeology of the ocean crust through long term monitoring, Oceanography, v. 19, no. 4, 30-41.

Solomon, E.A., Kastner, M., MacDonald, I., 2006. Methane fluxes to the atmosphere from perennial hydrocarbon plumes in the northern Gulf of Mexico, EOS. Trans. AGU, 87(52), Fall Meet. Suppl., Abstract B32A-02.

Kastner, M., Solomon, E.A., Wei, W., Chan, L.H., and Saether, O.M., 2006. Chemical and isotopic composition of pore fluids and sediments across the Middle America Trench, offshore Costa Rica, in Morris J., Villinger H., and Klaus A. (Eds.), Proc. ODP, Sci. Res. Leg 205: College Station, TX (Ocean Drilling Program), 1–21. doi:10.2973/odp.proc.sr.205.208.2006

Solomon, E.A., Kastner, M., and Robertson, G., 2005. Progressive barite distillation at the Costa Rica convergent margin: Implications for Ba contribution to the arc volcanoes, EOS Trans. AGU, 86(52), Fall Meet. Suppl., Abstract V31C-0626.

Kastner, M., Solomon, E.A.*, Wheat, G., et al., 2005. Continuous chemical and fluid flux monitoring in two distinct fluid flow systems at the Costa Rica subduction zone, EOS Trans. AGU, 86(52), Fall Meet. Supp., Abstract T12B-02.

Solomon, E.A., Kastner, M., Jannasch, H., Weinstein, Y., Robertson, G., 2005. Insights into the dynamics of in situ gas hydrate formation and dissociation at the Bush Hill gas hydrate field, Gulf of Mexico, Proceedings of the Fifth International Conference on Gas Hydrates, Trondheim, Norway, Paper 3035.

Kastner, M., Bartlett, D., MacDonald, I., and Solomon, E., 2005. CH_4 fluxes across the seafloor at three distinct gas hydrate fields: impacts on ocean and atmosphere chemistry, Proceedings of the Fifth International Conference on Gas Hydrates, Tronheim, Norway, Paper 3002.

Solomon, E.A., Kastner, M., Jannasch, H., Weinstein, Y., Roberston, G., Aubrey, A., 2004. Long-term continuous monitoring of fluid chemistry and flux at the Bush Hill gas hydrate field, Gulf of Mexico using a new flow meter, the MOSQUITO, EOS Trans. AGU, 85(47), Fall Meet. Suppl., Abstract T21C-0539.

Jannasch, H., Davis, E., Kastner, M., Morris, J., Pettigrew, T., Plant, J.N., Solomon, E., Villinger, H., and Wheat, C.G., 2003. CORK-II: long-term monitoring of fluid chemistry, fluxes, and hydrology in instrumented boreholes at the Costa Rica subduction zone. *In* Morris, J.D., Villinger, H.W., Klaus, A., et al., *Proc. ODP, Init. Repts.*, 205, 1-36 [CD-ROM]. Available from: Ocean Drilling Program, Texas A&M University, College Station TX 77845-9547, USA.

ABSTRACT OF THE DISSERTATION

The Dynamics of Fluid Flow and Associated Chemical Fluxes at Active Continental Margins

by

Evan Alan Solomon

Doctor of Philosophy in Earth Sciences

University of California, San Diego, 2007

Professor Miriam Kastner, Chair

Active fluid flow plays an important role in the geochemical, thermal, and physical evolution of the Earth's crust. This dissertation investigates the active fluid flow and associated chemical fluxes at two dynamic continental margins: The Costa Rica subduction zone and the northern Gulf of Mexico hydrocarbon province, using novel seafloor instrumentation for continuous monitoring of fluid flow rates and chemistry. Traditional pore fluid sampling methods and flow rate models only provide a steady-state view of these types of hydrogeochemical systems. The data presented in this thesis, however, show that these systems are dynamic with short period transients in both flow rates and chemistry having a wide range of implications.

Osmotically pumped fluid samplers and a new borehole fluid flow meter were deployed in CORKed borehole observatories installed in two active hydrogeochemical systems at the Costa Rica subduction zone. The data collected by this effort provide critical information on the average and transient hydrogeochemical state of the upper igneous basement and subduction thrust. The results suggest that the upper igneous basement provides an efficient pathway for fluids expelled from the forearc that should be included in models of subduction zone hydrogeology and deformation. Two transients in flow rates along the décollement are the result of aseismic slip dislocations that ruptured through the seismogenic zone. These observations provide insight into the dynamics of episodic strain and the associated fluid flow along the décollement, and may provide an analog for the strain and flow response prior to and during a large subduction zone earthquake.

Recent studies have shown that when the subduction flux of incompatible elements, such as Ba, in the incoming sediment section is high, the arc volcanoes erupt lavas enriched in these elements. Mass balance calculations based on the sedimentary input flux of Ba at reference sections drilled seaward of the trench and the enrichment of Ba in volcanic arcs, suggest 20-30% of the subducted sediment Ba budget is recycled to the arc. A detailed analysis of pore fluid and sediment Ba concentrations from Ocean Drilling Program (ODP) cores collected at the Costa Rica subduction zone, shows that barite dissolution in the forearc can have a profound impact on the amount of Ba recycled to the arc volcanoes and mantle. At the Costa Rica margin, approximately 60% of the incoming sedimentary Ba is lost in the shallow subduction zone, greatly reducing previous estimates of the Ba input flux to the depths of magma generation

based solely on the reference section seaward of the trench. These results suggest that current estimates of the global sediment Ba contribution to volcanic arcs should be reevaluated, and may need to be revised upwards.

Four newly designed fluid flow meters/chemical samplers, called the MOSQUITO, were deployed for 430 days at a seafloor gas hydrate outcrop in the northern Gulf of Mexico to determine how dynamic subsurface fluid flow influences gas hydrate stability and to quantify the associated methane fluxes into the ocean and atmosphere. The results show that gas hydrate continuously formed within the sediments despite a highly transient fluid flow field and variable bottom water temperatures. A model is proposed where gas hydrate formation occurred as a result of long-term emanation of CH_4 at focused gas vents followed by a more diffuse intergranular methane flux. From the long-term flow rate record, the estimated CH_4 flux across the seafloor to the water column from focused vents at the Bush Hill seep is $\sim 5 \cdot 10^6$ mol/yr.

The surface water CH_4 concentrations above the perennial hydrocarbon plumes emitted at these high-flux gas seeps are up to 2,000 times supersaturated. The estimated diffusive CH_4 fluxes to the atmosphere from individual plumes are 3-4 orders of magnitude greater than previously reported from the deepwater marine environment. Extrapolation over the Gulf of Mexico continental shelf and slope indicates that these perennial hydrocarbon plumes emit at least 0.1 to 2.3 Tg CH_4 yr^{-1}, and suggests submarine hydrocarbon seeps in the Gulf of Mexico and in other oil-rich regions are globally significant sources of ^{14}C-dead ("fossil") methane to the atmosphere.

Chapter 1

Introduction

1.1 The Role of Fluids in the Earth's Crust Beneath the Oceans

Fluids play an important role in the geochemical, thermal, and physical evolution of the Earth's crust. Fluid flow rapidly exchanges solutes, isotopes, and gases between the crust and seawater influencing seawater chemistry and the geochemical cycles of many elements and isotopes, and supports an expansive submarine biosphere. Fluid flow also transports significant amounts of heat, thus influencing the thermal structure of the oceanic crust and impacting the global heat budget. Over 50% of the volume of unconsolidated and semi-consolidated sediment is made up of free water, and ~5-10% of the upper 600 m of igneous crust is water. The global upper igneous crustal fluid reservoir alone has a mass comparable to that of water in ice caps and glaciers (Johnson and Pruis, 2003). As these fluids flow through the crust, fluid-solid diagenetic and metamorphic reactions such as serpentization of the uppermost mantle and authigenic mineral formation take place. These reactions change the rocks frictional characteristics and alter their rheology (Lockner and Byerlee, 1986; Scholz, 1998). Studies have also shown that pore fluid pressure affects fault strength and structural development, because it controls effective stress (Davis et al., 1983; Hubbert and Rubbey, 1959). High fluid pressures allow stable slip along faults, whereas a drop in pressure results in stick-slip behavior.

1.2 Overview of the Dissertation

As the title of the dissertation states, this thesis focuses on the dynamics of fluid flow and the associated chemical fluxes in continental margins. Most of what is currently known about fluid flow in the Earth's crust beneath the ocean comes from

advection-diffusion modeling of pore fluid and temperature profiles, as well as from heat flow surveys. These methods only provide a steady-state picture of the fluid flow field at the time the profile was collected or the survey was made, thus they do not render any information of the true steady hydrogeochemical state of the system or any transients in flow rates and chemical fluxes. At both the Costa Rica subduction zone and at the Bush Hill gas hydrate field in the northern Gulf of Mexico, continuous fluid samplers (OsmoSamplers) were deployed to collect a continuous time-series record of fluid chemistry. In addition, a novel borehole flow meter was deployed along the décollement at the Costa Rica subduction zone to document flow transients and their relation to fault stability and the dynamics of episodic plate boundary slip events. Likewise, a new flow meter/chemical sampler, called the MOSQUITO, was designed and deployed in the Gulf of Mexico to understand the time dependent variations in fluid flux, fluid chemistry, and temperature and their impact on gas hydrate stability and methane fluxes to the ocean. Overall, this dissertation improves our understanding of the average and transient hydrogeochemical state of subduction zones and gas-rich hydrological settings.

This Dissertation Consists of the Following Chapters

Chapter 2 presents the results from osmotically pumped fluid samplers and a new borehole flow meter deployed in CORKed borehole observatories installed in two active hydrogeochemical systems at the Costa Rica subduction zone. Downhole instrumentation was deployed during Ocean Drilling Program (ODP) Leg 205 at Site 1253 situated ~0.2 km seaward of the trench in the upper igneous basement and at Site 1255 located ~0.5 km landward of the trench in the décollement. The continuous

monitoring of fluid flow rates and chemistry is part of a larger coordinated effort involving simultaneous pressure and temperature recording. The data collected by this interdisciplinary effort constitute the first co-registered chemical, physical, and hydrological time-series from a subduction zone providing critical information on the average and transient hydrogeochemical state of the subduction thrust and upper igneous basement. The results have implications for the hydration of the upper igneous crust and geochemical mass balances at subduction zones, the role of the upper basement in fluid transport from the SZ, for the dynamics of episodic strain and fluid flow along the décollement and fault stability, and the temporal behavior of plate boundary ruptures during both seismic and interseismic periods.

Chapter 3 focuses on the shallow dissolution of barite in the forearc of the Costa Rica subduction zone, with implications for Ba contribution to the arc volcanoes. Traditionally, geochemical mass balances at subduction zones used a reference Hole seaward of the trench for sediment inputs and the output flux in arc volcanoes as the output. Estimates on the amount of sediment contributed to the arcs and the mantle in subduction zones are based on these box models. At the Costa Rica subduction zone, a transect of three sites were drilled across the trench, providing an ideal locality to look at processes occurring between the reference site and the deeper subduction zone, thus providing a better picture of the subduction inputs. This chapter shows that a significant portion of the incoming sedimentary Ba is distilled in the shallow forearc by the dissolution of barite in sulfate depleted pore fluids. This shallow dissolution causes a loss of as much as 60% of the incoming bulk Ba. This process should operate in all subduction zones, and likely reduces previous estimates of the Ba input fluxes, thus the

amount of sediment recycled to the volcanic arc based on bulk sediment Ba concentrations.

Chapter 4 focuses on the Bush Hill hydrocarbon seep site in the northern Gulf of Mexico, where gas hydrates outcrop at the seafloor. Four newly designed fluid flux meters/chemical samplers, called the MOSQUITO, were deployed for 430 days at Bush Hill to determine how dynamic subsurface fluid flow influences gas hydrate stability and to quantify the associated methane fluxes into the ocean. The flux meter measurements reveal that the subsurface hydrology in the vicinity of the mound is complex and variable with frequent changes from downward to upward flow ranging from -161 to 273 cm/yr, and with temporal variations in the horizontal component of flow. The continuous record of fluid chemistry indicates that gas hydrate actively formed in the sediments. We propose that long periods of downward flow of seawater adjacent to gas vents (up to 4 months) are driven by local sub-pressure resulting from gas ebullition through faults and fractures due to overpressure at depth. High frequency variations in flow rates (days to weeks) are likely due to temporal changes in sediment permeability and the 3-D fluid flow field as a result of active gas hydrate and authigenic carbonate precipitation. Gas hydrate formation occurred as a result of long-term emanation of CH_4 at focused gas vents followed by a more diffuse intergranular methane flux. The estimated CH_4 flux to the water column from focused gas vents across the Bush Hill seep is $\sim 5 \cdot 10^6$ mol/yr. This significant flux suggests that Bush Hill and similar hydrocarbon seeps in the northwestern Gulf of Mexico may be important natural sources of methane to the ocean and atmosphere.

In Chapter 5 I report ~500 m CH_4 concentration and isotopic depth profiles collected from a research submersible above seafloor perennial hydrocarbon plumes in the northern Gulf of Mexico. The profiles show that surface water CH_4 concentrations above perennial hydrocarbon plumes are up to 2,000 times supersaturated. The estimated diffusive CH_4 fluxes to the atmosphere from individual plumes are 3-4 orders of magnitude greater than previously reported from the deepwater marine environment. Oil lines the gas bubbles inhibiting aerobic methane oxidation in the water column, and diffusive methane fluxes to the atmosphere range from 641 to 16,397 μmol m^{-2} d^{-1}. Extrapolation over the Gulf of Mexico continental shelf and slope indicates that these perennial hydrocarbon plumes emit at least 0.1 to 2.3 Tg CH_4 yr^{-1}. This estimated Gulf of Mexico methane flux is ~35% of the estimated global oceanic flux and ~50% of the global mud volcano flux. These results suggest that estimates of the CH_4 flux from the global ocean and mud volcanoes are too low, and indicate submarine hydrocarbon seeps are significant sources of ^{14}C-dead ("fossil") methane to the atmosphere. **Chapter 6** is a summary and implications chapter.

1.3 Subduction Zone Hydrogeochemistry

The study of subduction zones is of great societal importance because they account for the majority of the global seismic energy release (Romanowicz, 1993) creating the most destructive earthquakes, and have the potential to create devastating tsunamis. Furthermore, subduction zones are associated with ubiquitous volcanism releasing large amounts of volcanic ash, volatiles, and lavas, which impact both local areas as well as global climate. Changes in the physical and mineralogical properties of

subducted sediment and igneous basement with depth and the associated evolution of fluids in subduction zones are intimately linked to the transition from aseismic (stable sliding) and seismic slip in the décollement and thrust faults in the prism, as well as arc volcanism at greater depths.

Fluids enter subduction zones on the incoming plate in pore spaces of the sediment and oceanic crust, as interlayer water in clay minerals and within the structure of hydrous minerals. The most important of these minerals are opal (~11 wt. % water), smectite (~15 wt.% interlayer water and 6-8 wt.% structural water), illite (total of 8.5 wt.% structural + interlayer water), and serpentine (~13 wt.% water). As the plate is subducted, the interstitial water is squeezed from the pore spaces of the underthrust sediments at shallow depths as the sediments are compacted (Figure 1.1). The original porosity of the incoming sediments is typically 50 ± 10% and it is reduced to <5-10% by a depth of 4 km (Kastner et al., 1991; Moore and Saffer, 2001). The shallow dewatering of the underthrust sediments by tectonic compaction produces elevated pore fluid pressures up to $\lambda^* = 0.85$ (Moore and Saffer, 2001), where $\lambda^* = [P_{fluid}-P_{hydrostatic}]/[P_{lithostatic}-P_{hydrostatic}]$; also referred to as the pore pressure ratio. As the sediments and igneous basement are subducted deeper into the subduction zone, temperatures increase, and dehydration and diagenetic reactions become important fluid sources (Fig. 1.1). Most of these shallow dehydration and diagenetic reactions occur between 50 and 160 ^{o}C and include the formation of thermogenic hydrocarbons, the transition from opal to quartz, and the smectite to illite transition. As the sediments and basement reach temperatures greater than 200 ^{o}C, phase transitions of high temperature hydrous minerals, such as serpentines, occur, releasing more water at depth from both

the sediments and altered igneous basement. At the depth of magma generation, ~100-150 km, additional hydrous minerals break down and release water to the overlying mantle wedge (Fig. 1.1). Below this depth, the remaining structural water tied up in select hydrous minerals, for example phengites, is transported into the mantle.

The fluids expelled from these processes are transported through permeable pathways driven by tectonic stresses and elevated pore pressures. The fluids squeezed from the consolidating sediment section at shallow depths in the forearc are transported both vertically and laterally through sand/silt horizons, ash layers, and microfractures within the underthrust section (Fig. 1.1; Saffer et al., 2000; Screaton and Saffer, 2005). Near the toe of the margin, some of these fluids can be channelized into the décollement. The flow rates from compaction dewatering of the underthrust sediments are expected to be minimal, because the permeabilities of the underthrust hemipelagic clays and pelagic carbonates are low. This is the reason pore fluid pressures can be so elevated in the underthrust sediments at shallow levels of the subduction zone. Clay-rich hemipelagic sediments have a range in pemeability from $7 \cdot 10^{-15}$ to $8 \cdot 10^{-20}$ m^2 (Gamage and Screaton, 2006; Saffer and McKiernan, 2005; Screaton et al., 2006) and subducted pelagic carbonate sediments have a permeability range of 10^{-15} to 10^{-16} m^2 (Screaton et al., 2006). Modeled permeabilities in the décollement and faults in the prism, however, can be quite high and range from 10^{-12} to 10^{-14} m^2 (Fisher and Zwart, 1996; Saffer and Bekins, 1998; Screaton et al., 2000; Spinelli et al., 2006). Thus, fluids produced from dehydration reactions at depth flow along the décollement and thrust faults along the margin wedge, as well as normal faults in the mid-slope region of the forearc (Fig. 1.1.). The upper igneous basement has traditionally been considered as a

no-flow boundary in finite-difference models of subduction zone hydrogeology (e.g. Ge and Screaton, 2005; Saffer and Bekins, 1999; Screaton and Saffer, 2005; Spinelli et al., 2006). Recent studies have indicated that the upper igneous basement is highly permeable ranging from 10^{-10} to 10^{-12} m^2 at the eastern flank of the Juan de Fuca Ridge (Fisher et al., 2003) and from 10^{-8} to 10^{-10} m^2 on the EPR crust offshore Costa Rica (Hutnak et al., 2007). Thus, the permeable upper oceanic basement likely serves as an efficient fluid flow pathway for fluids being expelled from the prism and consolidating underthrust sediments. The role of the igneous basement as a flow pathway is discussed in more detail in Chapter 2 of this thesis.

The fluid sources, flow pathways, and flow rates are all intimately linked to deformation and the onset of seismogenesis at subduction zones. The seismogenic zone is the region where large earthquakes rupture, and is theoretically fully coupled, or locked. The frictional stability of fault materials is more important than the absolute strength of the materials controlling unstable failure in seismogenic zones (Scholz, 1998). Scholz (1998) defines a frictional stability parameter:

$$\zeta = (a-b)\sigma_e \qquad \text{(Eq. 1.1)}$$

where (a-b) is the frictional velocity dependence, defined as the change in steady-state sliding friction for an increase in sliding velocity, and σ_e is the effective normal stress, which decreases with elevated pore pressures and increases as pore pressures diminish. Materials characterized by a positive velocity dependence are velocity strengthening, and are stable (ζ is positive). Those with negative velocity dependence are velocity weakening, and may exhibit unstable slip (locking) or conditionally stable behavior. The lower the effective stress, the more stable the frictional behavior of the fault. Thus,

velocity strengthening occurs from the trench to the seismogenic zone along the décollement, and below the seismogenic zone. These aseismic zones accommodate strain from plate convergence by stable sliding. The seismogenic zone is characterized by velocity strengthening material and elevated effective stress and does not accommodate strain by sliding, but rather releases the accumulated strain through rupture.

It has long been known that prism sediments are weak and overpressured and that consolidation and lithification are required for seismogenesis (e.g. Byrne, 1988). Vrolijk (1990) argued that the transition from smectite to illite controls the mechanics of the subduction thrust and the location of the aseismic to seismic transition. Hyndman et al. (1995; 1997) showed that modeled temperatures of the up-dip limit of the seismogenic zone in Japan, Alaska, and Chile occur at a temperature of 100-150 ^{o}C, which is the temperature range of the smectite to illite transition.

Recent studies have shown that the location of the seismogenic zone is not simply controlled by the smectite to illite transition (Ikari et al., 2007; Moore and Saffer, 2001; Saffer and Marone, 2003; Spinelli and Saffer, 2004). For example, smectite is not always abundant in the incoming sediment section, at some margins the 150 ^{o}C isotherm is reached far before the depth of seismogenesis (e.g. Costa Rica), and there is a host of other diagenetic reactions that occur within this temperature range. Furthermore, recent laboratory studies have shown that illite is actually velocity strengthening under all conditions that would be encountered up-dip and within the seismogenic zone (Marone, 2006; Saffer and Marone, 2003), thus would enable stable sliding rather than stick-slip behavior as hypothesized in earlier models. Other

diagenetic reactions, however, could lead to velocity weakening behavior. Moore and Saffer (2001) highlight the principle diagenetic and low-grade metamorphic reactions that occur within this temperature window: (1) opal to quartz transition; (2) smectite to illite transition (complete by ~150 ^{o}C); (3) low-grade metamorphic reactions such as zeolite formation; calcite precipitation and cementation, and pressure solution and quartz cementation.

All of these dehydration reactions, including the smectite-illite transition, and subsequent fluid flow and compaction dewatering decrease λ^*, increasing the effective normal stress and enabling stick-slip behavior. However, this does not preclude the localized development of transiently high fluid pressures within the seismogenic zone that are associated with the initiation of earthquakes (Saffer and Bekins, 1999). Thus, there is no "smoking gun" for the cause of the onset of stick-slip behavior in the seismogenic zone, but in light of these recent studies, it is likely due to a combination of the decrease in pore pressures caused by mineral dehydration and secondary mineral precipitation and cementation by clays, zeolites, carbonates, and quartz, all of which are coupled to consolidation.

The current models of subduction zone hydrogeology and processes and reactions leading to the onset of seismogenesis are for steady-state conditions. Though the seismogenic zone is fully locked at some subduction zones (e.g. Peru-Chile trench; Gagnon et al., 2005), the seismogenic zone is often only partially locked and patchy at others. For example, the seismogenic zone offshore Costa Rica is only ~60% locked (Norabuena et al., 2004). Recent onshore GPS measurements (Dragert et al., 2001; Dragert et al., 2004; Obara et al., 2004; Protti et al., 2004) and novel offshore borehole

monitoring, geodetic techniques, flow meter measurements near the toe of subduction zones (Brown et al., 2005; Davis et al., 2006; Davis and Villinger, 2006; Gagnon et al., 2005) are beginning to shed light on the short-term, transient hydrotectonic state of subduction zones with implications for the nature and controls on spatial changes in plate coupling, episodic strain release, deformation, and fluid flow. These monitoring programs have observed slow aseismic slip events both up-dip and down-dip of the seismogenic zone that are accompanied by no associated detectable earthquakes, but rather seismic signals that resemble volcanic and non-volcanic tremors. The slow slip events recorded offshore initiate near the up-dip limit of the seismogenic zone and propagate seaward. The events recorded onshore are interpreted to originate down-dip of the seismogenic zone and terminate at the down-dip limit. Thus the down-dip events act to increase the stress on the locked portion of the subduction thrust, while the offshore deformational events act to incrementally relieve stress locally along the subduction thrust and to load neighboring areas. These observations have shown that the prism is far from inactive during interseismic intervals, and the slow slip events could potentially serve as analogs for the strain and hydrological responses at the time of great subduction earthquakes.

The intent of this short review on subduction zone hydrogeology was to present the state of knowledge of fluid sources and pathways at subduction zones and their relation to the seismogenic zone, and to highlight recent advances in the field. Though much has been learned in the past few decades, there are still many questions and problems to be solved. Of critical importance is the understanding of the relationship of temporal hydrogeochemical processes and seismicity. A major focus of this dissertation

is on the long-term monitoring of hydrogeochemical transience at the Costa Rica subduction zone with implications for: (1) the magnitude of fluid egress at subuction zones, (2) the temporal variability in fluid flow and composition, (3) the forces that drive fluid flow during the seismic cycle, and (4) the shallow cycling of fluid-soluble elements, such as barium, in the subduction zone forearc.

1.4 The Costa Rica Subduction Zone

1.4.1 ODP Leg 170 and Leg 205 Drilling and Geologic Setting

The Middle America Subduction Zone, and more specifically the Costa Rica margin west of the Nicoya Peninsula, has been an area of focused research during the past decade. A portion of this research focuses on elucidating the mass balance of chemical species and material within the subduction system. More recently, research has focused on ascertaining the temporal relationships among stess, strain, and fluid composition throughout the earthquake cycle, and determining the effect of earthquakes on the hydrologic system. Ocean Drilling Program (ODP) Leg 170 (Kimura et al., 1997) and Leg 205 (Morris et al., 2003) have investigated fluid flow across the margin, in the context of lithology, structure, tectonics, and thermal history of the incoming plate, the overriding plate, and the décollement. Sites for the two legs were drilled across the deformation front outboard of the Nicoya Peninsula (Fig. 2.1). Sites 1039 (Leg 170) and 1253 (Leg 205) penetrate the sedimentary and upper igneous sections of the incoming plate. They are located ~1km and 0.2 km seaward of the deformation front, respectively. Sites 1040 and 1254 were drilled ~1.5 km landward of the deformation front. Both sites penetrated the forearc prism sediments and the

décollement, and Site 1040 cored the entire underthrust sediment section and the top of a gabbro sill on the incoming plate (Fig. 2.1). Sites 1043 and 1255 were drilled ~0.4 km inboard of the deformation front. Both site penetrated the sediment prism and the décollement. CORKs (long-term borehole observatories) were installed during ODP Leg 205 at Site 1253 and 1255; these installments are discussed in Section 1.3.2.

The convergence rate of the Cocos Plate relative to the Caribbean Plate is ~88 mm/yr offshore Costa Rica (DeMets et al., 1990). The convergence direction offshore the Nicoya Peninsula is nearly perpendicular to the trench. The subducting Cocos Plate dips 6^{o} for the first 30 km of the subduction zone, beyond which the dip angle increases to 13^{o} (Christeson et al., 1999). The slope of the seafloor on the wedge is 5.4^{o}. The location of shallow earthquakes at the Nicoya segment of the Costa Rica margin occur ~75 km from the trench at a depth of ~20 km (Newman et al., 2002). Modeled temperatures along the plate boundary reach 150 ^{o}C by 48-60 km from the trench at the Nicoya Peninsula (Spinelli and Saffer, 2004). Analysis of marine magnetic measurements (Barckhausen et al., 1998; 2001) shows that ~20 km southeast of the Leg 170 and 205 transects, a fracture zone trace separates lithosphere formed at the EPR from that formed at the Cocos-Nazca (CNS) spreading center, indicating that the igneous crust at the Leg 205 sites is ~24 Ma. The sediment of the subducting Cocos Plate is ~400 m thick consisting of a 250 m thick pelagic carbonate section overlain by 150 m of diatomaceous hemipelagic mud (Kimura et al., 1997). During Leg 205, a gabbro sill was encountered at ~400 mbsf, which was underlain by an additional 20 m of pelagic carbonates. Below this depth an igneous complex was drilled comprised of numerous sills with minor interbedded “baked” sediments (Morris et al., 2003).

Heat flow data from the Global Heat Flow Database and from more detailed studies in the area (Langseth and Silver, 1996; Ruppel and Kinoshita, 2000; Fisher et al., 2003; Hutnak et al., 2007) show that the heat flow on the EPR generated crust is much lower than across the fracture zone trace (FZT) on the CNS crust. North of the FZT, heat flow values average ~ 30 mW/m^2, which is about ⅓ of the expected value from conductive lithospheric cooling of 24 Ma old oceanic crust (Stein and Stein, 1992). The CNS crust is of about the same age as the EPR crust in the area, and values jump to an average of ~110 mW/m^2, consistent with the lithospheric cooling models. These heat flow data indicate significant lateral fluid flow in the EPR crust efficiently cooling the incoming plate (Fisher et al., 2003; Heesemann et al., 2006; Hutnak et al., 2007; Langseth and Silver, 1996), which has implications for the depth of the seismogenic zone inboard of the EPR and CNS sections (Newman et al., 2002; Spinelli et al., 2006).

Seismic data from the Costa Rica forearc and coring during Leg 170 (within 7 km of the trench) show that the bulk of the margin is a wedge-shaped high-velocity body made of rocks similar to the Nicoya ophiolite complex cropping out along the coast of the Nicoya Penisnsula (Kimura et al., 1997; Shipley et al., 2000; Vannucchi et al., 2001). The sediment chemistry is remarkably constant with depth (Morris et al., 2003), supporting this inference. ODP Leg 170 drilling showed that essentially the entire sediment cover on the subducting Cocos Plate is currently underthrust beneath the margin wedge, and little if any of the incoming material is accreted to the margin wedge (Kimura et al., 1997; Silver et al., 2000; von Huene et al., 2000). The décollement

clearly separates the undethrust sediments from the prism sediments (Fig. 2.1). There are also numerous thrust faults, mostly in the deeper part of the margin (Shipley et al., 1992), and normal faults at the mid-slope region of the forearc (von Huene et al., 2004) that act as fluid conduits. An out-of-sequence thrust fault was sampled at Site 1040/1254 and 1043/1255 (Kimura et al., 1997; Morris et al., 2003), and it is also a fluid flow pathway (Chan and Kastner, 2000; Morris et al., 2003).

The composition of arc lavas records the sediment contribution from the subducting plate, constraining sediment dynamics at depths greater than can be reached by drilling or seismic imaging. Chemical differences between the arc lavas from Nicaragua and Costa Rica suggest that the upper portion of the sediment subducting past the past the Leg 170 and 205 sites is likely underplated at greater depths, with the deeper carbonate section dominating the volcanic outputs (e.g. Carr et al., 2003; Morris et al., 1990; Shaw et al., 2003). In addition to the evidence for sediment subduction and underplating beneath the Nicoya segment, the seismic stratigraphy, multibeam bathymetry, and sedimentology indicate a significant amount of mass wasting and extension and subsidence of the margin during much of the Miocene (e.g. Ranero and Von Huene, 2000; Vannucchi et al., 2001; 2003). This process has been termed tectonic erosion and is speculated to be controlled by the roughness of the incoming plate. For the purposes of this thesis, it is important to note that subduction erosion does occur at the Costa Rica margin, but it may be episodic rather than a steady-state feature of the margin and is likely controlled by seamount subduction. It is also important to note that the margin offshore Nicoyal Peninsula is not currently accreting sediments, and all of the sediments fed to the trench over the past few million years are

subducted beneath our study sites greatly simplifying estimates of the mass and element fluxes in the shallow part of this subduction zone, with underplating not playing a role until much farther down-dip.

1.4.2 The Three Fluid Flow Systems and CORK Installation

Sediment composition and physical properties, pore fluid chemical composition, temperature, and pressure obtained during ODP Legs 170 and 205 identified two distinct active hydrologic systems (Chan and Kastner, 2000; Silver et al., 2001). A third system was inferred from pore pressures from sediment consolidation tests and simple fluid flow modeling (Saffer et al., 2000). The first hydrological system exists within upper basaltic basement beneath the sedimentary sequence on the incoming plate (ODP Site 1039/1253; Fig. 2.1). Low heat flow values of ~ 30 mW/m^2 exist near these sites with Site 1253 having a heat flow of only 10 mW/m^2 (Heesemann et al., 2006; Langseth and Silver, 1996). These values represent ~30 and 10%, respectively, of the expected value from conductive cooling of the underlying lithosphere, indicating significant fluid flow within the crust. Similarly, pore fluid chemical and isotopic profiles in the basal sediments suggest a return towards approximately seawater concentrations (i.e. Li, Ca, Mg, Sr, $^{87}Sr/^{86}Sr$, ^{7}Li). This requires the upper igneous basement to be hydrologically connected to bottom seawater, with recharge occurring at distant igneous outcrops and requiring rapid lateral advection within upper basement beneath the sediments (Fisher et al., 2003; Hutnak et al., 2007; Langseth and Silver, 1996). Heat flow data collected during recent cruises show that seamounts are sites of fluid discharge and recharge (Fisher et al., 2003) and modeling suggests that lateral flow rates of 1-30 m/yr occur

within the upper 600 m of EPR-generated crust, requiring high permeabilities ranging from 10^{-10} to 10^{-8} m^2 (Hutnak et al., 2007; Silver et al., 2000). In addition to cooling the uppermost part of the plate, which has ramifications for the seismogenic zone (Harris and Wang, 2002), this fluid flow system may further alter and hydrate the igneous crust, affecting mass balances and, in particular, the transfer of volatiles to great depths where they can be released arcward of the deformation front along the volcanic arc.

The second fluid flow system occurs along the plate boundary, the décollement, and in an out-of-sequence thrust in the prism (Fig. 2.1). This flow system was sampled at two sites; Sites 1040 and 1254 which are ~1.6 km landward of the trench, and Sites 1043 and 1255, which are ~0.5 km landward of the trench (Kimura et al., 1997; Morris et al., 2003). Elevated Li concentrations are observed in pore waters recovered from the décollement and the out-of-sequence thrust fault at Sites 1040 and 1254 (Chan and Kastner, 2000). Enrichments in Ca and higher molecular weight hydrocarbon concentrations (propane to hexane), and depletions in K, Cl, and Mg concentrations are also observed (Kimura et al., 1997; Morris et al., 2003). The same chemical anomalies are observed within the décollement at Sites 1043/1255, located seaward of Sites 1040 and 1254, albeit to a lesser extent. Similar depletions in Cl and K, enrichments in Li, Ca, and B, and heavier hydrocarbon concentrations have been observed in fluids sampled in mud volcanoes along the Costa Rican and Mariana margins (Grevemeyer et al., 2004; Hensen et al., 2004; Fryer et al., 1999), and sampled in the Barbados and Nankai accretionary prisms (Martin et al., 1996; Kastner et al., 1993; Spivack et al., 2002). Collectively, these data indicate that a fraction of the fluids sampled along the décollement and thrust fault are derived from depths within the subduction zone where

the temperatures are ~80-150 ^{o}C (Chan and Kastner, 2000; Hensen et al., 2004; James et al., 2003; Martin et al., 1996; Wei et al., submitted; You et al., 1996; You and Gieskes, 2001). These temperatures occur ~50 km from the deformation front (Spinelli et al., 2006) near the up-dip limit of the seismogenic zone (Newman et al., 2002). These chemical anomalies are very sharp along the two fault zones, requiring rapid advection of these fluids in the recent past, potentially during the last major subduction thrust earthquake at the Nicoya margin.

An inferred third fluid flow system was suggested for Sites 1040 and 1043 where compaction of the underthrust sediments causes dewatering and pore fluid migration vertically and laterally to the trench (Saffer et al., 2000; Screaton and Saffer, 2005). Consolidation tests suggest the presence of relatively high pressures (Saffer, 2003; maximum pore pressure ratio $\lambda^* = 0.7$), but they provide only indirect estimates of pore pressure gradients. Abrupt changes in pore fluid geochemistry across the décollment indicate that this flow system does not communicate with the décollement flow system, and that drainage is primarily horizontal (Kimura et al., 1997; Morris et al., 2003; Solomon et al., 2006). Results from the consolidation tests (Saffer et al., 2000; Saffer, 2003) indicate that there is more rapid drainage and greater compaction in the hemipelagic sediments that the pelagic sediments that may result from more abundant coarse-grained high-permeability ash layers that focus flow, or significant permeability anisotropy in the hemipelagic sediments.

On the basis of these findings, two CORK (Circulation Obviation Retrofit Kit) long-term borehole observatories were successfully installed during ODP Leg 205 in the two fluid flow systems: one in a fractured interval in the upper igneous basement in

the incoming plate at Site 1253 and one in the décollement at Site 1255. The CORK seals the borehole from the overlying bottom water and allows long-term hydrogeologic monitoring in the formation of interest (Becker and Davis, 2006). Downhole instruments continuously recorded fluid flow rates and collected a time series of fluids for analysis of dissolved and gaseous species over a period of ~700 days from October 2002 to September 2004. The continuous fluid flow rate and chemical monitoring is part of a larger coordinated effort involving pressure and temperature recording (Davis and Villinger, 2006; Heesemann et al., 2006; Jannasch et al., 2003). Initially plans to also monitor the underthrust hydrologic system were conceived, but time constraints during ODP Leg 205 limited the CORK installations to the two most active flow systems.

The data collected during this interdisciplinary effort is presented in Chapter 2 of this dissertation, and constitutes the first co-registered chemical, physical, and hydrologic time series from a subduction zone system. The results of this comprehensive monitoring program have implications for the hydration of the upper igneous crust and geochemical mass balances at subduction zones, the role of the upper basement as a pathway for fluids being expelled from the subduction zone, the impact of episodic strain on fluid flow along the décollement and fault stability, and the temporal behavior of plate boundary ruptures during both seismic and interseismic periods.

1.5 Gas Hydrates – A significant reservoir of methane and their potential role in global climate change and slope stability

One of the most recent and intensively studied aspects of both passive and active margins is marine gas hydrates and the associated methane and hydrocarbon gases, and they are the focus of Chapters 4 and 5 of the dissertation. Gas hydrates are ice-like minerals in which hydrocarbon and non-hydrocarbon gases occupy cages within a framework structure of water molecules. Methane is the most common natural gas molecule in gas hydrate, but, in the marine environment, hydrates can also contain considerable amounts of ethane, propane, CO_2, and H_2S (Kastner et al., 1998; Sloan and Koh, 2008). Gas hydrate stability is exponentially dependent on temperature and linearly dependent on pressure (Sloan and Koh, 2008), and also depends on the composition of the gas molecules and on the pore fluid chemistry (Dickens and Quinby-Hunt, 1997; Handa, 1990; Zatsepina and Buffet, 1998). Higher molecular weight hydrocarbons, H_2S, CO_2, and lower salt concentrations increase the stability field in pressure-temperature (P-T) space (Dickens and Quinby-Hunt, 1997; Englezos and Bishnoi, 1998; Sloan and Koh, 2008). The P-T constraints on gas hydrate stability restrict their formation to two natural environments on Earth, (1) in the modern ocean regime, primarily on continental margins, at water depths >500 m (in polar regions water depths >150 m), where the sediments contain organic matter concentrations >0.5 wt.%, and (2) in polar regions associated with permafrost. Methane availability is one of the most critical factors controlling the occurrence of natural gas hydrates in the marine environment. The origin of the gas in marine gas hydrates is mainly biogenic methane, but thermogenic methane and higher molecular weight hydrocarbons are important in petroleum basins like the Gulf of Mexico and the Caspian Sea.

Bacteria rapidly consume the concentrations of electron acceptors such as O^{2-}, NO_3-, Mn (IV), and Fe (III) to oxidize organic matter. After the depletion of these pore water constituents, sulfate becomes the most important electron acceptor for organic matter oxidation. In sediments with relatively high organic carbon content (>0.5 wt.%), SO_4^{2-} is typically depleted within the first few centimeters to tens of meters depth (D'Hondt et al., 2002). Once the sulfate is depleted, methanogenesis and fermentation are the principal remaining avenues for metabolic activity in the sediment column. The principle biologically mediated reactions for methanogenesis are as follows (Claypool and Kaplan, 1974):

$$CO_2 + 4H_2 \rightarrow CH_4 + 2H_2O \qquad (CO_2 \text{ reduction})$$

$$CH_3COOH \rightarrow CO_2 + CH_4 \qquad (\text{acetate fermentation})$$

CO_2-reduction is the most important reaction in the marine environment, because acetate is also reduced during SO_4^{2-} reduction (Reeburgh, 2007), limiting its availability at depth. The $\delta^{13}C$ of the methane produced biogenically is typically less than -65‰, and the methane produced within the gas hydrate stability zone (GHSZ) is precipitated as gas hydrate. The methane produced below the GHSZ is transported into the GHSZ by diffusion, intergranular fluid flow, and advective fluid flow along faults and fractures. The occurrence of gas hydrate in clay-rich sediments is typically disseminated within the sediment pore space with the pore space occupancy typically being <5%. The occurrence of gas hydrate can be more massive along regions of focused fluid flow such as faults and fractures. Gas hydrate is often detected by free

gas below the GHSZ that produces a bottom simulating reflector (BSR) in seismic surveys (Shipley et al., 1979).

Thermogenic gases are produced by a catagenesis process characterized by high temperatures (>170 ^{o}C) producing relatively large amounts of ethane and higher hydrocarbons in addition to methane (Sloan and Koh, 2008). In the Gulf of Mexico, the amount of thermogenic gas hydrates is approximately equal to the biogenic gas hydrates (Sassen et al., 1999). Due to the high temperature required for the formation of the thermogenic gases, they must migrate from great depths along faults and fractures to the cooler gas hydrate stability zone to precipitate hydrates. The flux of these gases is typically high along faults, and can lead to the formation of gas hydrate deposits on the seafloor (e.g. MacDonald et al., 1994; 2003; Roberts and Carney, 1997). Because of the association of thermogenic gas hydrates with flow conduits, such as faults and salt diapirs, thermogenic gas hydrate deposits are often localized and massive. The association of methane with higher hydrocarbon gases causes the formation of Structure II gas hydrates (Sloan and Koh, 2008), which have a larger stability field in P-T space than Structure I gas hydrates that are composed primarily of methane. Thermogenic methane can be distinguished from biogenic methane based on its carbon isotopic ratio; thermogenic methane has a $\delta^{13}C\text{-}CH_4$ values ranging from -25 to - 55‰.

Thus, gas hydrates occur on most continental margins, and they are typically disseminated in the pore spaces of sediments at relatively low concentrations (<5% of the pore space) and they are found in dynamic settings characterized by high fluid flow rates as massive deposits along localized fault zones. The estimated total amount of methane carbon in marine gas hydrates ranges between $\sim 5 \cdot 10^{17}$ and 10^{19}g (Kvenvolden,

1999; Milikov et al., 2003), and represents one of the largest reservoirs of methane on the planet. The actual amount of global gas hydrate in the marine environment is poorly constrained because of the heterogeneous nature of gas hydrate occurrence. Early estimates based on regional BSRs were overestimates, because they only indicate the presence of gas hydrate in the sediment, and not the absolute amount. Recent drilling projects (ODP Leg 164, ODP Leg 204, IODP Leg 311, and NGHP Expedition 01) have confirmed that pore space occupancy is relatively low in "diffuse" settings and that massive deposits are typically lithologically and structurally controlled, attesting to the very heterogeneous nature of gas hydrate distribution. Key to assessing the size of the global gas hydrate reservoir is calibration of drilling indicators (IR imagery and pore fluid chemical profiles) with remote sensing techniques such as seismic reflection and electromagnetic surveys, which is the focus of ongoing research. Despite the poor constraints on the size of the global gas hydrate reservoir, even with the most conservative estimates, it is clear that the recoverable CH_4 in these gas hydrate deposits is likely to be significant and may serve as a future non-renewable energy resource (Sloan and Koh, 2008). Now that the mode of gas hydrate occurrence in different margins is better understood from recent drilling projects, the focus of upcoming drilling projects is on the recovery of massive, continuous sections of gas hydrate in the marine environment as well as from permafrost (e.g. JIP II and Mallik).

Recent interest in marine gas hydrates has resulted from the realization that sea-level changes and global warming may destabilize enormous quantities of gas hydrate in marine sediments, potentially triggering continental margin slope instability (Dillon et al., 1998; Nisbet and Piper, 1998) that may cause a significant release of methane into

the ocean and possibly the atmosphere (Revelle, 1983; MacDonald, 1990; Nisbet, 1990; Brewer, 1999). Large-scale dissociation of gas hydrates and subsequent release of methane into the ocean has been proposed as the cause of the excursions in the $\Delta^{13}C$ records during the Paleocene-Eocene thermal maximum (Dickens et al., 1997; Norris and Rohl, 1999) and glacial interstadials over the past 60,000 years (Behl and Kennet, 1996; Kennet et al., 2000). The catastrophic release of methane to the atmosphere would have a positive feedback to global warming, because it is a radiatively important greenhouse gas in the atmosphere.

Key to understanding the fate of methane during a catastrophic release from decomposing gas hydrate is the understanding of the sinks of methane transported in the modern day sediment column not utilized during gas hydrate precipitation. Anaerobic oxidation of methane (AOM) is an important CH_4 removal process in diffusion-dominated sediment systems (Boetius et al., 2000), where most to all of the methane is consumed before it reaches the overlying water column (D'Hondt et al., 2002). AOM is accomplished by a syntrophic consortium of bacteria and archaea and follows the net reaction:

$$SO_4^{2-} + CH_4 \rightarrow HCO_3^- + HS^- + H_2O \quad \text{(AOM)}$$

The carbonate produced through AOM is precipitated as authigenic carbonate reducing alkalinity:

$$Ca^{2+} + 2HCO_3^- \rightarrow CaCO_3\,(s) + H_2O + CO_2 \quad \text{(authigenic catrbonate precipitation)}$$

This reaction acts as a net sink of methane and carbon in all gas-rich hydrogeochemical settings. At advective hydrocarbon seeps, methane advection rates are greater than

AOM rates, thus AOM is not complete, and significant quantities can enter the ocean system. As methane enters the water column, it is subjected to further aerobic oxidation of methane by water column microorganisms:

$$CH_4 + 2O_2 \rightarrow CO_2 + 2H_2O \qquad \text{(aerobic } CH_4 \text{ oxidation)}$$

Thus, in low flux settings, all of the methane is consumed in the sediment column, and in high flux settings, the methane is typically fully consumed in the water column (e.g. Valentine et al., 2001). In some regions, the gas flux is high enough that the methane emitted at seeps survives water column oxidation and makes it to the oceanic mixed layer. Once in the mixed layer, the methane is free to exchange with the atmosphere. In the northern Gulf of Mexico, hydrocarbon plumes are visible throughout the water column on echo sounder records extending from the seafloor to the sea surface (e.g. deBeukelaer et al., 2003; Roberts, 2001). The bubble emitted at Gulf of Mexico seeps are coated with a thin layer of oil, and the hydrocarbon plumes form oil slicks at the sea surface that are detected by satellite remote sensing (MacDonald et al., 2002). Thus, in some environments a fraction of the methane emitted to the water column can be transferred to the atmosphere, which may serve as an analog for a catastrophic release of methane from a large-scale gas hydrate dissociation event.

1.6 The Northern Gulf of Mexico Hydrocarbon Province and Seafloor Gas Hydrate Deposits

The Texas-Louisiana slope in the northwestern Gulf of Mexico (GOM) is a salt-diapirism controlled setting dislplaying a complex hummocky bathymetry (Fig. 4.1). In

the late Jurassic, when Pangaea separated, the first rifting episode initiated the formation of the basin. The second rifting episode in the Middle Jurassic was associated with the basin-wide deposition of thick evaporates. The Louann salt precipitated during this period sequestered ~8% of the world ocean NaCl (Land et al., 1988). Subsequently, during the early Cenozoic, the northwestern gulf basin established regionally extensive shallow-water siliclastic sediment deposits, and in the Miocene became the major depocenter for the sediments draining the central part of North America (Weimer et al., 1998). This large scale sediment deposition caused the original autochthonous salt layers to deform in one or more allochthonous levels due to extensive loading (Weimer et al., 1998).

Further active sedimentation, salt flow, and associated deformation resulted in the dynamic evolution of a series of salt highs and intraslope basins, creating the highly irregular topography in the northwestern Gulf of Mexico. The salt movement produced normal basinward dipping faults, thrust faults, and ramp faults. These faults trap prolific and expansive Mesozoic petroleum reservoirs at depth (Kennicutt et al., 1988) and provide efficient conduits for fluid and hydrocarbon migration to the seafloor (Roberts and Carney, 1997).

Thus the northern Gulf of Mexico is a “leaky” hydrocarbon province in which faults generated by active salt tectonics provide rapid migration of thergmogenic oil and hydrocarbons that have accumulated beneath large salt sheets. The extensive network of faults has created hundreds of active seafloor seeps (MacDonald et al., 1993; 2005; deBuekaelear, 2003) over a large area of seafloor (120,000 km^2 area) extending from ~200 to 2,000 m water depth. The seafloor manifestations of this prolific hydrocarbon

flux include gas vents, oils seeps, gas hydrates, chemosynthetic biological communities, and mud volcanoes (Milikov and Sassen, 2003; Roberts, 2001; Roberts and Carney, 1997; Sassen et al., 1994). The advecting methane, propane, and other gases form both Structure I and Structure II gas hydrates, which occur in shallowly buried deposits on the seafloor (Brooks et al., 1984). Not all of the seeps in the Gulf of Mexico are thermogenic, and there is a considerable amount of seeps fed by biogenic methane as well. The gas hydrates deposited at the seafloor in the northern Gulf of Mexico are near the P-T conditions at the 3-phase stability boundary (Sloan and Koh, 2008). Thus, unlike in settings with less vigorous methane fluxes where gas hydrates are buried tens to hundreds of meters below the seafloor, the shallow gas hydrates in the northern GOM are particularly vulnerable to changes in the bottom water temperature and subsurface methane flux.

Chapter 4 of this dissertation focuses on the dynamic fluid flow and chemical fluxes associated with seafloor gas hydrate deposits in the northern GOM, and Chapter 5 focuses on quantifying the methane flux to the atmosphere from perennial hydrocarbon plumes in the GOM. These chapters focus on 3 of the over 350 seeps in the northern GOM, that occur at depths ranging from ~550-600 m, and are representative of a variety of seafloor features and seepage processes in the Gulf of Mexico (Fig. 5.1). Sites GC 185 and GC 234 (lease block number) are fault related seeps containing gas hydrate outcrops that breach the seafloor. Perennial bubble plumes and drops of oil escape from numerous gas vents adjacent to the gas hydrate outcrops at these sites. GB 425 is a mud volcano occurring at a depth of ~600 m. Hydrocarbons are discharged in a steady stream in the center of the volcano.

GC 185, also known as Bush Hill, is the main GOM study site in this dissertation, and a brief review of its principle features is provided here. Bush Hill located at 27°47.5'N and 91°30.5'W is a fault-related seep at ~ 540 m water depth at the top of a ~500 m wide, ~40 m high topographic high (MacDonald et al., 2003). The Bush Hill site contains a persistent 2-3 m wide and ~ 0.65 m high gas hydrate mound only moderately covered by sediment, with gas hydrate outcropping at its flanks (Vardaro et al., 2005). The study area also contains several gas vents situated around the hydrate mound that continuously emit methane and other hydrocarbons to the water column. The Bush Hill vent site receives hydrocarbon gas and oils from a fault that is antithetic to growth faults that trap the Jolliet Field oil and gas reservoirs in nearby lease block GC 184 (Cook and D'Onfro, 1991; Roberts et al., 1992). The oil and gas venting at the Bush Hill site are linked to a 6-10 km deep Mesozoic hydrocarbon system that accumulates as oil and gas at 2-3 km depth beneath Jolliet Field (Kennicutt et al., 1988; Sassen et al., 1994, 2001), and the methane in the gas hydrates outcropping at the seafloor is dominantly thermogenic in origin. Thus, the gas hydrates are mainly structure-II type (Brooks et al., 1984; Sassen et al., 1999).

Seafloor photographic observations indicate that the morphology of the gas hydrate mound can alter significantly from year to year, with lobes intermittently breaking off, releasing methane and exposing fresh gas hydrate. Furthermore, spontaneous gas expulsion episodes at vents around the mound were recorded when bottom water temperatures exceeded 8 °C. (MacDonald et al., 1994). To this date, only a few long-term measurements of *in situ* temperature and fluid flux have been made at these seafloor gas hydrate deposits (Tryon and Brown, 2004; MacDonald et al., 2005).

In Chapter 4 we present the results of the continuous measurements of fluid chemistry, fluid flux, and temperature with a new fluid flow meter/chemical sampler, called the MOSQUITO, over a 15-month deployment period, and their time dependent variations and impact on gas hydrate stability and methane fluxes to the overlying water column. In Chapter 5 we present flux estimates of methane to the atmosphere from hydrocarbon plumes venting at Bush Hill and the two other seep sites in the northern Gulf of Mexico.

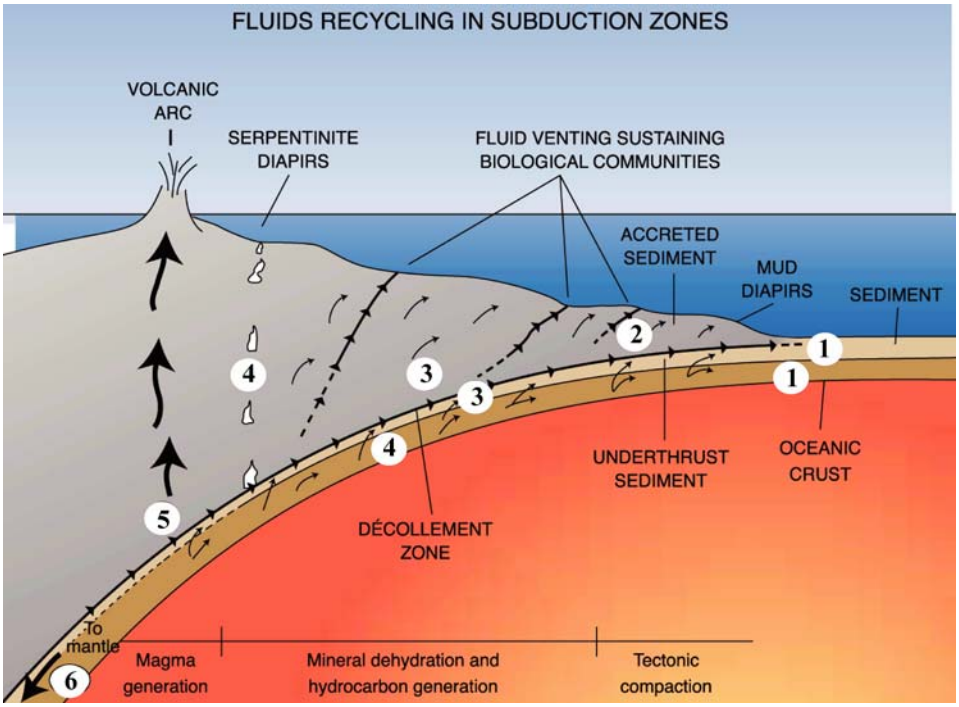

Figure 1.1 Schematic showing the fluid sources and flow pathways in subduction zones (modified from Kastner, 1997). 1. Fluid enters the subduction zone as sediment pore fluids, associated with clay minerals, in hydrous silicates, and in the hydrated oceanic crust; 2. clay dehydration and hydrocarbon generation; 3. dehydration of the oceanic crust and high temperature hydrous silicates; 4. serpentinization and diapirism; 5. magma generation; 6. residual water in mineral structures is transported to the mantle. Fluid pathways are diffuse to low advection through permeable sediments, advection along the décollement and thrust faults in the prism, and along the permeable oceanic basement.

References

Barckhausen, U., Ranero, C.R., von Huene, R., Cande, S.C., Reser, H.A., 2001. Revised tectonic boundaries in the Cocos Plate off Costa Rica: implications for the segmentation of the convergent margin and for plate tectonic models. J. Geophys. Res. 106, 19,207-19,220.

Barckhausen, U., Roeser, H.A., von Huene, R., 1998. Magnetic signature of upper plate structures and subducting seamounts at the convergent margin off Costa Rica. J. Geophys. Res. 103, 7079-7094.

Becker, K., Davis, E.E., 2006. A review of CORK designs and operations during the Ocean Drilling Program, in: Fisher, A.T., Urabe, T., Klaus, A. (Eds.), Proc. IODP Init. Rep. 301, College Station, TX (Integrated Ocean Drilling Program), doi:10.2204/iodp.proc.301.103.2005, pp. 39-52.

Behl, R.J., Kennet, J.P., 1996. Brief interstadial events in the Santa Barbara basin, NE Pacific, during the past 60 kyr. Nature 379, 243-246.

Bischoff, J.L., Pitzer, K.S., 1985. Phase relations and adiabats in boiling seafloor geothermal systems. Earth Planet. Sci. Lett. 75, 327-338.

Boetius, A., *et al.* Microscopic identification of a microbial consortium apparently mediating anaerobic methane oxidation above marine gas hydrates. *Nature* **407**, 623-626 (2000).

Brewer, P.G., 1999. Gas hydrates and global climatic change, in: Gas Hydrates, Challenges for the Future, Annals, N.Y. Acad. Sci.. 912, 195-199.

Brooks, J.M., Kennicutt II, M.C., Fay, R.R., MacDonald, T.J., Sassen, R., 1984. Thermogenic gas hydrates in the Gulf of Mexico. Science. 225, 409-411.

Brown, K.M., Tryon, M.D., DeShon, H.R., Dorman, L.M., Schwartz, S.Y., 2005. Correlated transient fluid pulsing and seismic tremor in the Costa Rica subduction zone. Earth Planet. Sci. Lett. 238, 189-203.
Byrne, T., 1988. Seismicity, slate belts and coupling along convergent plate boundaries. EOS, Trans. Am. Geophys. Union 79, p. W-114.

Carr, M.J., Feigenson, M.D., Patino, L.C., Walker, J.A., 2003. Volcanism and geochemistry in Central America: progress and problems, in: Eiler, J. (Ed.), Inside the Subduction Factory. AGU Geophys. Monogr. 138, pp. 153-174.

Chan, L.H., Kastner, M., 2000. Lithium isotopic compositions of pore fluids and sediments in the Costa Rica subduction zone: implications for fluid processes and sediment contribution to the arc volcanoes. Earth Planet. Sci. Lett. 183, 275-290.

Christeson, G.L., McIntosh, K. D., Shipley, T.H., Fleuh, E.R., Goedde, H., 1999. Structure of the Costa Rica convergent margin, offshore Nicoya Peninsula. J. Geophys. Res. 104, 25,443-25,468.

Claypool, G.E., Kaplan, I.R., 1974. The origin and distribution of methane in marine sediments, in: Natural Gases in Marine Sediments, Plenum, New York, pp. 99-139.

Cook, D., D'Onfro, P, 1991. Jolliet Field thrust fault structure and stratigraphy, Green Canyon block 184, offshore Louisiana. Trans. Gulf Coast Assoc. Geol. Soc. 41, 100-121.

D'Hondt, S., Rutherford, S., Spivack, A.J., 2002. Metabolic activity of subsurface life in deep-sea sediments. Science 295, 2067-2070.

Davis, D.J., Suppe, J., Dahlen, F.A., 1983. Mechanics of fold-and-thrust belts and accretionary wedges. J. Geophys. Res. 88, 1153-1172.

Davis, E. E., Villinger, H.W., 2006. Transient formation fluid pressures and temperatures in the Costa Rica forearc prism and subducting oceanic basement: CORK monitoring at ODP Sites 1253 and 1255. Earth. Planet. Sci. Lett. 245, 232-244.

Davis, E.E., Becker, K., Wang, K., Obara, K., Ito, Y., Kinoshita, M., 2006. A discrete episode of seismic and aseismic deformation on the Nankai trough subduction zone accretionary prism and incoming Philippine Sea Plate. Earth Planet. Sci. Lett. 242, 73-84.

De Beukelaer, S.M., 2003. Remote sensing analysis of natural oil and gas seeps on the continental slope of the northern Gulf of Mexico. [MSc. Thesis]: College Station, Texas A&M University, 128 p.

De Beukelaer, S.M., MacDonald, I.R., Guinnasso Jr., N.L., Murray, J.A., 2003. Distinct side-scan sonar, RADARSAT SAR, and acoustic profiler signatures of gas and oil seeps on the Gulf of Mexico slope. Geo-Mar Lett. 23, 177-186.

DeMets, C., Gordon, R.G., Argus, D.F., Stein, S., 1990. Current plate motions. Geophys. J. Int. 101, 425-478.

Dickens, G.R., Castillo, M.M., Walker, J.C.G., 1997. A blast of gas in the latest Paleocene: simulating first-order effects of massive dissocation of oceanic methane hydrate. Geology. 25, 259-262.

Dickens, G.R., Quinby-Hunt, M.S., 1997. Methane hydrate stability in pore water: a simple theoretical approach for geophysical applications. J. Geophys. Res. 102, 773-783.

Dillon, W.P., Danforth, W.W., Hutchinson, D.R., Drury, R.M., Taylor, M.H., Booth, J.S., 1998. Evidence for faulting related to dissociation of gas hydrate and release of methane from the southeastern United States, Gas Hydrates: Relevance to World Margin Stability and Climatic Change, in: Henriet, P.P., Mienert, J. (Eds.), Geol. Soc. Lond. Spec. Pub. 137, 293-302.

Dragert, H., Wang, K., James, T., 2001. A silent slip event on the deeper Cascadia subduction interface. Science 292, 1525-1528.

Dragert, H., Wang, K., Rogers, G., 2004. Geodetic and seismic signatures of episodic tremor and slip in the northern Cascadia subduction zone. Earth Planets Space 56, 1143-1150.

Fisher A, Stein, C.A., Harris, R.N., Wang, K., Silver, E.A., Pfender, M., Hutnak, M., Cherkaoui, A., Bodzin, R., Villinger, H., 2003. Abrupt thermal transition reveals hydrothermal boundary and role of seamounts within the Cocos Plate. Geophys. Res. Lett. 30 (11), doi:10.29/2002GL016766.

Fisher, A., Zwart, G., 1996. Relation between permeability and effective stress along a plate-boundary fault, Barbados accretionary complex. Geology 24, 317-310.

Fisher, A.T., Becker, K., 2000. Channelized fluid flow in oceanic crust reconciles heat-flow permeability data. Nature 403, 71-74.

Fisher, A.T., Davis, E.E., Hutnak, M., Spiess, V., Zuhlsdorff, L., Cherkaoui, A., Christiansen, L., Edwards, K., MacDonald, R., Villinger, H., Mottl, M.J., Wheat, C.G., Becker, K., 2003. Hydrothermal recharge and discharge across 50 km guided by seamounts on a young ridge flank. Nature 421, 618-621.

Fisher, A.T., Giambalvo, E., Sclater, J., Kastner, M., Ransom, B., Weinstein, Y., Lonsdale, P., 2001. Heat flow, sediment and pore fluid chemistry, and hydrothermal circulation on the east flank of the Alacron Ridge, Gulf of California. Earth Planet. Sci. Lett. 188, 521-534.

Fryer, P., Wheat, C.G., Mottl, M.J., 1999. Mariana blueschist mud volcanism: Implications for conditions within the subduction zone. Geology 27, 103-106.

Gagnon, K., Chadwell, C., Norabuena, E., 2005. Measuring the onset of locking in the Peru-Chile trench with GPS and acoustic measurements. Nature 434, 205-208.

Gamage, K., Screaton, E., 2006. Characterization of excess pore pressures at the toe of the Nankai accretionary complex, Ocean Drilling Program sites 1173, 1174, and 808: results of one-dimensional modeling. J. Geophys. Res. 111, B04103, doi:10.1029/2004JB003572.

Ge, S., Screaton, E., 2005. Modeling seismically induced deformation and fluid flow in the Nankai subduction zone. Geophys. Res. Lett. 32, doi:10.1029/2005GL023473.

Grevemeyer, I., Kopf, A.J., Fekete, N., Kaul, N., Villinger, H.W., Heesemann, M., Wallmann, K., Spiel, V., Gennerich, HH., Muller, M., Weinbre, W., 2004. Fluid flow through active mud dome Mound Culebra offshore Nicoya Peninsula, Costa Rica: Evidence from heat flow surveying. Mar. Geol. 207, 145-157.

Handa, Y.P., 1990. Effect of hydrostatic pressure and salinity on the stability of gas hydrates. J. Pys. Chem. 94, 2652-2657.

Harris, R.N., Fisher, A.T., Chapman, D., 2004. Fluid flow through seamounts and implications for global mass fluxes. Geology 38(2), 725-728.

Heesemann, M., Villinger, H., Jannasch, H.W., Kastner, M., and the Expedition 301T Scientists, 2006. Data Report: Long-term temperature measurements in Holes 1253A and 1255A off Costa Rica, ODP Leg 205. In: Morris, J.D., Villinger, H.W., Klaus, A. (Eds.), Proc. ODP, Sci. Results 205, College Station, TX (Ocean Drilling Program), 1–20. doi:10.2973/odp.proc.sr.205.209.2006

Hensen, C., Wallman, K., Schmidt, M., Ranero, C.R., Suess, E., 2004. Fluid expulsion related to mud extrusion off Costa Rica-A window to the subducting slab. Geology 32, 201-204.

Hubbert, M.K., Rubey, W.W., 1959. Role of fluid pressure in mechanics of overthrust faulting: I. Mechanics of fluid filled porous solids and its application to overthrust faulting. GSA Bulletin 70, 115-166.

Hutnak, M., Fisher, A.T., Stein, C.A., Harris, R., Wand, K., Silver, E., Spinelli, G., Pfender, M., Villinger, H., MacKnight, R., Costa Pisani, P., DeShon, H., Diamente, C., 2007. The thermal state of 18-24 Ma upper lithosphere subducting below the Nicoya Peninsula, northern Costa Rica margin. In: Interplate Subduction Zone Seismogenesis, Dixon, T., Moore, C. (Eds.), Columbia University Press, New York, pp. 86-122.

Hyndman, R.D., Wang, K., 1993. Thermal constraints on the zone of major thrust earthquake failure: The Cascadia subduction zone. J. Geophys. Res. 98, 2039-2060.

Hyndman, R.D., Wang, K., Yamano, M., 1995. Thermal constraints on the seismogenic portion of the southwestern Japan subduction thrust. J. Geophys. Res. 100, 15,373-15,392.

Hyndman, R.D., Yamano, M., Oleskevich D.A., 1997. The seismogenic zone of subduction thrust faults. Island Arcs 6(3), 244-260.

Ikari, M., Saffer, D.M., Marone, C., 2007. Effect of hydration state on the frictional properties of montmorillonite-based fault gouge. J. Geophys. Res. 112, B06423, doi:10.1029/2006JB004748.

James, R.H., Allen, D.E., Seyfried, W.E., 2003. An experimental study of alteration of oceanic crust and terrigeneous sediments at moderate temperatures (51 to 350 ^{o}C): Insights as to chemical processes in near-shore ridge-flank hydrothermal systems. Geochim. et Cosmochim. Acta 67, 681-691.

Jannasch, H., Davis, E.E., Kastner, M., Morris, J.D., Pettigrew, T.L., Plant, J.N., Solomon, E.A., Villinger, H.W., Wheat, C.G., 2003. CORK-II: Long-term monitoring of fluid chemistry, fluxes, and hydrology in instrumented boreholes at the Costa Rica subduction zone, in: Morris, J.D., Villinger, H.W., Klaus, A. (Eds.), Proc. ODP, Init. Repts. 205 [CD-ROM]. Available from: Ocean Drilling Program, Texas A&M University, College Station TX 77845-9547, USA.

Johnson, H.P., Pruis, M.J., 2003. Fluxes of fluid and heat from the oceanic crustal reservoir. Earth Planet. Sci. Lett. 216, 565-574.

Kastner, M., Elderfield, H., Jenkins, W.J., Gieskes, J.M., Gamo, T., 1993. Geochemical and isotopic evidence for fluid flow in the Western Nankai Subduction Zone, Japan, in: Winkler, W.R., Stewart, N.J. (Eds.), Proc. ODP Sci. Results 131, Ocean Drilling Program, College Station TX, pp. 397-413.

Kastner, M., Elderfield, H., Martin, J.B., 1991. Fluids in convergent margins: what do we know about their composition, origin, role in diagenesis, and important for oceanic chemical fluxes? Philisoph. Transact. Royal Society – London A 335, 243-259.

Kastner, M., 1997. Recycling processes and fluid fluxes in subduction zones, ODP's Greatest Hits, Joint Oceanographic Institutions, p. 16.

Kastner, M., Kvenvolden, K.A., Lorenson, T.D., 1998. Chemistry, isotopic composition, and origin of a methane-hydrogen sulfide hydrate at the Cascadia subduction zone. Earth Planet. Sci. Let. 156, 173-183.
Kennet, J.P., Cannariato, K.G., Hendy, I.L., Behl, R.J., 2000. Carbon isotope evidence for methane hydrate instability during quaternary interstadials. Science. 288, 128-133.

Kennicutt II, M.C., Brooks, J.M., Brigidare, R.R., Denoux, G.J., 1988. Gulf of Mexico hydrocarbon seep communities I. Regional distribution of hydrocarbon seepage and associated fauna. Deep Sea Res. Part A. 36, 1639-1651.

Kimura, G., Silver, E., Blum, P., et al., 1997. Proc. ODP, Init. Repts., 170: College Station, TX (Ocean Drilling Program).

Kvenvolden, K.A., 1999. Potential effects of gas hydrate on human welfare. Proc. Nat. Ac. Sci. 96, 3420-3426.

Land, L.S., Kupecz, J.A., Mack, L.E., 1988. Louann Salt geochemistry (Gulf of Mexico sedimentary basin, U.S.A.): a preliminary synthesis. Chem. Geol. 74, 25-35.

Langseth, M.G., Silver E.A., 1996. The Nicoya convergent margin: a region of exceptionally low heat flow. Geophys. Res. Lett. 23, 891-894.

Lockner, D., Byerlee, J., 1986. Laboratory measurements of velocity-dependent frictional strength. U.S. Geological Survey Open-File Report 86-417, 26p.

MacDonald, G., 1990. Role of methane clathrates on past and future climate. Climate Change. 16, 247-281.

MacDonald, I.R., Bender, L.C., Vardaro, M., Bernard, B., Brooks, J.M., 2005. Thermal and visual time-series at a seafloor gas hydrate deposit on the Gulf of Mexico slope. Earth Planet. Sci. Lett. 233, 45-59.

MacDonald, I.R., *et al.*, 1993. Natural oil slicks in the Gulf of Mexico visible from space. J. Geophys. Res. 98, 16,351-16,364.

MacDonald, I.R., Guinasso Jr., N.L., Sassen, R., Brooks, J.M., Lee, L., Scott, K.T., 1994. Gas hydrate that breaches the seafloor on the continental slope of the Gulf of Mexico. Geology. 22, 699-702.

MacDonald, I.R., Kastner, M., Leifer, I., 2005. Estimates of natural hydrocarbon flux in the Gulf of Mexico basin from remote sensing data. EGU General Assembly Proceedings, Abstract EGU-05-A-09970.

MacDonald, I.R., Leifer, I., Sassen, R., Stine, P., Mitchell, R., Guinasso J.R., N., 2002. Transfer of hydrocarbons from natural seeps to the water column and atmosphere. Geofluids. 2, 95-107.

MacDonald, I.R., Sager, W.W., Peccini, M.B., 2003. Gas hydrate and chemosynthetic biota in mounded bathymetry at mid-slope hydrocarbon seeps; northern Gulf of Mexico. Mar. Geol. 198, 133-158.

Marone, C., Saffer, D.M., 2007. Fault friction and the upper transition from seismic to aseismic faulting, in: Interplate Subduction Zone Seismogenesis, Dixon, T., Moore, C. (Eds.), Columbia University Press, New York, 30 pp.

Martin, J.B., Kastner, M., Henry, P., Le Pichon, X, Lallement, S., 1996. Chemical and isotopic evidence for sources of fluids in a mud volcano field seaward of the Barbados accretionary wedge, J. Geophys. Res., 101, 20325-20346, 10.1029/96JB00140.

Milikov, A.V., Sassen, R., 2003. Two-dimensional modeling of gas hydrate decomposition in the northwestern Gulf of Mexico: significance to global change assessment. Global and Planet. Change 36, 31-46.

Milikov, A.V., Claypool, G.E., Lee, Y-J., Xu, W., Dickens, G.R., Borowski, W.S., 2003. In situ methane concentrations at Hydrate Ridge, offshore Oregon: New constraints on the global gas hydrate inventory from an active margin Geology. 31, 833-836.

Moore, C.J., Saffer, D., 2001. Updip limit of the seismogenic zone beneath the accretionary prism of southwest Japan: An effect of diagenetic to low-grade metamorphic processes and increasing effective stress. Geology 29, 183-186.

Moore, J.C., Vrolijk, P., 1992. Fluids in accretionary prisms. *Rev. Geophys.* 30, 113-135.

Morris, J.D., Leeman, W.P., Tera, F., 1990. The subducted component in island arc lavas: constraints from Be isotopes and B-Be systematics. Nature 344, 31-36.

Morris, J.D., Villinger, H.W., Klaus, A., et al., 2003. Proc. ODP, Init. Rep., 205, Ocean Drilling Program, Texas A&M University, College Station, TX.

Newman, A.V., Schwartz, S.Y., Gonzalez, V., DeShon, H.R., Protti, J.M., Dorman, L.M., 2002. Along-strike variability in the seismogenic zone below Nicoya Peninsula, Costa Rica. Geophys. Res. Lett. 29, doi:10.1029/2002GL015409.

Nisbet, E.G., 1990. The end of the ice age. Can. J. of Earth Sci. 27, 148-157.

Nisbet, E.G., Piper, D.J.W., 1998. Giant submarine landslides. Nature 393, 329-330.

Norabuena, E., Dixon, T.H., Schwartz, S.Y., DeShon, H.R., Newman, A., Protti, M., Gonzalez, V., Dorman, L.M., Flueh, E.R., Lundgren, P., Pollitz, F., Sampson, D., 2004. Geodetic and seismic constraints on some subduction zone processes in Costa Rica. J. Geophys. Res. 109, doi:10.1029/2003JB002931.

Norris, R.D., Rohl, U., 1999. Carbon cycling and the chronology of climate warming during the Paleocene/Eocene transition. Nature 401, 775-778.

Obara, K., Hirose, H., Yamamizu, F., Kasahara, K., 2004. Episodic slow slip events accompanied by non-volcanic tremors in southwest Japan subduction zone. Geophys. Res. Lett. 31, doi:10.1029/2004GL020848.

Protti, M., Gonzalez T., Kato, T., Iinuma, T., Miyazaki, S., Obana, K., Kaneda, Y., LaFemina, P., Dixon, T., Schwartz, S., 2004. A creep event on the shallow interface of

the Nicoya Peninsula, Costa Rica seismogenic zone. EOS, Trans. Am. Geophys. Union, Fall Meet. Program Abstr. 85, F1378.

Ranero, C., von Huene, R., 2000. Subduction erosion along the Middle America convergent margin. Nature 404, 748-752.

Reeburgh, W.S., 2007. Oceanic methane biogeochemistry. Chem. Rev. 107, 486-513.

Reitz, A., Haeckel, M., Wallmann, K., Hensen, C., Heeschen, K., 2007. Origin of salt-enriched pore fluids in the northern Gulf of Mexico. Earth Planet. Sci. Lett. 259, 266-282.

Revelle, R., 1983. Methane hydrates in continental slope sediments and increasing atmospheric carbon dioxide, in: Changing Climate, National Acad. Press, Washington, DC, pp. 252-261.

Roberts, H.H., 2001. Fluid and gas expulsion on the northern Gulf of Mexico continental slope: mud-prone to mineral-prone responses, in: Paull, C.K., Dillon, W.P. (Eds.), Natural Gas Hydrates: Occurrences, Distribution, and Detection, Geophysical Monograph 124, Am. Geophys. Un., Washington, DC, pp. 145-161.

Roberts, H.H., Carney, R., 1997. Evidence of episodic fluid, gas, and sediment venting on the northern Gulf of Mexico slope. Econ. Geol. 92, 863-879.

Roberts, H.H., Cook, D.J., Sheedlo, M.K., 1992. Hydrocarbon seeps of the Louisiana continental slope: seismic amplitude signature and seafloor response. Gulf Coast Assoc. Geol. Soc. Trans. 42, 349-361.

Romanowicz, B., 1993. Spatiotemporal patterns in the energy release of great earthquakes. Science 260, 1923-1926.

Ruppel, C., Dickens, G., Castellini, D.G., Gilhooly, W., Lizarralde, D., 2005. Heat and salt inhibition of gas hydrate formation in the northern Gulf of Mexico. Geophys. Res. Lett. 32, L04605, doi:10.1029/2004GL021909.

Ruppel, C., Kinoshita, M., 2000. Fluid, methane, and energy flux in an active margin gas hydrate province, offshore Costa Rica. Earth Planet. Sci. Lett. 179, 153-165.

Saffer, D., McKiernan, A., 2005. Permeability of underthrust sediments at the Costa Rican subduction zone: scale dependence and implications for dewatering. Geophys. Res. Lett. 32, L02302, doi:10.1029/2004GL021388.

Saffer, D.M., 2003. Pore pressure development and progressive dewatering in underthrust sediments at the Costa Rican subduction margin: comparison with northern Barbados and Nankai. J. Geophys. Res. 108, 2261-2276.

Saffer, D.M., Bekins, B.A., 1998. Episodic fluid flow in the Nankai accretionary complex: timescale, geochemistry, flow rates and fluid budget. J. Geophys. Res. 103, 30351-30370.

Saffer, D.M., Bekins, B.A., 1999. Fluid budgets at convergent plate margins: Implications for the extent and duration of fault-zone dilation. Geology 27(12), 1095-1098.

Saffer, D.M., Marone, C., 2003. Comparison of smectite- and illite-rich gouge frictional properties: Application to the up-dip limit of the seismogenic zone along subduction megathrusts. Earth Planet. Sci. Lett. 215, 219-235.

Saffer, D.M., Silver, E.A., Fisher, A.T., Tobin, H., Moran, K., 2000. Inferred pore pressures at the Costa Rica subduction zone: Implications for dewatering processes. Earth Planet. Sci. Lett. 177, 193-207.

Sassen, R., Joye, S., Sweet, S.T., deFreitas, D.A., Milikov, A.V., MacDonald, I.R., 1999. Thermogenic gas hydrates and hydrocarbon gases in complex chemosynthetic communities, Gulf of Mexico continental slope. Org. Geochem. 30, 485-497.

Sassen, R., Losh, S.L., Cathles III, L., Roberts, H.H., Whelan, J.K., Milikov, A.V., Sweet, S.T., DeFreitas, D.A.,, 2001. Massive vein-filling gas hydrate: relation to ongoing gas migration from the deep subsurface of the Gulf of Mexico. Mar. Pet. Geol. 18, 551-560.

Sassen, R., MacDonald, I.R., Requejo, A.G., Guinasso, N.L., Kenicutt II, M.C., Sweet, S.T., Brooks, J.M., 1994. Organic geochemistry of sediments from chemosynthetic communities, Gulf of Mexico slope. Geo. Mar. Lett. 14, 110-119.

Scholz, C.H., 1998. Earthquakes and friction laws. Nature 391, 37-42.

Screaton, E., Carson, B., Davis, E., Becker, K., 2000. Permeability of a decollement zone: results from a two-well experiment in the Barbados accretionary complex. J. Geophys. Res. 105, 21,403-21,410.

Screaton, E., Hays, T., Gamage, K., Martin, J., 2006. Data report: Permeabilities of Costa Rica subduction zone sediments, in: Proc. ODP Sci. Res. 205 [Online], Available from World Wide Web: http://www-odp.tamu.edu/publications/205_SR/204/204.htm.

Screaton, E.J., Saffer, D.M., 2005. Fluid expulsion and overpressure development during initial subduction at the Costa Rica convergent margin. Earth Planet. Sci. Lett. 233, 361-374.

Shaw, A.M., Hilton, D.R., Fischer, T.P., Walker, J.A., Alvarado, G.E., 2003. Constrasting He-C relationships in Nicaragua and Costa Rica: insights into C cycling through subduction zones. *Earth Planet. Sci. Let.*, 214:499-513.

Shipley, T.H., Houston, M.H., Buffler, R.T., Richard, T., Shaub, F.J., McMillen, K.J., Ladd, J.W., Worzel, J.L., 1979. Seismic evidence for widespread possible gas hydrate horizons on continental slopes and rises. Bull. Am. Assoc. Pet. Geol. 62, 2204-2213.

Shipley, T.H., McIntosh, K.D., Silver, E.A., Stoffa, P.L., 1992. Three-dimensional seismic imaging of the Costa Rica accretionary prism: structural diversity in a small volume of the lower slope. J. Geophys. Res. 97, 4439-4459.

Sloan, E.D., Koh, C.A., 2008. Clathrate Hydrates of Natural Gases, 3rd Edition, CRC Press, Boca Raton, FL, 721 pp.

Solomon, E.A., Kastner, M., Robertson, G., 2006. Barium cycling at the Costa Rica convergent margin, in: Morris, J.D., Villinger, H.W., Klaus, A. (Eds.), Proc. ODP, Sci. Res. 205, College Station, TX (Ocean Drilling Program), doi:10.2973/odp.proc.sr.205.2006, pp. 1-22.

Spinelli, G.A., Saffer, D.M., 2004. Along-strike variations in underthrust sediment dewatering on the Nicoya margin, Costa Rica related to the updip limit of seismicity. Geophys. Res. Lett. 31, doi:10.1029/2003GL018863.

Spinelli, G.A., Saffer, D.M., Underwood, M.B., 2006. Hydrogeologic responses to three-dimensional temperature variability, Costa Rica subduction margin. J. Geophys. Res. 111, B04403, doi:10.1029/2004JB003436.

Spivack, A.J., Kastner, M., Ransom, B., 2002. Elemental and isotopic chloride geochemistry and fluid flow in the Nankai Trough. Geophys. Res. Lett. 29, doi:10.1029/2001GL014122.

Stein, C.A., Stein, S., 1992. A model for the global variation in oceanic depth and heat flow with lithospheric age. Nature 359, 123-137.

Tryon, M.D., Brown, K.M., 2004. Fluid and chemical cycling at Bush Hill: implications for gas-and hydrate-rich environments. Geochem. Geohpys. Geosyst. 5, doi:10.1029/2004GC000778.

Valentine, D.L., Blanton, D.C., Reeburgh, W.S., Kastner, M., 2001. Water column methane oxidation adjacent to an area of active hydrate dissociation, Eel River Basin. Geochim. et Cosmochim. Acta 65(16), 2633-2640.

Vannucchi, P., Ranero, C.R., Galeotti, S., Staub, S.M., Scholl, D.W., McDougall-Reid, K., 2003. Fast rates of subduction erosion along the Costa Rica margin: Implications for nonsteady rates of crustal recycling at subduction zones. J. Geophys. Res. 108, doi:10.1029/2002JB002207.

Vannucchi, P., Scholl, D.W., Meschede, M., McDougall-Reid, K., 2001. Tectonic erosion and consequent collapse of the Pacific margin of Costa Rica: combined implications from ODP Leg 170, seismic offshore data, and regional geology of the Nicoya Peninsula. Tectonics 20, 649-668.

Vardaro, M.F., MacDonald, I.R., Bender, L.C., Guinasso, Jr., N.L., 2005. Dynamic processes observed at a gas hydrate outcropping on the continental slope of the Gulf of Mexico. Geo. Mar. Lett. 26. 6-15.

Von Huene, R., Ranero, C.R., Vannucchi, P., 2004. Generic model of subduction erosion. Geology 32(10), 913-916.

Von Huene, R., Ranero, C.R., Weinrebe, W., Hinz, K., 2000. Quaternary convergent margin tectonics of Costa Rica, segmentation of the Cocos Plate, and Central American volcanism. Tectonics 19, 314-334.

Von Huene, R., Scholl, D. W., 1991. Observations at convergent margins concerning sediment subduction, subduction erosion, and the growth of continental crust. Reviews of Geophysics 29(3), 279-316.

Vrolijk, 1990. On the mechanical role of smectite in subduction zones. Geology 18, 703-707.

Wei, W., Kastner, M., Spivack, A.J., in press. Chlorine stable isotopes and halogen concentrations in convergent margins with implications for the Cl isotopes cycle in the ocean. Earth Planet. Sci. Lett., Manuscript No. EPSL-D-07-00670.

Weimer, P., Rowan, M.G., McBride, B.C., Kligfield, R., 1998. Evaluating the petroleum system of the Northern deep Gulf of Mexico though integrated analysis: an overview. AAPG Bull. 82(5B), 865-877.

You, C.F., Castillo, P.R., Gieskes, J.M., Chan, L.H., Spivack, A.J., 1996. Trace element behavior in hydrothermal experiments: Implications for fluid processes at shallow depth in subduction zones. Earth Planet. Sci. Let. 140, 41-52.

You, C.F., Gieskes, J.M., 2001. Hydrothermal evolution of hemi-pelagic sediments: experimental evaluation of geochemical processes in subduction zones. Applied Geochem. 16, 1055-1066.

Zatsepina, O.Y., Buffet, B.A., 1998. Thermodynamic conditions for the study of gas hydrate in the seafloor. J. Geophys. Res. 103, 24,127-24,139.

Chapter 2

Hydrogeochemical Transience Along the Décollement and Subducting Igneous Basement at the Costa Rica Margin

2.1 Abstract

Osmotically pumped fluid samplers and a new borehole fluid flow meter were deployed during Ocean Drilling Program (ODP) Leg 205 in CORKed borehole observatories installed in two active hydrogeochemical systems at the Costa Rica subduction zone. Downhole instrumentation was deployed at Site 1253 situated ~0.2 km seaward of the trench in the upper igneous basement and at Site 1255 located ~0.5 km landward of the trench in the décollement. The continuous monitoring of fluid flow rates and chemistry is part of a larger coordinated effort involving simultaneous pressure and temperature recording. The data collected by this interdisciplinary effort constitute the first co-registered chemical, physical, and hydrological time-series from a subduction zone providing critical information on the average and transient hydrogeochemical state of the subduction thrust and upper igneous basement. The results from the long-term fluid monitoring at Site 1253 indicate that the basement fluid is a 2-component mixture of modified seawater (~90%) and a subduction zone fluid originating within the forearc (~10%). The significant fraction of subduction zone fluids suggests the upper basement serves as an efficient pathway for fluids expelled from the forearc that should be included in models of subduction zone hydrogeology and deformation. The estimated steady-state fluid flow rate in the basement section is 0.3 m/yr and the coupled chemical and pressure time-series indicate that the uppermost igneous basement is highly permeable. At Site 1255, three transients in fluid flow rates were observed along the décollement, two of which coincided with stepwise increases in formation pressure. These two transients are manifested by a rise in flow rates a few days prior to the pressure pulses, and correlate with onshore deformational events

recorded on the Nicoya Peninsula. We suggest they are the result of aseismic slip dislocations that ruptured through the seismogenic zone and propagated up-dip over the course of ~2 weeks, with slip terminating before reaching Site 1255, or the trench. The nature and temporal behavior of strain and the associated hydrological response during these slow slip events may provide an analog for the response prior to and during large subduction zone earthquakes.

2.2 Introduction

Active fluid flow in subduction zones can have a profound impact on the shallow thermal structure and fluid content of the subducting plate (e.g. Hyndman and Wang, 1993; Lansgseth and Silver, 1996; Scholz, 1998; Spinelli and Saffer, 2004; Zhao et al., 1997), fault zone stability and seismogenesis (e.g. Davis et al., 1983; Hubbert and Rubey, 1959), and the transfer of elements and isotopes to the oceans, volcanic arc, and the mantle (e.g. Chan and Kastner, 2000; Fryer et al., 1999; Martin et al., 1996; Moore and Vrolijk, 1992). However, the magnitude of fluid egress, the temporal variability of fluid flow and composition, and the forces that drive fluid flow during the seismic cycle are poorly constrained. Thus, constraining the nature and magnitude of fluid flow at convergent margins is critical in understanding the impact of hydrogeochemical processes on seismicity and volcanism at subdcution zones.

Ocean Drilling Program (ODP) Legs 170 (Kimura et al., 1997) and 205 (Morris et al., 2003) were dedicated to the investigation of tectonic and hydrological processes, and the study of mass and geochemical fluxes at the Costa Rica subduction zone (SZ), offshore the Nicoya Peninsula (Fig. 2.1a). The Costa Rica margin is an erosional

margin (Ranero and Von Huene, 2000; Vannucchi et al., 2001; 2003), where all of the incoming sediment is initially subducted beneath the prism (Fig. 2.1b). Sediment composition and physical properties, the pore fluid chemical composition, pressure, and temperature obtained during ODP Legs 170 and 205 identified two distinct active hydrological systems (Chan and Kastner, 2000; Silver et al., 2000). The first occurs within the upper igneous basement beneath the sedimentary sequence on the incoming plate (ODP Sites 1039/1253; Fig. 2.1b). Low heat flow values of ~30 mW/m^2 exist in the EPR-generated crust offshore Costa Rica, and the heat flow value at Site 1253 is extremely low at 10 mW/m^2 (Fisher et al., 2003; Heesemann et al., 2006; Langseth and Silver, 1996). These values represent ~30 and 10%, respectively, of the expected value from conductive lithospheric cooling models for a Cocos crust age of 24 Ma (Stein and Stein, 1994), indicating effective hydrothermal cooling of the upper oceanic crust in the study area. This inference is corroborated by pore fluid chemical and isotopic profiles in basal sediments that show a return to seawater values near the upper igneous basement (Chan and Kastner, 2000; Morris et al., 2003; Silver et al., 2000). The geochemical results indicate that the basement is hydrologically coupled to a fluid chemically similar to bottom water with recharge and discharge occurring at distant igneous outcrops (Fisher et al., 2003; Hutnak et al., 2007; Langseth and Silver, 1996). In addition to the cooling effect, the vigorous lateral flow of contemporaneous seawater in the upper crust offshore Costa Rica must also alter and hydrate the igneous crust, affecting chemical and isotopic mass balances, as well as the transfer of volatiles to the depth of magma generation and the mantle.

The second fluid flow system is observed along the plate boundary, the décollement, and in an out-of-sequence thrust fault in the prism. It was sampled at two sites: 1040/1254 and 1043/1255 at ~1.6 km and ~0.5 km landward of the deformation front, respectively (Fig. 2.1b). The pore fluids recovered in the décollement and thrust fault at Sites 1040 and 1254 have elevated Li concentrations (Chan and Kastner, 2000), are enriched in Ca and C_3-C_6 hydrocarbons, and depleted in K, Cl, and Mg concentrations (Kimura et al., 1997; Morris et al., 2003). Similar depletions in Cl and K, enrichments in Li, Ca, B, and heavier hydrocarbons have been observed in fluids sampled in mud volcanoes along the Costa Rica and Marianas margins (Grevemeyer et al., 2004; Hensen et al., 2004; Fryer et al., 1999), and in the Barbados and Nankai accretionary prisms (Kastner et al., 1993; Martin et al., 1996; Spivack et al., 2002). Collectively, these data indicate that this flow system is active and a fraction of the fluid is derived from depths within the SZ where temperatures are ~80-150 ^{o}C (Chan and Kastner, 2000; Hensen et al., 2004; Martin et al., 1996; You et al., 1996; Wei et al., in press), which is near the temperature estimated for the up-dip limit of the seismogenic zone (Hyndman et al., 1997; Spinelli and Saffer, 2004).

On the basis of these findings, two CORK (Circulation Obviation Retrofit Kit) long-term borehole observatories were successfully installed during ODP Leg 205 in the two fluid flow systems: one in a fractured interval in the upper igneous basement in the incoming plate at Site 1253 and one in the décollement at Site 1255 (Fig. 2.1b). Downhole instruments continuously recorded fluid flow rates and collected a time series of fluids for analysis of dissolved and gaseous species over a period of ~700 days from October 2002 to September 2004. The continuous fluid flow rate and chemical

monitoring is part of a larger interdisciplinary coordinated effort involving simultaneous pressure and temperature recording (Davis and Villinger, 2006; Heesemann et al., 2006; Jannasch et al., 2003). The data collected constitute the first co-recorded chemical, physical, and hydrologic time series from a SZ system. The results have implications for the hydration of the upper igneous crust and geochemical mass balances at subduction zones, the role of the upper basement in fluid transport from the SZ, for episodic strain and fluid flow along the décollement, and the temporally variable behavior of plate boundary motion during both seismic and interseismic periods.

2.3 Methods

2.3.1 CORK-II Installations and Borehole Instrumentation

Two CORK-II subseafloor hydrogeological observatories were installed at ODP Sites 1253 and 1255 for long-term sampling of fluids and gases, as well as for monitoring fluid pressure, temperature, and flow rates (Morris, Villinger, and Klaus et al., 2003). Complete descriptions of the CORK-IIs are given in Becker and Davis (2006), Davis and Villinger (2006), Jannasch et al. (2003), and Kastner et al. (2006). Thus, only a brief summary is provided here. These CORK-IIs contain two mechanical seals (1) at the seafloor, between the primary 10 ¾ in. diameter formation casing and the 4 ½ in. CORK-II casing, to prevent flow of bottom water into the borehole (Fig. 2.2a), and (2) located at the bottom of the 4 ½ in. casing where the downhole instrumentation is located, to restrict mixing of formation fluids with bottom water introduced into the borehole during drilling operations. The 4 ½ in. casing contains a single external inflatable packer at an intermediate position within the formation that

isolates the interval that spans from the bottom of the hole to the packer (Fig. 2.2a). Formation pressures are transmitted to sensors at the wellhead by hydraulic umbilicals that terminate within screened intervals. The fluid samplers powered by osmotic pumps (OsmoSamplers) are situated below the seal at the base of the CORK-II casing, along with a fluid flow meter (at Site 1255) and temperature sensors that continuously record at sub-mK resolution (Jannasch et al., 2003). The OsmoSampler packages are positioned to sample within the screened interval (Fig. 2.2a). The screen wraps around the full circumference of the OsmoSampler package, and is 7.6 m long.

The OsmoSampler (OS) consists of two chambers separated by semi-permeable membranes, one filled with distilled water and the other with saturated saline solution as described in Jannasch et al. (2003; 2004). A contiguous small bore Teflon coil (copper for gases), filled with de-gassed distilled water, is connected to the distilled water chamber (Fig. 2.2b). The osmotic pressure drives a net flow of distilled water across the membranes to the saturated saline chamber, and continuously pulls distilled water through the Teflon tubing and samples in situ pore fluids at the other end. Sample smearing due to static and dynamic diffusion and mixing is kept to a minimum by the use of the small bore tubing (1.2 mm ID) and low pump rates (~0.45 ml/day). The flow meter pumps sampled at a rate of 0.22 ml/day. The OsmoSamplers and coils (Fig. 2.2b) were housed in a protective stainless steel outer tube that fits within the 4 ½ in. CORK-II casing annulus. After recovery, the Teflon tubing is divided into sections of appropriate length for chemical analyses and desired temporal resolution, and the copper tubing is crimped and frozen. The OsmoSampler coils were subsampled at 10-

day resolution, and the flow meter coils were sub-sampled at ~7-day resolution. The data points were time-stamped at the midpoint of each integrated sample.

The OS package at Site 1255 is capable of being recovered and redeployed without losing pressure within the sampling environment. This is the only CORK site with this capability, and is accomplished with a custom OS seat which has a plunger-seal design that is penetrated with a titanium sampling probe (Jannasch et al., 2003). The OS seat contains a 1 ½ in. hole sealed with a plunger that can be pushed down by the sampling probe to expose a 12 in. inner section of screen open to the pressurized décollement. The plunger is pulled up and closes the 12 in. inner screen during recovery. The outer screen is 7.6 m long to concentrate flow within its depth range to the 12 in. inner screen. The OS packages at Site 1255 contained 2 Teflon and 2 copper OsmoSamplers and a newly designed Osmoflow-meter. The OSs are encapsulated in a pressure housing that sits above the OS seat and is rigidly attached to the Ti sampling probe. The intakes of the OS coils sample formation fluid through the Ti probe below the pressure seal in the screened interval at 140 mbsf in the décollement. The packages were deployed in November 2002 and recovered in September 2004, providing a ~670 day record of fluid chemistry and flow rates. They were redeployed in September 2004 for an additional four years of continuous sampling.

Two OS packages were deployed within fractured intervals in the igneous basement at Site 1253, each consisting of 2 Teflon and 2 copper OSs. The OS packages contained a simple pressure seal above the sampling depth. Unlike at Site 1255, the pressure seal at Site 1253 is broken during redeployment, briefly allowing bottom water to enter the formation. The upper OS package was positioned within the screened

interval at 500 mbsf, and the lower OS package was located at 516 mbsf below the casing in the open hole. Both OS packages were deployed in October 2002 and recovered fluids for ~700 days, and were redeployed in September 2004. During the instrument recovery in September 2004, the line connecting the two packages snapped, and only the upper OS package was recovered. The lower OS package is currently on the seafloor, and will be recovered during the next CORK servicing expedition.

The Osmoflow-meter deployed at Site 1255 consists of two perpendicular ¼ in. holes bored through the Ti sampling probe. A rubidium tracer solution was added directly into the center, and four OsmoSamplers sample 1 cm away from the tracer input in each of the four branches (Fig. 2.2c). The tracer is injected continuously from a coil connected to the brine output of one of the OsmoSamplers. The flow meters record the relative direction of fluid flow by the presence and concentration of the tracer. The flow rate is computed from the relative dilution of the tracer across the central tracer injection point (Fig. 2.2c). The flow rate calculations are provided in the supplementary information section. Due to variations in the sampling rates between Pump 3 (P_3, Fig. 2.2c) and Pump 4, there was insufficient time overlap between samples to compute flow rates. Thus, only the flow rates between Pumps 1 and 2 (P_1 and P_2, Fig. 2c) are presented in this manuscript.

2.3.2 Analytical Methods

Pore fluid samples collected by the OsmoSamplers were filtered through disposable 0.45 μm Gelman polysulfone filters. Sub-samples for Mg, Ca, Sr, Ba, K, Li, Rb, and B concentrations, $^{87}Sr/^{86}Sr$ ratios, and δ^7Li values were stored in acid-cleaned polypropylene centrifuge tubes and acidified with Optima nitric acid. Aliquots for

sulfate analyses were added to centrifuge tubes containing a 50% $CdNO_3$ solution to precipitate the sulfide. Sub-samples for $\delta^{18}O$ analyses were stored in glass ampoules. Ca, Mg, Sr, SO_4, K, and B concentrations were determined via inductively coupled plasma-optical emission spectrometry (ICP-OES). Lithium, Rb, and Ba concentrations were analyzed by inductively coupled plasma-mass spectrometry (ICP-MS). The Sr isotope ratios and Li isotopic compositions were measured by thermal ionization mass spectrometry (TIMS), and $\delta^{18}O$ via a stable isotope ratio mass spectrometer (SIRMS).

All samples, standards, and blanks were prepared in a clean laboratory, and all dilutions were made with 18.2 M-ohm milli-Q water. Elemental concentrations were determined by working curves, and the reproducibility of the elemental analyses expressed as percent precisions from multiple determinations of certified standards are: Mg = 0.55%, Ca = 0.63%, Sr = 0.8%, Ba = 0.5%, SO_4 = 0.8%, K = 1%, Li = 0.7%, Rb = 0.5%, and B = 0.9%. The average accuracy of each analysis was determined by analyzing certified standards as unknowns and are: Mg = 1.1%, Ca = 0.9%, Sr = 1%, Ba = 0.9%, SO_4 = 0.8%, K = 1.4%, Li = 1%, Rb = 1%, and B = 0.9%. All of the analytes measured, including the fluid flow tracer at Site 1255 (Rb), were above detection limits. Strontium isotope ratios were fractionation corrected to $^{86}Sr/^{88}Sr = 0.1194$ and are reported relative to $^{87}Sr/^{86}Sr = 0.710257$ for NBS 987. The 2σ errors in the Sr isotope ratios are smaller than the external precision of ±0.000020. The isotopic abundance of dissolved Li was determined using Li_3PO_4 as ion source material with a precision of ~1‰. The Li isotopic compositions are expressed as δ^7Li, per mil deviation of $^7Li/^6Li$ from that of the L-SVEC lithium carbonate standard (You and Chan, 1996). The

oxygen isotopic compositions are expressed as $\delta^{18}O$, per mil deviation from VSMOW, with an average 2σ error of ± 0.03‰.

Select sediment samples collected during ODP Legs 170 and 205 were analyzed for $^{87}Sr/^{86}Sr$ ratios. The sediment samples were digested with a 2:1 mixture of HF and HNO_3 following the methods outlined in Solomon et al. (2006). All digestions and subsequent dilutions were performed in a clean laboratory, and the average 2σ standard deviation of the $^{87}Sr/^{86}Sr$ analyses was ± 0.000018.

2.4 Results

2.4.1 Igneous Basement Formation Fluid Chemistry at Site 1253

Evidence for vigorous shallow flow of seawater within the igneous basement at Sites 1253 and 1039 has been provided by heat flow surveys (Fisher et al., 2003; Langseth and Silver, 1996; Hutnak et al., 2007) and pore fluid chemical profiles (Chan and Kastner, 2000; Morris et al., 2003; Silver et al., 2000). The results of the long-term monitoring of pressure and temperature at Site 1253 (Davis and Villinger, 2006; Heesemann et al., 2006) corroborate these inferences. The long-term temperature record reaches an asymptote of 7.944 ^{o}C over the 700-day deployment, which corresponds to a Site 1253 heat flux of 10 mW/m^2 (Heesemann et al., 2006). Pressure recorded in the upper basement is subhydrostatic by ~6 kPa (Davis and Villinger, 2006), despite the close proximity to the consolidating subduction complex. This slight underpressure suggests that the upper basement is highly permeable and well-connected to points of seawater recharge at distant igneous outcrops (e.g. Hutnak et al., 2007).

Given the high basement permeability and near hydrostatic state, it could serve as an efficient pathway for fluids being expelled from the prism and subducting sediments.

During coring, only sediments can be sampled for pore fluids; the igneous basement fluid composition can only be inferred from these pore fluid profiles. The OsmoSamplers, however, directly sample the basement formation fluid, and can monitor temporal variations in the fluid chemistry. Previous studies have interpreted the return to approximate seawater concentrations in basal sediment pore water profiles of Ca, Mg, Li, and SO_4 to be the result of rapid lateral flow of unaltered seawater in the basement at Site 1253/1039 (Morris et al., 2003; Silver et al., 2000). The results of the long-term continuous sampling of formation fluid chemistry in the igneous basement, however, shows the fluid to be moderately altered with respect to modern seawater (Fig. 2.3 and 2.4).

Mg, Ca, Sr, Li, Rb, and B concentrations rapidly evolve from near-seawater to near-steady-state concentrations that are altered with respect to seawater within 34 days after the OsmoSampler installation (Fig. 2.3 and 2.4). This rapid evolution from bottom water values to steady-state formation concentrations requires vigorous flow of formation fluid and efficient mixing of formation fluids with introduced borehole fluids below the pressure seal. After the first 34 days, the concentrations gradually change to steady-state values from November 14, 2002 to March 4, 2004, reflecting a slower fluid flow rate and more gradual mixing of formation fluids with the residual borehole fluids (Fig. 2.3). On March 4, 2004, there is an abrupt change in concentrations to seawater-like values when the borehole was briefly opened during an *Alvin* instrument recovery attempt (Fig. 2.3 and 2.4). During the recovery attempt, the seal above the OS packages

was briefly opened. The borehole then remained closed for six months until the instrument recovery in September 2004. During this period, the elemental concentrations did not return to the previous steady-state values, and the rate of change of the concentrations was similar to that in the middle of the deployment period (Fig. 2.3).

The steady-state Ca and Mg concentrations are ~3 times and ½ seawater concentration, respectively (Fig. 2.3a), and the B concentrations sampled in the basement are ¼ seawater value (Fig. 2.3c). The elevated Ca and depleted Mg and B concentrations are consistent with typical seawater-basalt reactions at low temperatures along ridge-flanks (e.g. Gieskes and Lawrence, 1981; Lawrence et al., 1975; McDuff, 1981; McDuff and Gieskes, 1976; Spivack and Edmond, 1987). The steady-state Sr concentration is 23% greater than seawater, and the Li concentrations are ~2 times seawater value (Fig. 2.3b). Rb and Ba concentrations are elevated with respect to seawater; ~2.5 and 4 times seawater value, respectively (2.3c, 2.4a). Potassium and SO_4 concentrations are slightly below seawater value (2.4 b,c), and the $\delta^{18}O$ values sampled in the basement are depleted with respect to seawater, indicating minor hydration of the upper oceanic crust in the study area (Fig. 2.3b).

There are two well studied ridge flank hydrothermal systems in the vicinity of Site 1253, ODP Site 504B on the southern flank of the Costa Rica rift (Mottl, 1989) and a TicoFlux site on the Cocos Plate ~30 km to the east of Site 1253 (Parsons et al., submitted). The Ca concentrations sampled in the igneous basement at Site 1253, though elevated above bottom water value, are only 31% of those at the nearby TicoFlux site and 60% of the Ca value at Site 504B. Likewise, Mg concentrations are

five and ~25 times those measured at the TicoFlux site and Site 504B, respectively. These two systems have much higher formation temperatures than Site 1253 enabling more effective chemical exchange between seawater and basalt. The relatively lower Ca and higher Mg concentrations reflects less chemical exchange at the low *in situ* temperate of 7.94 ^{o}C at Site 1253. The strong depletion in boron concentrations further suggests that seawater is modified by secondary hydrous mineral formation in the basement. This inference is corroborated by the slight depletion in the $\delta^{18}O$ values, also indicative of hydrous mineral formation. The low temperature alteration of the uppermost basement impacts the hydration state and physical properties of the subducting slab, and the formation of hydrous minerals provides a source of water to deeper levels of the subduction zone. Collectively the chemical data at Site 1253 suggest the main component of the fluid sampled in the upper basement is modified seawater typical of low temperature ridge-flank fluids that is likely part of the regional fluid flow system that is responsible for the low heat flow in the Cocos plate in this region. The elevated Li, Rb, Sr, and Ba concentrations, however, indicate there may be another fluid source that is not typical of ridge-flank fluids.

Results from seawater-basalt experiments at temperatures ranging from 51 to 350 ^{o}C (James et al., 2003) and detailed fluid sampling at the eastern flank of the Juan de Fuca Ridge (Butterfield et al., 2001; Wheat and Mottl, 2000) show that Li is typically depleted in ridge flank hydrothermal systems due to secondary Mg-mineral precipitation, and that Rb concentrations are typically that of seawater or slightly depleted. The moderately elevated Li concentrations measured at Site 1253 (~60 μM) and enriched Rb suggest that a component of the fluid sampled in the basement may be

from an additional source, which is clearly indicated by the steady-state $^{87}Sr/^{86}Sr$ isotopic ratio in the formation fluid sampled at Site 1253 (Fig. 2.5a). Twelve samples were analyzed for $^{87}Sr/^{86}Sr$ ratios, and the average formation fluid $^{87}Sr/^{86}Sr$ ratio is 0.709690, which is more radiogenic than modern seawater (seawater = 0.70916). The Sr isotopic composition of the upper igneous basement fluid is not typical of ridge flank fluids, which exhibit Sr isotope ratios that are less radiogenic than seawater. The $^{87}Sr/^{86}Sr$ ratio of the nearby TicoFlux fluids is 0.7071 (Parsons et al., submitted) and the $^{87}Sr/^{86}Sr$ ratio of East Pacific Rise fluids is 0.7041 (Von Damm, 1995; Fig. 2.5a). Relict seawater would also have a Sr isotope ratio that is less radiogenic than modern seawater (Paytan et al., 1993). Thus, the Site 1253 formation fluid Sr-isotopic composition indicates mixing of seawater with a sediment component that is more radiogenic than modern seawater.

The OSs collected fluids in a gabbro sill complex with interbedded "baked" sediments (Morris et al., 2003). The basal sediments at Site 1253/1039 are pelagic carbonates dated at ~16 Ma (Muza, 2000; Strasser et al., 2006). Given the Cocos Plate convergence rate of 87 km/Myr (DeMets et al., 1990) and the age of the sediments, the basal pelagic sediments as well as the "baked" sediments were deposited near the equator 1,390 km southwest of the current position of Site 1253. This position indicates that these sediments should be predominantly carbonates with very little clay content. The gabbro sill complex is the result of Galapagos overprinting 10-14 Ma (Dreyer et al., 2006), and the interbedded sediments and pelagic sediments above the sill complex should have a $^{87}Sr/^{86}Sr$ ratio of 16 my old seawater or less due to hydrothermal overprinting. Thus, the source of the radiogenic sediment component is most likely

from within the Costa Rica SZ. The $^{87}Sr/^{86}Sr$ ratios of representative fluids sampled from key formations during ODP Legs 170 and 205 are presented in Figure 2.5a. The Sr isotope ratios of the fluids collected from Site 1253/1039, as well as from the décollement and underthrust sediments at Site 1254/1040 are also less radiogenic than seawater.

In an effort to constrain the source of the radiogenic end member, the bulk Sr-isotopic composition of a representative suite of sediment samples collected during Legs 170 and 205, including the "baked" sediments, were analyzed (Table 2.1). All the samples analyzed to date are less radiogenic than seawater, ranging from 0.705778 in the prism at Site 1040 to 0.708525 for the "baked" sediments at Site 1253, with differences in the isotopic composition reflecting varying amounts of volcanic ash. This does not preclude the sediment source from originating within the SZ, the average $^{87}Sr/^{86}Sr$ ratio of global subducted sediment is 0.7173 (Plank and Langmuir, 1998), but if this is the case, it indicates that the sediment source was not sampled during Legs 170 and 205. Overall, the radiogenic Sr isotope ratios and elevated Li and Rb concentrations in the fluids sampled in the upper igneous basement at Site 1253 are not typical of contemporary seawater or a ridge-flank fluid, and indicate that a portion of the fluid likely originates within the subduction complex (Fig. 2.6). This supports the inference that the basement serves as an efficient hydrologic pathway channeling fluids from the prism and subducting sediments as shown schematically in Fig. 2.6.

2.4.2 Fluid Flow Rates and Chemistry in the Décollement at Site 1255

The borehole instrumentation at Site 1255 focused on sampling within the décollement at ~140 mbsf where fluid flow rates are the highest based on anomalies in

Cl, K, and Ca concentration depth profiles (Morris et al., 2003; Fig. 2.6). Fluid flow rates measured by the new borehole flow meter are highly transient (Fig. 2.7), ranging from 0.02 to 5 cm/yr with an average flow rate of 1 cm/yr. A baseline flow rate of ~0.5 cm/yr was reached by January 2003 after a 3 month period of elevated flow rates likely related to post-installation borehole recovery and the collapse of the formation around the screened interval, as also observed in the pressure record (Davis and Villinger, 2006).

Superimposed on the background flow rates are three transient events, two of which correlate with changes in the long-term pressure record (Fig. 2.7). The first transient is manifested by an increase in flow rates on May 21, 2003 with a peak flow rate of 1.7 cm/yr on May 28, 2003, followed by a steady decline to background flow by June 22. This event is observed in the pressure record as a sharp increase in formation pressures over a 2-day period with a peak on May 24 (Fig. 2.7). The second flow rate transient was much weaker, occurred on October 12, 2003, and is coincident with an increase in fluid pressure. Both transients correlate with deformational episodes observed during a continuous GPS monitoring experiment at 3 sites directly onshore from the CORK sites on the Nicoya Peninsula (Protti et al., 2004). Both onshore deformation events initiated near the coast and propagated inland over a 2-3 week period with no associated detectable earthquakes, suggesting they reflect aseismic slow slip events. The third transient in flow rates occurred on March 12, 2004 manifested by a 4-fold increase in flow rates that persisted to the end of the deployment period. Unfortunately, the pressure record only spans from the CORK installation to the *Alvin*

recovery attempt on March 4, 2004, thus this transient is not present in the pressure record collected most recently.

All of the analytes measured in the formation fluids exhibit the same temporal concentration patterns, thus only Sr is presented in Figure 2.7. During the first 3 months of deployment, Sr concentrations decline from seawater value to concentrations that reflect surface seawater introduced into the borehole and formation during drilling operations. Sr concentrations slowly increase from January 2003 to the first transient event on May 28, 2003. During the first event, there is a rapid acceleration to concentrations slightly less than those observed in the décollement at Site 1255 during ODP Leg 205 (Kastner et al., 2006), indicating efficient flushing of the borehole within the screened interval with in situ formation fluids. After the May 28 event, Sr concentrations increase monotonically to near-steady-state décollement values at the end of the instrument deployment.

2.5 Discussion

The data collected during this interdisciplinary effort constitute the first co-recorded chemical, physical, and hydrological time-series from a SZ system, with implications for temporal changes in slip processes on the subduction thrust, the role of permeable igneous basement as a flow pathway for fluids expelled from the subduction zone, and for chemical and fluid fluxes to the ocean. In the following sections we discuss the fluid sources and flow rates in the igneous basement at Site 1253 and the mechanisms controlling the transient fluid flow rates and pressure along the dècollement at Site 1255.

2.5.1 Subduction Zone Component of the Basement Fluid at Site 1253

The radiogenic $^{87}Sr/^{86}Sr$ isotopic signature and the elevated Li and Rb concentrations in the fluids sampled in the upper igneous basement at Site 1253 suggests the fluid consists of a 2-component mixture of modified seawater typical of low temperature ridge-flank fluids a SZ fluid. Seawater basalt reactions in the igneous basement along the fluid flow path from points of recharge to Site 1253 drive an increase in Ca concentrations and a depletion in Mg, B, and $\delta^{18}O$ values. Considering only the elements and isotope ratios not strongly affected by these low temperature water-rock reactions, Sr, Ba, SO_4, K, Li, Rb, and δ^7Li, the chemical and isotopic composition of the fluid indicates a mixture between seawater and a SZ fluid. This is most clearly observed in the Li and Sr data collected by the OSs in the upper basement at Site 1253 (Fig. 2.5b), and indicates the SZ fluid sampled is similar to the deep-sourced fluid sampled in the décollement at ODP Site 1040/1254 (Fig. 2.5b). The chemical and isotopic compositions of the Site 1040/1254 fluid indicate that it originates at a temperature of 80-150 ^oC, ~50 km landward of the trench at from a depth of ~11 km (Chan and Kastner, 2000; Hensen et al., 2004; Spinelli and Saffer, 2004). Even the more reactive elements (Ca & Mg) show a mixture between seawater and the deep-sourced fluid at Site 1040/1254 (Fig. 2.5c), but plot to the right of the binary mixing line due to low temperature reactions in the basement. A simple binary mixing calculation was employed to estimate the relative contributions from subduction zone fluid and seawater to the fluid sampled within the basement at Site 1253. Considering the binary mixture between seawater and the Site 1040/1254 dècollement fluid

illustrated by the solid line in Figure 2.5b, the fraction of bottom water (f_{BW}) and, hence, the fraction of SZ fluid $f_{SZ} = (1\text{-}f_{BW})$ is computed by:

$$f_{BW} = (X)_{OS} - (X)_{SZ}/(X)_{BW} - (X)_{SZ} \qquad \text{(Eq. 2.1)}$$

where X denotes the concentration of an element that does not react strongly with the basement, and the subscripts BW, SZ, and OS denote bottom water, subduction zone fluid, and fluid sampled by the OsmoSamplers at Site 1253. Using the Sr, Ba, SO_4, K, and Li concentrations, as well as the δ^7Li values, of each of these fluids, the percent contribution of bottom water ranges from 84-94% and the fraction of the SZ fluid ranges from 6-16% (Table 2.2).

The $^{87}Sr/^{86}Sr$ ratios of bottom water and the fluid sampled by the OSs at Site 1253 were used to estimate the $^{87}Sr/^{86}Sr$ of the SZ fluid by:

$$^{87}Sr/^{86}Sr_{OS} = (f_{BW} \times {}^{87}Sr/^{86}Sr_{BW}) + (f_{SZ} \times {}^{87}Sr/^{86}Sr_{SZ}) \qquad \text{(Eq. 2.2)}$$

With these isotope ratios and ~90% bottom water and ~10% subduction zone fluid, we compute an $^{87}Sr/^{86}Sr$ ratio of the SZ source fluid of 0.71446, which is fairly similar to the $^{87}Sr/^{86}Sr$ ratio of global subducted sediment (0.7173; Plank and Langmuir, 1998). Overall, these results indicate that the main source of the fluid sampled at Site 1253 is from the contemporaneous flow of seawater recharging at igneous outcrops on the EPR crust (Hutnak et al., 2007). The significant contribution from the SZ indicates that the permeable oceanic basement is also an efficient pathway for fluids being expelled from the consolidating sediment section and from mineral dehydration reactions, potentially at depths >10 km, that should be included in mathematical models of subduction zone hydrogeology and deformation (Fig. 2.6).

In order to confirm that the radiogenic Sr source is from the incoming sediment section and/or prism, a comprehensive suite of representative sediment samples collected during Legs 170 and 205 were analyzed for $^{87}Sr/^{86}Sr$ isotope ratios (Table 2.1). None of the samples analyzed exhibit Sr isotope ratios more radiogenic than seawater, indicating that the radiogenic sedimentary end member likely occurs further arcward and at greater depth than drilled during these two legs. Since ~16 Ma, subduction erosion has been the dominant process controlling the tectonic evolution of the Costa Rica margin (Vannucchi et al., 2001; 2003). The frontal erosion by subducting seamounts (Ranero and von Huene, 2000) and basal erosion remove rock from the forearc at an average rate of 107-123 km^3/Myr km since 16 Ma (Vannucchi et al., 2003) causing long-term subsidence of the margin. As a result, Mesozoic Nicoya Complex and Cretaceous and early Tertiary sedimentary sequences deposited in the shallow marine environment exposed on the Nicoya Peninsula onshore from the CORK sites, were sampled at Site 1042, ~7 km from the trench, at 3900 m water depth and 360 mbsf (Vannucchi et al., 2001). Thus, these older shallow marine siliclastic sequences have been eroded and subsequently subducted to greater depths in the forearc. The Nicoya Ophiolite complex is likely to have non-radiogenic Sr isotope ratios on average. However, these siliclastic sediments could potentially be more radiogenic than seawater. It is also possible that other terrigenous sediment sources with elevated Sr isotope ratios exist and have been transported to the toe of the prism and subsequently subducted in the recent past, potentially driven by the recent uplift of the Talamanca Range. Constraining the source and the depth of the fluid-rock reactions with the subducted sediments is currently in progress, and Sr isotopic analyses of samples from

exposures of the Cretaceous and early Tertiary sedimentary sequences on the Nicoya Peninsula will be critical in identifying the enigmatic source of the radiogenic fluids sampled in the upper igneous basement at Site 1253.

2.5.2 Estimated Igneous Basement Flow Rates

During drilling operations, bottom water rapidly flows down the borehole and surface water is pumped down the drill string to flush cuttings from the hole. The bottom water is cooler (~2 ^{o}C) and more dense than the formation fluids (~8 ^{o}C), and this loads ("charges") the formation (Fig. 2.8a) generating superhydrostatic formation pressures (~8 kPa) at the beginning of the deployment period (Davis and Villinger, 2006). As a result, there is a zone within the formation outside the borehole that contains a radially varying mixture of fluids introduced during drilling and *in situ* formation fluid. The flow of seawater out of the borehole is driven by the combination of natural formation underpressure, the negative buoyancy of cool bottom water in the borehole, and the pressure created by drilling circulation. When the OSs are latched into place and the CORK is sealed at the wellhead, bottom water no longer flows into the borehole, however it is still filled with a column of dense bottom water. This residual column of bottom water maintains the pressure differential/density gradient and continues to drive the downward flow of bottom water remaining below the instrument seal into the formation supporting the rapid exchange of formation fluids with the borehole fluids (Fig. 2.8a). This occurs at a fraction of the flow rate that existed before the borehole was sealed. At first, the fluid entering the borehole is likely a mixture between seawater and formation fluids, and later becomes more representative of *in situ* formation fluids. This is observed in the OS chemical time series by the rapid evolution

from seawater values to near steady-state formation concentrations within ~1 month after the instrument deployment (Fig. 2.3; 2.8c). During this same period, the formation pressure changes from superhydrostatic to subhydrostatic (Davis and Villinger, 2006), indicating the density driven flushing of the borehole has waned due to thermal equilibrium. The subhydrostatic conditions are believed to reflect the true hydrologic state of the upper igneous basement at Site 1253 (Davis and Villinger, 2006).

From November 2002 to March 4, 2004, a gradual change in the solute time series to steady-state values is observed (Fig. 2.3; 2.8b), indicating a return to the natural fluid flow rates in the upper igneous basement. During this period, the background fluid flow in the basement is slowly carrying the "contaminated" borehole fluid downstream of the CORK site, and carrying "pristine" formation fluids into the borehole. During the *Alvin* recovery attempt on March 4, 2004, the borehole was briefly opened, and cold/dense bottom water once again flowed down the borehole into the formation. This is manifested by an abrupt change in the chemical time series to bottom water-like values (Fig. 2.3; 2.8c). However, the borehole was only opened briefly, for a period of minutes rather than weeks as during the drilling operations, thus there was no observed flow overprinting on the background flow field, and the rate of change in solute concentrations was similar to the middle portion of the chemical record (Fig. 2.3, 2.8c).

The rate of change in the fluid composition during the three periods provides an estimate for fluid flow rates within the igneous basement at Site 1253. A simple mathematical model was employed to estimate the rate of fluid influx into the borehole during the three periods. In the model it is assumed that cold seawater enters the

borehole prior to sealing and mixes with formation fluids creating a radial cloud around the borehole in the basement. This is likely an oversimplification since the permeability of the upper igneous basement is likely anisotropic with most of the fluid flow occurring along discrete fractures. However, due to the lack of sufficient data on the permeability distribution at Site 1253, it is assumed that the permeability is isotropic. After the hole is sealed, the mixture of formation fluids and seawater enters the borehole, mixes with the entire ~100 m borehole between TD and the packer and OS seal (4.5 in. casing and 9.875 in. open hole), and departs through the basement. It is assumed that convection within the borehole keeps the chemical composition homogenized. After the ~1 month period of rapid exchange between borehole fluids and basement fluid, it is assumed that the "contaminated" fluid, for the most part, has been flushed from the formation, and "pristine" formation fluids are entering the hole. In order to simplify the model, the volumetric flow of formation fluids into the borehole does not decrease as the density gradient decreases during the first month of deployment, thus the calculated flow rate is an average flow rate. With these assumptions, the model follows a first-order sink equation and is used to compute a single variable residence time assuming the fluid flow rate over each period is constant and mass is conserved over the time modeled; hence the volumetric discharge is computed by:

$$dVC_{BH}/dt = QC_{in} - QC_{BH} \qquad \text{(Eq. 2.3)}$$

Since the borehole volume and the volumetric discharge into the borehole are constant:

$$C_{BH}(t) = [C_{BH}{}^{o} - C_{in}]e^{-t(V/Q)} + C_{in} \qquad \text{(Eq. 2.4)}$$

where V is the volume of the borehole below the packer and OS seal, Q is the volumetric flow passing through the borehole, C_{BH} is the solute concentration in the borehole, C_{in} is the steady-state solute concentration in the formation, C_{BH}^{o} is the borehole solute concetration at time zero, and t is time. The flow rates for the three periods were estimated from the Ca, Mg, and Rb concentration time series, and the modeled Ca concentrations are presented in Fig. 2.8c. The volumetric flow through the borehole ranges from ~800 m^3/yr at the beginning of the deployment period to 7.3 m^3/yr after the *Alvin* recovery attempt (Table 2.3). Given the range in volumetric flow and 107 m of igneous basement exposed to the screen and open hole, the volumetric flux in the basement ranges from 17 m/yr at the beginning of the deployment to ~0.15 m/yr after the *Alvin* recovery attempt (Table 2.3). The flow rate between November 2002 and March 2004 of 0.3 m/yr is the least affected by drilling-induced and instrument-recovery perturbations, thus likely is the most representative of the true formation flow rate.

The crustal structure in the vicinity of Site 1253 is not representative of the upper 600 m of typical oceanic basement that generally consists of basaltic pillow basalts and sheet flows. In typical oceanic crust, the pillow basalts are highly permeable ($k > 10^{-11}$ m^2) and permeability decreases with depth (e.g. Becker and Fisher, 2000; Fisher, 1998). At Site 1253, the OsmoSamplers were deployed in an igneous complex comprised of a series of gabbro sills generated by Galapagos overprinting that intruded the EPR-generated crust ~10-14 Ma (Dreyer et al., 2006; Morris et al., 2003). Presumably, beneath this sill complex, lies the “true” EPR-generated basement. Thus, unlike most regions, the permeability at Site 1253 likely increases with depth from the

gabbro sills into the EPR basement. The modeled fluid flux of 0.3 m/yr in the upper 100 m of basement at Site 1253 is an order of magnitude lower than previous estimates at the same location based on heat flow surveys and thermal models for lateral fluid flow in the basement (Hutnak et al., 2007) that indicate flow rates ranging from 3-30 m/yr and basement permeabilities from 10^{-10} to 10^{-8} m^2. The results of the borehole flow model at Site 1253, however, are consistent with advection-diffusion models of pore fluid profiles in the basal sediments at Site 1253 (Silver et al., 2000). The extremely low heat flow in the crust offshore Costa Rica requires rapid lateral advection of seawater and efficient hydrothermal transport. Thus, the basement flow rates at depths greater than 100 m are likely to be greater than those measured in the gabbro sills as suggested by the heat flow models (Hutnak et al., 2007). This indicates the igneous crust offshore Costa Rica is likely composed of several fluid flow systems (aquifers) with differing permeabilities and flow rates, each of which may have different points of fluid recharge and discharge, as well as varying fluid chemistry (Fig. 2.6). The significant fluid flow rates and formation underpressure in the gabbro sills at Site 1253 indicates they are also permeable; potentially only 1-2 orders of magnitude less than the permeability estimated in the EPR-generated crust below. These results, combined with the radiogenic Sr isotopes, suggest the uppermost igneous basement underthrust at Costa Rica serves as an efficient hydrologic conduit that channels fluids from the prism and subducted sediment section and should be considered in models of subduction zone hydrogeology and deformation.

2.5.3 Hydrogeochemical Transients Related to Slow Slip Events Along the Décollement

The results of the long-term continuous monitoring of fluid flow rates, chemistry, and pressure within the décollement at Site 1255 indicate that the subduction thrust is far from inactive during interseismic periods (Fig. 2.7). Three transients in flow rates were recorded during the 670-day deployment, two of which coincide with recorded stepwise increases in pressure (Fig. 2.7), in late May and October 2003. There is a clear association between these two transients and two coincident deformational episodes observed during a GPS monitoring campaign on the Nicoya Peninsula, directly onshore from Site 1255 (Protti et al., 2004). The deformational episodes are interpreted as slow slip events initiating in late May and early October 2003, with the October event showing larger displacement than the May event (Protti et al., 2004). Simple dislocation modeling of the October transient event suggests that it was consistent with several cm of slip initiating at ~10-20 km depth on the plate interface and propagating down-dip over a period of three weeks. The fluid flow and pressure transients observed 0.5 km from the trench, ~60 km west of the Nicoya Peninsula, occurred ~1-2 weeks after the initiation of the GPS-recorded strain events on the coast. This indicates two mirrored dislocations propagated up-dip at similar rates as the onshore deformational episodes with no associated, detectable earthquakes.

Models of poroelasticity in SZs indicate stress resulting from the dislocation along fault surfaces cause co-rupture pore pressure changes that subsequently initiate transient fluid flow (Wang, 2000). In the case of an up-dip propagating thrust slip dislocation, the prism sediments near the toe of the wedge would experience

compression, whereas the sediments down-dip would experience dilation (Fig. 2.9). Thus, pressure and flow rates rise as the dislocation approaches a fixed position along the décollement, and decrease as the dislocation passes the fixed point (Ge and Screaton, 2005; Screaton and Ge, 2007; Roeloffs, 1996; Masterlark, 2003). The two positive transients in pressure coupled with the increase in fluid flow rates along the décollement are consistent with the formation experiencing compression during thrust slip (Fig. 2.7). It is unlikely that a down-dip propagating dislocation located near the Nicoya Peninsula would directly impact flow rates and pore pressures 10's of kilometers away at Site 1255; the magnitude of strain at this distance from a minor dislocation is simply too small. Therefore, the flow rate and pressure data suggest that a mirrored dislocation propagated up-dip at the same time and at a similar rate as observed on the Nicoya Peninsula. During the May event, the fluid velocity began to increase prior to the sharp pressure change (Fig. 2.7), further suggesting flow along the décollement triggered by an approaching dislocation reaching the borehole prior to the direct effects of strain. The flow rate sample resolution is too low to determine exactly the time lag between the increase in flow rates and the pressure transient, as one flow rate sample represents an integration of 7 days of continuous sampling, but flow likely preceded the pressure rise by a period greater than a day in order to be observed in both samples. The formation pressures do not decline after the sudden rise, indicating the dislocation did not pass Site 1255 and the rupture area did not extend to the trench. The termination of slip prior to reaching Site 1255 would act to increase stress in the region between the seismogenic zone and our monitoring site.

The pore fluid chemistry changed to that of the in situ formation fluids in the décollement at Site 1255 during the May 2003 slow slip event and remained constant during the second event in October (Fig. 2.7). If the strain pulses in the hanging wall were controlled by a solitary pressure pulse diffusing along the décollement from the rupture depth (~10-20 km), the formation fluid chemistry would be expected to transition to a more altered composition similar to that observed in the deep-sourced fluid sampled along the décollement at Site 1254/1040, ~1 km to the east of Site 1255. The rather constant in situ fluid chemistry suggests that the pressure anomalies and related fluid flow are indeed the result of strain, not signals hydrologically transmitted from depth.

Recent terrestrial and marine monitoring programs have observed slow slip events at the down-dip portion of the seismogenic zone at other convergent margins (e.g. Dragert et al., 2001; 2004; Obara et al., 2004; Rogers and Dragert, 2003; Gagnon et al., 2005, Schwartz and Rokosky, 2007), but there have been few observations of slow slip events up-dip of the seismic rupture zone (Brown et al., 2005; Davis et al., 2006; Davis and Villinger, 2006; Sagiya and Thatcher, 1999), because these offshore areas are difficult to observe using conventional methods. The down-dip slow slip events observed onshore have been interpreted to occur below the “locked” portion of the thrust and to add stress on the seismogenic portion of the fault. At many of the subduction zones where slow slip events have been observed, the plate interface is nearly entirely locked within the seismogenic zone (e.g. Cascadia, Tokai, and Boso; Schwartz and Rokosky, 2007; and references therein). At the Costa Rica subduction zone, seismic coupling is heterogeneous and the plate interface is only partially locked

(Norabuena et al., 2004). This is the first time that such slow slip events have been monitored simultaneously with several different, independent time series records (flow rate, pressure, GPS, and chemistry) both up-dip and down-dip of the seismogenic zone. The flow rate, pressure, and chemical time series records at Site 1255 indicate up-dip propagation of slip dislocation, and the GPS determined deformation on land propagated simultaneously in a down-dip direction. The correlated datasets indicate that during both events the slip area must have included the seismogenic zone along the décollement with no associated detectable earthquakes. These observations suggest that the May and October 2003 slip events propagated through the seismogenic zone, incrementally relieved stresses locally along the subduction thrust, and acted to increase stress on neighboring regions, including the seaward-most part of the subduction prism. This was clearly observed in the pressure and flow rate time series during and after the May 2003 slow slip event manifested by the maintenance of elevated formation fluid pressures after the initial effects of strain. This indicates that locking is "patchy" and stress release is often aseismic and transient.

These results highlight the importance of subseafloor hydrogeochemical observatories as strain indictaors for aseismic as well as seismic events. Our observations of two aseismic slow slip events may provide an analog for strain and hydrologic response during a great subduction earthquake. There is now a growing body of evidence of subtle pre-rupture signals that indicate fault breakdown before rupture initiation (Segall et al., 2006; Koizumi et al., 1999; Dal Moro and Zardo, 1999; Claesson et al., 2004). GPS observations at Kilauea volcano in Hawaii show that slow slip events occurred immediately before seismic rupture, implying they caused an

increase in stress in the locked portion of the fault zone and triggered the earthquakes (Segall et al., 2006). The third transient with elevated flow rates and higher flow variability that began in March 2004 and persisted to the end of the deployment, may reflect a longer period of strain release with multiple slow slip events, which would act to increase stress in other regions of the prism. It is intriguing that this period of flow transience occurred prior to, and likely during, two large subduction thrust earthquakes near the Nicoya Peninsula. On October 9, 2004 (~1 month after the instrument recovery) there was a M_w 7.1 earthquake offshore Nicaragua and on November 20, 2004 there was a M_w 6.4 earthquake just south of the Nicoya Peninsula. There is the potential that the flow transience observed at Site 1255 at the end of the recording period was a precursor to these larger earthquakes. The recovery of the instrument packages that were deployed in September 2004 and of the pressure data recorded since March 2004, will shed light on the possible relationship between the period of transient flow and these larger seismic events.

As a consequence of a up-dip slip propagation along the subduction thrust, a decrease in the formation pressure would be expected in the seaward part of the underthrust plate (Ge and Screaton, 2004; Screaton and Ge, 2007; Fig. 2.9). Neither of the first two transient events recorded in the flow rate time series at Site 1255 were observed in the pressure record in the upper igneous basement at Site 1253. However, the Li concentration time series in the upper basement at Site 1253 shows an increase in concentrations from 50 μM to 65 μM on May 27, 2003, coinciding exactly with the first event (Fig. 2.3b). The Li concentrations of fluids expelled from the SZ are expected to be higher than ridge-flank fluids and bottom water due to sediment-fluid interaction.

Thus, the increase in Li during the first event suggests an increase in flow of fluids from the SZ in the upper igneous basement during the first event; it was not observed in the pressure record because of the high basement permeability and the small magnitude of strain at this location.

2.6 Conclusions

This is the first co-registered chemical and hydrologic time series at a SZ system. Results of long-term continuous monitoring of fluid flow rates, fluid composition, and pressures at two borehole observatories established near the toe of the Costa Rica subduction zone indicate that the underthrusting upper igneous basement serves as an efficient hydrologic conduit that channels fluids from the prism and subducted sediments. Thus, the uppermost basement should be considered in models of subduction zone hydrology and deformation. A simple mixing calculation based on the formation fluid chemistry and isotopic ratios at Site 1253 indicates that approximately 10% of the fluid sampled in the basement originates from the SZ landward of the trench. The remaining 90% of the fluid is modified seawater that recharges at distant basement outcrops and is responsible for the low heat flow in the incoming EPR crust offshore Costa Rica. The low temperature alteration of the uppermost basement in this region impacts the hydration state and physical properties of the subducting slab. The formation of hydrous minerals provides a sink for formation fluid Mg, B, and K, and they are a source of water that is transported to deeper levels of the subduction zone.

Three hydrogeochemical transients were observed along the décollement at Site 1255, two of which are clearly related to slow slip events observed down-dip from Site

1255 during a GPS monitoring campaign on the Nicoya Peninsula 60 km to the east (Protti et al., 2004). These events must have ruptured through the seismogenic zone. These deformational events likely act to incrementally relieve stress locally along the décollement and to increase stress on neighboring regions. These results highlight the usefulness of subseafloor hydrogeochemical observatories as strain indicators up-dip of the seismogenic zone, where the nature and magnitude of slip is difficult to observe using conventional methods. The strain and associated hydrologic response to the slow slip events observed during this monitoring period may provide an analog for the response to great subduction earthquakes. A longer record from these CORK sites is required to better understand the nature and magnitude of strain and hydrologic transients during larger seismogenic events, and any pre-rupture signals prior to these events.

2.7 Acknowledgements

We greatly appreciate the engineering and technical expertise of T. Pettigrew and the shipboard personnel of the *JOIDES Resolution*. The pressure data presented in this manuscript was kindly provided by E. Davis. We thank L.-H. Chan for the Li isotope analyses. J. Plant is acknowledged for his assistance with preparing the OsmoSamplers for deployment, and W. Wei, M. Heesemann, and T. Hensley for shipboard and shore-based laboratory assistance. We thank E. Davis and J. Morris for very thoughtful and helpful comments that helped improve this chapter.

2.8 Chapter Acknowledgement

Chapter 2, in full, is the material in preparation for submission to Earth and Planetary Science Letters, Solomon, E.A., Kastner, M., Wheat, C.G., Jannasch, H., Robertson, G., in prep. Hydrogeochemical transience along the décollement and subducting igneous basement at the Costa Rica margin. Earth Planet. Sci. Let. to be submitted Jan. 2008.

2.9 Appendix – Calculation of Fluid Flow Rates at Site 1255

The Osmoflow-meter measures the relative direction of flow and the flow rate by continuously sampling tracer concentrations in four mutually perpendicular branches at a 1 cm distance from the central tracer injection. The tracer solution was chosen to mimic the bulk chemistry and density of the décollement fluid sampled at Site 1255 so that the tracer solution did not sink or diffuse away upon injection. The solution was spiked with rubidium (Rb) as a tracer because of its low concentration in pore fluids and ease of measurement by ICP-MS. As with benthic flux meters (e.g. Tryon et al., 2001), one of the flow meter coils will either contain all tracer or no tracer and the other coil(s) will contain a seawater/tracer mixture. Assuming that fluid flow is in the direction of Pump 1 (P_1, Fig. 2.2C), if Pump 1 sampled tracer and Pump 2 did not sample tracer, then the volumetric flow rate (Q) is less than the pump rate of P_1. If Pump 1 contains no tracer, then $Q>P_1$. The volumetric flow rate (Q) in the Ti sampling probe is then determined by the relationships presented below, where f is the fraction of tracer in the sample ($f = C_{sample}/C_{input}$). C_{input} is the concentration of Rb in the tracer solution injected into the flow meter and C_{sample} is the measured concentration of Rb in the sample.

Case 1: If $Q<P_1$, then $f_2 = ¼$, $f_3 = ¼$, $f_4 = ¼$, $f_1 = ¼ - Q/P_1$

Case 2: If $Q>P_1$, then $f_1 = 0$, $f_2 = ([P_1+P_2+P_3+P_4]•1/4)/(Q/3+P_1)$

Depending on the case, the appropriate equation is used, and the equation is solved for Q to compute the flow meter volumetric discharge. To compute the flow velocity through the flow meter, Q is divided by the cross sectional area of the intake annulus. The diameter of the flow meter intake is ¼ in., thus the cross sectional area is 0.3168 cm^2. From this linear velocity, the flow rate in the formation can be estimated by the equation of continuity ($A_1V_1 = A_2V_2$) assuming the full 7.6 m thickness of the formation surrounding the screened interval collapsed after CORK installation. Assuming flow only enters through half of the cylindrical area comprising the screened section, $V_{formation} = Q_{Osmo}/28{,}700\ cm^2$, where $V_{formation}$ is the décollement fluid flow rate and Q_{osmo} is the volumetric discharge in the Osmoflow-meter.

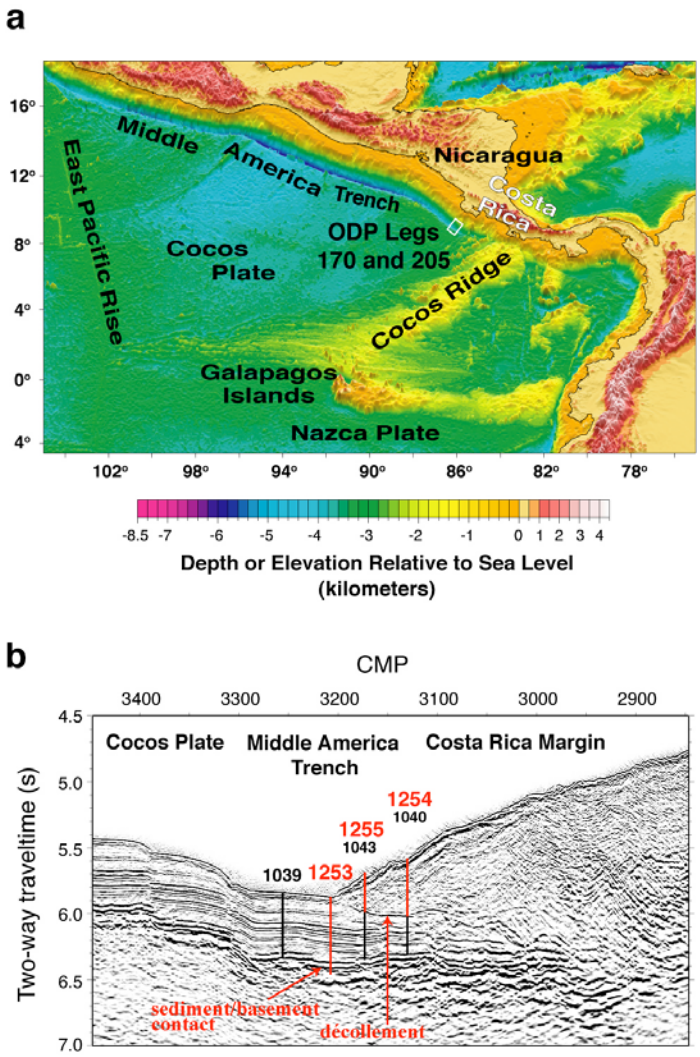

Figure 2.1. a. Bathymetric map of the eastern central Pacific modified after Vannucchi et al. (2003). The white box marks the drilling location of ODP Legs 170 and 205 offshore the Nicoya Peninsula, Costa Rica. **b.** Migrated multichannel seismic profile BGR-99-44 (modified from Morris et al., 2003) across the Middle America Trench offshore Costa Rica. The thick red lines are Leg 205 sites and the thin black lines are Leg 170 sites. Site 1253 is ~0.2 km seaward of the deformation front and Site 1254/1040 is ~1.6 km landward of the deformation front. CMP = common midpoint. The thickness of the incoming sediment section is ~400 m.

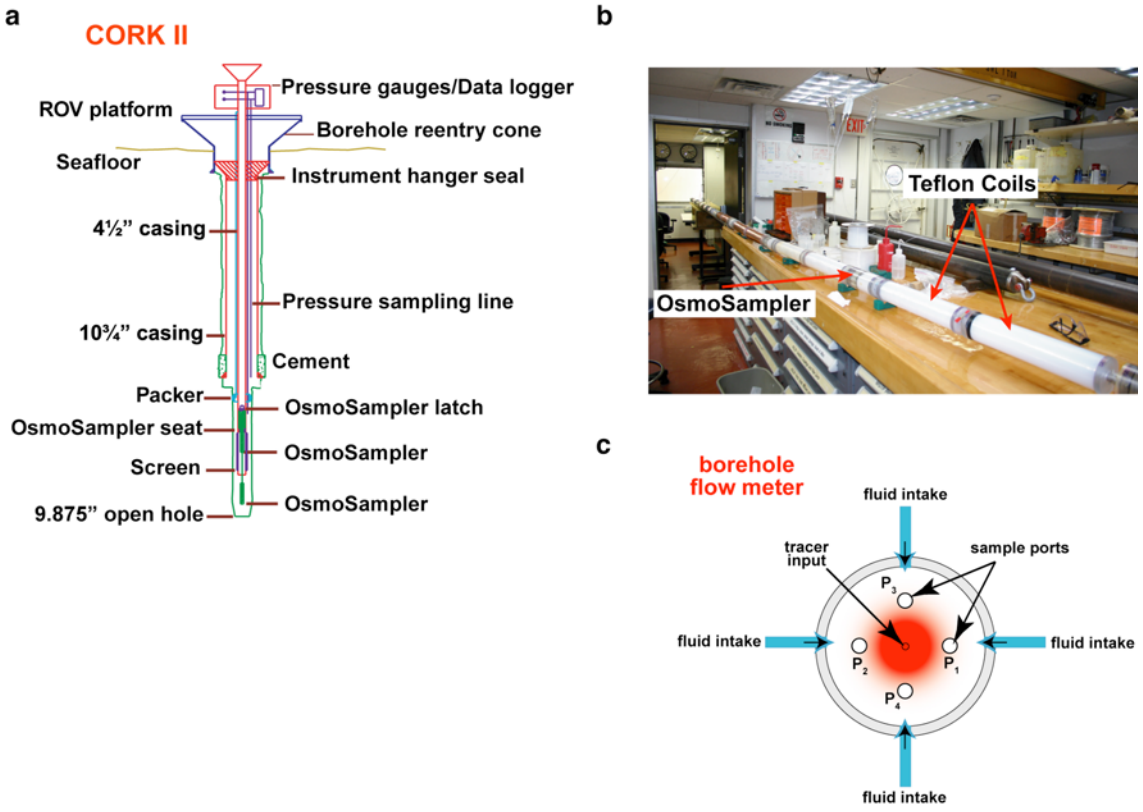

Figure 2.2 a. Schematic illustration of the CORK-II installations at ODP Sites 1253 and 1255 (modified from Davis and Becker, 2006). The OsmoSamplers collected fluid at 500 and 516 mbsf within the upper igneous basement at Site 1253 and at 140 mbsf along the décollement at Site 1255. **b.** Photograph of the OsmoSampler packages deployed at both sites. The copper sampling coils were located at the top of the package and are visible in the back of the photograph. **c.** Schematic of the OsmoFlow-meter deployed in the décollement at Site 1255. The density and salinity compensated tracer solution is injected at the center at a constant rate, and mixes with naturally flowing formation fluids. The fluid is continuously sampled at four mutually perpendicular ports, and the concentration and presence of tracer are used to determine flow rates and direction.

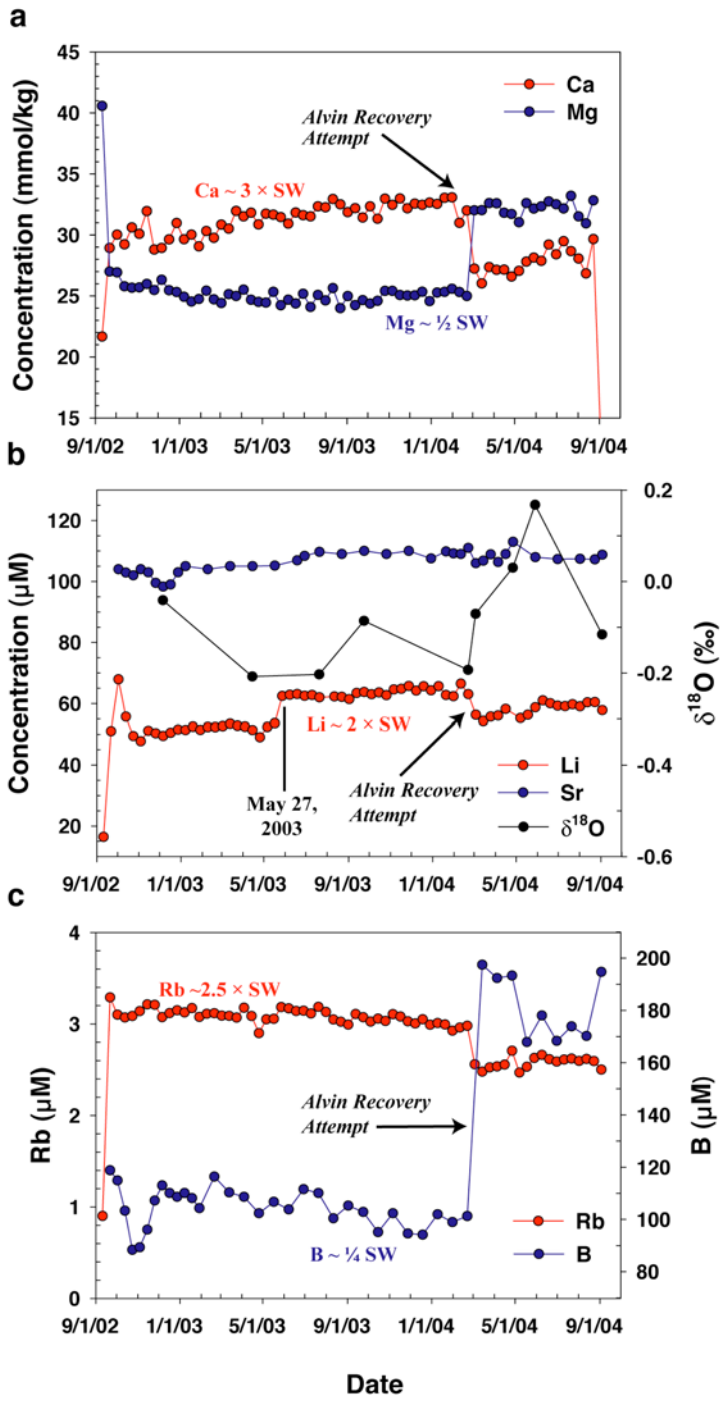

Figure 2.3 a. Ca and Mg concentration time series in the upper igneous basement at ODP Site 1253. SW = seawater value; Ca = 10.55 mM and Mg = 54.0 mM. The *Alvin* recovery attempt was on May 4, 2004. **b.** Li and Sr concentration time series at Site 1253. Seawater Li and Sr values are 26 μM and 87 μM, respectively. The $\delta^{18}O$ time series is represented by the black symbols and line. **c.** Rb and B concentration time series at Site 1253. Seawater Rb and B values are 1.4 and 418 μM, respectively.

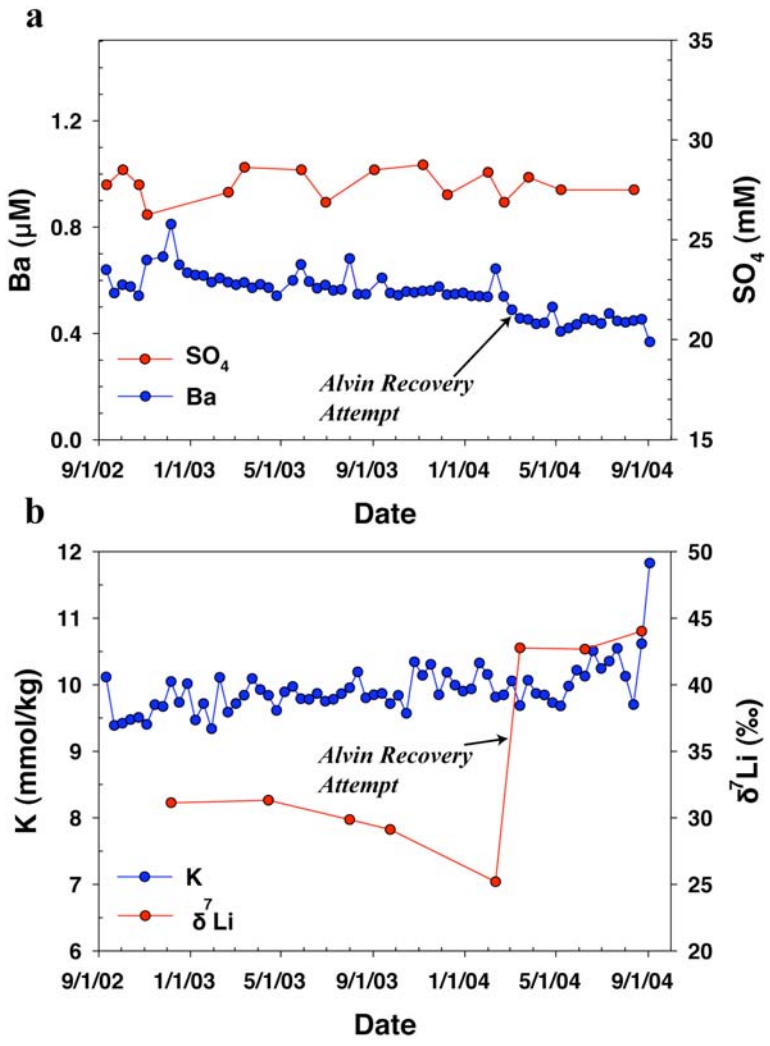

Figure 2.4 a. Ba and SO_4 concentration time series in the upper igneous basement at ODP Site 1253. Ba concentrations are ~4 times seawater value (0.13 μM) and SO_4 concentrations are slightly less than seawater (28.9 mM). The *Alvin* recovery attempt was on May 4, 2004. **b.** K concentration and δ^7Li time series at Site 1253. Seawater K value is 10.44 mM and seawater δ^7Li is 32.4‰. The increase in δ^7Li after the *Alvin* recovery attempt is due to contaminated borehole fluids entering the sampling interval after the OS seal was broken.

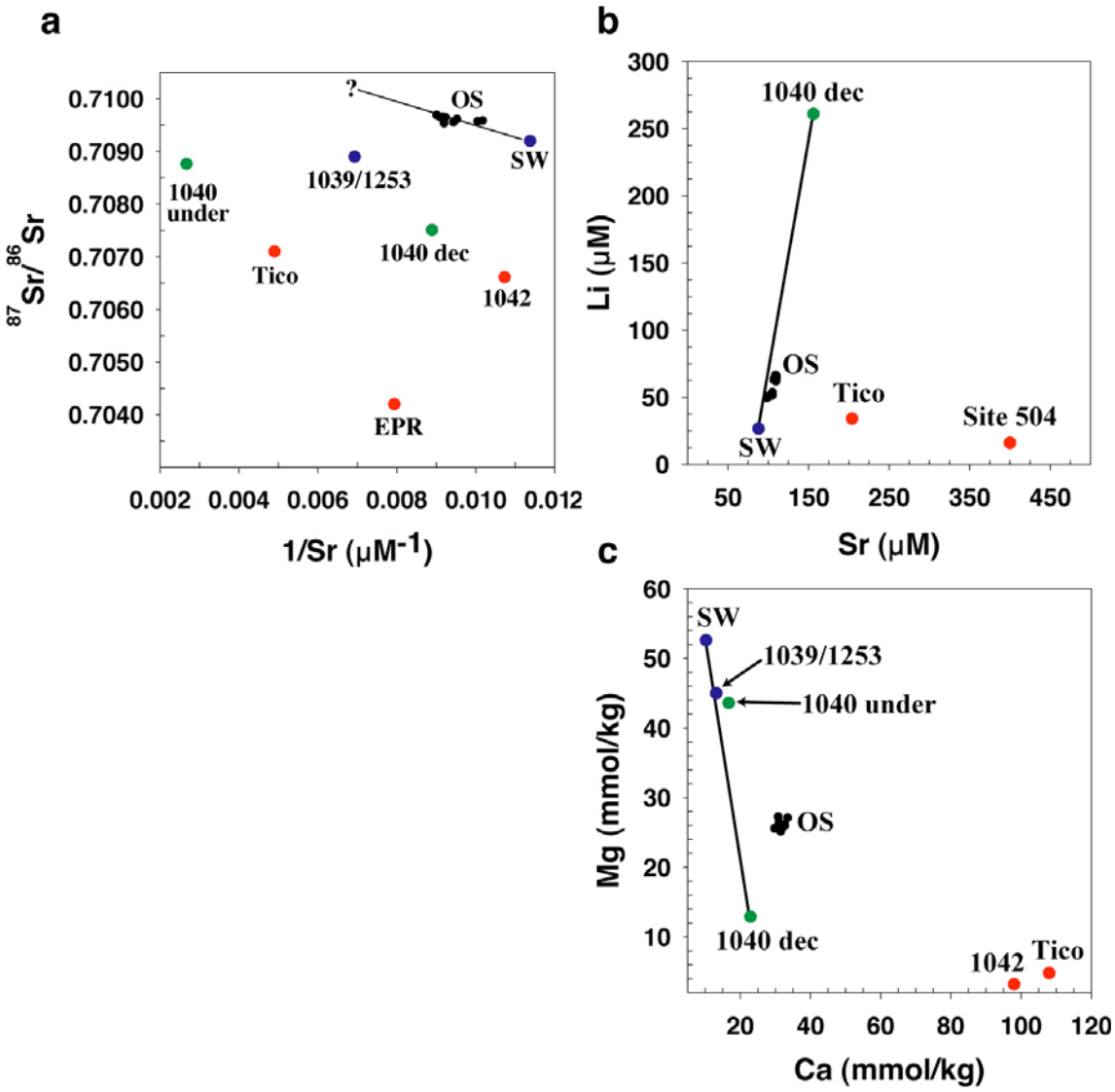

Figure 2.5 Plots of **a.** $^{87}Sr/^{86}Sr$ vs. 1/Sr, **b**. Li versus Sr, and **c.** Mg versus Ca of the fluids collected by the OsmoSamplers in the upper igneous basement at Site 1253 and representative fluids from key reservoirs seaward of Site 1253 (Tico and EPR) and within the Costa Rica forearc. 1040 under = underthrust fluids sampled at Site 1040, 1039/1253 = fluids collected from the basal carbonates at Sites 1039/1253, 1040 dec = décollement fluid at Site 140, 1042 = fault fluid sampled at ODP Site 1042 ~7 km landward of the deformation front, Tico = TicoFlux fluid, EPR = East Pacific Rise hydrothermal fluid, ODP Site 504 = ridge flank hydrothermal fluid, OS = OsmoSampler fluid collected at Site 1253. The $^{87}Sr/^{86}Sr$ of the OS fluid is not representative of typical ridge-flank fluids or fluids sampled within the forearc, and clearly indicates a radiogenic end member, likely fluid-sediment interaction within the subduction zone.

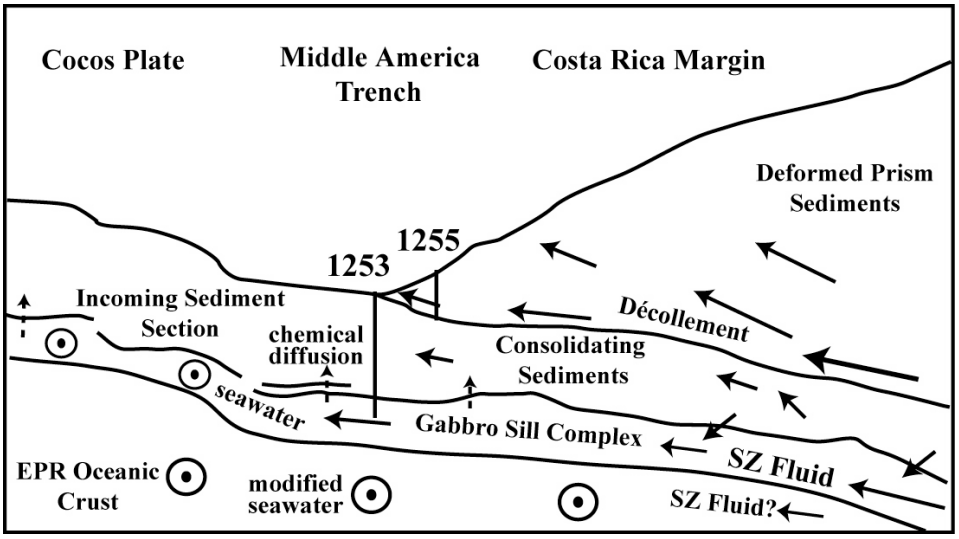

Figure 2.6 Schematic depicting inferred fluid flow paths within the subduction zone and in the igneous basement at Site 1253. Fluid advection is shown with solid arrows and chemical diffusion between flow systems are represented with dashed arrows. Circles with dots in the middle indicate fluid flow out of the plane of the section, based on regional heat flow surveys (Fisher et al., 2003). The schematic shows that the fluids sampled in the upper 100 m of the basement (in the gabbro sills) are derived from rapid lateral advection of contemporaneous/modified seawater with a 10% contribution from fluid expelled from the subduction zone. A portion of the fluids sampled along the décollement and prism thrust faults at Site 1255 are from a deep-source originating at a temperature of ~150 ^{o}C within the subduction zone.

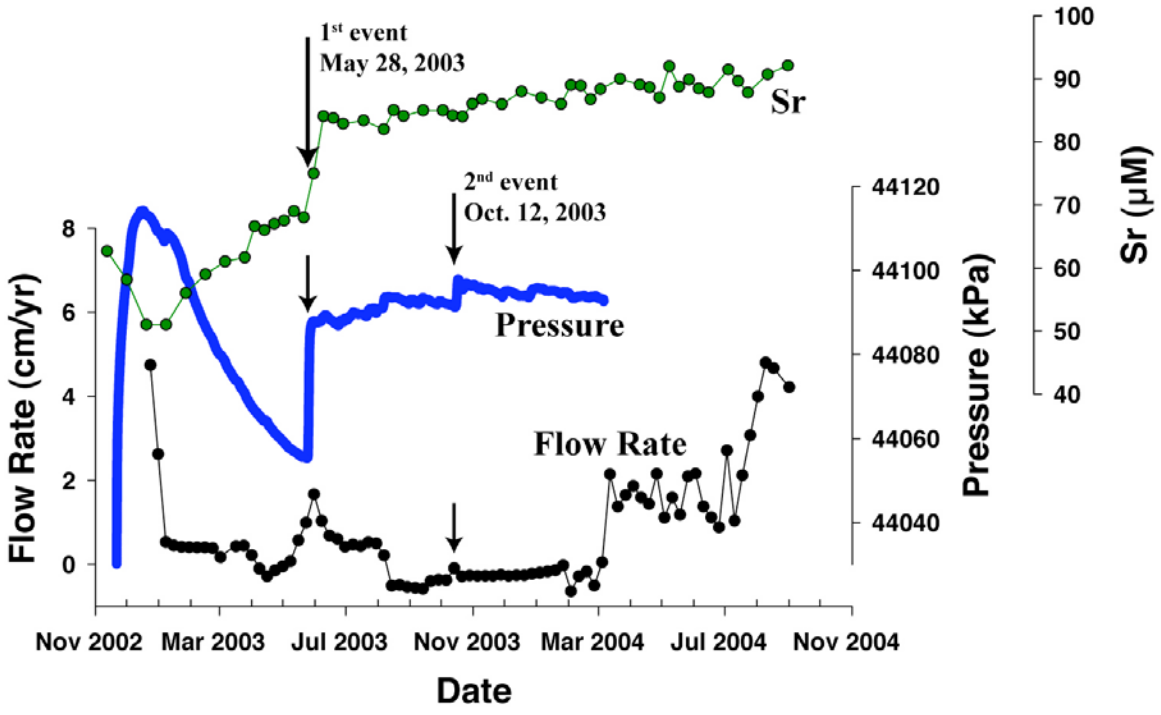

Figure 2.7 Strontium concentration (green), pressure (blue), and fluid flow rate (black) time series from the décollement at Site 1255. Two of the transients in fluid flow rates, chemistry, and pressure are marked by arrows with the approximate dates of the events. In the case of the May 2003 event, fluid flow rates start to increase prior to the increase in pressure. The pressure data are from Davis and Villinger (2006).

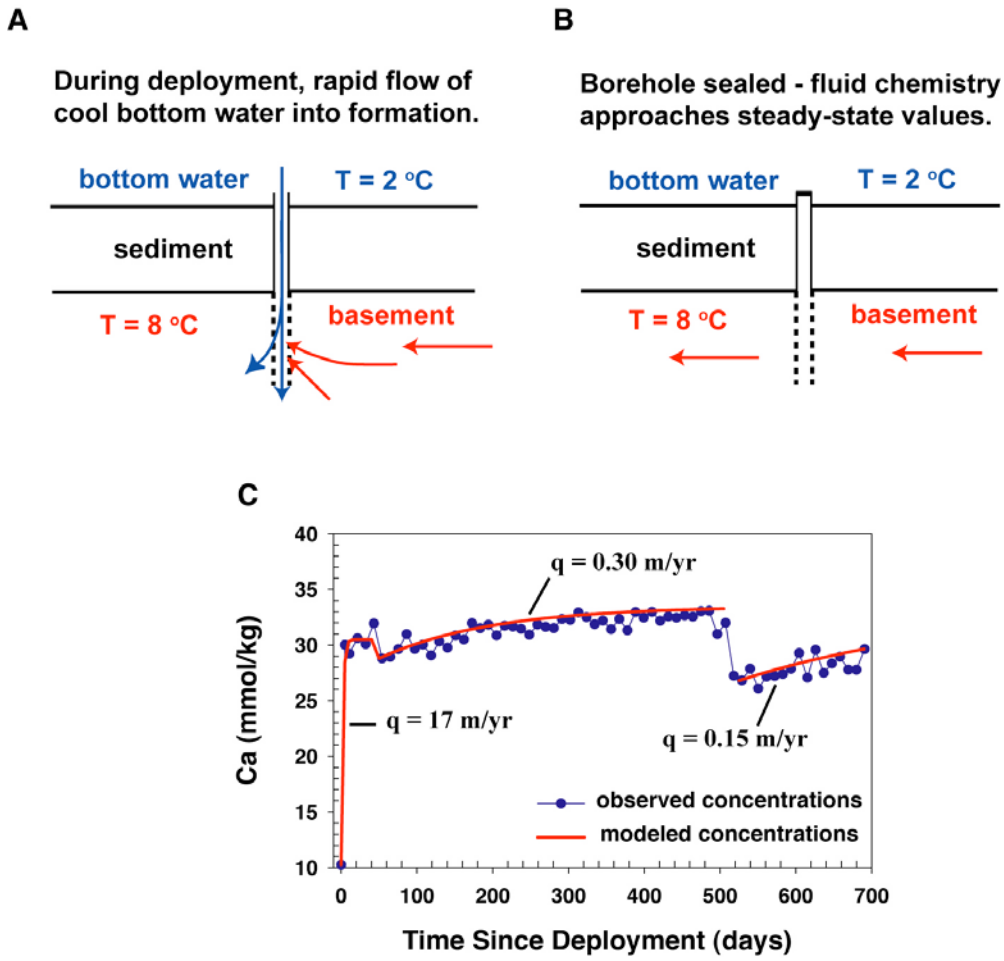

Figure 2.8 Schematic showing the three flow periods in the basement at Site 1253. **a.** After instrument installation, rapid inflow of cold/dense bottom water into the formation continued to the end of November 2002, which created a density gradient driving vigorous exchange of borehole fluids with formation fluids. The borehole was briefly opened again during the March 2004 *Alvin* recovery attempt, causing another period of rapid flow of bottom water into the formation. **b.** After November 2002, there was no longer flow of dense bottom water into the formation, and conditions reflect the true hydrological state of the basement until the *Alvin* recovery attempt in March 2004. **c.** Observed Ca concentration time series at Site 1253 (blue) and modeled Ca concentrations (red) and flow rates during the three periods. q is the specific discharge, and the steady-state specific discharge in the basement is estimated to be 0.3 m/yr.

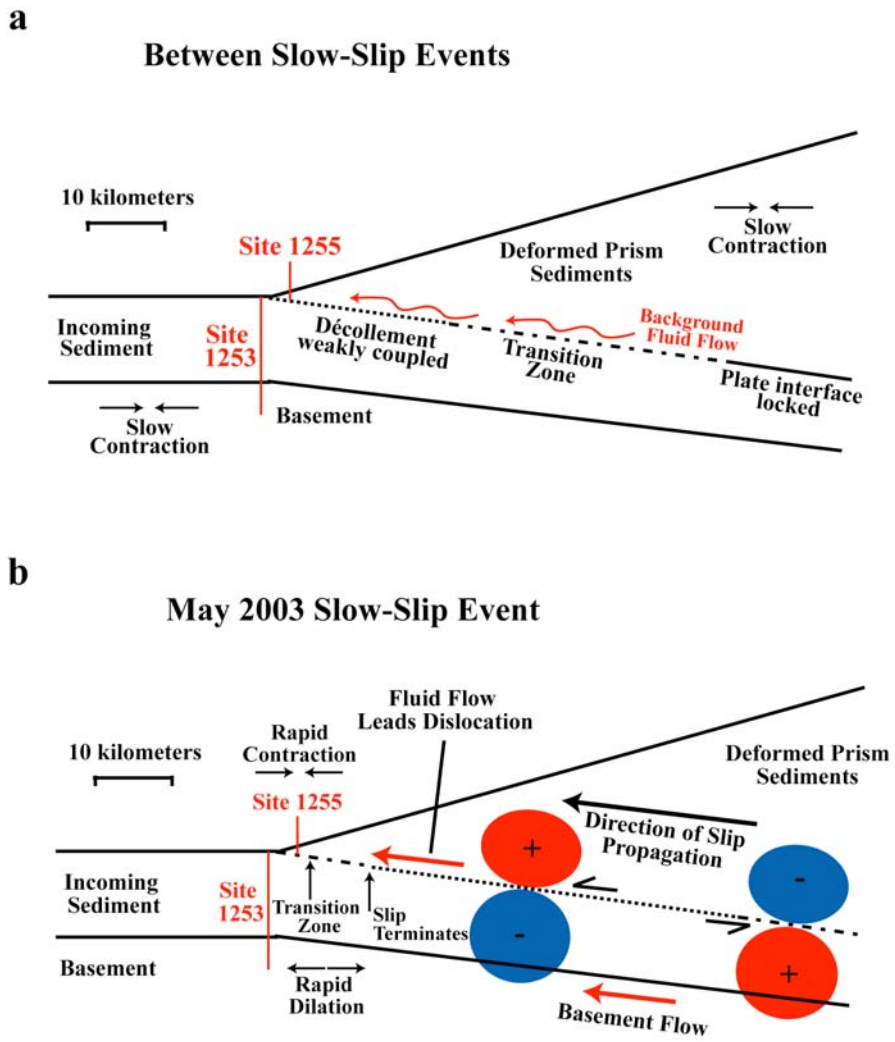

Figure 2.9 Conceptual model relating formation fluid flow rate and pressure transients observed along the décollement at Site 1255 to slow slip events. **a.** Motion between the Cocos and Caribbean plates is absorbed by contractional elastic deformation of the prism and oceanic lithosphere seaward and landward of the locked portion of the décollement. Pressures are moderately super-hydrostatic along the décollement and flow rates are typical of the "background" fluid flow field. **b.** Initiation of a slow slip event causes a rupture dislocation to propagate up-dip from the seismogenic zone causing contractional loading of the prism seaward of the dislocation, and dilation of the oceanic lithosphere. The poroelastic strain field and associated pressure drives fluid flow ahead of the propagating dislocation. Thus, elevated flow rates are observed prior to the direct effects of strain at Site 1255. The rupture terminates landward of Site 1255, loading the formation and keeping pore pressures elevated.

Table 2.1 Sr isotopic values of representative sediment samples from ODP Sites at the Costa Rica margin in comparison to the basement fluid $^{87}Sr/^{86}Sr$ ratio sampled by the OsmoSamplers.

Sample[a]	**Depth (mbsf)**	**$^{87}Sr/^{86}Sr$**[b]	**Description/Lithology**
205-1253-25R-1	513.0	0.708525	"baked sediment" between sills
205-1253-27R-1	519.2	0.708417	"baked sediment" between sills
205-1254-16R-3	366.2	0.706758	underthrust sediments, claystone
170-1040-18R-2	325.7	0.705778	prism, silty clay
170-1041-21R-3	350.6	0.705803	prism sediment
170-1042-02R-1	323.6	0.708652	breccia-sediment
170-1042-03R-1	333.3	0.707123	breccia
170-1042-06R-1	362.0	0.706033	sediment/base of fault zone
OS fluid	**500.0**	**0.709690**	**more radiogenic than seawater**[c]

[a] Samples denoted as ODP Leg – Site – Core – Section

[b] Average values, the 2σ standard deviation is 0.000018

[c] OS fluid value is the average of 12 samples. $^{87}Sr/^{86}Sr$ of modern seawater = 0.70916

Table 2.2 Two-component mixing of fluids in the igneous basement at Site 1253

% Contribution	K	SO_4	Sr*	Li	Ba	δ^7Li
% Seawater	92	93	88	84	95	86
% SZ Fluid	8	7	12	16	5	14

The calculation for all constituents except Sr are based on Site 1040 décollement fluid composition and seawater value.

* Sr calculation based on the average concentration between Site 1040 pore fluids in the basal sediments and the Site 1040 décollement fluid.

Table 2.3 Modeled borehole flow rates in the igneous basement at ODP Site 1253.

October to November 2002			
Solute	Q (m^3/y)[a]	q (m/yr)[b]	v_x (m/yr)[c]
Ca^{2+}	803	17	166
Rb^{+}	913	19	189
Mg^{2+}	1022	21	211

November 2002 to March 2004			
Solute	Q (m^3/ y)[a]	q (m/yr)[b]	v_x (m/yr)[c]
Ca^{2+}	15	0.3	2.3

March to September 2004			
Solute	Q (m^3/ y)[a]	q (m/yr)[b]	v_x (m/yr)[c]
Ca^{2+}	7.3	0.15	1.5
Rb^{+}	9.1	0.19	1.9

[a] Volumetric flow
[b] Fluid flux (specific discharge)
[c] Average linear velocity, based on a basement porosity of 10%

References

Becker, K., Fisher, A.T., 2000. Permeability of upper oceanic basement on the eastern flank of the Endeavor Ridge determined with drill-string packer measurements. J. Geophys. Res. 105, 897-912.

Becker, K., Davis, E.E., 2006. A review of CORK designs and operations during the Ocean Drilling Program, in: Fisher, A.T., Urabe, T., Klaus, A. (Eds.), Proc. IODP Init. Rep. 301, College Station, TX (Integrated Ocean Drilling Program), doi:10.2204/iodp.proc.301.103.2005, pp. 39-52.

Brown, K.M., Tryon, M.D., DeShon, H.R., Dorman, L.M., Schwartz, S.Y., 2005. Correlated transient fluid pulsing and seismic tremor in the Costa Rica subduction zone. Earth Planet. Sci. Lett. 238, 189-203.

Butterfield, D.A., Nelson, B.K., Wheat, C.G., Mottl, M.J., Roe, K.K., 2001. Evidence for basaltic Sr in midocean ridge-flank hydrothermal systems and implications for the global oceanic Sr isotope balance. Geochim. et Cosmochim. Acta 65(22), 4141-4153.

Chan, L.H., Kastner, M., 2000. Lithium isotopic compositions of pore fluids and sediments in the Costa Rica subduction zone: implications for fluid processes and sediment contribution to the arc volcanoes. Earth Planet. Sci. Lett. 183, 275-290.

Claesson, L., Skelton, A., Graham, C., Dietl, C., Mörth, M., Torssander, P., Kockum., I., 2004. Hydrogeochemical changes before and after a major earthquake. Geology 32(8), 641-644.

Dal Moro, G., Zardo, M., 1999. Remarkable tilt-strain anomalies preceding two seismic events in Friuli (NE Italy); their interpretation as precursors. Earth Planet Sci. Lett. 170, 119-129.

Davis, D.J., Suppe, J., Dahlen, F.A., 1983. Mechanics of fold-and-thrust belts and accretionary wedges. J. Geophys. Res. 88, 1153-1172.

Davis, E.E., Becker, K., Wang, K., Obara, K., Ito, Y., Kinoshita, M., 2006. A discrete episode of seismic and aseismic deformation on the Nankai trough subduction zone accretionary prism and incoming Philippine Sea Plate. Earth Planet. Sci. Lett. 242, 73-84.

Davis, E. E., Villinger, H.W., 2006. Transient formation fluid pressures and temperatures in the Costa Rica forearc prism and subducting oceanic basement: CORK monitoring at ODP Sites 1253 and 1255. Earth. Planet. Sci. Lett. 245, 232-244.

DeMets, C., Gordon, R.G., Argus, D.F., Stein, S., 1990. Current plate motions. Geophys. J. Int. 101, 425-478.

Dragert, H., Wang, K., James, T., 2001. A silent slip event on the deeper Cascadia subduction interface. Science 292, 1525-1528.

Dragert, H., Wang, K., Rogers, G., 2004. Geodetic and seismic signatures of episodic tremor and slip in the northern Cascadia subduction zone. Earth Planets Space 56, 1143-1150.

Dreyer, B., Chavagnac, V., Morris, J., Font, L., 2006. Source and petrogenesis of the igneous complex cored during ODP Leg 205: Implications for off-axis plume-ridge interaction on the Cocos Plate, in: Morris, J.D., Villinger, H.W., Klaus, A. (Eds.), Proc. ODP Sci. Res. 205, College Station, TX (Ocean Drilling Program), doi:10.2973/odp.proc.sr.205.2006.

Fisher, A.T., 1998. Permeability within basaltic oceanic crust. Rev. Geophys. 36, 143-182.

Fisher A, Stein, C.A., Harris, R.N., Wang, K., Silver, E.A., Pfender, M., Hutnak, M., Cherkaoui, A., Bodzin, R., Villinger, H., 2003. Abrupt thermal transition reveals hydrothermal boundary and role of seamounts within the Cocos Plate. Geophys. Res. Lett. 30 (11), doi:10.29/2002GL016766.

Fryer, P., Wheat, C.G., Mottl, M.J., 1999. Mariana blueschist mud volcanism: Implications for conditions within the subduction zone. Geology 27, 103-106.

Gagnon, K., Chadwell, C., Norabuena, E., 2005. Measuring the onset of locking in the Peru-Chile trench with GPS and acoustic measurements. Nature 434, 205-208.

Ge, S., Screaton, E., 2005. Modeling seismically induced deformation and fluid flow in the Nankai subduction zone. Geophys. Res. Lett. 32, doi:10.1029/2005GL023473.

Gieskes, J.M., Lawrence, J.R., 1981. Alteration of volcanic matter in deep sea sediments: evidence from the chemical composition of interstitial waters from deep sea drilling cores. Geochimica et Cosmochimica Acta 45, 1687-1703.

Grevemeyer, I., Kopf, A.J., Fekete, N., Kaul, N., Villinger, H.W., Heesemann, M., Wallmann, K., Spiel, V., Gennerich, HH., Muller, M., Weinbre, W., 2004. Fluid flow through active mud dome Mound Culebra offshore Nicoya Peninsula, Costa Rica: Evidence from heat flow surveying. Mar. Geol. 207, 145-157.

Heesemann, M., Villinger, H., Jannasch, H.W., Kastner, M., and the Expedition 301T Scientists, 2006. Data Report: Long-term temperature measurements in Holes 1253A and 1255A off Costa Rica, ODP Leg 205. In: Morris, J.D., Villinger, H.W., Klaus, A. (Eds.), Proc. ODP, Sci. Results 205, College Station, TX (Ocean Drilling Program), 1–20. doi:10.2973/odp.proc.sr.205.209.2006

Hensen, C., Wallman, K., Schmidt, M., Ranero, C.R., Suess, E., 2004. Fluid expulsion related to mud extrusion off Costa Rica-A window to the subducting slab. Geology 32, 201-204.

Hubbert, M.K., Rubey, W.W., 1959. Role of fluid pressure in mechanics of overthrust faulting: I. Mechanics of fluid filled porous solids and its application to overthrust faulting. GSA Bulletin 70, 115-166.

Hutnak, M., Fisher, A.T., Stein, C.A., Harris, R., Wand, K., Silver, E., Spinelli, G., Pfender, M., Villinger, H., MacKnight, R., Costa Pisani, P., DeShon, H., Diamente, C., 2007. The thermal state of 18-24 Ma upper lithosphere subducting below the Nicoya Peninsula, northern Costa Rica margin. In: Interplate Subduction Zone Seismogenesis, Dixon, T., Moore, C. (Eds.), Columbia University Press, New York, pp. 86-122.

Hyndman, R.D., Wang, K., 1993. Thermal constraints on the zone of major thrust earthquake failure: The Cascadia subduction zone. J. Geophys. Res. 98, 2039-2060.

Hyndman, R.D., Yamano, M., Oleskevich D.A., 1997. The seismogenic zone of subduction thrust faults. Island Arcs 6(3), 244-260.

James, R.H., Allen, D.E., Seyfried, W.E., 2003. An experimental study of alteration of oceanic crust and terrigeneous sediments at moderate temperatures (51 to 350 ^{o}C): Insights as to chemical processes in near-shore ridge-flank hydrothermal systems. Geochim. et Cosmochim. Acta 67, 681-691.

Jannasch, H., Davis, E.E., Kastner, M., Morris, J.D., Pettigrew, T.L., Plant, J.N., Solomon, E.A., Villinger, H.W., Wheat, C.G., 2003. CORK-II: Long-term monitoring of fluid chemistry, fluxes, and hydrology in instrumented boreholes at the Costa Rica subduction zone, in: Morris, J.D., Villinger, H.W., Klaus, A. (Eds.), Proc. ODP, Init. Repts. 205 [CD-ROM]. Available from: Ocean Drilling Program, Texas A&M University, College Station TX 77845-9547, USA.

Jannasch H. W., Wheat, C.G., Plant, J., Kastner, M., Stakes, D., 2004. Continuous chemical monitoring with osmotically pumped water samplers: OsmoSampler design and applications. Limnol. Oceanogr. Methods 2, 102-113.

Lawrence, J.R., Gieskes, J.M., Broecker, W.S., 1975. Oxygen isotopes and cation composition of DSDP pore waters and the alteration of Layer II basalts. Earth Planet. Sci. Let. 27, 1-10.

Kastner, M., Elderfield, H., Jenkins, W.J., Gieskes, J.M., Gamo, T., 1993. Geochemical and isotopic evidence for fluid flow in the Western Nankai Subduction Zone, Japan, in: Winkler, W.R., Stewart, N.J. (Eds.), Proc. ODP Sci. Results 131, Ocean Drilling Program, College Station TX, pp. 397-413.

Kastner, M., Becker, K., Davis, E., Fisher, A.T., Jannasch, H.W., Solomon, E.A., Wheat, G. 2006. New insights into the hydrogeology of the ocean crust through long-term monitoring. Oceanography 19, 30-41.

Kimura, G., Silver, E., Blum, P., et al., 1997. Proc. ODP, Init. Repts., 170: College Station, TX (Ocean Drilling Program).

Koizumi, N., Tsukuda, E., Kamigaichi, O., Matsumoto, N., Takahashi, M., Sato, T., 1999. Preseismic changes in groundwater level and volumetric strain associated with earthquake swarms off the east coast of the Izu Peninsula, Japan. Geophys. Res. Lett. 26, 3509-3512.

Langseth, M.G., Silver E.A., 1996. The Nicoya convergent margin: a region of exceptionally low heat flow. Geophys. Res. Lett. 23, 891-894.

Martin, J.B., Kastner, M., Henry, P., Le Pichon, X, Lallement, S., 1996. Chemical and isotopic evidence for sources of fluids in a mud volcano field seaward of the Barbados accretionary wedge, J. Geophys. Res., 101, 20325-20346, 10.1029/96JB00140.

Masterlark, T., 2003. Finite element model predictions of static deformation from dislocation sources in a subduction zone; sensitivities to homogeneous, isotropic, Poisson-solid, and half-space assumptions. J. Geophys. Res. 108, doi.10.1029/2002JB002296.

McDuff, R.E., Gieskes, J.M., 1976. Calcium and magnesium profiles in DSDP interstitial waters: diffusion or reaction? Earth Planet. Sci. Let. 33, 1-10.

McDuff, R.E., 1981. Major cation gradients in DSDP interstitial waters: the role of diffusive exchange between seawater and upper oceanic crust. Geochim. et Cosmochim. Acta 45, 1705-1713.

Moore, J.C., Vrolijk, P., 1992. Fluids in accretionary prisms. *Rev. Geophys.* 30, 113-135.

Morris, J.D., Villinger, H.W., Klaus, A., et al., 2003. Proc. ODP, Init. Rep., 205, Ocean Drilling Program, Texas A&M University, College Station, TX.

Mottl, M.J., 1989. Hydrothermal convection, reaction, and diffusion in sediments on the Costa Rica Rift flank: pore-water evidence from ODP Sites 677 and 678, in: Becker, K., Sakai, H. (Eds.), Proc. ODP Sci. Res. 111, Ocean Drilling Program, College Station, TX, pp. 195-213.

Muza, J.P., 2001. Calcareous nannofossil biostratigraphy from a 15-km transect (Cocos Plate to Caribbean Plate) across the Middle America Trench, Nicoya Penisnula, Costa

Rica, in: Silver, E.A., Kimura, G., Blum, P., Shipley, T.H. (Eds.), Proc. ODP Sci. Res. 170 [CD ROM]. Available from: Ocean Drilling Program, Texas A&M University, College Station, TX, pp. 1-63.

Norabuena, E., Dixon, T.H., Schwartz, S.Y., DeShon, H.R., Newman, A., Protti, M., Gonzalez, V., Dorman, L.M., Flueh, E.R., Lundgren, P., Pollitz, F., Sampson, D., 2004. Geodetic and seismic constraints on some subduction zone processes in Costa Rica. J. Geophys. Res. 109, doi:10.1029/2003JB002931.

Obara, K., Hirose, H., Yamamizu, F., Kasahara, K., 2004. Episodic slow slip events accompanied by non-volcanic tremors in southwest Japan subduction zone. Geophys. Res. Lett. 31, doi:10.1029/2004GL020848.

Parsons, P.K.F., Wheat, C.G., Fisher, A.T., Silver, E.A., Underwood, M., Hutnak, M., submitted. Hydrothermal seepage of altered crustal fluids seaward of the Middle America Trench, offshore Costa Rica. J. Geophys. Res.

Paytan, A., Kastner, M., Martin, E.E., MacDougall, J.D., Herbert, T., 1993. Marine barite as a monitor of seawater strontium isotope composition. Nature 366, 445-449.

Plank, T., Langmuir, C.H., 1998. The chemical composition of subducting sediment and its consequences for the crust and mantle. Chem. Geol. 145, 325-394.

Protti, M., Gonzalez T., Kato, T., Iinuma, T., Miyazaki, S., Obana, K., Kaneda, Y., LaFemina, P., Dixon, T., Schwartz, S., 2004. A creep event on the shallow interface of the Nicoya Peninsula, Costa Rica seismogenic zone. EOS, Trans. Am. Geophys. Union, Fall Meet. Program Abstr. 85, F1378.

Ranero, C.R., Von Huene, R., 2000. Subduction erosion along the Middle America convergent margin. Nature 404, 748-752.

Roeloffs, E.A., 1996. Poroelastic techniques in the study of earthquake-related hydrologic phenomena. Adv. Geophys. 37, 135-195.

Rogers, G., Dragert, H., 2003. Episodic tremor and slip on the Cascadia subduction zone: the chatter of silent slip. Science 300, 1942-1943.

Sagiya, T., Thatcher, W., 1999. Coseismic slip resolution along a plate boundary megathrust: the Nankai Trough, southwest Japan. J. Geophys. Res. 104, 1111-1130.

Scholz, C.H., 1998. Earthquakes and friction laws. Nature 391, 37-42.

Schwartz, S.Y., Rokosky, J.M., 2007. Slow slip events and seismic tremor at circum-pacific subduction zones. Rev. Geophys. 45, RG3004, paper number 2006RG000208.

Screaton, E.J., Ge, S., 2007. Modeling of the effects of propagating thrust slip on pore pressures and implications for monitoring. Earth Planet. Sci. Lett. 258, 454-464.

Segall, P., Desmarais, E.K., Shelly, D., Miklius, A., Cervelli, P., 2006. Earthquakes triggered by silent slip events on Kilauea volcano, Hawaii. Nature 442, 71-74.

Silver, E.A., Kastner, M., Fisher, A.T., Morris, J.D., McIntosh, K.D., Saffer D.M., 2000. Fluid flow paths in the Middle America Trench and Costa Rica margin. Geology 28, 679-682.

Solomon, E.A., Kastner, M., Robertson, G., 2006. Barium cycling at the Costa Rica convergent margin, in: Morris, J.D., Villinger, H.W., Klaus, A. (Eds.), Proc. ODP, Sci. Res. 205, College Station, TX (Ocean Drilling Program), doi:10.2973/odp.proc.sr.205.2006, pp. 1-22.

Spinelli, G.A., Saffer, D.M., 2004. Along-strike variations in underthrust sediment dewatering on the Nicoya margin, Costa Rica related to the updip limit of seismicity. Geophys. Res. Lett. 31, doi:10.1029/2003GL018863.

Spivack, A.J., Kastner, M., Ransom, B., 2002. Elemental and isotopic chloride geochemistry and fluid flow in the Nankai Trough. Geophys. Res. Lett. 29, doi:10.1029/2001GL014122.

Spivack, A.J., Edmond, J.M., 1987. Boron isotope exchange between seawater and the oceanic crust. Geochim. et Cosmochim. Acta 51, 1033-1043.

Stein, C.A., Stein, S., 1994. Constraints on hydrothermal heat flux through the oceanic lithosphere from global heat flow. J. Geophys. Res. 99, 3081-3095.

Strasser, M., Weissert, H., Bernasconi, S.M., 2006. Carbon and oxygen isotope geochemistry along a subducting pelagic section offshore Costa Rica (ODP Legs 170 and 205), in: Morris, J.D., Villinger, H.W., Klaus, A. (Eds.), Proc. ODP Sci. Res. 205, College Station, TX (Ocean Drilling Program), doi:10.2973/odp.proc.sr.205.2006.
Vannucchi, P., Scholl, D.W., Meschede, M., McDougall-Reid, K., 2001. Tectonic erosion and consequent collapse of the Pacific margin of Costa Rica: Combined implications from ODP Leg 170, seismic offshore data, and regional geology of the Nicoya Peninsula. Tectonics 20(5), 649-668.

Vannucchi, P., Scholl, D.W., Meschede, M., McDougall-Reid, K., 2001. Tectonic erosion and consequent collapse of the Pacific margin of Costa Rica: combined implications from ODP Leg 170, seismic offshore data, and regional geology of the Nicoya Peninsula. Tectonics 20, 649-668.

Vannucchi, P., Ranero, C.R., Galeotti, S., Staub, S.M., Scholl, D.W., McDougall-Reid, K., 2003. Fast rates of subduction erosion along the Costa Rica margin: Implications for

nonsteady rates of crustal recycling at subduction zones. J. Geophys. Res. 108, doi:10.1029/2002JB002207.

Von Damm, K.L., 1995. Controls on the chemistry and temporal variability of seafloor hydrothermal fluids, in: Humphris, S.E., Zierenberg, R.A., Mullineaux, L.S., Thomson, R.E. (Eds.), Seafloor Hydrothermal Systems: Physical, Chemical, Biological, and Geological Interactions. AGU, Geophysical Monograph 91, Washington DC, pp. 222-247.

Wang, H.F., 2000. Theory of Linear Poroelasticity, With Applications to Geomechanics and Hydrogeology, Princeton University Press, Princeton, N.J.

Wei, W., Kastner, M., Spivack, A.J., in press. Chlorine stable isotopes and halogen concentrations in convergent margins with implications for the Cl isotopes cycle in the ocean. Earth Planet. Sci. Lett., Manuscript No. EPSL-D-07-00670.

Wheat, C.G., Mottl, M.J., 2000. Composition of pore and spring waters from Baby Bare: global implications of geochemical fluxes from a ridge flank hydrothermal system. Geochim et Cosmochim. Acta 64(4), 629-642.

Wheat, C.G., Jannasch, H.W., Kastner, M., Plant, J.N., DeCarlo, E.H., 2003. Seawater transport and reaction in upper oceanic basaltic basement: chemical data from continuous monitoring of sealed boreholes in a ridge flank environment. Earth Planet. Sci. Lett. 216, 549-564.

You, C.F., Chan, L.H., 1996. Precise determination of lithium isotopic composition in low concentration natural samples. Geochim et Cosmochim Acta 60, 909-915.

You, C.F., Castillo, P.R., Gieskes, J.M., Chan, L.H., Spivack, A.J., 1996. Trace element behavior in hydrothermal experiments: Implications for fluid processes at shallow depth in subduction zones. Earth Planet. Sci. Let. 140, 41-52.

Zhao, D., Xu, Y., Wiens, D.A., Dorman, L., Hildebrand, J., Webb, S., 1997. Depth extent of the Lau back-arc spreading center and its relation to subduction processes. Science 278, 254-257

Chapter 3

Progressive Barite Dissolution at the Costa Rica Convergent Margin: Implications for Ba Contribution to the Arc Volcanoes

3.1 Abstract

Convergent margins are important regions for geochemical cycling between major reservoirs such as seawater, oceanic sediment and igneous basement, continental crust, and the mantle. Recent studies have shown that when the subduction flux of incompatible elements, such as Ba, in the incoming sediment section is high, the arc volcanoes erupt lavas enriched in these elements. Based on the bulk input flux of sedimentary Ba from reference sections drilled seaward of the deformation front at Ocean Drilling Program (ODP) sites, a mass balance of the Ba input and the Ba output at volcanic arcs suggest 20-30% of the subducted sediment Ba budget is recycled to the arc, with the remainder assumed to continue past the arc window and potentially into the mantle. These estimates are based on the inference that many of these fluid-soluble sediment tracers are largely retained in metasedimentary rocks at depths greater than 15 km, but due to lack of sufficient data, do not consider element cycling in the forearc (<15 km). Here we report a detailed analysis of Ba concentrations in pore fluids and sediments across the Middle America Trench offshore Costa Rica. In addition, barite ($BaSO_4$) concentrations were determined on select sediment samples at the reference site seaward of the trench. The results show that SO_4^{2-} becomes progressively depleted in the underthrust sediments arcward of the trench, and as sulfate becomes depleted barite becomes undersaturated releasing dissolved Ba^{2+} to the pore fluid. Ba^{2+} concentrations rise several orders of magnitude, and the Ba-enriched fluid is transported seaward through flow conduits by compaction-induced fluid flow. This progressive barite dissolution from the subducting sediment column dramatically decreases the bulk sediment Ba concentration. In the upper hemipelagic sediments, ~1.6 km from the

trench, barite dissolution coupled to SO_4^{2-} depletion decreases bulk sediment Ba by 18%. Assuming the entire sediment section becomes progressively SO_4^{2-}-depleted as the sediments are transported deeper within the subduction zone, as much as 60% of the bulk sediment Ba at the reference site may be distilled from barite in the sediments in the forearc. This distillation of Ba from the mineral barite from sediments in the shallow levels of the subduction zone should operate in many convergent margins, and the loss of Ba in the forearc reduces previous estimates of the Ba input flux to depths of magma generation that was based solely on the reference section seaward of the trench. These results may have profound implications for current estimates of the amount of global sedimentary Ba recycled to volcanic arcs based on the bulk sediment Ba concentration of incoming sediment sections at subduction zones.

3.2 Introduction

Convergent margins are areas of high tectonic activity and dynamic hydrology, making them important regions for geochemical cycling between major reservoirs such as seawater, oceanic sediment and crust, continental crust, and the mantle. The distillation and loss of some volatiles and fluid-soluble elements from the shallow subduction zone may change the composition of the slab (sediments and igneous basement) delivered to the depths of magma generation beneath volcanic arcs and, ultimately, the mantle. Barium is a large-ion lithophile element (LILE) that is incompatible and enriched in oceanic sediments and the continental crust at convergent margins. Arc geochemists attempt to unravel the subduction signature of sediment-derived fluid and sediment melts from basalt-derived fluids using the LILEs such as Ba.

However, care must be taken in interpreting arc chemistry, because the subduction interface can be viewed as a semi-permeable membrane whose properties change with depth, allowing element distillation from the slab at a wide range of pressures and temperatures.

In some studies of arc geochemistry, seafloor compositions (inputs) at reference sections seaward of the subduction zone are simply compared with arc magmas (outputs), with little or no discussion of the possible effects of shallow subduction zone chemical processing. Investigations of elemental releases from shallow subduction fluids in the forearc are in a preliminary stage, and little is known about their net flux. Many elements of interest to arc geochemists (i.e. boron, lithium, barium, and strontium) are enriched in pore fluids sampled along the décollement zone of sedimentary forearc prisms to concentrations well above seawater composition (Kopf and Dehyle, 2002; Kastner et al., 2000; You et al., 1994; 1996; Chan and Kastner, 2000). It is currently unknown, however, if forearc losses of these elements from the downgoing slab in the upper ~15 km of the subduction zone compose a significant fraction of the subducting element budget.

Though there is little known about the net loss of incompatible elements from the subducting sediment section in the shallow forearc, there have been several studies that focused on constraining the cycling of LILEs and other incompatible elements at intermediate depths in subduction zones (>15 km), as well as at the depths of magma generation (Zack et al., 2001; Morris and Ryan, 2003; Bebout, 2007). Recent studies have shown that the metamorphic loss of Ba, as well as other incompatible elements useful for tracing the sediment component of arc magmas, is relatively restricted at

depths greater than 15 km to the depths of magma generation beneath volcanic arcs (e.g. Zack et al., 2001; Bebout, 2007). Thus, there is limited prograde Ba mobilization from mineral phases in the sediment column at intermediate depths. At the higher temperatures present at the depth of magma generation, Ba and other incompatible elements are partitioned into the fluid phase and incorporated into the melt. The extraction of Ba from the sediments beneath volcanic arcs is not entirely complete, and an estimated 70-80% of the Ba present in the sediments at intermediate depths passes through the arc window to the rear-arc, and possibly to the mantle (Morris and Ryan, 2003). Nevertheless, Ba is enriched in arc magmas worldwide and the output flux of Ba at the arc volcanoes reflects the sediment input fluxes to the depths of magma generation (Morris, 1991; Plank and Langmuir, 1993); at subduction zones where incoming sediment sections have relatively high Ba concentrations, the arc volcanoes erupt lavas enriched in Ba.

Using the bulk sediment input fluxes of Ba and other incompatible elements, coupled with the volcanic output fluxes, the amount of sediment contributed to the arcs as well as the elemental fluxes to the mantle have been estimated. (e.g., Plank and Langmuir, 1993; Patino et al., 2000). These estimates are based on the inference that Ba is stably retained in slab mineral phases at intermediate depths to the depths of magma generation. These estimates, due to lack of adequate data, also assume there is negligible loss of Ba from the subducting sediments with fluids expelled from the shallow forearc of subduction zones. There is the potential for significant losses of these incompatible elements, especially Ba, from the subducting sediments in the shallow forearc, and constraining this loss is critical for the accurate quantification of

elemental mass balances at subduction zones. In this chapter, I investigate the coupled SO_4^{2-}-depletion and barite ($BaSO_4$) dissolution in the shallow forearc of the Costa Rica subduction zone with implications for the shallow cycling of Ba and consequences for estimates of the amount sedimentary Ba delivered to the depths of magma generation beneath the volcanic arc and, ultimately, the mantle.

3.3 Background and Geologic Setting

The distribution of Ba in deep-sea sediments is variable. High concentrations are typically found in sediments underlying high productivity waters (Dymond et al., 1992, 1996; Paytan et al., 1996; Eagle et al., 2003) and are thought to result from the rapid release of dissolved Ba from labile particulate Ba during the early stages of plankton decomposition either by cell lysis or decay of labile organic matter in surface waters (Ganeshram et al., 2003). A fraction of the released Ba precipitates abiotically as barite ($BaSO_4$) within supersaturated microenvironments, where it is deposited on the seafloor (Dehairs et al., 1980; Bishop, 1988; Ganeshram et al., 2003). Ba is also contained in other biogenically related phases such as refractory organic matter and biogenic carbonate, as well as inorganic phases like detrital silicates and Fe-Mn oxides and oxyhydroxides (e.g. Dymond et al., 1992; McManus et al., 1998; Plank and Langmuir, 1998; Eagle et al., 2003). The concentration of these biogenic phases, as well as the detrital phases, may represent a significant fraction of the total Ba in the sediment column, especially at continental margin settings. Gonneea and Paytan (2006) performed a sequential mineral leaching procedure on surface sediments collected from 22 cores from the Southern Ocean, equatorial Pacific, Atlantic Ocean, and the Pacific

margin to quantify the amount of Ba present in various mineral phases typical of marine sediments. They found that the Ba concentration in carbonates ranges from 0-7% of the total bulk sediment Ba, and the amount of Ba in organic matter and ferromanganese oxyhydroxides range from 1-30% and 0-40%, respectively. The amount of Ba included in aluminosilicates and terrigeneous detritus, mainly clays (e.g. illite), zeolites, and feldspars, range from 2-67%, and the amount of Ba in the mineral barite ($BaSO_4$) ranges from 0-87% of the total Ba (Gonneea and Paytan, 2006). The total Ba concentration in typical marine sediments ranges from ~100-6,000 ppm (Gonneea and Paytan, 2006), ~600 ppm in green clay (Plank and Langmuir, 1998), and is generally <200 ppm in volcaniclastic sediments (Elliot et al., 1997; Plank and Langmuir, 19998). In general, sediment samples with total Ba concentrations >1000 ppm contain up to 70% Ba associated with the mineral barite (Eagle et al., 2003). Sediments with high concentrations of barite are typically found in regions with high biological productivity. Barite concentrations in marine sediments are diluted by terrigenous material close to the continents, and the higher the terrigenous sedimentation rate, the greater the dilution of barite. Sediments that are rich in biogenic phases and poor in continental detritus generally have a higher concentration of marine barite.

The Ba in aluminosilicates is typically immobile during sediment diagenesis; however, the Ba in barite is affected by variations in pore fluid sulfate concentrations (Dymond et al., 1992; McManus et al., 1998; Torres et al., 1996a). In organic-rich sediments, microbial degradation of organic matter leads to sulfate reduction and methanogenesis; the pore fluid SO_4^{2-} is consumed by oxidation of organic carbon and, at some locations, also by oxidation of methane. When pore fluid sulfate becomes

depleted, the solubility of barite increases greatly and dissolved Ba^{2+} concentrations can rise by several orders of magnitude (Brumsack and Gieskes, 1983; Torres et al., 1996b; Dickens, 2001). In tectonically active regions, like convergent margins where SO_4^{2-} depletion is pervasive, the dissolved Ba can be transported both upward and seaward by compaction-induced fluid expulsion in the underthrust sediments and fluid advection along higher permeability conduits in the décollement and upper fault zones (Figure 3.1). The dissolved Ba is then reprecipitated as barite when it reaches SO_4^{2-}-rich water (Torres et al., 2003). Recently, cold seep authigenic barite deposits have been discovered in a wide variety of continental margin environments. Torres et al. (1996a) sampled barite chimneys as high as 15 cm along a scarp failure at the Peru convergent margin. Other deposits have been discovered in the San Clemente Basin (Lonsdale, 1979; Torres et al., 2002), Monterey Bay (Naehr et al., 2000), the Sea of Okhotsk (Greinert et al., 2002), and the Gulf of Mexico (Fu et al., 1994).

Most of the Ba not associated with the mineral barite, especially the Ba in aluminosilicate minerals, bypasses this filter and can be transported deeper within the subduction zone. Prograde metamorphic reactions in the sediments and oceanic crust from 15 to 100 km depth cause clays, which are stable in the shallow levels of the subduction zone, to metamorphose to potassium-rich phengitic white micas. Recent studies have shown that the whole rock budget of Ba is nearly completely contained in phengites at intermediate depths of the subduction zone (>15 km, i.e. Moran et al., 1992; Bebout, 1999; Zack et al., 2001). The phengites can be relatively stable to the depths of magma generation, and possibly to pressures of 7 GPa and temperatures as high as 900 ^{o}C (Domanik and Holloway, 1996; Ono, 1998). Due to the stability of

phengites, Ba concentrations change little in metasedimentary subduction assemblages until amphibolite grade is reached (Morris and Ryan, 2003). Barium enrichment in lavas well above that of sediment melting is indicative of Ba mobility in fluids at depths of magma generation, and most of the Ba enrichment in arc lavas must be derived from the sediments. The remaining Ba tied up in phengites likely passes through the arc window and potentially makes it to the rear-arc and mantle (Morris and Ryan, 2003). However, the possible shallow distillation of Ba from barite in the forearc indicates that the slab composition delivered to the depths greater than ~15 km may be quite different from that entering the trench.

The incoming sediment section offshore the Nicoya Peninsula of Costa Rica contains 152 m of diatom-rich hemipelagic sediments overlying 226 m of pelagic calcareous nannofossil oozes and chalks. The subducting sediment section offshore Guatemala (Deep Sea Drilling Project [DSDP] Site 495) is nearly identical to that drilled offshore Costa Rica (Figure 3.2). Ba/La and Ba/Th ratios (Carr et al., 1990; Leeman et al., 1994; Patino et al., 2000), coupled with ^{10}Be isotopic concentrations of the Central American lavas (Tera et al., 1986; Morris et al., 1990, 2002), suggest that the entire sediment section is subducting to depths of magma generation beneath Nicaragua, whereas there is little contribution from the uppermost hemipelagic sediments and a proportionally larger contribution from the pelagic carbonate section at Costa Rica. Since the entire sediment section is initially subducted at Costa Rica, the low ^{10}Be in the Costa Rican volcanics must be due to sediment dynamics under the forearc, such as sediment underplating or subduction erosion (Morris et al., 2002). In addition to barite dissolution, the forearc erosion and/or underplating could also affect

the amount of Ba delivered to the depths of magma generation at the Costa Rica subduction zone.

Ocean Drilling Program (ODP) Legs 170 and 205 drilled a transect of three boreholes across the Middle America Trench with a reference site seaward of the trench in the incoming sediments and igneous basement (Sites 1039/1253) and two sites landward of the trench that drilled through the margin wedge, the décollement, and the underthrust sediments (Sites 1040/1254 and 1043/1255) (Figure 3.3). At Sites 1039/1253, sulfate concentrations reach a minimum of ~13 mM within the uppermost 20 m of the hemipelagic sediment section and are near seawater value within the pelagic carbonate section (Kimura, Silver, Blum, et al., 1997) (Figure 3.4C). At Sites 1040/1254, ~1.6 km landward of the trench, sulfate is totally depleted within the prism sediments and a zero-sulfate zone is also observed in the underthrust hemipelagic sediments to a depth of ~30 m below the décollement (Kimura, Silver, Blum, et al., 1997; Morris, Villinger, Klaus, et al., 2003), despite the fact that SO_4^{2-} concentrations ranged from seawater value to a minimum of ~13 mM at the reference site in the uppermost hemipelagic section. This suggests that upon underthrusting, the supply of sulfate from seawater by diffusion ceased and the sulfate reducing bacteria in the underthrust sediments utilized the remaining SO_4^{2-} at the top of the section (Figure 3.4D). Once this sulfate was depleted, barite became undersaturated and started dissolving causing a significant release of dissolved Ba^{2+} to the pore fluids (Figure 3.1). As the incoming sediment section is further underthrust, sulfate depletion would reach deeper levels in the sediment section, further liberating Ba^{2+} from barite. This progressive barite dissolution could have a profound impact on the amount of Ba that

originally was present within the sedimentary section at Sites 1039/1253 reaching depths of magma generation under the Costa Rican arc volcanoes. This process should operate in all convergent margins and may reduce estimates of Ba input flux to the subduction factory in margins subducting sediments with an appreciable amount of biogenic barite (i.e., bulk sediment Ba > ~1000 ppm).

3.4 Methods

Seventeen pore fluid and 13 sediment samples from ODP Sites 1253 and 1254 (Leg 205) were analyzed for Ba concentrations. In addition, 83 pore fluid and 29 sediment samples were analyzed for Ba concentrations from ODP Sites 1039 and 1040 (Leg 170). Most of the sediment samples were from pore water "squeezed cakes," and the intervals with ash layers were not analyzed. Since dissolved sulfate is only depleted in lithologic Unit U1 pore fluids at Sites 1040/1254, sampling was at a higher frequency in this unit. Pore fluid samples were analyzed for Ba concentrations by inductively coupled plasma–mass spectrometry (ICP-MS), as well as by inductively coupled plasma–optical emission spectrometry (ICP-OES). All of the sediment samples were analyzed for Ba concentrations by ICP-MS.

3.4.1 *Sampling Strategy and Compaction Correction*

In order to correlate sediment samples across holes (from Sites 1039/1253 to 1040/1254), percent compaction estimates for the underthrust sediment, based on weight percent $CaCO_3$ measured shipboard during Leg 170, were employed (Kimura, Silver, Blum, et al., 1997; Figure 3.5). Assuming that the entire section is underthrust at

Costa Rica, the $CaCO_3$ depth profiles from both sites indicate that there was a 36% reduction in thickness of lithologic Unit U1 and Subunit U2A (hemipelagic clayey section; Fig. 3.5), a 62% reduction of thickness of Subunits U2B and U3A (hemipelagic clayey and transition sections), and a 24% reduction of thickness in Subunits U3B and U3C (pelagic calcareous section) (Kimura, Silver, Blum, et al., 1997; Figure 5). These estimates are similar to those presented in Saffer et al. (2000) based on logged bulk density from Leg 170, where the authors estimate a 33% reduction in thickness of the hemipelagic section by Site 1040 and ~20% reduction in thickness of the lower pelagic calcareous section. To correlate the sample depths at Site 1039/1253 to their appropriate depths at Sites 1040/1254, the following equations were used:

$$d_{1040} = (d_{1039} \times \Delta t) + 371 \text{ and} \tag{3.1}$$

$$d_{1040(n)} = (\Delta d_{1039} \times \Delta t) + d_{1040(n-1)}, \tag{3.2}$$

where

d_{1040} = corresponding depth at Site 1040,

d_{1039} = depth at Site 1039,

Δt = percent reduction in thickness of each lithologic unit at Sites 1040/1254 determined from the $CaCO_3$ concentration depth profiles at Sites 1039 and 1040,

371 = depth of the base of the décollement at Site 1040,

Δd_{1039} = vertical distance between adjacent samples at Site 1039, and

$d_{1040(n-1)}$ = cross-correlated depth of the previous sample.

Equation 3.1 is only used for the shallowest sample at Site 1039, and equation 3.2 is used for all subsequent samples. Compared with the estimates of Saffer et al. (2000), the cross-hole compaction corrected depths in lithologic Units U1 and U2 at Site 1040 would be nearly identical and depths in Unit U3 would be shifted ~15 m deeper as a result of greater compaction in the transition section based on the $CaCO_3$ concentration depth profiles (Figure 3.5).

3.4.2 *Pore Fluid Analyses*

A total of 35 pore fluid samples were analyzed for Ba concentrations on a ThermoQuest/Finnigan Element 2 ICP-MS (see Table 3.1). All sample and standard preparations were made in a clean laboratory. Samples and standards were diluted with double-distilled deionized water containing 0.4-N HNO_3 and spiked with a 1.0-ppb In internal standard. All standard and calibration solutions were prepared from certified stock solutions. Two unknowns and 20 pore fluid samples were analyzed for each batch of analyses. A 1.0-ppb drift standard was analyzed after every four samples. Blanks were interspersed at random during each batch of analyses, and calibration was achieved with five standard solutions ranging from 0.1 to 5.0 ppb. Pore fluid samples were diluted 100 times at Sites 1039/1253, 1000 times in lithologic Unit P1 at Site 1254, 10,000 times in Unit U1 at Sites 1254/1040, and 100 times in Units U2 and U3 at Site 1040 to achieve a final concentration of ~1.0 ppb, thus matching the concentration of the drift standard and internal standard. Prior to analysis, the ICP-MS was tuned using the ^{115}In internal standard to maximize the intensity of the elements to be

analyzed, and mass calibrations were performed after every 20 samples. Instrumental drift was corrected online by normalization of the intensity of the analyte with the intensity of the ^{115}In standard. A second drift correction was applied offline using repeated analyses of the 1.0-ppb Ba drift standard made by dilution of the primary certified stock solution. The accuracy of the preparation of the samples (dilution) was monitored by analyses of standards as unknowns and the precision was monitored by multiple analyses of several 1.0-ppb standards. The average dilution accuracy and precision was <1.0% and <0.7%, respectively. The accuracy and precision of multiple analyses were monitored by repeated analyses of the two unknowns and the 1.0-ppb drift standard. The average accuracy was <1%, and the average precision was <0.65%.

In addition, a total of 65 pore fluid samples were analyzed for Ba concentrations by standard addition on a Perkin Elmer Optima 3000 ICP-OES. The average precision of the ICP-OES analyses determined by multiple analyses of drift and calibration standards was <7%. The average accuracy based on analyses of three prepared standards as unknowns was <4%. The results of the ICP-MS and ICP-OES determinations agree fairly well (Figure 3.4A,B; Table 3.1) and are within the quoted precision of the ICP-OES analyses.

Pore fluid sulfate concentrations at Sites 1039 and 1040 were measured shipboard during Leg 170 by ion chromatography (IC) using a Dionex DX-100. The reproducibility of the analyses, expressed as 1σ standard deviations of means of multiple determinations of International Association of Physical Sciences of the Ocean (IAPSO) standard seawater was ~1% (Kimura, Silver, Blum, et al., 1997). Sulfate concentrations at Sites 1253 and 1254 were measured shipboard during Leg 205 by IC

using a Dionex DX-120. The reproducibility of the analyses, expressed as percent precision from multiple determinations of IAPSO standard seawater was <2%.

3.4.3 *Bulk Sediment Chemical Analyses*

Sediment samples were dried in an oven for 24 hr at 60°C then ground into a fine powder. The samples were weighed before and after drying to determine the weight of water evaporated. Since the sediment samples were taken from pore water squeezed cakes, Ba concentrations of the pore water splits were used to compute the amount of Ba precipitated as salts during the drying process. Ten milligrams of the powdered sample was weighed and placed in a tightly capped, acid-cleaned polytetrafluoroethylene (PTFE) beaker. All sediment digestions were performed in a clean room. Two U.S. Geological Survey (USGS) certified rock standards were digested with each batch of sediments, typically four sediment samples. MAG-1 (marine mud) and SCO-1 (Cody Shale) were chosen as standards because they are marine sediments and have certified values for Ba. The digestion procedure consisted of five steps. Each step included adding an Optima-grade reagent, placing the tightly capped beaker in an ultrasonicator for 60 min, and evaporating to dryness in a PTFE evaporating unit under a heat lamp. The samples were digested by (1) adding 4-N HNO_3 to convert the carbonate to CO_2, (2) adding 30% hydrogen peroxide to oxidize the organic matter, (3) adding a 2:1 mixture of concentrated HF and HNO_3 to digest the sample, and (4-5) twice treating the samples with concentrated nitric acid. The samples were then diluted 2000-fold by weight with a pre-prepared 2.5% nitric acid solution in double-distilled deionized water.

All of the sediment samples were analyzed on a ThermoQuest/Finnigan Element 2 ICP-MS. The final dilution was 1×10^6 times by weight. All solutions were spiked with a 1.0-ppb In internal standard. The method of sediment analysis by ICP-MS was identical to that performed on the pore fluid samples outlined above. Digestion precision and accuracy were monitored by repeated digestion of reference USGS certified rock standards MAG-1 and SCO-1. Similar final dilutions were made for the sediment standards as the sediment samples. The average percent accuracy and precision of multiple determinations of MAG-1 were <1% and 0.5%, respectively. The average percent accuracy and precision of multiple determinations of SCO-1 were <1.3% and <1%, respectively. A few shipboard X-ray fluorescence (XRF) data analyzed during Leg 170 have been included in Figure 6. The samples were measured on an ARL 8420 XRF with reported percent accuracy and precision of 2–3% (Kimura, Silver, Blum, et al., 1997).

3.4.4 *Sequential Barite Extraction*

A barite separation procedure (Paytan, 1996; Eagle et al., 2003) was performed on four samples from Unit U1 and one sample from Unit U3 at Site 1039. The barite was separated from the sediment using a sequential leaching procedure that includes reaction with acetic acid, sodium hypochlorite, hydroxylamine, and an HF-HNO_3 mixture (Paytan, 1996). During the extraction, each of the leaching steps targets a major sedimentary fraction leaving a final residue composed of barite and a few other refractory minerals. The insoluble residue of the sequential leaching procedure is then

examined under a scanning electron microscope (SEM) to determine the barite content. The most common minerals other than barite in the residue are rutile and anatase (TiO_2), which are easily differentiated from barite by size and shape, as well as by an energy dispersive spectrometer (EDS) coupled to the SEM. The barite content in the residue (% of total residue) was determined using a backscattered electron imaging detector (BEI) mounted on the SEM and the EDX® imaging/mapping program (version 3.3) in Adina Paytan's laboratory at Stanford University. The percent area of the view occupied by barite was illuminated with the BEI detector, and was done five times per sample and averaged to determine the Ba_{barite} concentrations (concentration of Ba in leachate residue). The average yield of the barite extraction is ~95% (Eagle et al., 2003). The detection limit of the entire procedure is ~20 ppm barite, and the error in the estimate of Ba_{barite} is ± 8%.

3.5 Results

3.5.1 *Pore Fluid*

Pore fluid barium and sulfate concentrations at Sites 1039/1253 and Sites 1040/1254 are presented in Table 3.1. At Site 1039, sulfate concentrations are approximately seawater value (28.9 mM) at 1.45 meters below seafloor (mbsf) and decrease to a minimum of 13 mM at 24 mbsf (Figure 3.4C). Sulfate concentrations increase to values seen in surface sediments by 146 mbsf and increase to near-seawater concentration in the basal carbonate section.

Ba concentrations are higher than seawater value (~0.15 μM) and variable from

9 to 146 mbsf, which is approximately the base of lithologic Unit U2 (Figure 3.4A). The dissolved Ba^{2+} concentrations in the upper 146 m of Site 1039 range from 0.378 to 4.257 μM (Table 3.1). Below 146 mbsf, Ba concentrations are nearly constant and slightly above bottom water concentration. Ba concentrations are more variable at Site 1253, at the base of the pelagic carbonate section, due to fluid-rock reactions with the gabbro sill and metalliferous sediments. The Ba concentrations within lithologic Units U1 and U2 at Site 1039 are as much as 26 times seawater value and may be due to Ba mobilization from organic matter as well as Fe-Mn oxides and oxyhydroxides during organic matter diagenesis, as suggested by McManus et al. (1998). Ba concentrations are supersaturated with respect to barite at all depths at Site 1039/1253 (Monnin, 1999; Rushdi et al., 2000). Barite undersaturation would only occur if SO_4^{2-} concentrations decreased below ~0.2 mM at the Ba concentrations encountered at this site.

The pore fluid within the prism sediments at Sites 1040 and 1254 is totally depleted in dissolved SO_4^{2-} to the base of the décollement at 371 mbsf (Figure 3.4D). The zero-sulfate zone is also observed in the uppermost ~30 m of the underthrust section to a depth of 401 mbsf. The base of lithologic Unit U1 is at 423 mbsf at Site 1040, and within the other two units, sulfate concentrations gradually increase with depth to a value of 28 mM at the base of the pelagic section (Figure 3.4D). The depletion of sulfate in the uppermost hemipelagic sediments at Site 1040 suggests that upon underthrusting the supply of sulfate from seawater by diffusion ceased, and the sulfate-reducing bacteria within the underthrust sediments utilized the remaining SO_4^{2-} at the top of the section. Since the underthrust sediment section is the only remaining source of dissolved SO_4^{2-}, the depth of sulfate depletion must increase arcward. Ba

concentrations are elevated above seawater value (0.130 μM) in the prism sediments, with concentrations ranging from 6.37 to 13.2 μM, The elevated Ba concentrations indicate some Ba mobilization from barite dissolution. The maximum Ba concentrations within the prism sediments occur within the upper fault zone and the décollement (Table 3.1), and Ba concentrations are relatively constant at ~6 μM between these two flow conduits. Drilling during Legs 170 and 205 sampled a deeply sourced fluid within these two intervals originating at temperatures as high as ~150°C (Chan and Kastner, 2000; Hensen et al., 2004). Some distillation of Ba at the depth of the deep-sourced fluid may occur.

Most striking are the extremely high Ba concentrations immediately below the base of the décollement in the underthrust sediment section at both Sites 1040 and 1254. The concentrations in lithologic Unit U1 range from 17.26 to 209.57 μM, with the highest concentration occurring at the base of the décollement at 372 mbsf (Figure 3.4B). The concentration at 372 mbsf is ~53 times higher than the Ba concentration of the equivalent sample at Site 1039 and ~1400 times higher than the bottom water value. In contrast, the maximum Ba concentration measured within the décollement and upper fault zone at Site 1254 are 9.95 and 13.2 μM, respectively (Table 1). Thus, the extremely high pore fluid Ba^{2+} concentration immediately below the décollement is ~20 times higher than the concentrations measured within the two fluid flow conduits in the prism sediments. At 401 mbsf, where SO_4^{2-} concentrations start to increase, Ba concentrations decrease to values similar to those measured at the reference site (Table 3.1). The extremely high concentrations in the upper 30 m of the hemipelagic section at Site 1040 indicate intense Ba^{2+} liberation from the mineral barite due to increased

$BaSO_4$ solubility coupled to SO_4^{2-} depletion. As the subducting sediments move arcward the sulfate depletion zone will become thicker, eventually consuming the pore water SO_4^{2-} in lithologic Units U2 and U3 and liberating Ba^{2+} from barite.

3.5.2 *Sediments*

Bulk sediment samples were analyzed for Ba to determine if the amount of Ba liberated from barite in the shallow forearc significantly impacts the amount of sedimentary Ba delivered deeper into the subduction zone. The bulk sediment Ba concentration depth profiles for Sites 1039/1253 and 1040/1254 are shown in Figure 3.6. Ba concentrations are the highest at the base of lithologic Unit U2 and in the pelagic carbonate section (Unit U3) where there is less dilution of biogenic Ba by detrital material. Unit U1 and the top of Unit U2 (hemipelagic sediments) have nearly uniform Ba concentrations. The sharp increase in Ba from 2852 to 7408 ppm between 117.53 and 168.45 mbsf (Figure 6A) is caused by a change in sedimentation rate from ~46 to ~6 m/m.y. (Kimura, Silver, Blum, et al., 1997). Most Ba concentrations measured at Site 1039 range from 1000 to 3000 ppm, suggesting that barite is a significant fraction of the Ba-containing phases offshore Costa Rica (Eagle et al., 2003). The Ba concentration-depth profile in the underthrust sediments at Site 1040 is almost identical to that at Site 1039, except concentrations in lithologic Unit U1 are lower than those measured in Unit U1 at Site 1039 (Figure 3.6B; Table 3.2). Three samples were analyzed for Ba concentrations in the prism sediments at Site 1254. The concentrations are fairly uniform with depth and are 25%–30% of the concentrations measured in the underthrust section, reflecting dilution of biogenic barite by terrigeneous material

deposited by debris and gravity flows (Morris, Villinger, Klaus et al., 2003).

Average bulk Ba compositions of each of the lithologic units (Units 1, 2, and 3) at Sites 1039/1253 and 1040/1254 are presented in Table 3.3. The total sedimentary Ba lost or gained across the trench as well as the percent difference in concentration of each unit is also presented in Table 3.3. Unit U1 shows an 18% loss in bulk sedimentary Ba from Site 1039 to Site 1040. Unit U2 displays a 4% loss in Ba, whereas Unit U3 exhibits a 5% gain in Ba between the two sites (Table 3.3). The sampling resolution within Units U2 and U3 is much lower than in Unit U1. It is apparent that the percent difference in Unit U1 is approximately four times that in Units U2 and U3, indicating that significant Ba distillation due to barite dissolution had occurred and is occurring, effectively changing the bulk Ba composition of Unit U1 as sulfate becomes depleted. As dissolved sulfate rapidly becomes further depleted arcward, greater losses of sedimentary barite must exist not only in Unit U1 but in the deeper Units U2 and U3 as well.

Figure 3.7 shows cross plots of Ba at Site 1039 vs. Ba at Site 1040 for samples that correlate well across sites. The diagonal line has a slope of 1; therefore, if there were no changes from Site 1039 to Site 1040, then all samples would plot along the 1:1 line. Eighty percent of the samples from lithologic Unit U1 plot well above the line, signifying that the bulk Ba concentrations at Site 1039 are higher than those at Site 1040, whereas samples from Units U2 and U3 plot close to the 1:1 line and are both above and below the line. The pore fluid Ba concentration depth profile at Site 1040/1254 (Figure 3.4B) shows the highest dissolved Ba concentrations to occur immediately below the décollement, thus, assuming a homogeneous sediment section,

one would expect the shallowest samples at Sites 1039/1253 to plot the furthest left of the 1:1 line, which is not observed (Figure 3.7A).

The uppermost hemipelagic sediment section at Sites 1039/1253 is heterogeneous, reflecting varying amounts of detrital material input (Kimura, Silver, Blum, et al., 1997), thus differing rates of biogenic barite accumulation with depth, and thus with time. Therefore, Figure 3.7 does not show a clear trend of the deepest samples in Unit U1 plotting closer to the 1:1 line and the shallowest samples plotting furthest from the line. This is clearly observed in the results of the sequential barite extractions (Table 3.4). Four samples were analyzed in Unit U1 from the reference site, and Ba_{barite} concentrations vary with depth ranging from below the detection limit at 1.4 mbsf to 600 ppm at 65 mbsf. In Figure 3.7A, the sample at 65 mbsf plots the furthest from the 1:1 line and the sample at 9.4 mbsf plots the closest to the line. Thus, the sample with the highest barite concentration plots the furthest and the sample with the lowest barite concentration plots the closest to the 1:1 line (Table 3.4).

The depletion in bulk sediment Ba in Unit U1 from Site 1039 to Site 1040 is compared with the Ba_{barite} at the reference site in Table 3.4. The difference in bulk sediment Ba concentrations ranges from 277 ppm for sample 2H-5 to 628 ppm for sample 8H-4. The Ba lost from the sediments between Sites 1039 and 1040 is nearly equal to the barite concentration at Site 1039. This is exactly what would be expected from barite dissolution coupled to SO_4^{2-} depletion as the sediments are subducted. It should be noted, however, that the Ba concentrations in the uppermost hemipelagic sediments off Costa Rica at Site 1039 are ~1/2 those in the hemipelagic sediments seaward of the deformation front offshore Guatemala (Plank and Langmuir, 1998),

indicating there is some latitudinal variability in the Ba content of the sediments between the two areas, which are separated by >550 km. The Ba content of the pelagic sediments offshore Costa Rica and Guatemala are almost identical. Thus, there is some variability in the barite deposition rates along the Middle America Trench due to along strike variations in terrgineous sediment inputs and/or biogenic sedimentation. Site 1039 and Site 1040 are only ~2 km apart, therefore it is unlikely that they would have experienced differing amounts of biogenic and terrigeneous sediment deposition. However, minor variations in the supply of terrigenous sediments between Site 1039 and Site 1040 cannot be ruled out, which would lead to minor intrinsic variations in the barite concentrations between the two sites. The very good agreement between the change in bulk Ba across the trench from Site 1039 to Site 1040 and the Ba_{barite} at Site 1039 are very striking, and support the conclusion that the change is most likely the result of barite dissolution due to SO_4^{2-}-depletion. These results indicate that 80-100% of the barite originally present at the reference site is dissolved in the sulfate depletion zone in the upper ~30 m of hemipelagic sediments at Site 1040. The pore fluid SO_4 is completely consumed and most to all of the barite is dissolved in the upper 30 m of the subducting sediments, 1.6 km after being underthrust, in ~18,000 years.

The pelagic sediments of Unit U3 are predominantly biogenic carbonates deposited southwest of the current position of Site 1039/1253 near the equator. The barite content of these sediments is expected to be much higher due to the lower dilution by detrital material and higher paleoproductivity, hence, barite deposition. One sample was analyzed for Ba_{barite} from Unit U3 at Site 1039/1253, sample 19X-5 (135-150). The bulk Ba concentration of this sample is 7408 ppm and the Ba_{barite}

concentration is 6490 ppm, thus 88% of the Ba is in the mineral barite, consistent with the suggestion that barite concentrations in Unit U3 should be elevated relative to concentrations in Unit U1. Thus, as the sediments are subducted to greater depths within the subduction zone, a higher proportion of Ba^{2+} would be liberated from the sediment column, profoundly impacting the amount of sedimentary Ba reaching the depths of magma generation.

3.6 Summary and Discussion

3.6.1 *SO_4^{2-} Depletion and Barite Dissolution in the Upper Hemipelagic Sediments at Site 1040/1254*

At the reference site (1039), in the uppermost hemipelagic section, SO_4^{2-} concentrations range from seawater value to a minimum of ~13 mM. At Site 1040/1254, 1.6 km from the deformation front, however, sulfate is totally depleted within the prism sediments and the zero-sulfate zone is also observed in the underthrust sediments to a depth of ~30 m below the décollement. This suggests that upon underthrusting, the supply of sulfate by diffusion from seawater ceased and the sulfate reducing bacteria utilized the remaining SO_4^{2-} at the top of the section (Fig. 3.4). Ba^{2+} concentrations within the uppermost hemipelagic sediments at Site 1040/1254 are extremely high with values ranging from 17.26 to 209.57 μM, which is ~53 times higher than at the equivalent depth at Site 1253 and 1400 times the bottom water concentration. The elevated Ba^{2+} concentrations are the result of barite dissolution due to the increased solubility of $BaSO_4$ in the SO_4^{2-} depleted pore fluid.

The pore fluid Ba^{2+} concentrations measured immediately below the

décollement in the uppermost hemipelagic sediments at Site 1040/1254 are ~20 times higher than those measured within the regions of maximum fluid flow in the prism sediments (décollement and upper fault zone). The upper fault zone is situated at ~200 mbsf, whereas the décollement zone extends from ~340 to 371 mbsf at Sites 1040/1254. The décollement and upper fault zone exhibit sharp peaks in lithium, calcium, and C_1-C_3 hydrocarbon concentrations, as well as low chloride and potassium concentrations, indicating advection of a deeper sourced fluid along these horizons originating at temperatures of ~150°C (Silver et al., 2000; Chan and Kastner, 2000). Though the décollement and upper fault zone are separated by ~130 m, they have nearly identical dissolved Ba^{2+} concentrations that are elevated relative to the pore fluid barium concentrations in the prism sediments between them. The sharp discontinuity in Ba^{2+} concentrations between the décollement and underthrust sediments, but similarity in Ba^{2+} concentrations between the décollement and upper fault zone, ~130 m apart, precludes any significant contribution of barium from the uppermost hemipelagic sediments to the décollement by advective or diffusive flux, indicating that the underthrust sediment and décollement fluid flow systems are effectively decoupled. Thus, the Ba^{2+}-enriched pore fluid is transported seaward within permeable conduits such as ash layers and sand/silt horizons in the upper hemipelagic sediments driven by compaction-induced fluid flow as suggested by Saffer et al. (2000). The dissolved Ba is re-precipitated as barite when the fluid reaches sulfate-enriched fluids.

The distillation of Ba from the sediment column by barite dissolution is clearly observed in the change in bulk sediment Ba concentrations from Site 1039 to Site 1040 (Table 3.3). Concentrations analyzed in the uppermost hemipelagic sediments at Site

1040 are 18% lower than in the equivalent section at Site 1039. The change in bulk sediment Ba concentration is nearly equivalent to the Ba_{barite} concentration at Site 1039, clearly indicating that dissolution of barite is responsible for the Ba lost across the trench. Because SO_4^{2-} becomes progressively depleted as the sediments are being subducted, the barite in Units U2 and U3 must also dissolve. Assuming most of this dissolved Ba^{2+} is lost by fluid expulsion, the Ba input flux to the depths of magma generation is much lower than estimates based solely on the reference section seaward of the trench.

3.6.2 *Progressive Barite Dissolution and Sediment Ba Flux to Greater Depths*

Based on the high-resolution sampling in the upper hemipelagic sediments at Sites 1039/1253 and 1040/1254 presented in this study, we have relatively good control on the change in bulk sediment Ba due to barite dissolution across the trench. The bulk sediment sample resolution in the transition sediments (Unit U2) and pelagic carbonate section (Unit U3) is adequate, however only one sample in Unit U3 has been analyzed for Ba_{barite}. The pelagic carbonate section was deposited in an area of high biological productivity and low terrigeneous input close to the equator, thus barite was likely the major phase carrying particulate Ba in the water column, but minor amounts of Ba may have also been associated with terrigeneous aluminosilicates, organic matter, and Fe oxides and hydroxides. To estimate the amount of barite in a bulk sediment sample from the bulk Ba concentration, Dymond et al. (1992) suggested an algorithm to compute a term called Ba_{excess}, which is essentially the Ba in the sediment column not associated with aluminosilicate minerals, but is operationally defined as the Ba in barite

from a bulk sediment sample. Ba_{excess} is computed using the following equation (Dymond et al. 1992):

$$[Ba_{excess}] = [Ba_{total}]_{ppm} - (Ba/Al_{terrigeneous}) \times [Al_{total}]_{ppm} \quad (3.3)$$

where Ba/Al is representative of the terrigenous input to the ocean and serves as a correction factor for subtracting Ba associated with terrigenous inputs. $[Ba_{total}]$ is the bulk sediment Ba concentration, $[Al_{total}]$ is the bulk sediment Al concentration, and $[Ba_{excess}]$ is the concentration of Ba as the mineral barite in the bulk sediment sample. The Al concentrations were measured shipboard by XRF during Leg 170 (Kimura, Silver, and Blum et al., 1997) and by ICP-OES during ODP Leg 205 (Morris, Villinger, and Klaus et al., 2003) with an average percent precision of <2%. One potential complication of the barite estimation using bulk Al concentrations is that it does not take into account the Ba associated with organic matter or Fe oxides and hydroxides. Organic matter concentrations are relatively low (<0.5 %) in the pelagic carbonate section at Site 1039 (Kimura, Silver, and Blum et al., 1997), however the amount of Fe oxides and hydroxides within the sediment column is not constrained. Despite this unknown, we assumed that the amount of Fe oxyhydroxides is negligible and computed Ba_{excess} in the sediment samples analyzed for bulk Ba at Site 1039/1253 using the Ba/Al ratio of 0.0075 for average shale (Dymond et al., 1992; Bonn et al., 1998; Bains et al., 2000). The calculated Ba_{excess} values are presented in Table 3.5. The estimated Ba_{excess} computed using Equation 3.3 compares fairly well with Ba_{barite} concentrations analyzed

from the sequential barite extraction technique (last column, Table 3.5). The percent difference from Ba_{barite} measured directly is 5% for sample 1039-19X-5, 17% for 8H-4, 16% for 5H-4, 58% for 2H-5, and 0% for 1H-1. These results indicate that the Ba_{excess} estimate is more accurate in formations/units with a higher overall bulk Ba concentration, like the pelagic carbonate unit (U3). The geometric mean of the average error in the Ba_{excess} versus Ba_{barite} concentrations is ~20%. The estimated Ba_{excess} concentrations show that the barite content of Unit U3 is approximately twice that of Unit U1, which is consistent with the higher relative dilution of biogenic barite in Unit U1 by terrigenous sediments.

The sedimentary Ba input flux to the subduction zone was estimated for three cases: (1) no dissolution of barite present in the incoming sediment section, (2) an 18% loss of sedimentary Ba due to barite dissolution (as observed in the upper hemipelagic section), and (3) all of the barite in the incoming sediment section is dissolved in the forearc associated with progressive sulfate-depletion, computed from the measured and calculated concentrations of Ba_{barite} in each of the units. The input flux of sediment Ba was computed using the elemental flux equation presented in Plank and Langmuir (1998):

$$Flux_{Ba} = C_{Ba}tL\rho R \qquad (3.4)$$

where C_{Ba} is the weighted sedimentary Ba concentration, t is the sediment thickness, L is the length of the subduction zone, ρ is the sediment density, and R is the plate convergence rate. To compute the weighted sediment Ba concentrations for all three

cases, the average Ba concentration in each sedimentary unit (U1, U2, and U3) was multiplied by the weighted thickness of the unit (unit thickness/total sediment thickness), then the weighted Ba concentrations of each unit were added together. The weighted bulk sediment Ba concentration for each case is presented in Table 3.6. As shown in the table, if all of the sedimentary barite is dissolved, measured and calculated as Ba_{excess} at Site 1039, from the entire incoming sediment section due to progressive SO_4^{2-} depletion during subduction, then up to 60% of the incoming sediment Ba is distilled from the sediments in the shallow forearc. Thus, only 40% of the original bulk sediment Ba, primarily associated with aluminosilicate phases, present at the reference site will be delivered deeper within the subduction zone. This suggests that the input flux of Ba to the depth of magma generation is 40% of the estimated flux based solely on the reference section seaward of the deformation front. The Ba input flux at the Costa Rica margin is presented in Table 3.6 and ranges from 615 g/yr per cm trench length for the case of no barite dissolution to 240 ± 48 g/yr per cm trench if all the estimated barite in the incoming section dissolves in the forearc.

These results have no bearing on the measured Ba concentrations or estimated output flux at the volcanic arc, the output flux remains the same, but there is as much as a 60% decrease in the estimated input flux from the subducting sediment section. The 60% decrease in the Ba flux assumes that all of the Ba lost from barite dissolution in the shallow forearc is transported seaward and re-precipitated as barite upon reaching SO_4^{2-}-rich pore fluids. This is likely considering the limited adsorption of Ba onto clay minerals compared to other cations and the inference that most of the pore fluids expelled from the consolidating underthrust sediments is transported upward into the

hemipelagic sediment section and seaward along permeable pathways (Saffer et al., 2000). This process does not affect the Ba associated with aluminosilcates minerals such as primary feldspars and illite, which are likely to be the main phases hosting the residual 40% of the bulk sediment Ba delivered to deeper levels of the subduction zone. The major implication of the reduced flux of Ba into the subduction zone is that in order to balance the output flux at the volcanic arc with the lower input flux requires a much larger sediment component delivered to the depths of magma generation and recycled to the volcanic arc. Current estimates of the amount of Ba recycled to the Central American volcanic arc are based on mass balance calculations of the input flux of sediment Ba at the trench and arc enrichments in Ba corrected for mantle melting effects. These calculations indicate that ~20-30% of the Ba budget in the subducted sediments is recycled to the volcanic arc with 70-80% continuing past the arc window (Morris and Ryan, 2003; Plank and Langmuir, 1993). Using our revised estimate of the Ba input flux based on complete barite dissolution from the underthrust sediment section in the Costa Rica forearc, ~32-48% of the Ba budget is recycled to the volcanic arc, with 52-68% of the Ba passing through the arc window and potentially subducting to the mantle. The shallow dissolution of marine barite in the shallow forearc should occur in most subduction zones, profoundly impacting the amount of sediment Ba delivered to the depths of magma generation worldwide. This process should be considered in global mass balances of the subducted sedimentary Ba budget.

3.7 Acknowledgements

This research used samples and/or data provided by the Ocean Drilling Program

(ODP). ODP is sponsored by the U.S. National Science Foundation (NSF) and participating countries under management of Joint Oceanographic Institutions (JOI) Inc. This work was funded by JOI-U.S. Science Support Program (USSSP) Grants to E.A. Solomon and M. Kastner. We thank A. Paytan and K. Ke Yan for assistance with barite concentration analyses. Helpful reviews were provided by Julie Morris and Kristina Faul.

3.8 Chapter Acknowledgement

Chapter 3, in part, has been submitted for publication as it appears in Solomon, E.A., Kastner, M, and Robertson, G, 2006. Barium cycling at the Costa Rica convergent margin. *In* J.D. Morris, H.W. Villinger, and A. Klaus (Eds.), *Proc. ODP Sci. Results*, 205, 1-22.

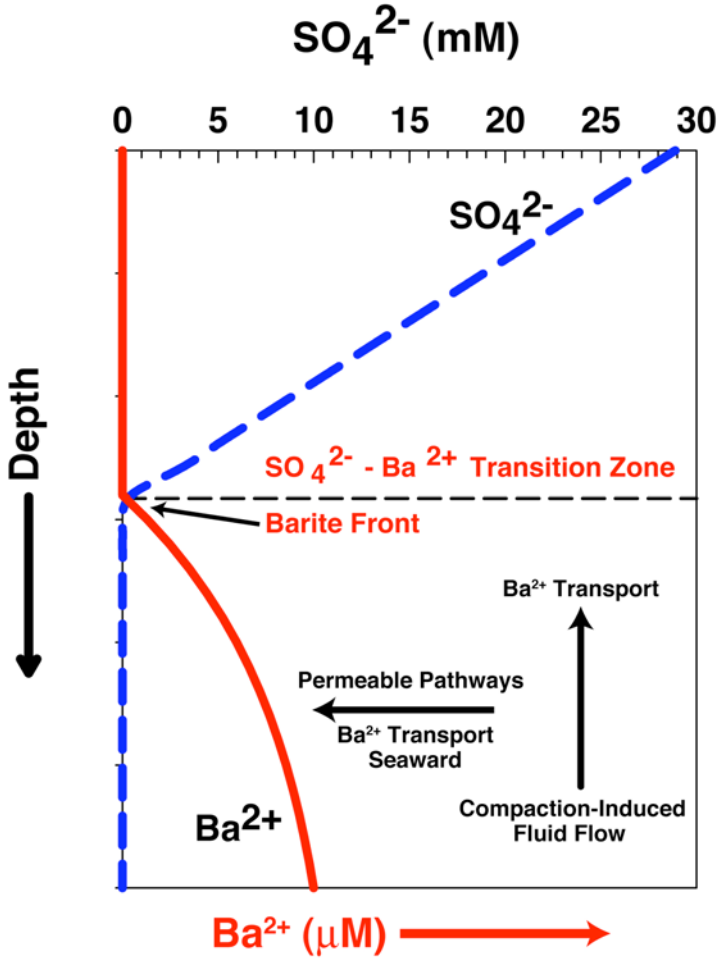

Figure 3.1 Generalized schematic showing cycling of Ba^{2+} in convergent margin sediments. The blue dashed line is the SO_4^{2-} concentration-depth profile and the red solid curve is the Ba^{2+} concentration-depth profile. When pore fluid SO_4^{2-} becomes depleted, barite dissolves and pore fluid Ba^{2+} concentrations rise by several orders of magnitude. The dissolved Ba^{2+} is transported upward by compaction-induced fluid expulsion. Some of the Ba^{2+} is recycled at the SO_4^{2-}-Ba^{2+} transition zone, where it precipitates as a barite front. Due to lateral pressure gradients, some of the Ba^{2+} is transported seaward along higher permeability conduits.

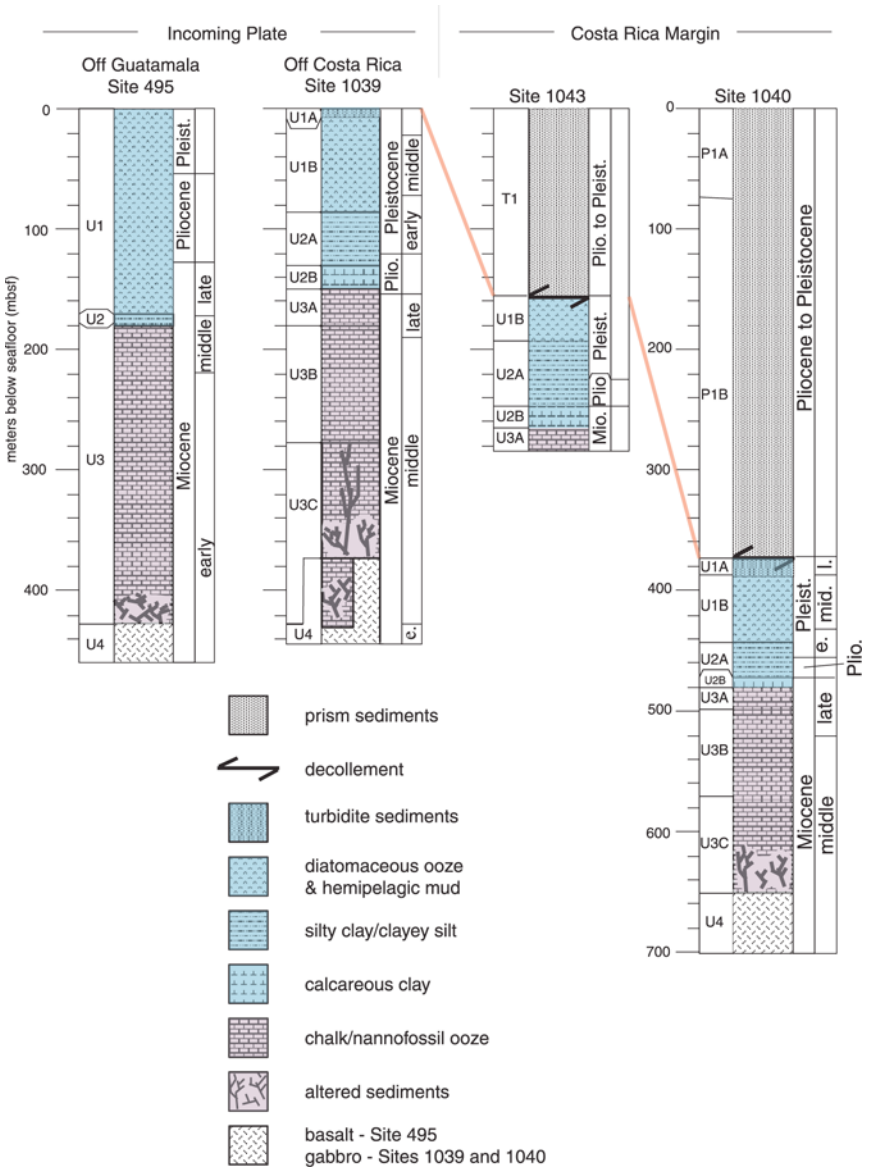

Figure 3.2 Incoming sediment sections offshore Guatemala (Site 495) and Costa Rica (Site 1039). The incoming sediment section at Site 1039 is the same beneath the décollement at Sites 1043 and 1040 arcward of the trench at Costa Rica, suggesting there is no sediment accretion at the toe of the wedge at present (modified from Morris, Villinger, and Klaus et al., 2003). Stratigraphic column at Site 1253 is nearly identical to that at Site 1039.

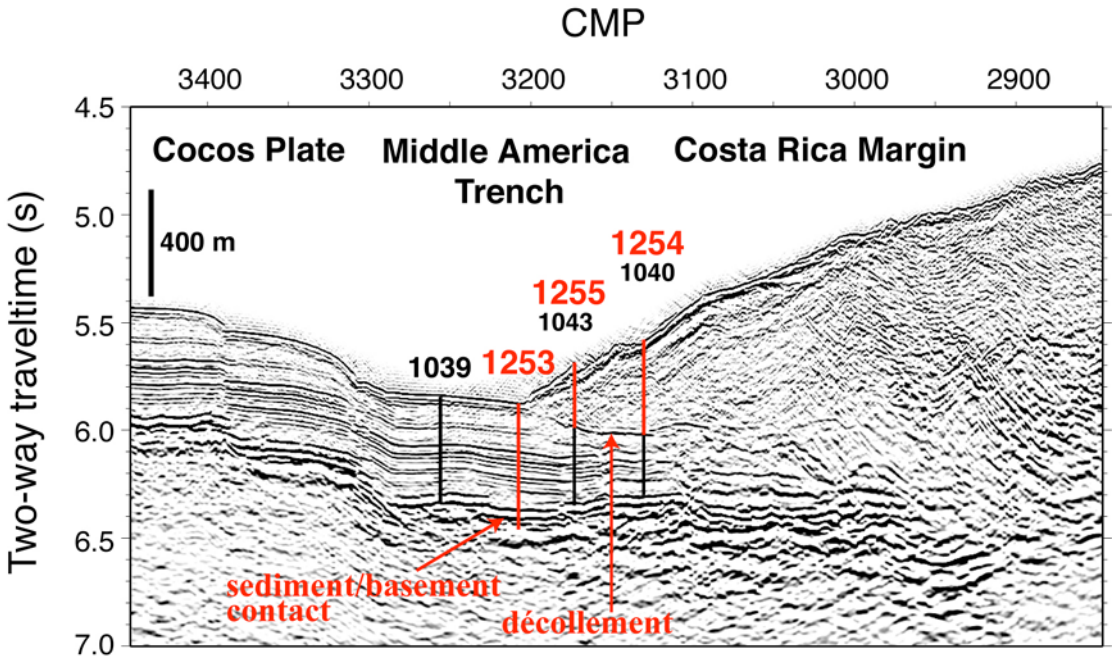

Figure 3.3 Migrated multichannel seismic Profile BGR-99-44 (Morris, Villinger, and Klaus et al., 2003) across the Middle America Trench offshore Costa Rica. Red lines are Leg 205 sites and thin black lines are Leg 170 sites. Site 1253 is ~0.2 km seaward of the deformation front, and Site 1040/1254 is ~1.6 km arcward of the deformation front. CMP = common midpoint.

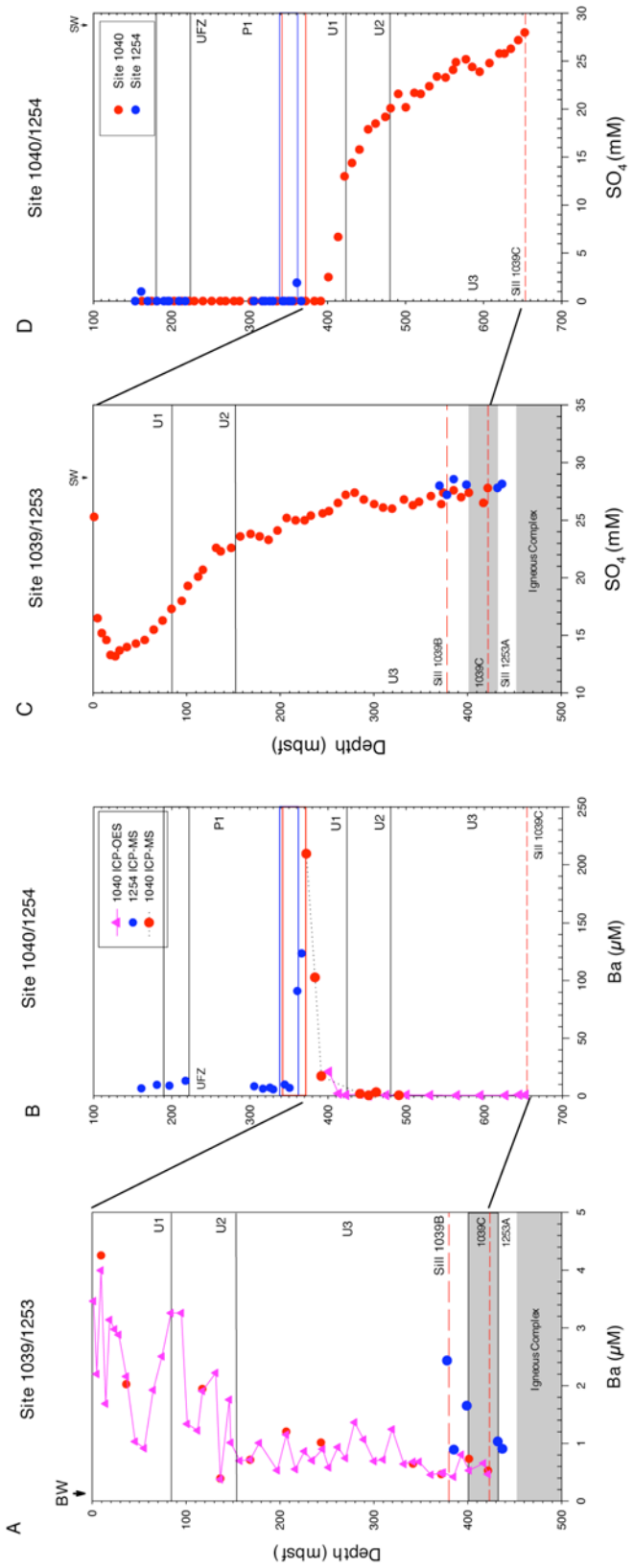

Figure 3.4 Pore fluid Ba and SO_4 concentration depth profiles along the transect across the Middle America Trench. **A,C** Ba and SO_4 concnentrations at Sites 1039/1253. **B,D** Ba and SO_4 concentrations at Sites 1040/1254. Note the difference in the Ba concentration scale at the two sites. Dashed red lines in A and C are the sill depths in Holes 1039B and 1039C. Thin gray shaded area is the sill at Site 1253, and the thick gray shaded area is the igneous complex. The depth interval delineated by black lines in B and D is the upper fault zone (UFZ), the area delineated by the blue lines is the décollement at Site 1254, and the area delineated by the solid red lines is the décollement at Site 1040. SO_4 concentrations are from Kimura, Silver, Blum et al. (1997) and Morris, Villinger, Klaus et al. (2003). BW = bottom water Ba concentration for the region, SW = seawater, ICP-OES = inductively coupled plasma-optical emission spectrometry, ICP-MS = inductively coupled plasma-mass spectrometry.

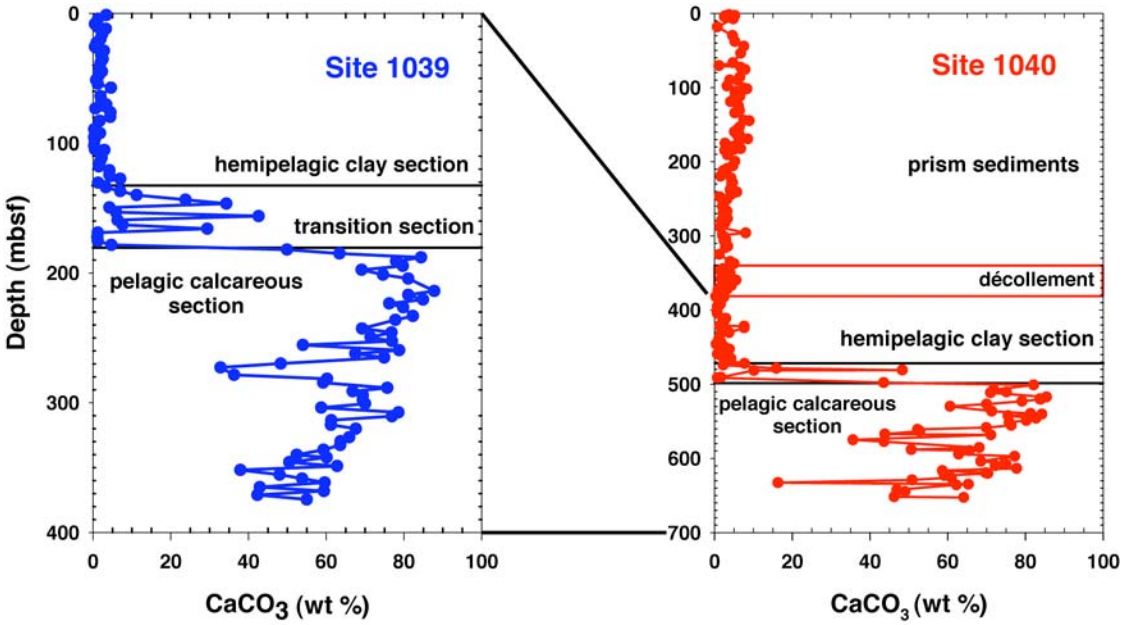

Figure 3.5 $CaCO_3$ concentration depth profiles at Sites 1039 and 1040. $CaCO_3$ data from Kimura, Silver, Blum et al. (1997).

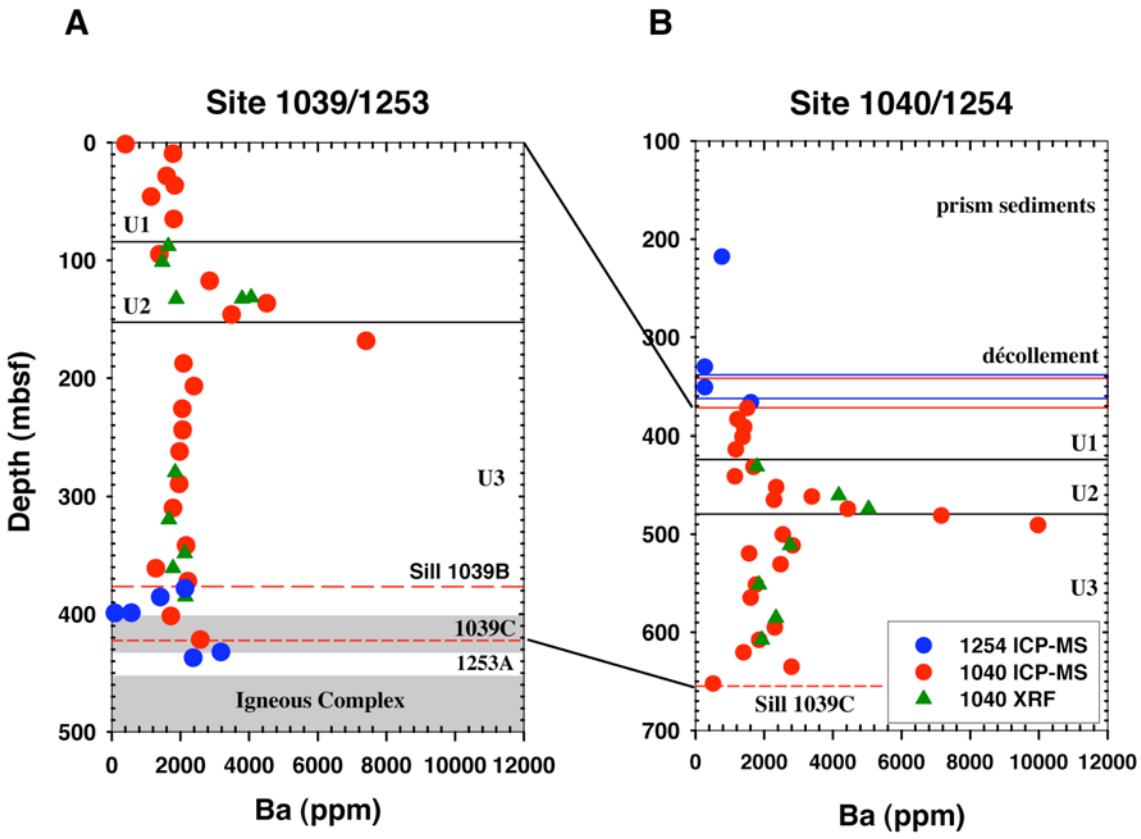

Figure 3.6 Bulk sediment Ba concentration-depth profiles at (**A)** Sites 1039/1253 and (**B)** Sites 1040/1254. Dashed red lines in A are the sill depths in Holes 1039B and 1039C. The thin gray shaded area is the sill at Site 1253, and the thick gray shaded area is the igneous complex. The area delineated by blue lines is the décollement zone at Site 1254, and the area delineated by solid red lines is the décollement zone at Site 1040. X-ray fluorescence (XRF) data are from Kimura, Silver, Blum et al. (1997). ICP-MS = inductively coupled plasma-mass spectrometry.

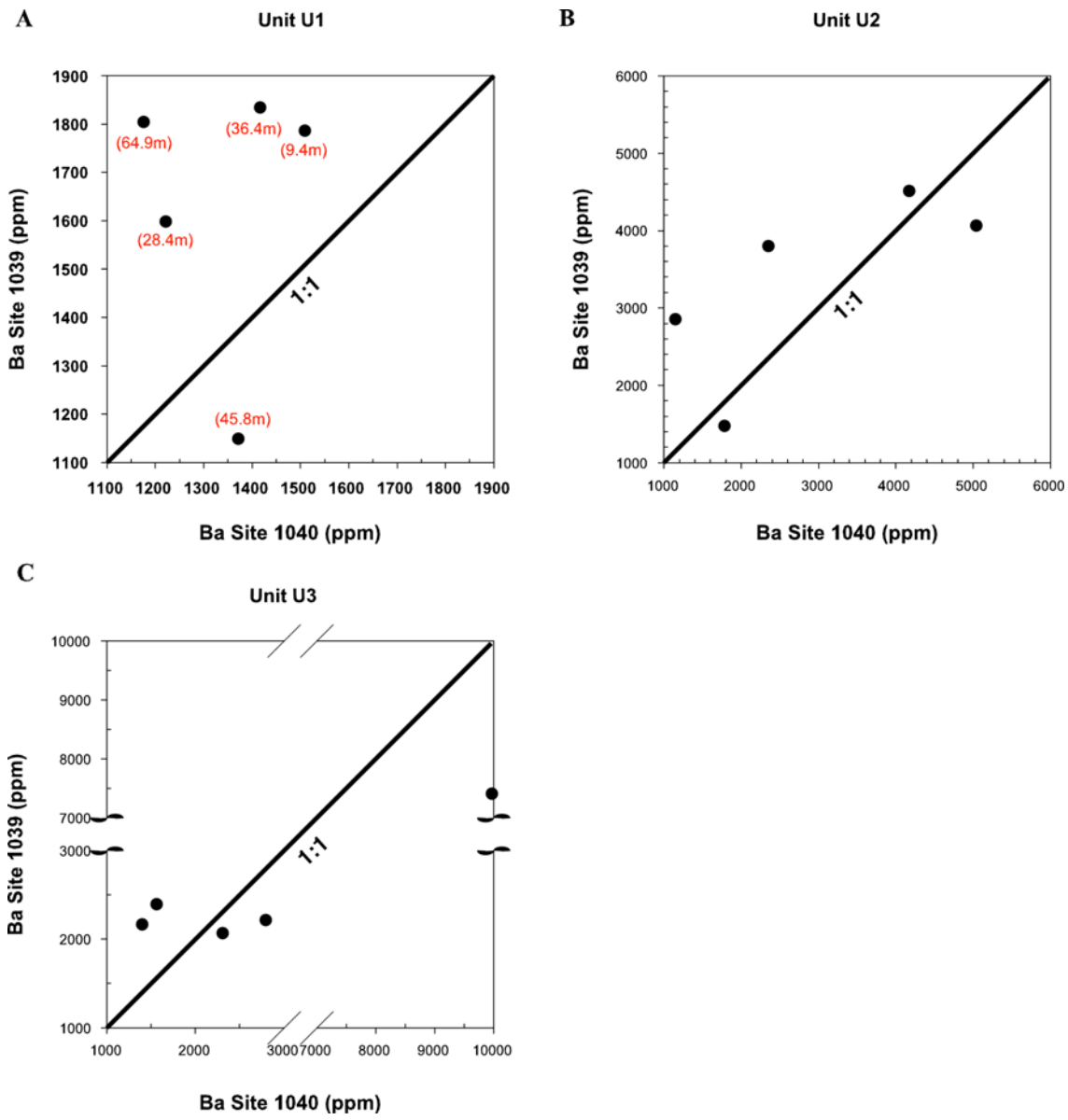

Figure 3.7 Bulk sediment Ba concentrations at Site 1039 v. bulk sediment Ba concentrations at Site 1040 for samples that correlate across holes for lithologic (**A**) Unit U1, (**B**) Unit U2, and (**C**) Unit U3. Numbers in parentheses are sample depths in mbsf at Site 1039. The correlated samples would plot along the 1:1 line in the figures if there were no change in bulk sediment Ba across the trench. Depths that plot above the 1:1 line indicate a loss of bulk sediment Ba from Site 1039 to Site 1040.

Table 3.1 Pore fluid Ba concentrations, ODP Sites 1039/1253 and 1040/1254

Core, section, interval (cm)	Depth (mbsf)	Ba (μM) ICP-MS	Ba (μM) ICP-OES	SO_4* (mM)
170-1039B-				
1H-1, 145-150	1.5	-	3.46	25.3
2H-2, 140-150	5.0	-	2.20	16.5
2H-5, 140-150	9.4	4.26	4.00	15.2
3H-2, 140-150	14.4	-	1.69	14.6
3H-5, 140-150	18.7	-	3.14	13.3
4H-2, 140-150	23.9	-	2.98	13.2
4H-5, 140-150	28.4	-	2.88	13.7
5H-4, 140-150	36.4	2.03	2.16	14.0
6H-4, 134-150	45.8	-	1.03	14.3
7H-4, 140-150	55.4	-	0.914	14.6
8H-4, 140-150	64.9	-	1.92	15.5
9H-4, 140-150	74.4	-	2.51	16.3
10H-4, 140-150	83.9	-	3.26	17.3
11H-5, 140-150	94.9	-	3.26	18.0
12X-3, 135-150	101.4	-	1.34	19.3
13X-6, 135-150	112.4	-	1.22	20.1
14X-3, 135-150	117.5	1.95	1.91	20.7
15X-6, 135-150	131.6	-	2.22	22.6
16X-3, 135-150	136.6	0.394	0.378	22.3
17X-3, 130-150	146.1	-	1.76	-
17X-4, 135-150	147.7	-	1.01	22.6
18X-4, 135-150	157.3	-	0.700	23.6
19X-5, 135-150	168.5	0.717	0.719	23.8
20X-5, 135-150	178.0	-	1.01	23.6
22X-5, 135-150	197.2	-	0.534	24.1
23X-5, 135-150	206.9	1.21	1.15	25.2
24X-5, 135-150	216.5	-	0.552	25.0
25X-5, 135-150	226.1	-	0.863	25.0
26X-4, 135-150	234.3	-	0.704	25.4
27X-5, 135-150	245.4	1.02	0.901	25.6
28X-3, 135-150	252.1	-	0.584	25.8
29X-3, 135-150	261.8	-	0.936	26.5
30X-2, 135-150	270.0	-	0.746	27.2
31X-3, 130-150	279.5	-	1.36	27.4
32X-2, 130-150	289.2	-	1.07	26.8
33X-3, 130-150	300.3	-	0.693	26.4
34X-3, 130-150	309.9	-	0.718	34.0
35X-3, 130-150	319.5	-	1.24	26.0
36X-5, 130-150	332.1	-	0.643	26.8
37X-5, 130-150	341.7	0.647	0.682	26.3
38X-3, 130-150	348.3	-	0.682	26.6
39X-5, 130-150	360.9	-	0.458	27.1
40X-6, 130-150	372.0	0.467	0.485	26.4
41X-1, 130-150	374.1	-	0.492	27.4

Table 3.1 Continued Pore fluid Ba concentrations, Sites 1039/1253 and 1040/1254

Core, section, interval (cm)	Depth (mbsf)	Ba (μM) ICP-MS	Ba (μM) ICP-OES	SO_4* (mM)
170-1039C-				
3R-2, 132-150	385.0	-	0.420	27.6
4R-1, 132-150	393.2	-	0.803	27.0
5R-1, 000-006	401.5	0.734	0.530	27.4
6R-4, 128-142	417.0	-	0.656	26.5
7R-1, 085-100	421.7	0.530	0.467	27.8
205-1253A-				
2R-2, 85-104	378.1	2.44	-	27.2
3R-1, 7-23	385.4	0.893	-	28.6
4R-3, 100-120	399.0	1.65	-	28.1
10R-2, 59-73	432.1	1.03	-	27.8
11R-1, 81-96	437.0	0.907	-	28.2
205-1254A-				
2R-4, 125-160	161.4	6.67	-	1.1
4R-5, 45-90	181.3	9.74	-	0.0
6R-2, 125-166	197.2	9.02	-	0.0
8R-4, 0-45	217.9	13.21	-	0.0
9R-5, 0-45	305.7	8.37	-	0.0
10R-6, 0-40	316.9	6.37	-	0.0
11R-5, 63-103	325.9	7.26	-	0.0
12R-1, 101-141	330.1	5.69	-	0.0
13R-5, 69-109	344.9	9.95	-	0.0
14R-3, 0-44	351.0	7.01	-	0.0
15R-3, 0-44	360.9	91.1	-	0.0
16R-3, 49-89	366.4	123.6	-	0.0
170-1040C-				
23R-1, 115-150	372.2	209.6	-	0.0
24R-2, 120-150	381.8	102.8	-	0.0
25R-1, 125-150	391.5	17.3	-	0.0
26R-1, 125-150	401.1	-	20.9	2.5
27R-3, 125-150	413.7	-	1.99	6.7
28R-2, 125-150	423.4	-	0.817	13.0
30R-2, 125-150	441.0	1.99	1.80	15.8
31R-3, 125-150	452.1	0.578	0.464	17.9
32R-3, 125-150	461.8	3.372	-	18.5
33R-5, 120-150	474.2	-	0.709	19.2
35R-3, 132-150	490.8	0.670	-	21.6
36R-3, 135-150	500.4	-	0.943	20.2
39R-4, 115-150	530.6	-	0.691	22.4
43R-1, 130-150	564.7	-	0.596	24.9
46R-2, 130-150	595.1	-	0.548	23.9
49R-4, 115-150	626.9	-	0.578	25.8
51R-3, 120-140	644.6	-	1.06	27.2
52R-2, 125-150	652.8	-	0.961	28.0

*Data from Kimura, Silver, and Blum et al. (1997)

Table 3.2 Bulk sediment Ba concentrations for representative samples, ODP Sites 1039/1253 and 1040/1254

Core, section, interval (cm)	Depth (mbsf)	Lithology	Ba (ppm)
170-1039B-			
1H-1, 145-150	1.5	diatomaceous ooze w/interbedded silt, sand	400
2H-5, 140-150	9.5	diatomaceous ooze with radiolarians	1786
4H-5, 140-150	28.5	siliceous ooze with minor ash	1598
5H-4, 140-150	36.5	silty siliceous and diatomaceous ooze	1834
6H-4, 140-150	45.9	siliceous ooze with minor ash	1148
8H-4, 140-150	65.0	siliceous ooze with minor ash	1804
11H-5, 140-150	95.0	silty clay with diatoms and vitric ash	1388
14X-3, 135-150	117.5	silty clay with radiolarians and diatoms	2852
16X-3, 135-150	136.6	clay with calcareous layers and ash	4512
17X-3, 135-150	146.2	calcareous clay	3493
19X-5, 135-150	168.5	Clayey biogenic ooze	7408
21X-5, 135-150	187.6	calcareous nannofossil ooze with diatoms	2091
23X-5,135-150	206.9	nannofissil ooze with diatoms	2394
25X-5, 135-150	226.1	nannofossil ooze w/ diatoms	2056
27X-4, 135-150	243.9	siliceous nannofossil ooze	2067
29X-3, 135-150	261.8	diatomaceous nannofossil ooze	1977
32X-2, 130-150	289.3	nannofossil ooze w/ diatoms	1962
34X-3, 130-150	309.9	siliceous nannofossil ooze	1783
37X-5, 130-150	341.7	siliceous nannofossil ooze	2165
39X-5, 130-150	361.0	calcareous ooze w/ fossils, minor ash	1285
40X-6, 130-150	372.0	Matrix supported breccia, biogenic ooze	2216
170-1039C-			
5R-1, 0-6	401.5	Nannofossil ooze w/ diatoms	1724
7R-1, 85-100	421.7	Diatomaceous nannofossil ooze	2580
205-1253A-			
2R-2, 85-104	378.1	Clay w/ nannofossils and ash	2134
3R-1, 7-23	385.4	nannofossil chalk w/ forams+clay rich laminations	1413
4R-3, 91-93	398.8	silicic ash w/clay and opaques ("big white ash")	572.4
4R-3, 100-120	399.0	nannofossil chalkw/ clay and volcanic ash	93.19
10R-2, 59-73	432.1	volcanic ash,nannofossils,clay mixed sed	3180
11R-1, 81-96	437.0	claystone w/ zeolites and spicules	2372
25R-1, 0-3	513.0	"baked sediment" claystone w/ recrystallized calcite	281.2
27R-1, 7.5-9.0	519.3	"baked sediment" claystone w/ recrystallized calcite	154.1
42R-2, 96-100	592.4	green clay and zeolite vein	1.98
205-1254A-			
8R-4, 0-45	217.9	Claystone	771.4
12R-1, 101-141	330.1	Calcite-rich claystone	269.1
14R-3, 0-40	351.0	Claystone w/ silt, ash, ad opaques	277.0
16R-3, 49-89	366.4	Claystone w/ ash and diatoms	1614

Table 3.2 Continued Bulk sediment Ba concentrations for representative samples, ODP Sites 1039/1253 and 1040/1254

Core, section, interval (cm)	Depth (mbsf)	Lithology	Ba (ppm)
170-1040C-			
23R-1, 115-150	372.2	Dark olive green silty clay w/ diatoms	1509
24R-2, 120-150	383.5	Sandy siltstone w/ diatoms	1221
25R-1, 125-150	391.6	Olive green diatomaceous ooze w/ ash	1417
26R-1, 125-150	401.2	Diatomaceous silty clay	1371
27R-3, 125-150	413.8	Siliceous mudstone w/ ash	1176
29R-2, 118-150	431.4	silty clay	1689
30R-2, 125-150	441.1	Olive green silty claystone	1147
31R-3, 125-150	452.2	Light greyish-green silty claystone w/ ash	2351
32R-3, 125-150	461.8	silty claystone	3386
32R-6, 14-17	465.0	Calcareous claystone w/ diatoms and ash	2284
33R-5, 120-150	474.4	silty clay	4434
34R-3, 125-150	481.1	calcareous claystone	7157
35R-3, 132-150	490.8	Claystone w/ vitric ash and diatoms	9971
36R-3, 135-150	500.4	Siliceous nannofossil chalk	2543
37R-4, 135-150	511.5	diatomaceous nannofossil chalk	2829
38R-3, 130-150	519.7	Siliceous nannofossil chalk	1562
39R-4, 115-150	530.7	Siliceous nannofossil chalk	2476
41R-5, 130-150	551.5	Siliceous nannofossil chalk	1762
43R-1, 130-150	564.8	Siliceous nannofossil chalk	1606
46R-2, 130-150	595.2	Green diatomaceous chalk	2309
47R-4, 130-150	607.8	Siliceous nannofossil chalk	1854
48R-6, 130-150	620.5	Diatomite w/ calcareous nannofossils	1397
50R-3, 130-150	635.2	Diatomite w/ nannofossils and ash	2796
52R-2, 74-80	652.3	Olive green chalk w/ accessory zircon	514.1

Table 3.3 Bulk sediment Ba composition for lithologic units U1, U2, and U3, ODP Sites 1039/1253 and 1040/1254

Site	Unit	Thickness (m)	Avg. Ba (ppm)	Site	Unit	Thickness (m)	Avg. Ba (ppm)	Δ Ba (ppm)	% Δ Ba
1039/1253	U1	84.4	1643	1040/1254	U1	51.6	1339	-295.42	-18
	U2	68.1	3127		U2	57.1	2997	-129.7	-4
	U3	268.5	2807		U3	173.8	2958	+ 151.2	+5

Table 3.4 Results of sequential barite extraction at Site 1039/1253 compared with the change in bulk Ba across the trench

Core, section, interval (cm)	Ba_{barite} (ppm)	Ba_{bulk} (ppm)	$Ba_{bulk\ 1040}$* (ppm)	ΔB_{Bulk} (ppm)	% Barite$^{\zeta}$ dissolved
170-1039B-					
1H-1, 145-150	0	400	-	-	-
2H-5, 140-150	196	1786	1509	277	100
5H-4, 140-150	520	1834	1417	417	80
8H-4, 140-150	600	804	1176	628	100
19X-5, 135-150	6490	7408	-	-	-

*Equivalent sample at Site 1040 corrected for compaction

$^{\zeta}$ % barite present at Site 1039 dissolved assuming all of the bulk sediment Ba lost across the trench from Site 1039 to Site 1040 is due to barite dissolution.
Note a dash indicates not determined

Table 3.5 Excess Ba at Site 1039/1253

Core, section, interval (cm)	Depth (mbsf)	Ba (ppm)	Al* (ppm)	Ba_{excess} (ppm)	Ba_{barite}** (ppm)
170-1039B-					
1H-1, 145-150	1.5	400	174900	0	0
2H-5, 140-150	9.5	1786	174900	474	196
4H-5, 140-150	28.5	1598	169000	331	-
5H-4, 140-150	36.5	1834	161800	621	520
6H-4, 140-150	45.9	1148	161800	0	-
8H-4, 140-150	65.0	1804	172300	512	600
11H-5, 140-150	95.0	1388	181500	27	-
14X-3, 135-150	117.5	2852	157000	1675	-
16X-3, 135-150	136.6	4512	178500	3173	-
17X-3, 135-150	146.2	3493	122900	2571	-
19X-5, 135-150	168.5	7408	76000	6838	6490
21X-5, 135-150	187.6	2091	85000	1491	-
23X-5,135-150	206.9	2394	80000	1794	-
25X-5, 135-150	226.1	2056	82500	1438	-
27X-4, 135-150	243.9	2067	82500	1448	-
29X-3, 135-150	261.8	1977	90000	1302	-
32X-2, 130-150	289.3	1962	81500	1362	-
34X-3, 130-150	309.9	1783	110000	958	-
37X-5, 130-150	341.7	2165	99400	1420	-
39X-5, 130-150	361.0	1285	87700	627	-
40X-6, 130-150	372.0	2216	87700	1559	-
170-1039C-					
5R-1, 0-6	401.5	1724	144900	637	-
7R-1, 85-100	421.7	2580	140000	1530	-

*Data from Kimura, Silver, Blum et al. (1997). If Al was not analyzed for a sample, the nearest value was used in the calculation. All of the nearest samples were within 5 m of the Ba sample. **Ba_{barite} from barite sequential extractions. A dash indicates not determined.

Table 3.6 Barite distillation and Ba sediment flux to the depths of magma generation

Site 1039/1253	Weighted Bulk Sediment Ba (ppm)	% Ba Lost by Barite Dissolution	Sediment Ba Flux (g yr^{-1} cm^{-1})
No barite distillation	2378	0	615
18% loss in all units	1950	18	504
Complete barite distillation*	929	60	240

*Computed from Ba_{excess} and measured Ba_{barite}. Estimate based on complete SO_4^{2-} reduction in the underthrust sediments arcward of the trench, and subsequent dissolution of barite in all three sedimentary units.

References

Bains, S., Norris, R.D., Corfield, R.M., and Faul, K.L., 2000. Termination of global warmth at the Palaeocene/Eocene boundary through productivity feedback. *Nature*, 407:171-174.

Bebout, G.E., Ryan, J.G., Leeman, W.P., Bebout, A.E., 1999. Fractionation of trace elements during subduction zone metamorphism: impact of convergent margin thermal evolution. *Earth Planet. Sci. Let.* 171: 63-81.

Bebout, G.E., 2007. Trace element and isotopic fluxes/subducted slab, *In:* Treatise on Geochemistry v. 3, Elsevier Ltd., pp. 1-50.

Bishop, J.K.B., 1988. The barite-opal-organic carbon association in oceanic particulate matter. *Nature* (*London, U. K.*), 332:341–343. doi:10.1038/332341a0

Bonn, W.J., Gingele, F.X., Brobe, H., Mackensen, A., and Futterer, D., 1998. Palaeoproductivity at the Antarctic continental margin: opal and barium records for the last 400 ka. *Palaeoclimatol. Palaeoecol*., 139:195-211.

Brumsack, H.-J., and Gieskes, J.M., 1983. Interstitial water trace-metal chemistry of laminated sediments from the Gulf of California, Mexico. *Mar. Chem.,* 14:89–106. doi:10.1016/0304-4203(83)90072-5

Carr, M.J., Feigenson, M.D., and Bennett, E.A., 1990. Incompatible element and isotopic evidence for tectonic control of source mixing and melt extraction along the Central American arc. *Contrib. Mineral. Petrol.,* 105:369–380.

Chan, L.-H., and Kastner, M., 2000. Lithium isotopic compositions of pore fluids and sediments in the Costa Rica subduction zone: implications for fluid processes and sediment contribution to the arc volcanoes. *Earth Planet. Sci. Lett.,* 183:275–290. doi:10.1016/S0012-821X(00)00275-2

Condie, K.C., 1993. Chemical composition and evolution of the upper continental crust: contrasting results from surface samples and shales. *Chem. Geol.,* 104:1–370. doi:10.1016/0009-2541(93)90140-E

Dehairs, F., Chesselet, R., and Jedwab, J., 1980. Discrete suspended particles of barite and the barium cycle in the open ocean. *Earth Planet. Sci. Lett.,* 49:528–550.
Dickens, G.R., 2001. Sulfate profiles and barium fronts in sediment on the Blake Ridge: present and past methane fluxes through a large gas hydrate reservoir.

Geochim. Cosmochim. Acta, 65:529–543. doi:10.1016/S0016-7037(00)00556-1

Domanik, K.J., Holloway, J.R., 1996. The stability and composition of phengitic muscovite and associated phases from 5.5 to 11 GPa: implications for deeply subducted sediments. *Geochim et Cosmochim. Acta* 60:4133-4150.

Dymond, J., Suess, E., and Lyle, M., 1992. Barium in deep-sea sediment: a geochemical proxy for paleoproductivity. *Paleoceanography,* 7:163–181. Dymond, J., and Collier, R., 1996. Particulate barium fluxes and their relationships to biological productivity. *Deep Sea Res. Part II,* 43:1283–1308. doi:10.1016/0967-0645(96)00011-2

Eagle, M., Paytan, A., Arrigo, K.R., van Dijken, G., and Murray, R.W., 2003. A comparison between excess barium and barite as indicators of carbon export. *Paleoceanography,* 18(1). doi:10.1029/2002PA000793

Elliott, T., Plank, T., Zindler, A., White, W., and Bourdon, B., 1997. Element transport from subducted slab to volcanic front at the Mariana arc, *J. Geophys. Res.*, 102:14991–15019. doi:10.1029/97JB00788

Fu, B., Aharon, P., Byerly, G.R., and Roberts, H.H., 1994. Barite chimneys on the Gulf of Mexico slope: initial report on their petrography and geochemistry. *Geo-Mar. Lett.*, 14:81–87. doi:10.1007/BF01203718

Ganeshram, R., Francois, R., Commeau, J., and Brown-Leger, S., 2003. An experimental investigation of barite formation in seawater. *Geochim. Cosmochim. Acta,* 67:2599–2605. doi:10.1016/S0016-7037(03)00164-9

Gonneea, M.E., Paytan, A., 2006. Phase associations of barium in marine sediments. *Mar. Chem.* 100: 124-135.

Greinert, J., Bollwerk, S.M., Derkachev, A., Bohrmann, G., and Suess, E., 2002. Massive barite deposits and carbonate mineralization in the Derugin Basin, Sea of Okhostsk: precipitation processes at cold seep sites. *Earth Planet. Sci. Lett.*, 203:165–180. doi:10.1016/S0012-821X(02)00830-0

Hensen, C., Wallman, K., Schmidt, M., Ranero, C.R., and Suess, E., 2004. Fluid expulsion related to mud extrusion off Costa Rica—a window to the subducting slab. *Geology,* 32(3):201–204. doi:10.1130/G20119.1

Hutnak, M., Fisher, A.T., Stein, C.A., Harris, R., Wand, K., Silver, E., Spinelli, G., Pfender, M., Villinger, H., MacKnight, R., Costa Pisani, P., DeShon, H., Diamente, C., 2007. The thermal state of 18-24 Ma upper lithosphere subducting below the Nicoya Peninsula, northern Costa Rica margin. *In* Interplate Subduction Zone Seismogenesis, T. Dixon and C. Moore (Eds.), Columbia

University Press, New York, 86-122.

Kastner, M., Morris, J., Chan, L.H., Saether, O., Luckge, A., 2000. Three distinct fluid systems at the Costa Rica subduction zone: chemistry, hydrology, and fluxes. *Goldschmidt 2000 J. Conf. Abstr.* 5, 572.

Kimura, G., Silver, E.A., Blum, P., et al., 1997. *Proc. ODP, Init. Repts.*, 170: College Station, TX (Ocean Drilling Program). [HTML]

Kopf, A., Dehyle, A., 2002. Back to the roots: boron geochemistry of mud volcanoes and its implications for mobilization depth and global B cycling. *Chem. Geol.* 192: 195-210.

Leeman, W.P., Carr, M.J., and Morris, J.D., 1994. Boron geochemistry of the Central American volcanic arc: constraints on the genesis of subduction-related magmas. *Geochim. Cosmochim. Acta*, 58:149–168. doi:10.1016/0016-7037(94)90453-7

Lonsdale, P., 1979. A deep hydrothermal site on a strike-slip fault. *Nature (London, U.K.)*, 281:531–535. doi:10.1038/281531a0

McManus, J., Berelson, W.M., Klinkhammer, G.P., Johnson, K.S., Coale, K.H., Anderson, R.F., Kumar, N., Burdige, D.J., Hammond, D.E., Brumsack, H.-J., McCorkle, D.C., and Rushdi, A., 1998. Geochemistry of barium in marine sediments: implications for its use as a paleoproxy. *Geochim. Cosmochim. Acta*, 62:3453–3473. doi:10.1016/S0016-7037(98)00248-8

Monnin, C., 1999. A thermodynamic model for the solubility of barite and celestite in electrolytic solutions and seawater to 200 ^{o}C and to 1 kbar. *Chem. Geol.* 153: 187-209.

Moran, A.E., Sisson, V.B., Leeman, W.P., 1992. Boron depletion during progressive metamorphism: implications for subduction processes. *Earth Planet. Sci. Let.* 111: 331-349.

Morris, J.D., 1991. Applications of cosmogenic 10Be to problems in the earth sciences. *Ann. Rev. Earth Planet Sci. Lett.*, 19:313–350.

Morris, J.D., Leeman, W.P., and Tera, F., 1990. The subducted component in island arc lavas: constraints from Be isotopes and B-Be systematics. *Nature* (*London, U. K.*), 344:31–36.

Morris, J.D., Valentine, R., and Harrison, T., 2002. 10Be imaging of sediment accretion, subduction along the northeast Japan and Costa Rica convergent margins. *Geology*, 30:59–62. doi:10.1130/0091-

7613(2002)030<0059:BIOSAA>2.0.CO;2

Morris, J.D., and Ryan, J.G., 2003. Subduction zone processes and implications for changing composition of the upper and lower mantle. *In* Treatise on Geochemistry v. 2, Elsevier Ltd., pp. 451-470.

Morris, J.D., Villinger, H.W., Klaus, A., et al., 2003. *Proc. ODP, Init. Repts.,* 205 [CDROM]. Available from: Ocean Drilling Program, Texas A&M University, College Station TX 77845-9547, USA. [HTML]

Naehr, T.H., Stakes, D.S., and Moore, W.S., 2000. Mass wasting, ephemeral fluid flow, and barite deposition on the California continental margin. *Geology,* 28(4):315–318. doi:10.1130/0091-7613(2000)028<0315:MWEFFA>2.3.CO;2

Ono, S., 1998. Stability limits of hydrous minerals in sediment and mid-ocean ridge basalt compositions: implications for water transport in subduction zones. *J. Geophys. Res.* 103: 18253-18267.

Patino, L.C., Carr, M.J., and Feigenson, M.D., 2000. Local and regional variations in Central American arc lavas controlled by variations in subducted sediment input. *Contrib. Mineral. Petrol.,* 138:265–283. doi:10.1007/s004100050562

Paytan, A., 1996. Marine barite, a recorder of oceanic chemistry, productivity, and circulation [Ph.D. thesis]. Scripps Inst. Oceanogr., Univ. Calif. San Diego.

Paytan, A., Kastner, M., and Chavez, F., 1996. Glacial to interglacial fluctuations in productivity in the equatorial Pacific as indicated by marine barite. *Science,* 274:1355-1357. doi:10.1126/science.274.5291.1355

Plank, T., and Langmuir, C.H., 1993. Tracing trace elements from sediment input to volcanic output at subduction zones. *Nature* (*London, U. K.*), 362:739–743. doi:10.1038/362739a0

Plank, T., and Langmuir, C.H., 1998. The chemical composition of subducting sediment and its consequences for the crust and mantle. *Chem. Geol.,* 145:325–394. doi:10.1016/S0009-2541(97)00150-2

Rushdi, A.I., McManus, J., Collier, R.W., 2000. Marine barite and celestite saturation in seawater. *Mar. Chem.* 69: 19-31.

Saffer, D.M., and Screaton, E.J., 2003. Fluid flow at the toe of convergent margins: interpretation of sharp pore-water geochemical gradients. *Earth Planet. Sci. Lett.,* 213:261–270. doi:10.1016/S0012-821X(03)00343-1

Saffer, D.M., Silver, E.A., Fisher, A.T., Tobin, H., and Moran, K., 2000. Inferred pore

pressures at the Costa Rica subduction zone: implications for dewatering processes. *Earth Planet. Sci. Lett.,* 177:193–207. doi:10.1016/S0012-821X(00)00048-0

Silver, E., Kastner, M., Fisher, A., Morris, J., McIntosh, K., and Saffer, D., 2000. Fluid flow paths in the Middle America Trench and Costa Rica margin. *Geology,* 28(8):679–682.

Taylor, S.R., and McLennan, S.M., 1985. *The Continental Crust: Its Composition and Evolution:* Oxford (Blackwell Scientific).

Tera, F., Brown, L., Morris, J., Sacks, I.S., Klein, J., and Middleton, R., 1986. Sediment incorporation in island-arc magmas: inferences from 10Be. *Geochim. Cosmochim. Acta,* 50:535–550. doi:10.1016/0016-7037(86)90103-1

Torres, M.E., Bohrmann, G., Dube, T.E., and Poole, F.G., 2003. Formation of modern and Paleozoic stratiform barite at cold methane seeps on continental margins. *Geology,* 31(10):897–900. doi:10.1130/G19652.1

Torres, M.E., Bohrmann, G., and Suess, E., 1996a. Authigenic barites and fluxes of barium associated with fluid seeps in the Peru subduction zones. *Earth Planet. Sci. Lett.,* 144:469-481.

Torres, M.E., Brumsack, H.-J., Bohrmann, G., and Emeis, K.C., 1996b. Barite fronts in continental margin sediments: a new look at barium remobilization in the zone of sulfate reduction and formation of heavy barites in diagenetic fronts. *Chem. Geol.,* 127:125–139. doi:10.1016/0009-2541(95)00090-9

Torres, M.E., McManus, J., and Huh, C.-A., 2002. Fluid seepage along the San Clemente fault scarp: basin-wide impact on barium cycling. *Earth Planet. Sci. Lett.,* 203:181–194. doi:10.1016/S0012-821X(02)00800-2

You, C.-F., Morris, J.D., Gieskes, J.M., Rosenbauer, R., Zheng, S.H., Xu, X., Ku, T.L., Bischoff, J.L., 1994. Mobilization of beryllium in the sedimentary column at convergent margins. *Geochim et Cosmochim. Acta* 58: 4887-4897.

You, C.-F., Castillo, P., Gieskes, J.M., Chan, L., Spivack, A.J., 1996. Trace element behavior in hydrothermal experiments: implications for fluid processes at shallow depths in subduction zones. *Earth Planet. Sci. Let.* 140: 41-52.

Zack, T., Rivers, T., Foley, S.F., 2001. Cs-Rb-Ba systematics in phengite and amphibole: an assessment of fluid mobility at 2.0 GPa in eclogites from Trescolmen, Central Alps. *Contrib. Mineral. Petrol.* 140: 651-669.

Chapter 4

Dynamic Fluid Flow and Chemical Fluxes Associated with a Seafloor Gas Hydrate Deposit on the Northern Gulf of Mexico Slope

4.1 Abstract

Gas hydrates outcrop on the seafloor at the Bush Hill hydrocarbon seep site in the northern Gulf of Mexico. Four newly designed fluid flux meters/chemical samplers, called the MOSQUITO, were deployed for 430 days at Bush Hill to determine how dynamic subsurface fluid flow influences gas hydrate stability and to quantify the associated methane fluxes into the ocean. Three of the flux meters were deployed adjacent to an outcropping gas hydrate mound, while the fourth monitored background conditions. The flux meter measurements reveal that the subsurface hydrology in the vicinity of the mound is complex and variable with frequent changes from downward to upward flow ranging from -161 to 273 cm/yr, and with temporal variations in the horizontal component of flow. The continuous record of fluid chemistry indicates that gas hydrate actively formed in the sediments. We propose that long periods of downward flow of seawater adjacent to gas vents (up to 4 months) are driven by local sub-pressure resulting from gas ebullition through faults and fractures due to overpressure at depth. High frequency variations in flow rates (days to weeks) are likely due to temporal changes in sediment permeability and the 3-D fluid flow field as a result of active gas hydrate and authigenic carbonate precipitation. Gas hydrate formation occurred as a result of long-term emanation of CH_4 at focused gas vents followed by a more diffuse intergranular methane flux. The estimated CH_4 flux to the water column from focused gas vents across the Bush Hill seep is ~$5 \cdot 10^6$ mol/yr. This significant flux suggests that Bush Hill and similar hydrocarbon seeps in the northwestern Gulf of Mexico may be important natural sources of methane to the ocean and atmosphere.

4.2 Introduction

Marine gas hydrates are ice-like minerals in which hydrocarbon and non-hydrocarbon gases occupy cages within a framework structure of water molecules. Gas hydrate stability is exponentially dependent on temperature and linearly dependent on pressure (Sloan, 1998), and also depends on the composition of the gas and the pore fluid chemistry (Handa, 1990, Zatsepina and Buffet, 1998). The estimated total amount of methane carbon in marine gas hydrates ranges between ~ $5 \cdot 10^{17}$ and 10^{19}g (Kvenvolden, 1999; Milikov et al., 2003), and represents one of the largest reservoirs of methane on the planet. Recent interest in marine gas hydrates has resulted from the realization that they may play a role in submarine slope instability and global climate change (e.g. Brewer, 1999; Dickens et al., 1997, Dillon et al., 1998; Kennet et al., 2000; MacDonald, 1990). Most of the global marine gas hydrate reservoir is disseminated in sediments 100-300 meters below the seafloor at water depths >500 m (in polar regions >150 m), and is often detected by associated free gas that produces a bottom simulating reflector (BSR) (Shipley et al., 1979). At this depth, the gas hydrates are well insulated from most present day oceanic temperature and pressure changes.

The northern Gulf of Mexico (GOM) continental slope is characterized by a large belt (120,000 km^2 area) of seafloor extending from ~200 to 2,000 m water depth containing seafloor gas vents, oil seeps, gas hydrates, chemosynthetic biological communities, and subsurface oil and gas fields (Milikov and Sassen, 2003; Roberts and Aharon, 1994; Roberts and Carney, 1997; Sassen et al., 1994). Dynamic focused fluid flow along deformed salt bodies and faults (Roberts, 2001; Sassen et al., 2004) causes rapid expulsion of free hydrocarbon gas and provides conditions suitable for the

formation of massive gas hydrates close to or at the seafloor. Thus, the gas hydrates outcropping at the seafloor in the northern GOM provide an accessible and ideal location for monitoring, in situ, the dynamics of gas hydrate formation and dissociation with direct implications for the seafloor biochemical environment, ocean chemistry, and possibly the atmosphere.

Bush Hill (BH; lease block Green Canyon 185) in the northern GOM ($27^{o}47.5'$N and $91^{o}30.5'$W) is a fault-related seep at ~ 540 m water depth (Figure 4.1) at the top of a ~500 m wide, ~40 m tall topographic high (MacDonald et al., 2003). The BH site contains a persistent 2-3 m wide and ~ 0.65 m high gas hydrate mound. Several gas vents are situated within and adjacent to the hydrate mound that continuously emit methane and other hydrocarbons to the water column (MacDonald et al., 2002). The BH vent site receives hydrocarbon gas and oils from a fault that is antithetic to growth faults that trap the Jolliet Field oil and gas reservoirs in nearby lease block GC 184 (Cook and D'Onfro, 1991; Roberts et al., 1992). The methane in the gas hydrates outcropping at the seafloor is predominantly thermogenic in origin, and the gas hydrates are mainly structure-II type (Brooks et al., 1984; Sassen et al., 1999).

Seafloor photographic observations indicate that the morphology of the gas hydrate mound can alter significantly from year to year, and spontaneous gas expulsion episodes at vents around the mound were recorded when bottom water temperatures exceeded 8 ^{o}C. (MacDonald et al., 1994). Despite the short-term variations in the gas flux in response to small temperature fluctuations, the gas hydrate mound at BH has persisted at the same location for at least 12 years (MacDonald et al., 1994; 2005). In order to constrain the subsurface hydrogeochemistry at the BH gas hydrate mound, four

newly designed long-term, continuous fluid flow meter/chemical samplers called the MOSQUITO (Multiple Orifice Sampler and Quantitative Injection Tracer Observer) were deployed between June 2002 and August 2003. In this contribution we present the results of the continuous measurements of fluid chemistry, fluid flux, and temperature over the 15-month deployment period, and their time dependent variations and impact on gas hydrate stability and methane fluxes to the overlying water column.

4.3 Methods

4.3.1 *The MOSQUITO, a new seafloor fluid flow meter/chemical sampler*

The MOSQUITO uses osmotic pumps and a tracer injection device to continuously measure fluid flow rates and solute fluxes at multiple depths below the seafloor. The OsmoSampler (OS) is the heart of the MOSQUITO and consists of two chambers, one filled with distilled water and the other with saturated saline solution as described in Jannasch et al. (2004). A contiguous small bore Teflon coil, filled with de-gassed distilled water, is connected to the distilled water chamber (Figure 4.2). The osmotic pressure drives a net flow of distilled water across the membranes to the saturated saline chamber, and continuously pulls distilled water through the Teflon tubing and samples in situ pore fluids at the other end. After recovery, the Teflon tubing is divided into sections of appropriate length for chemical analyses and desired temporal resolution.

The MOSQUITO typically includes multiple OSs with the end of their Teflon coils connected to Ti capillary needles (Figure 4.3a,b). Another Ti needle is connected to a central tracer injection device (Kastner et al., 2000). It is deployed either via

manned submersible or with an ROV. On the seafloor, the Ti needles are inserted to pre-determined depths within the sediment. The tracer (fluorescein in this study) is injected as a point source, and fluid chemistry and tracer concentrations are continuously sampled simultaneously at multiple depths and lateral distances below the seafloor. The time-series tracer concentrations at each sampling depth are modeled using Fick's Second Law:

$$\partial C/\partial t = D_s \partial^2 C/\partial x^2 - v\partial C/\partial x \qquad (4.1)$$

where D_s is the sedimentary diffusion coefficient and v is the fluid velocity. The solution to the solute transport equation for the initial and boundary conditions present in this study is one where a point source mass M is injected into an infinite porous media at initial time zero in a velocity field. The mass is simultaneously advected by the velocity field and dispersed through the porous medium. Assuming these conditions and fluorescein adsorption is negligible (e.g. Sabatini and Austin, 1991; Sabatini, 2000), the point source solution of Baetsle (1969) is used:

$$C(x,y,z) = \frac{\mathbf{M}}{8(\pi t)^{3/2}\sqrt{D_{xx}D_{yy}D_{zz}}} \times \exp\left(-\frac{X^2}{4D_{xx}t} - \frac{Y^2}{4D_{yy}t} - \frac{Z^2}{4D_{zz}t}\right) \qquad (4.2)$$

where X, Y, and Z are the moving coordinates following the center of mass of solute and are defined as $X = x-v_xt$, $Y = y-v_yt$, and $Z = z-v_zt$. Fluid flow rates as low as 0.5 cm/yr are determined by comparing the tracer time series to forward model simulations, and the flow rates coupled with the contemporary chemical data yield the fluxes of chemical components across the sediment-ocean interface.

The molecular diffusion coefficient (D_m) of fluorescein was estimated from the empirical equations of Wilke and Chang (1955). The sedimentary diffusion coefficient

(D_s) was estimated from D_m corrected for temperature, salinity, and porosity effects (Iverson and Jörgensen, 1993; Boudreau, 1996). The porosity was measured from push cores collected adjacent to the MOSQUITOs and ranges from ~0.85 at 3 cmbsf to ~0.69 at 20 cmbsf. Using the average porosity below 12 cmbsf at the study area, D_s was estimated to be ~$9.0 \cdot 10^{-7}$ cm^2/s. An increase in temperature of 2^oC would only increase D_s by ~0.7%. The flow rates are sensitive to the sedimentary diffusion coefficient, however, with a 10%, 33%, and 100% increase in D_s producing a 23%, 45%, and 81% increase in the calculated flow rates, respectively.

Prior to the deployment at BH, the MOSQUITO was tested in the laboratory, Monterey Bay, and on the eastern flank of the Juan de Fuca Ridge. Four MOSQUITOS were deployed for ~430 days from June 2002 to August 2003 with Harbor Branch's Johnson Sea-Link research submersible. Three MOSQUITOs were deployed within 3 meters of the gas hydrate mound and ~5 m apart, adjacent to transient CH_4 vents, in a mussel field, a tubeworm field, and in bacterial mats. The fourth was deployed at a background site ~50 m away from the gas hydrate mound (Figure 4.4). Each of the MOSQUITOs carried four to five OSs, and the Ti sampling needles were inserted to depths ranging between 12 and 26 cm below seafloor (cmbsf), mostly below the depth of bioturbation. The tracer was injected as a point source at depths varying from 20 to 26 cmbsf. The OSs pumped/sampled fluid at a rate of ~1 ml/week, and each of the coils was sub-sampled at approximately weekly resolution. The data points were time-stamped at the midpoint of the weekly sample, and represent an integration of 7 days of continuous fluid sampling. Due to technical problems, mainly the bending of some of the Ti needles on subsurface carbonate pavements during deployment, our dataset

includes just one to four time series per MOSQUITO. The mussel field and background site MOSQUITOs carried TidBit temperature loggers (manufactured by Onset) and recorded seafloor temperature every 40 minutes with an accuracy of 0.2 ^{o}C.

4.3.2 *Peepers and Push Cores*

Peepers rely on diffusive exchange of solutes across a dialysis membrane between fluid-filled cells and the surrounding sediment to sample the pore fluid chemistry at various depths (Hesslein, 1976; Fig. 4.5). The peepers were inserted into the sediment with the Johnson Sea-Link submersible, sampled pore water every 2 cm to a depth of 24 cmbsf, and equilibrated with the surrounding pore fluid over 2-4 weeks. Three peepers were deployed next to the MOSQUITOs; in the mussel field, tubeworm field, and bacterial mats, and two in transient bubble plumes adjacent to the gas hydrate mound (Figure 4.4). Pore fluid was also extracted shipboard from push cores by sectioning and centrifuging sediment slices at *in situ* temperature (8 ^{o}C), under a nitrogen atmosphere.

4.3.3 *Analytical Methods*

Pore fluid samples collected by the MOSQUITOs, peepers, and push cores were filtered through disposable 0.45 μm Gelman polysulfone filters. Dissolved inorganic carbon (DIC) samples were poisoned with a saturated $HgCl_2$ solution and stored in vacutainers. Aliquots for sulfate analyses were added to centrifuge tubes containing a 50% $CdNO_3$ solution to precipitate the sulfide. Chloride concentrations were determined by titration with $AgNO_3$. Ca^{2+}, Mg^{2+}, K^{+}, Na^{+}, and SO_4^{2-} concentrations

were determined via inductively coupled plasma-optical emission spectrometry (ICP-OES), and δ^{13}C-DIC on a ThermoFinnigan Delta XP Plus stable isotope ratio mass spectrometer. The tracer (fluorescein) concentrations were determined on a Perkin Elmer LS50B scanning fluorimeter.

All samples, standards, and blanks were prepared in a clean laboratory, and all dilutions were made with Milli-Q water. The reproducibility of the analyses expressed as percent precision from multiple determinations of IAPSO standard seawater are: Ca^{2+} = 0.63%, Mg^{2+} = 0.55%, K^{+} = 0.9%, Na^{+} = 1.2%, SO_4^{2-} = 0.7%, and Cl^{-} = 0.2%. The average percent precision of the δ^{13}C-DIC and fluorescein analyses, determined from multiple determinations of NBS and in-house standards are 1.8% and 0.6%, respectively. All of the analytes measured, except fluorescein, were well above detection limits. The detection limit of the fluorescein analyses was 10^{-8} g/L.

4.4 Results

4.4.1 *Subsurface Hydrology*

The tracer concentration time series collected by the four MOSQUITOs exhibit sharp peaks and troughs, indicating the subsurface hydrology of the gas hydrate mound is dynamic and variable (Fig. 4.6a,b,e,f). For comparison, we present model simulations for steady-state diffusion only (no advection) for one sampling depth in each sub-environment (solid colored curves; Fig. 4.6a,b,e,f). These show that tracer concentrations rise sharply to a maximum then decline slowly when fluid flow rate is constant. The tracer arrival time and peak concentration depend on the fluid flow rate, input mass of tracer, distance from the point-source injection, and the sediment

diffusion coefficient of the tracer (Eq. 4.2). All of the steady-state simulations with no fluid advection show earlier tracer arrival times and a higher concentration maximum than those recorded by the MOSQUITOs (Fig. 4.6a,b,e,f). The lag in tracer arrival time behind what would be expected if there were no advection indicates either intense downward or lateral fluid flow at the beginning of the deployment period.

A major advantage of the MOSQUITO over traditional seafloor flow meters (e.g. benthic chambers) is that it can monitor fluid flow both vertically and horizontally. In addition to the vertical Ti sampling capillaries, the mussel field and bacterial mats MOSQUITOs contained sample intakes at a 7 cm horizontal distance from the point-source injection (Fig. 4.6a,b). The absence of tracer in both the vertical and horizontal sample intakes at the beginning of the deployment period confirms the net flow was downward. After the first 110 to ~145 days of deployment, however, there is evidence for a lateral component of fluid flow. In the bacterial mats, the two 7 cm lateral intakes were positioned on opposing sides of the tracer injection. In one of these sample intakes, the tracer arrives earlier and with a higher concentration than the opposing lateral intake, clearly indicating a horizontal component of flow (Fig. 4.6b). This is also manifested in the mussel field by the later tracer arrival at the horizontal intake in comparison to the vertical sample depths (green curve, Fig. 4.6a). However, the arrival time is generally earlier and the concentration maxima are higher in the vertical intakes, suggesting flow is predominantly vertical in the mussel field and bacterial mats.

The multi-peaked nature of the MOSQUITO time series reflects a dynamic hydrological system exhibiting upward (positive), downward (negative), and lateral flow in each of the sub-environments monitored. Variable flow rate forward simulations

that best fit the vertical tracer time-series are presented in Figure 4.6a,b,e,f (solid black curves). As noted above, the late arrival and low tracer concentrations at the mound sites is due to negative fluid flow during the beginning of the deployment period. In the mussel field, the simulated change from negative to positive flow occurred at ~110 days (Fig. 4.6a). In the bacterial mats, the tracer arrival occurred much later (>300 days) with the peak at ~400 days (Fig 4.6b). In this case, the best-fit solution at both sampling depths includes an early change to positive flow at ~145 days, followed by an increase in the flow rate at the tracer arrival time. A one-step simulation would not produce the sharp peak observed. The negative flow rates at the mound sites during the first ~145 days are the minimum modeled rates required to maintain the tracer below the respective sampling depths. However, this does not preclude short-period flow excursions during this time interval, suggesting the calculated negative flow rates are net flow rates.

Modeled positive flow rates range from 0-273 cm/yr (0.01-7.5 mm/day) and negative flow rates ranged from 2 to 161 cm/yr (0.05-4.4 mm/day), with the highest positive and negative flow rates occurring in the tubeworm field (Fig. 4.6c,d,g,h). Flow rates are most variable in the mussel and tubeworm fields. In all of the mounds sites, the net fluid flow distance, integration of the fluid flow rate over the 430-day deployment period, is into the sediment column (-5.39 to -14.2 cm, Table 1), whereas at the background site it is out of the sediment column (15.1 cm). Thus, all of the MOSQUITOs measured relatively low net flow rates of less than 13 cm/yr over the deployment period.

The tracer concentration time series between sites share some similarities, and are split into two periods. (1) The first 110 to ~145 days: all three mound MOSQUITOs measured net negative flow (-21 to -100 cm/yr). During this period, the fluid flow field at the background site was positive with a net flow rate of 70 cm/yr. (2) After ~145 days, net flow switched from negative to positive at the mound sites, and from positive to negative at the background site (Table 4.1). The change in polarity of net flow at the mound sites and background site at ~145 days, suggests there may be hydrologic coupling between the two areas. After ~200 days, flow rates in the mussel and tubeworm fields are extremely variable.

4.4.2 *Pore Fluid Geochemistry*

The pore fluid chemistry at BH varies significantly over short distances, which is manifested at the seafloor by sharp interfaces between benthic biological communities. Not surprisingly, pore fluids sampled by the mussel field MOSQUITO, deployed 1.0 m from the most active bubble plume, show the most modified chemistry (Figure 4.7). The mussel field MOSQUITO sampled Ca^{2+} and SO_4^{2-} concentrations that are depleted with respect to seawater values for the duration of the deployment period, indicating active SO_4^{2-} reduction producing DIC driving authigenic carbonate formation (Fig. 4.7). Pore fluid depth profiles of SO_4^{2-} from the peepers and push cores are presented in Figure 4.8 for comparison. The MOSQUITOs in the tubeworm field, bacterial mats, and background site sampled Ca^{2+} and SO_4^{2-} concentrations near seawater value for the duration of the deployment. However, in the tubeworm field both Ca^{2+} and SO_4^{2-} concentrations decreased after 275 days, with a strong minimum at

375 days (6.7 and 19.9 mM, respectively) and a small minimum at 415 days. These depletions are not due to gas hydrate dissociation, because Cl^- concentrations remain constant at these times (Fig. 4.7).

The $\delta^{13}C$-DIC in the push cores and peepers during the last two weeks of the MOSQUITO deployments varied between -5.2 and -23.9‰ in the mussel field, bacterial mats, and within a transient bubble plume (Fig. 4.8a), suggesting little to no SO_4^{2-} reduction by anaerobic oxidation of methane (AOM). The $\delta^{13}C$ of sediment organic matter in the northwestern GOM ranges from -20.9 to -21.7‰ (Goñi et al., 1998), while the $\delta^{13}C$ of CH_4 from BH vents ranges from -44.1 to -46.7‰ (Sassen et al., 1994), and the $\delta^{13}C$ of non-methane hydrocarbons advected from deep GOM reservoirs averages -27‰ (Kennicutt et al., 1988). Accordingly, the $\delta^{13}C$-DIC values in the push cores and peepers at BH indicate that the majority of electrons for sulfate reduction are supplied by the oxidation of terrestrial organic matter, seeping non-methane hydrocarbons, and/or oil, as also suggested by Joye et al. (2004) and Formolo et al. (2004). However, minor localized AOM cannot be excluded and may occur in some sub-environments at BH. The $\delta^{13}C$-DIC values may also be influenced by some mixing with seawater DIC (Fig. 4.8a). The two sharp minima in SO_4^{2-} and Ca^{2+} in the tubeworm field after day 275 are likely the result of pulses of CH_4 and subsequent sulfate reduction by AOM.

When gas hydrate forms, water molecules are removed from the surrounding pore fluid excluding dissolved ions, thus increasing the pore water salinity. Gas hydrate dissociation causes freshening of the in situ pore fluid. The mussel field MOSQUITO sampled Cl^- concentrations ~2% greater than bottom water value (559 mM) for the duration of the deployment period (Figure 4.7), indicating steady-state precipitation of

gas hydrate below the mussel field adjacent to the main gas vent at BH. The background site MOSQUITO also sampled elevated Cl^- concentrations during the first 350 days, indicating steady-state precipitation of gas hydrate during a period of sustained upward fluid advection (Fig. 4.6f). Both the bacterial mats and tubeworm field MOSQUITOS sampled Cl^- concentrations near seawater value during the 430-day deployment period. However, two abrupt Cl^- maxima were observed in the tubeworm field. The first (590 mM; ~6% greater than seawater value) occurred at 108 days (Fig. 4.7). The second maximum (580 mM; ~4% greater than seawater value) occurred at 234 days, and is coincident with very high positive flow rates (273 cm/yr; Fig. 4.6g). These two Cl^- maxima likely reflect periods of rapid gas hydrate formation.

The Ca^{2+} and SO_4^{2-} concentration time series are decoupled from the Cl^- time series as a result of biogeochemical reactions in the sediment column such as organic matter oxidation and authigenic carbonate precipitation. The Mg^{2+}, Na^+, K^+ concentration time series remain fairly constant, near bottom water values, over the 430-day period, with two short-lived variations (~2 weeks) likely controlled by gas hydrate formation, authigenic carbonate precipitation, and zeolite formation (see Supplementary Information in the appendix).

4.4.3 *Bottom Water Temperature*

Bottom water temperature varied between 6.9 ^oC and 9.6 ^oC over the 15-month deployment with a mean of 7.9 ^oC (Figure 6h). The temperature time-series exhibits asymmetric periodicity characterized by a relatively rapid rise in temperature followed by a gradual cooling occurring over periods averaging 9 weeks. These low frequency

temperature variations may be due to periodic invasions of warm loop current water on the northern Gulf of Mexico slope (MacDonald et al., 1994, 2005). Overprinted on these longer period temperature changes are higher frequency temperature oscillations of ~0.4 ^{o}C occurring over 24 hours corresponding to the K1 tidal frequency (23.9 hr). The gas hydrate outcropping at the seafloor at BH is predominantly Structure II (Brooks et al., 1984; Sassen et al., 1999), and is stable over this variable and dynamic thermal regime. The stability temperature for Structure II gas hydrate at the in situ pressure and salinity is ~16.5 ^{o}C, computed using the CSMHYD program of Sloan (1998) with a mean Jolliet Field feed gas composition (Sassen et al., 2001). Structure I gas hydrate, which is only stable to a temperature of 8.2 ^{o}C at the in situ pressure (feed gas = 99% C_1 and 1% C_2), however, was out of the methane hydrate stability field for a considerable portion of the deployment period.

The observed fluctuations in Cl^- concentrations and the variations in the subsurface hydrology at the gas hydrate mound do not appear to correlate with fluctuations in the temperature record. Thus, during this deployment period, bottom water temperature likely did not affect gas hydrate stability or the subsurface hydrology at BH. It should be noted, however, that the tracer and geochemical time series sample resolution is too low (~1 week) to sufficiently resolve a relationship with tidal variations in bottom water temperature.

4.5 Discussion

The results of the long-term continuous monitoring of fluid chemistry and flow rates indicate that the Bush Hill hydrogeochemical system is highly dynamic. In the

following sections the impact of the dynamic subsurface hydrogeochemistry on gas hydrate stability and methane fluxes to the overlying water column are discussed.

4.5.1 *Bush Hill Hydrogeochemistry and Gas Hydrate Stability*

The 430-day fluid flow rate time-series is comprised of two periods: (1) during the first 110-145 days, the net flow was negative at the three mound sites and positive at the background site; (2) from ~145 days to the end of deployment, the net flow was positive at the mound sites, and the mussel and tubeworm fields experience high frequency flow variability during most of this time. Fluid flow oscillated on long time scales (4 to 9 months) in the bacterial mats and background site, and varied over short time scales (days to weeks) in the mussel and tubeworm fields (Fig. 4.6). These short period oscillations most likely do not result from tidal fluctuations, because they were not observed at all sites. The days to weeks variations in flow rates are similar to those observed at Hydrate Ridge (Tryon et al., 1999; 2002), however, the longer period flow fluctuations have not been sampled to date.

We hypothesize that the long period of downward flow (~4 months) at the mound sites is the result of focused ebullition of hydrocarbon gas through focused gas vents, and the high frequency flow variations in the mussel and tubeworm fields after ~200 days are due to temporal changes in sediment permeability and the 3-D fluid flow field. A generalized hydrogeochemical model is suggested for the high and low frequency variations and the decoupling between intergranular hydrology and gas hydrate formation. The hydrological element of the conceptual model is similar to models that have been proposed for short-term observations of episodic gas venting at

Hydrate Ridge (Tryon et al., 1999; 2002) and used to explain gas migration through the hydrate stability zone at Blake Ridge (Flemings et al., 2003).

The generalized model includes a period prior to deployment of the MOSQUITOs, during which fluids carrying gas and dissolved hydrocarbons migrated up-dip along dilated faults and fractures beneath Bush Hill. The base of the gas hydrate stability zone (BGHZ) is at ~600 mbsf at Bush Hill, however gas is efficiently transferred through the hydrate stability zone to the seafloor, and only ~9% of the vent gas is precipitated as gas hydrate in the subsurface (Chen and Cathles, 2003). The migrating gas and hydrocarbons were trapped beneath a low permeability confining layer, likely gas hydrate filling the faults and fractures either at the BGHZ or within the GHSZ. Over time, a sufficiently thick interconnected gas column formed and concentrated below the low permeability gas hydrate layer (or "plug", Fig.4. 9A). Before the MOSQUITO deployment, the gas column reached a critical pressure that exceeded the strength of the confining layer, driving fractures that vented the over-pressured gas (e.g. Flemings et al., 2003). This gas vented up-dip along the more permeable antithetic fault and associated fractures through the GHSZ to focused vent sites at the gas hydrate mound (Fig. 4.9A). The active gas venting decreased pore fluid pressures to below hydrostatic, which locally led to the downward intergranular flow of seawater causing density-driven convection and fluid entrainment within the gas vents, as observed during the first four months at the mound sites (Fig. 4.6). The antithetic fault and related fractures favor the transport of gas, due to their higher relative permeability to gas over liquid (Ingebritsen and Sanford, 1998; Sorey et al., 1980), whereas pore spaces are more conducive to fluid transport. Thus, fluid flow was

positive at the background site ~50 m from the focused gas vents. During this stage, gas hydrate actively formed in the mussel and tubeworm fields, manifested by elevated Cl^- concentrations. The depletion in SO_4^{2-} and increase in alkalinity drove authigenic carbonate formation consuming Ca^{2+} in the mussel field (Fig. 4.7), decreasing the permeability at this site.

After the 110-145 days of focused gas expulsion and active gas hydrate formation, the gas reservoir was essentially depleted and focused gas venting waned. There was no longer sub-pressure in the shallow sediments of the mound sites, and the fluid flow field returned to background conditions, with a moderate net positive flow of fluids (~1-30 cm; Table 4.1). This flow regime persisted until the end of the deployment period (Fig. 4.9B). During this time interval, Cl^- concentrations in the mussel field are elevated with respect to seawater, indicating local formation of gas hydrates. Ca^{2+} and SO_4^{2-} remained depleted within the mussel field and concentration minima occurred in the tubeworm field after ~280 days, suggesting active precipitation of authigenic carbonates (Fig. 4.7). The SO_4^{2-} minima in the tubeworm field are likely the result of anaerobic oxidation of CH_4 that was advected to the depths of the MOSQUITO sample intakes over periods shorter than the flow rate sample resolution. Thus, the methane pulses likely occurred over periods of hours to days, while the subsequent oxidation occurred over periods of weeks. The continuous precipitation of authigenic carbonate and gas hydrate in the mussel field and the intermittent authigenic carbonate precipitation in the tubeworm field must act to decrease the sediment permeability over time at these two sub-environments.

The high frequency flow variations observed in the mussel and tubeworm fields (Fig 4.6c,g) are most likely due to repeated decreases in sediment permeability caused by active gas hydrate and carbonate precipitation (Fig. 4.7), as well as the presence of free gas in the sediment pore space. Permeability is one of the dominant controls on the spatial and temporal distribution of fluid flow. The transient injection of gas and hydrate/carbonate precipitation will cause the migration of flow conduits over time as permeable pathways are blocked and flow is diverted into new pathways. Thus, temporal changes in the permeability structure can cause significant changes in the 3-D fluid flow field within each sub-environment. These high frequency variations in both vertical and lateral flow rates due to spatial and temporal changes in permeability in the mussel and tubeworm fields are overprinted on the general trend of subvertical flow observed in the bacterial mats after day 145 (Fig 4.6b,d). There was no observed gas hydrate or authigenic carbonate precipitation in the bacterial mats, which is likely the reason this site lacks the flow variability observed at the other two mound sites.

In summary, the model is comprised of two distinct flow regimes. One is a steady-focused ebullition of CH_4 and heavier hydrocarbons through faults and fractures to the seafloor from an overpressured gas reservoir at depth. The second is a low to moderate subvertical flow of fluid and gas that characterizes the typical background flow regime. During both flow periods, fluid flow is highly variable with upward, downward, and lateral flow occurring in each sub-environment due to temporal changes in sediment permeability. Because most of the gas hydrate at Bush Hill is Structure II, the P-T condition for gas hydrate dissociation (~16.5 ^{o}C) was never met, thus stability was primarily a function of hydrocarbon supply. The constant elevated Cl^-

concentration in the mussel field and the maxima observed in the tubeworm field (Fig. 4.7), indicate that the gas hydrate mound receives an ample supply of methane by the high-volume focused gas venting followed by a more diffuse intergranular flow to keep the gas hydrates within the stability field. A significant portion of the hydrocarbons, however, is not utilized for in situ gas hydrate formation and is effectively transferred to the water column, which is manifested at the seafloor by transient bubble plumes (Leifer and MacDonald, 2003). The effective transfer of gas to the water column is a result of the high hydrocarbon flux combined with oil coating the bubbles, which inhibits gas hydrate formation within the gas hydrate stability zone.

4.5.2 *Comparison of MOSQUITO Chemical Time-Series with Conventional Methods*

The continuous and simultaneous pore fluid chemical and flow rate records from the MOSQUITOs provide invaluable information on the transience of gas hydrate and gas-rich hydrogeochemical settings. Conventionally, pore water is sampled by push cores, gravity cores, piston cores, and peepers. Figures 4.8b and 4.8c present a comparison between the SO_4^{2-} concentration depth profiles from the push cores, peepers, and the time-series from the MOSQUITOs in the mussel and tubeworm fields, and the bacterial mats. The push cores and peepers were collected during the last 2 weeks of the MOSQUITO deployment. Average sulfate concentrations sampled by both methods agree very well. For example, an average SO_4^{2-} concentration of ~27.8 mM was obtained by the MOSQUITO in the bacterial mats at a depth of 20 cmbsf, and the SO_4^{2-} concentration sampled via push core near the same depth was ~27.2 mM. The SO_4^{2-} concentrations sampled by the tubeworm field MOSQUITO during the last two

weeks of deployment also agrees well with the peeper data at the equivalent depth. However, the strong depletion in SO_4^{2-} from 275 to 400 days would only have been observed in the peeper profile if it was collected during that same time period. This indicates that in dynamic environments like BH, traditional sampling methods only provide a relatively instantaneous pore fluid profile, thus they provide an incomplete picture of the transient processes occurring in the sediment column.

4.5.3 *Methane Fluxes at Bush Hill*

Hydrocarbon gases are actively and continuously venting at the BH gas hydrate mound at the present time (e.g. MacDonald et al., 1994; 2002). The hydrocarbon plume is visible throughout the water column on echo sounder records centered on BH (Roberts, 2001). This and similar hydrocarbon plumes form oil slicks at the sea surface, that are detected by satellite remote sensing (MacDonald et al., 2002). In addition to the focused hydrocarbon venting at BH, the methane flux out of the sediments may contribute a considerable amount of CH_4 to the overlying water column. The concentration of CH_4 in the sediment is difficult to constrain due to pressure and temperature changes that occur during core recovery. Assuming equilibrium with methane hydrate at the in situ conditions and using the Pitzer equations presented in Tischenko et al. (2005), we compute a minimum pore water CH_4 concentration of 81 mmol/L.

At the beginning of the deployment period, the three mound MOSQUITOs recorded downward fluid flow, and the background site MOSQUITO recorded upward fluid flow. After ~130 days (Figure 4.6), fluid flow adjacent to the gas hydrate mound

was positive. During this period, conditions were more typical of the BH environment where there is a net sub-vertical displacement of pore fluid and dissolved methane through the sediment column (Figure 4.9b). Net fluid flow distances during this period (Table 4.1) were converted to fluid flow rates (Table 4.2). From these average flow rates, methane fluxes across the seafloor were estimated in each of the sub-environments and range from 0.89 mol/m^2yr in the mussel field to 29 mol/m^2yr in the bacterial mats (Table 4.2). Based on the δ^{13}C-DIC profiles in the peepers and push cores, there is only minor AOM in the sediment column at Bush Hill, thus it is reasonable to assume that almost all of the methane not utilized during gas hydrate formation is advected into the water column.

During the first ~145 days of the deployment period, fluid flow was negative adjacent to the gas hydrate mound associated with focused bubble venting at discrete discharge sites. Therefore, the gas vents are the main pathways for CH_4-rich fluids to enter the overlying water column during these periods. To estimate the flux rate of bubbles into the water column from focused vent sites during the first 130 days, we assumed that the net downward flow at the mound sites is proportional to the net outward flow of bubbles at the steady vent site. The net downward fluid flow varied between mound sub-environments with the highest occurring in the bacterial mats (39.7 cm), and the lowest in the mussel field (Table 4.1). The net downflow at each of the mound MOSQUITOs was considered to be representative of the entire sub-environment. The estimated area occupied by the tubeworm field, mussel field, and bacterial mats are 38, 23 and 24 m^2, respectively (Fig. 4.4). The area estimates are based on seafloor observations and videos collected during the 2002 and 2003 Johnson

Sea-Link dive programs. The volumetric fluid flow rates in the tubeworm and mussel fields, and bacterial mats were 18, 4.8, and 24 m^3/yr. These values were used to compute the gross bubble flux rate at the main gas vent at Bush Hill during the first ~130 days of the deployment to provide a flow rate of 48 m^3/yr or 1.5 cm^3/s. This value is very similar to the steady plume flux of 3.55 cm^3/s estimated by video photography at the same vent by Leifer and MacDonald (2003). The similarity in the bubble flux estimated by the two methods indicates that density driven convection and fluid entrainment do occur during episodes of gas expulsion at Bush Hill, drawing a significant amount of seawater into the sediments adjacent to the hydrate mound.

Using the areas occupied by the chemosynthetic communities (i.e. tubeworms and mussels) at BH that were identified in laser line-scan mosaics and ground-truth observations (MacDonald et al., 2003), the total methane flux to the overlying water column at BH can be estimated. The line-scan survey data presented in MacDonald et al. (2003) covers an area of 27,650 m^2, representing more than 80% of the BH seep. The flux rates computed for each of the mound sub-environments and the focused gas vents above were extrapolated over the total area covered by the survey at BH (Table 4.3). It was also assumed that discrete focused methane vents occupy 1% of the gas hydrate outcrops identified in the laser line-scan mosaic, and that fluid flow rates measured in the mussel field, tubeworm field, and bacterial mats adjacent to the hydrate outcrop are representative of the fluxes in these types of environments across the whole mound. With these assumptions and the chemosynthetic community estimations of MacDonald et al. (2003), the total CH_4 flux across the seafloor at Bush Hill is calculated to be $5.2 \cdot 10^6$ mol/yr or $8.3 \cdot 10^4$ kg/yr from June 2002 to August 2003.

There is only minor aerobic oxidation of methane emitted from focused gas vents in the overlying water column at BH (Kastner et al., 2003; Solomon et al., 2006). Assuming 10% of the methane emitted to the water column from the focused gas vents is oxidized, which is consistent with water column $\delta^{13}C\text{-}CH_4$ depth profiles (Solomon et al., 2006), and 70% of the CH_4 is lost to the water column by bubble dissolution and physical mixing, the BH flux was extrapolated to the 690 km^2 area in the northern Gulf of Mexico occupied by perennial sea surface oil slicks (Mitchell et al., 2000). This extrapolation indicates that ~500 Gg CH_4/yr potentially enters the atmosphere from hydrocarbon seeps in the northern Gulf of Mexico alone. This estimated methane flux is ~5% of the estimated global oceanic CH_4 flux to the atmosphere (Denman et al., 2007) and is ~10% of the global flux of methane from mud volcanoes (Dimitrov, 2003; Kvenvolden and Rogers, 2005). These results indicate the BH seep together with other hydrocarbon seeps in the GOM may be significant natural sources of methane to the atmosphere.

4.6 Conclusions

This is the first long-term (>3 months) continuous record of fluid flow and chemistry in a gas hydrate setting, and represents a unique and comprehensive dataset. The results show that the subsurface hydrology in the vicinity of the gas hydrate mound is complex with frequent changes in both the vertical and lateral components of flow. The long periods of negative flow at the mound sites (up to four months) have not been sampled before. This significant downward flow, less than a meter from focused gas vents attests to the heterogeneous nature of fluid flow in gas-rich hydrological settings.

The long periods of downflow must have a profound impact on the local benthic biological communities. During these periods, the seep fauna are effectively "cut-off" from essential nutrients such as H_2S and CH_4.

Gas hydrate continuously formed during the 430-day deployment, suggesting the gas hydrate mound receives an ample supply of CH_4 by high-volume focused gas venting followed by a more diffuse intergranular flow to keep the hydrates within the stability field. The results indicate that the BH gas hydrate deposit is presently stable despite the variable bottom water temperature and hydrological regime, and suggests instability will only occur if temperatures increase above ~16.5 ^{o}C or subsurface gas venting ceases. We estimate a CH_4 flux through gas vents across the BH seep of ~$5 \bullet 10^6$ mol/yr and extrapolate this flux to the area covered by perennial hydrocarbon plumes offshore Louisiana to arrive at a northwestern GOM atmospheric CH_4 flux of ~500 Gg/yr. This significant estimated hydrocarbon plume flux warrants a more extensive measurement program of atmospheric CH_4 fluxes from deep-water submarine seeps in the GOM.

4.7 Acknowledgements

We thank the crewmembers and pilots of the R/V Seaward Johnson and the Johnson Sea-Link for their support in meeting the objectives of the 2002 and 2003 dive programs. We greatly appreciate the shipboard and shore-based help of Ian MacDonald and Andrew Aubrey. We also thank Wei Wei, Liz Tirpak, and the numerous UCSD students for their shipboard help during the 2002 and 2003 research expeditions.

4.8 Chapter Acknowledgement

Chapter 4, in full, is the material as submitted to *Earth and Planetary Science Letters*: Solomon, E.A., Kastner, M., Jannasch, H., Robertson, G., and Weinstein, Y., 2007. Dynamic fluid flow and chemical fluxes associated with a seafloor gas hydrate deposit on the northern Gulf of Mexico slope. *Earth Planet. Sci. Let.*, in revision.

4.9 Appendix – Mg^{2+}, K^{+}, and Na^{+} Concentration Time Series

Magnesium, Na^{+}, and K^{+} concentrations remain fairly constant over the 430-day deployment period and are near seawater value at each of the deployment sites (Figure 4.10). The Na^{+} and K^{+} time series are decoupled from the Ca^{2+} and SO_4^{2-} time series because they are not involved in organic matter diagenesis and do not co-precipitate with authigenic carbonate. Superimposed on the steady-state Mg^{2+}-Na^{+}-K^{+} records are an abrupt increase in cation concentrations in the tubeworm field on day 108 and a depletion in Mg^{2+}, Na^{+}, and K^{+} on day 130 in the mussel field (Figure 4.10).

The increase in Mg^{2+}-Na^{+}-K^{+} concentrations in the tubeworm field on day 108 correlates with a 6% increase in Cl^{-} concentrations and reflects a period of rapid gas hydrate formation. The depletion in Mg^{2+}-K^{+}-Na^{+} in the mussel field on day 130 is enigmatic because there is no change in the Cl^{-} concentrations and only a slight decrease in Ca^{2+} and SO_4^{2-} concentrations. The percent decrease from seawater values for each ion is different with Mg^{2+}, Na^{+}, and K^{+} decreasing by 16%, 12%, and 9%, respectively. Thus, the Mg^{2+}-K^{+}-Na^{+} depletion is not due to gas hydrate dissociation. The cause of these depletions can only be speculated about. One possible explanation is

that they may be attributed to a pulse of a deeper-sourced fluid that caused a net intergranular transport of fluid of 10's of centimenters. A fluid at a depth greater than ~50 cmbsf would be expected to be SO_4^{2-}-depleted (Fig. 4.8), as well as silica enriched due to opal diagenesis (e.g. King et al., 2000 and references therein). The depletion in Mg^{2+} could be due to formation of high Mg calcite at low SO_4^{2-} concentrations and the depletion in Na^+ and K^+ could be due to localized zeolite precipitation due to H_4SiO_4 supersaturation (Kastner and Stonecipher, 1979). These localized reactions may also be the reason why an increase in cation concentrations was not observed on day 234 in the tubeworm field, when there was a 4% increase in Cl^- concentrations due to rapid gas hydrate formation. Thus, overall, the Cl^-, Ca^{2+}-SO_4^{2-}, and Mg^{2+}-Na^+-K^+ time series are decoupled as a result of a complex set of mineral precipitation reactions that include active gas hydrate and authigenic carbonate formation, and may include localized precipitation of zeolites and high Mg calcite.

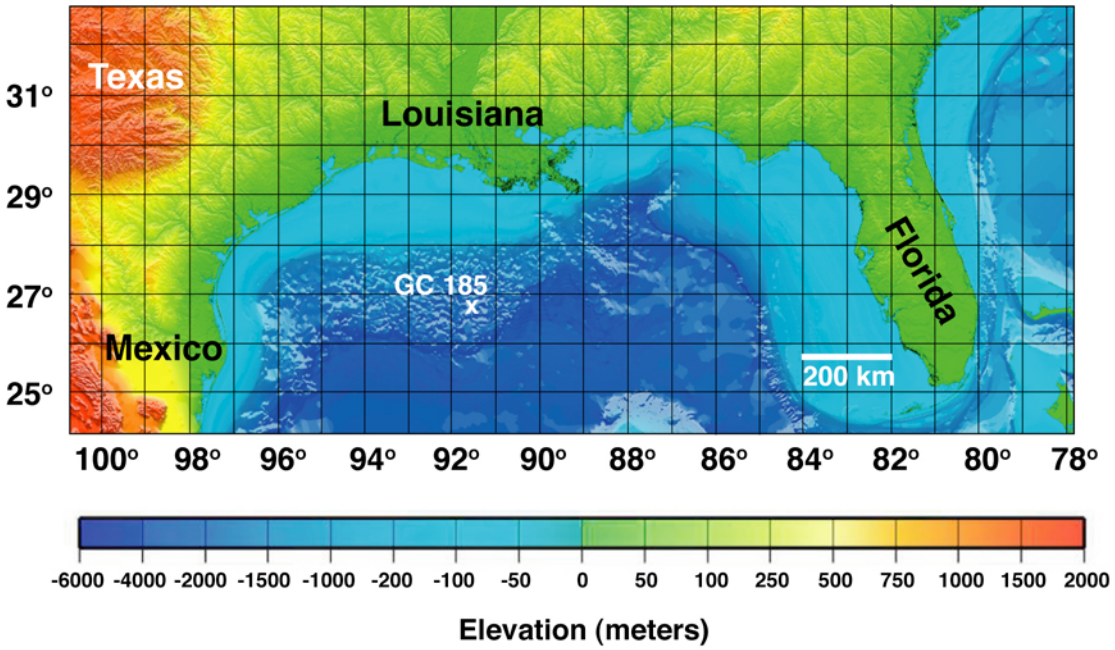

Figure 4.1 Bathymetric map of the northern Gulf of Mexico showing the location of the Bush Hill study site (Green Canyon 185).

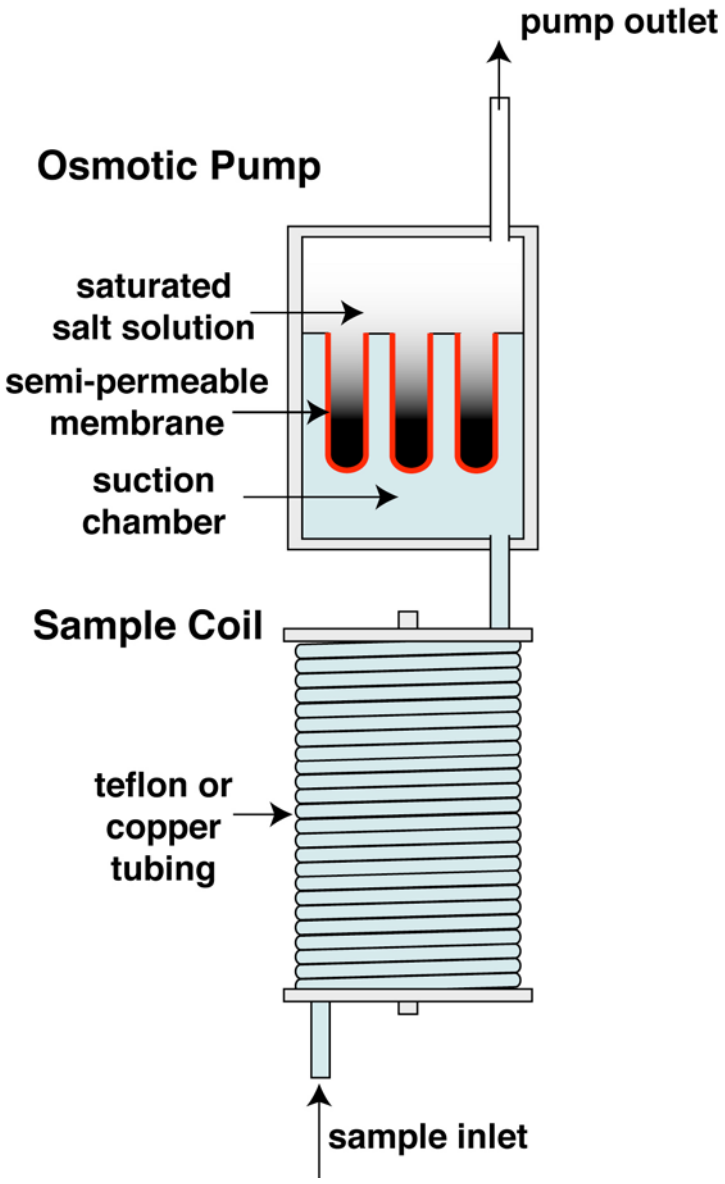

Figure 4.2 Schematic of an OsmoSampler. The rate of flow across the membranes is a function of membrane thickness, area, porosity, and the number of membranes in the pump, as well as temperature and the salinity gradient. Sample smearing due to static and dynamic diffusion and mixing is kept to a minimum by the use of the small bore tubing and low pump rates (~0.15 ml/d) as described in Jannasch et al. (2004).

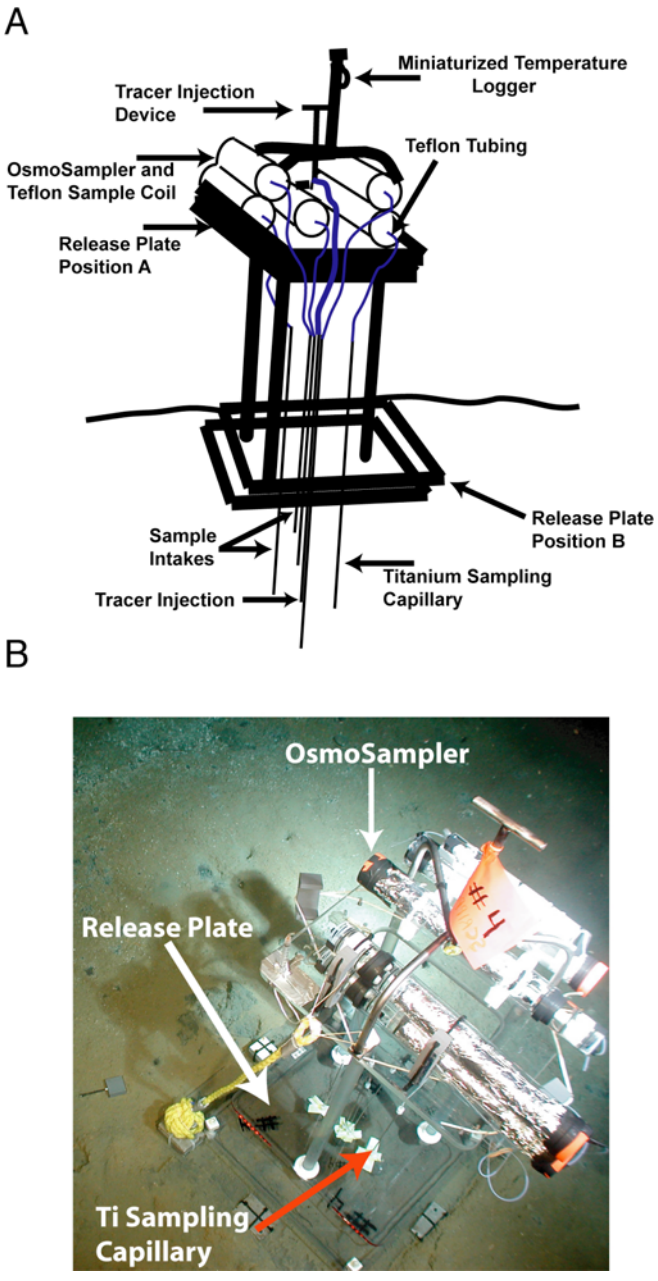

Figure 4.3 (A) Schematic representation of a MOSQUITO. Before deployment, the Ti sampling needles are held in the "up" position by the release plate (Position A). Once placed on the seafloor, the release plate is triggered, and the Ti needles are slowly pushed into the sediments at multiple pre-determined depths (Position B). After a short equilibration time, the tracer is injected. Pore fluid chemistry and tracer concentrations are sampled simultaneously. (B) Photograph of a MOSQUITO on the seafloor.

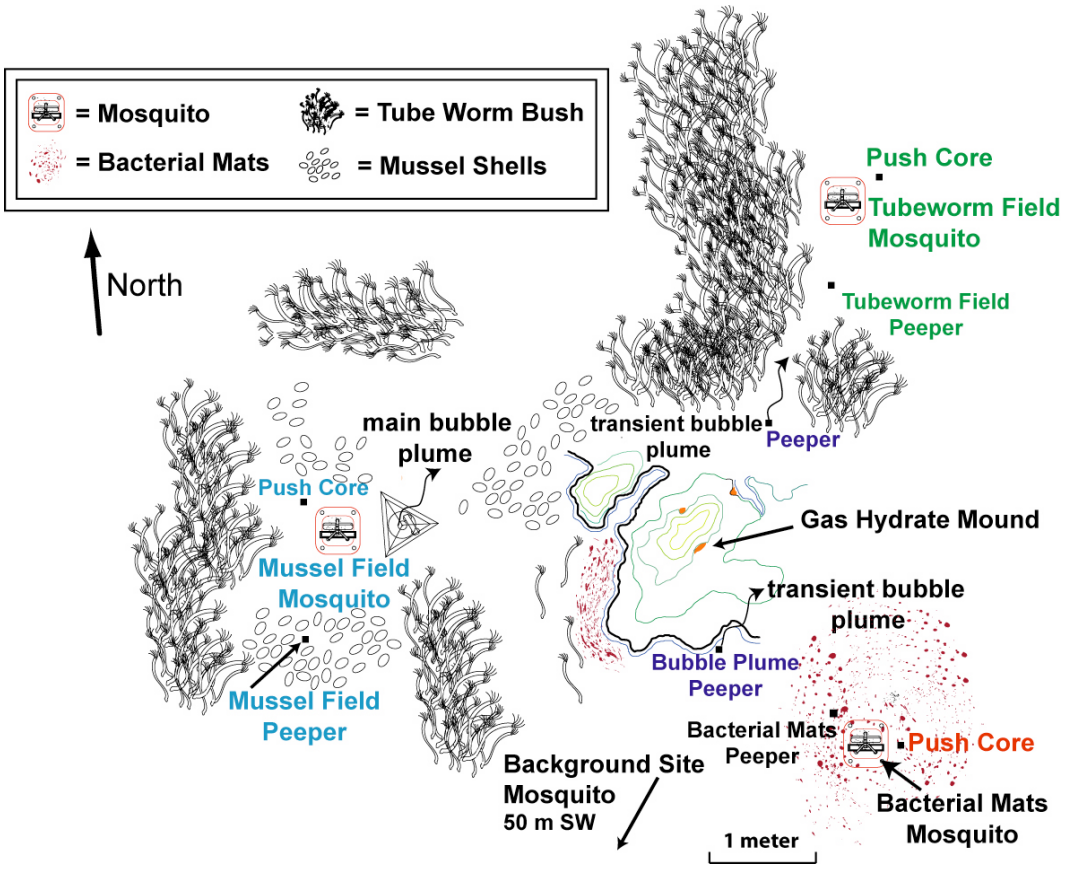

Figure 4.4 Schematic of the gas hydrate mound and surroundings at the Bush Hill study site showing the position of the MOSQUITOs, push cores, and peepers relative to the hydrate mound and benthic biological sub-environments. Relief of the gas hydrate mound is indicated by contours, which are approximately 10 cm. Schematic modified from Vardaro et al. (2005).

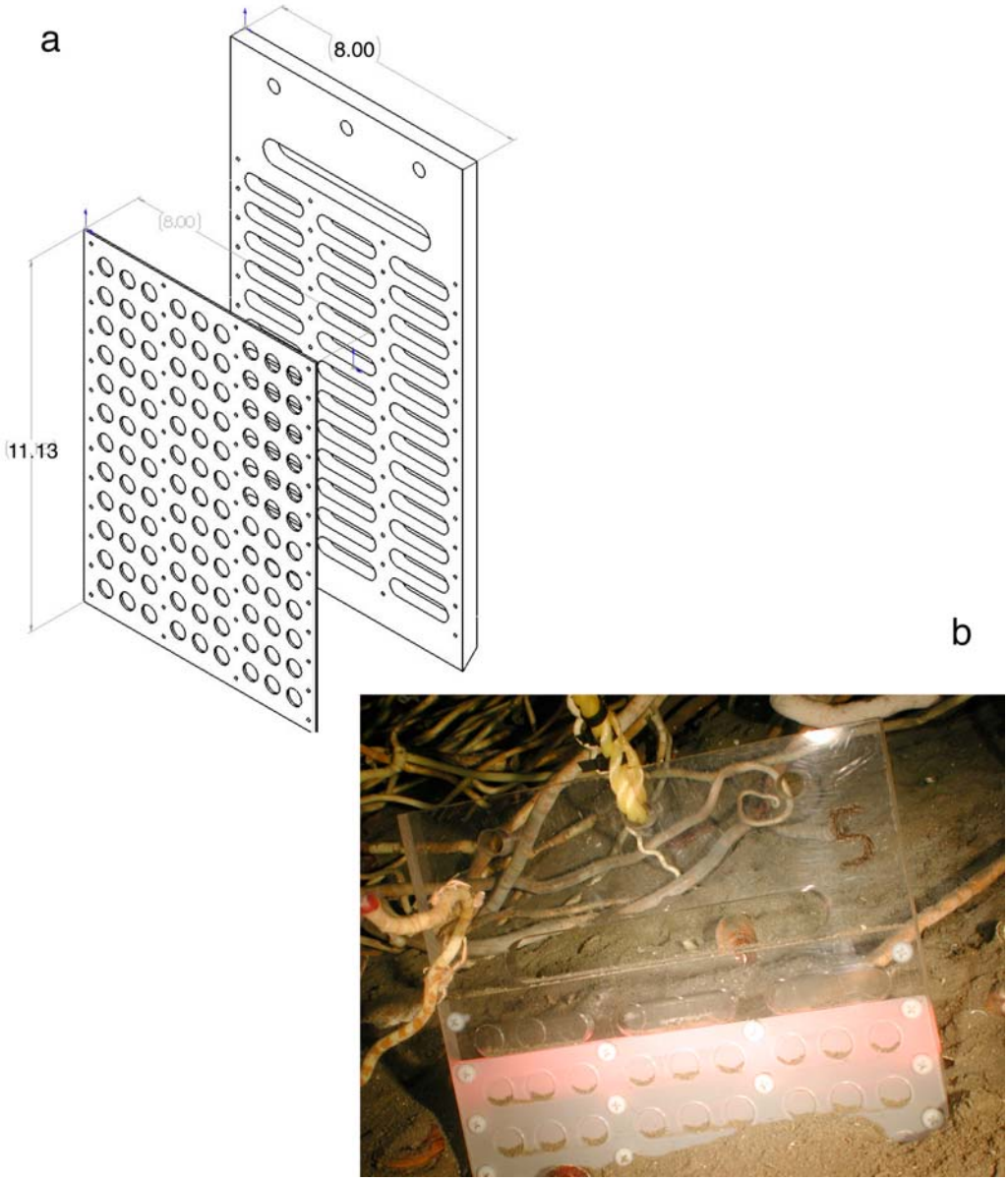

Figure 4.5 (a) Schematic of a peeper. Peepers rely on diffusive exchange of solutes across a dialysis membrane between fluid-filled cells and the surrounding sediment to sample the pore fluid chemistry at various depths. The peepers in this study were 8 in. in width and 11.13 in. in length. **(b)** Peeper deployed at Bush Hill. The upper two rows were positioned to sample bottom water. The bottom 9 rows sampled *in situ* pore fluids.

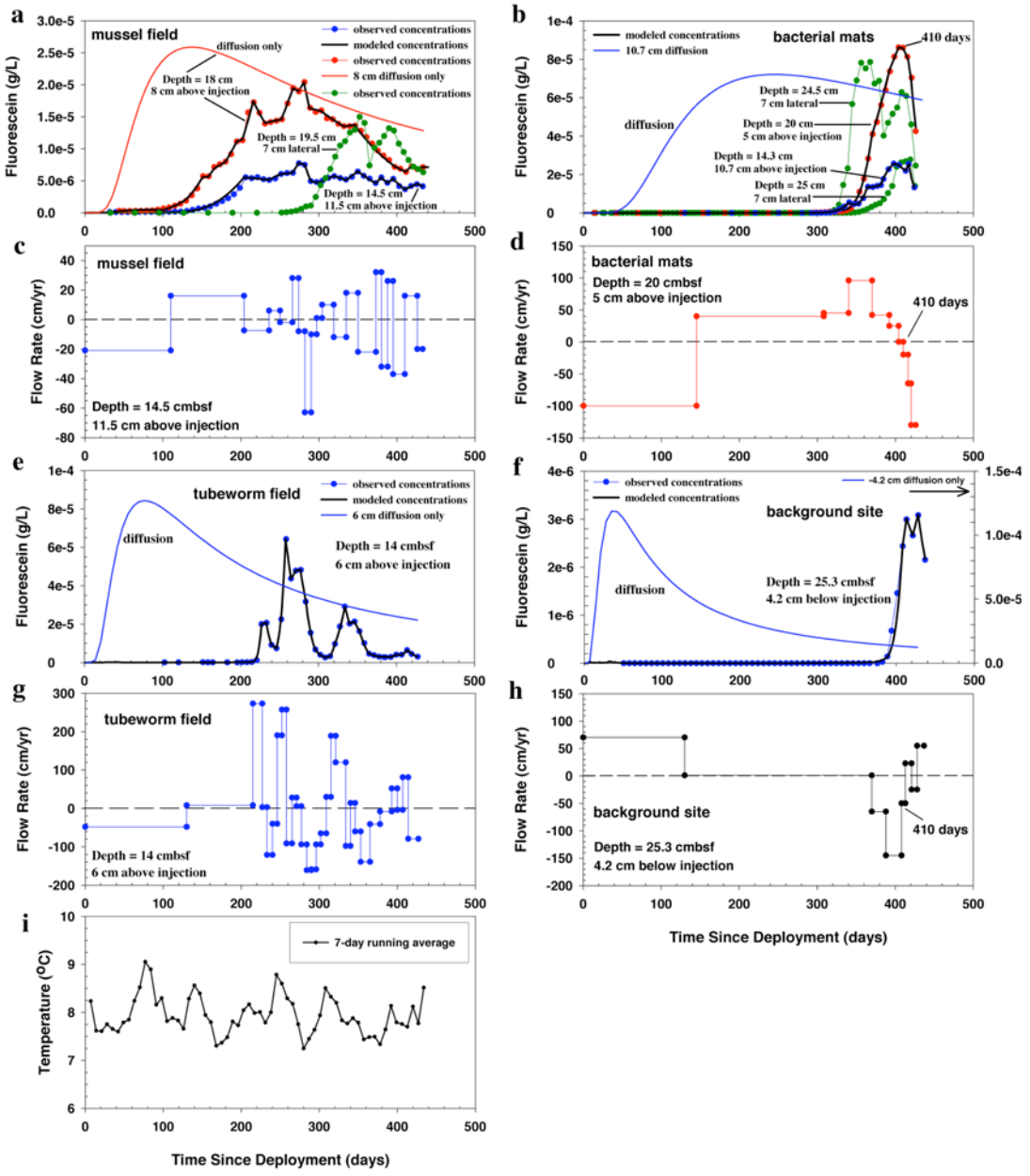

Figure 4.6 (a) Tracer concentration versus time for the vertical and horizontal MOSQUITO sample intakes in the mussel field. The solid colored curves are simulated concentrations for a steady-state fluid flow field. The black curves are the output concentrations from the variable flow rate forward simulation. (b) Observed and simulated tracer concentration versus time in the bacterial mats. (e) Observed and simulated tracer concentration versus time in the tubeworm field. (f) Observed and simulated tracer concentration versus time at the background site. Note that the sample intake was below the tracer injection and the different scales for the observed concentrations and simulated concentrations for diffusion-only. (c-d, g-h) Modeled flow rates over time for the MOSQUITOs. (i) 7-day running average of bottom water temperature at the Bush Hill gas hydrate mound.

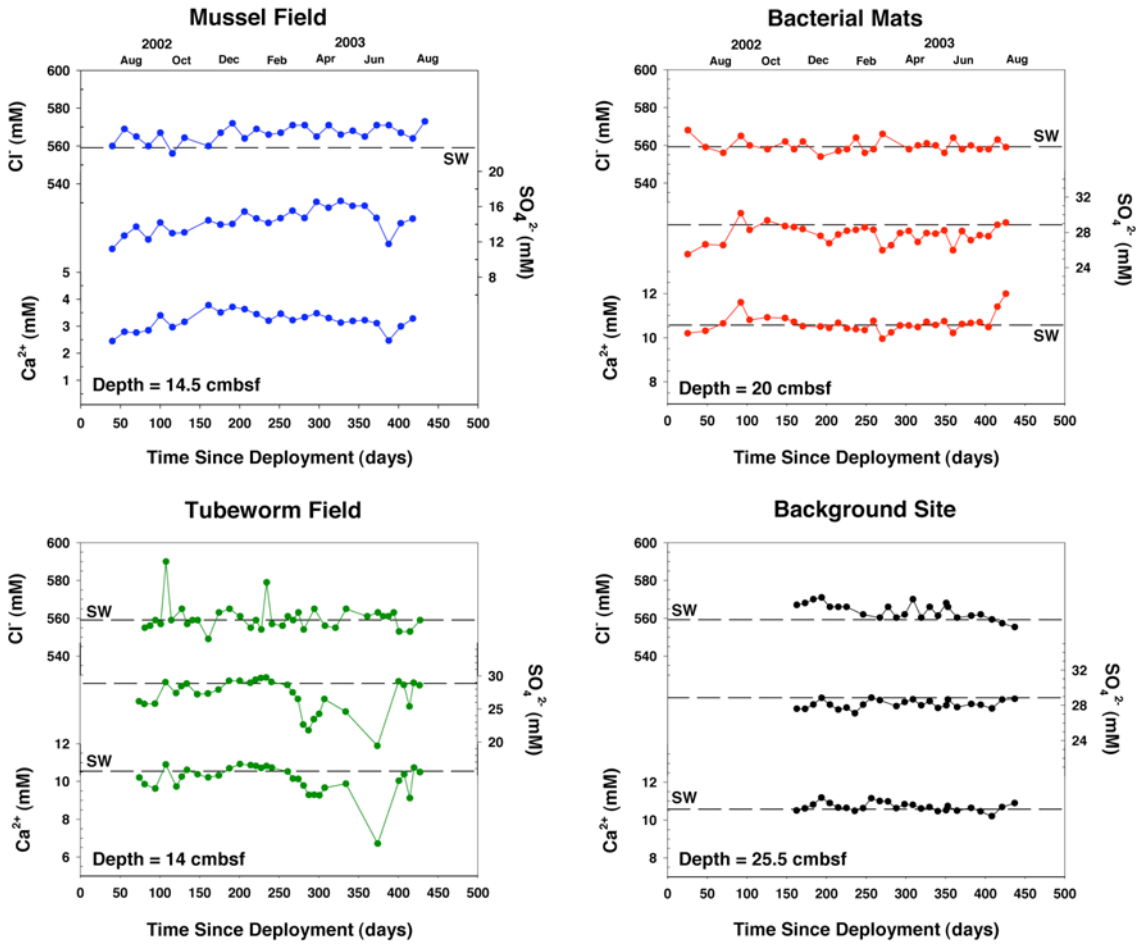

Figure 4.7 Plots of Cl^-, Ca^{2+}, and SO_4^{2-} concentrations versus time since deployment for each of the MOSQUITOs. Depth of Ti sampling capillaries are presented in the bottom-left corner of each graph.

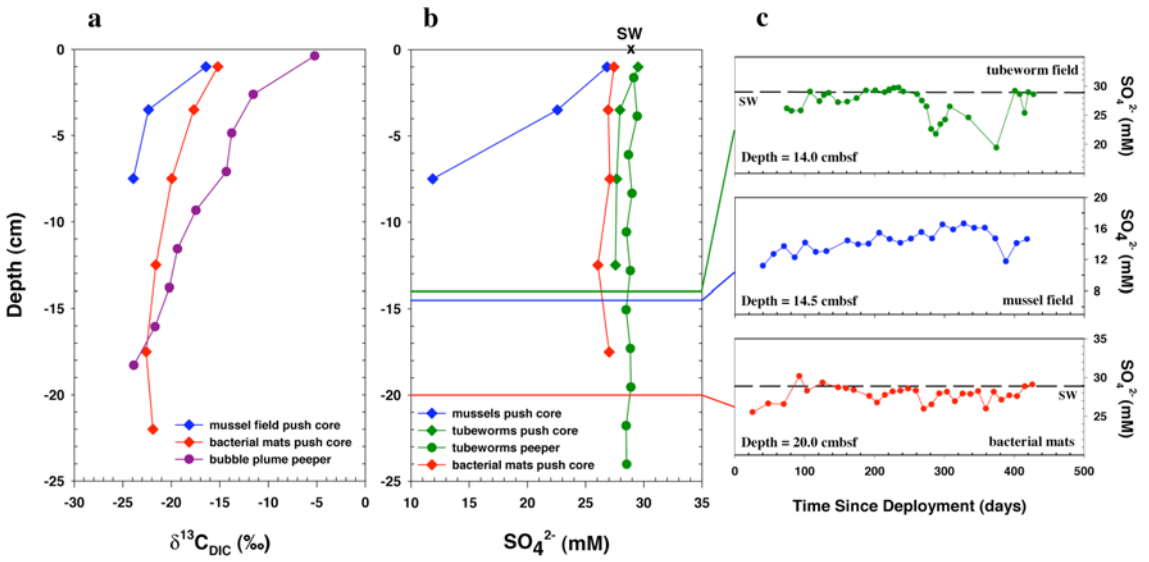

Figure 4.8 Pore fluid depth profiles from peepers and push cores of (a) δ^{13}C-DIC and (b) SO_4^{2-} in the mussel field, tubeworm field, bacterial mats, and within a transient bubble plume. The sulfate data are compared with (c) time-series SO_4^{2-} concentrations sampled by the MOSQUITOs. Solid lines in (b) are the MOSQUITO sampling depths. Dashed lines in (c) denote seawater SO_4^{2-} concentration.

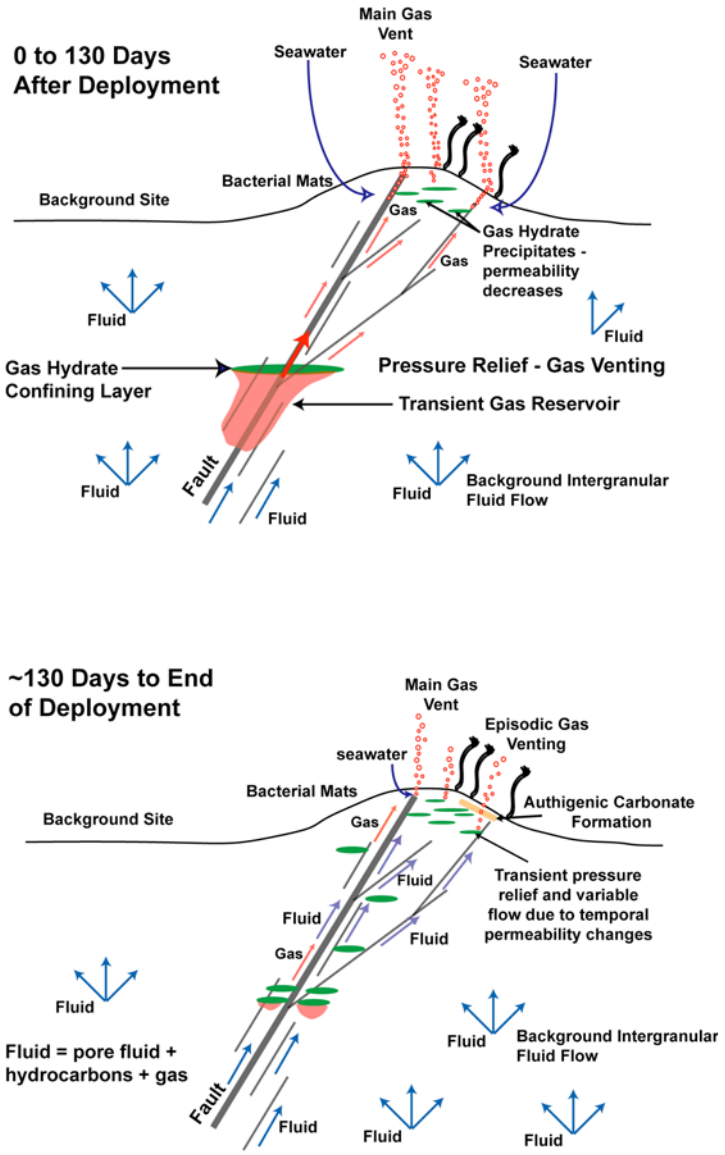

Figure 4.9 Conceptual model of the subsurface hydrogeochemistry at the Bush Hill site. The horizontal and vertical distance in the schematic is approximately 50 and 100 m, respectively. 0-130 days: a confining layer (likely gas hydrate) traps gas migrating through faults and fractures in the GHSZ leading to an overpressured reservoir prior to deployment. Gas overpressure drives fractures that vents the gas (red arrow). The focused gas ebullition is manifested at the seafloor by downward fluid flow at the mussel field, tubeworm field, and bacterial mats. During this period, the gas hydrate confining layer is disrupted. ~130 days to end of deployment: typical background fluid flow field. The confining layer had been disrupted during the focused gas expulsion episode during the first 130 days, thus there is no longer a subsurface gas reservoir. Intergranular flow variability is the result of temporal changes in sediment permeability due to active gas hydrate and authigenic carbonate precipitation.

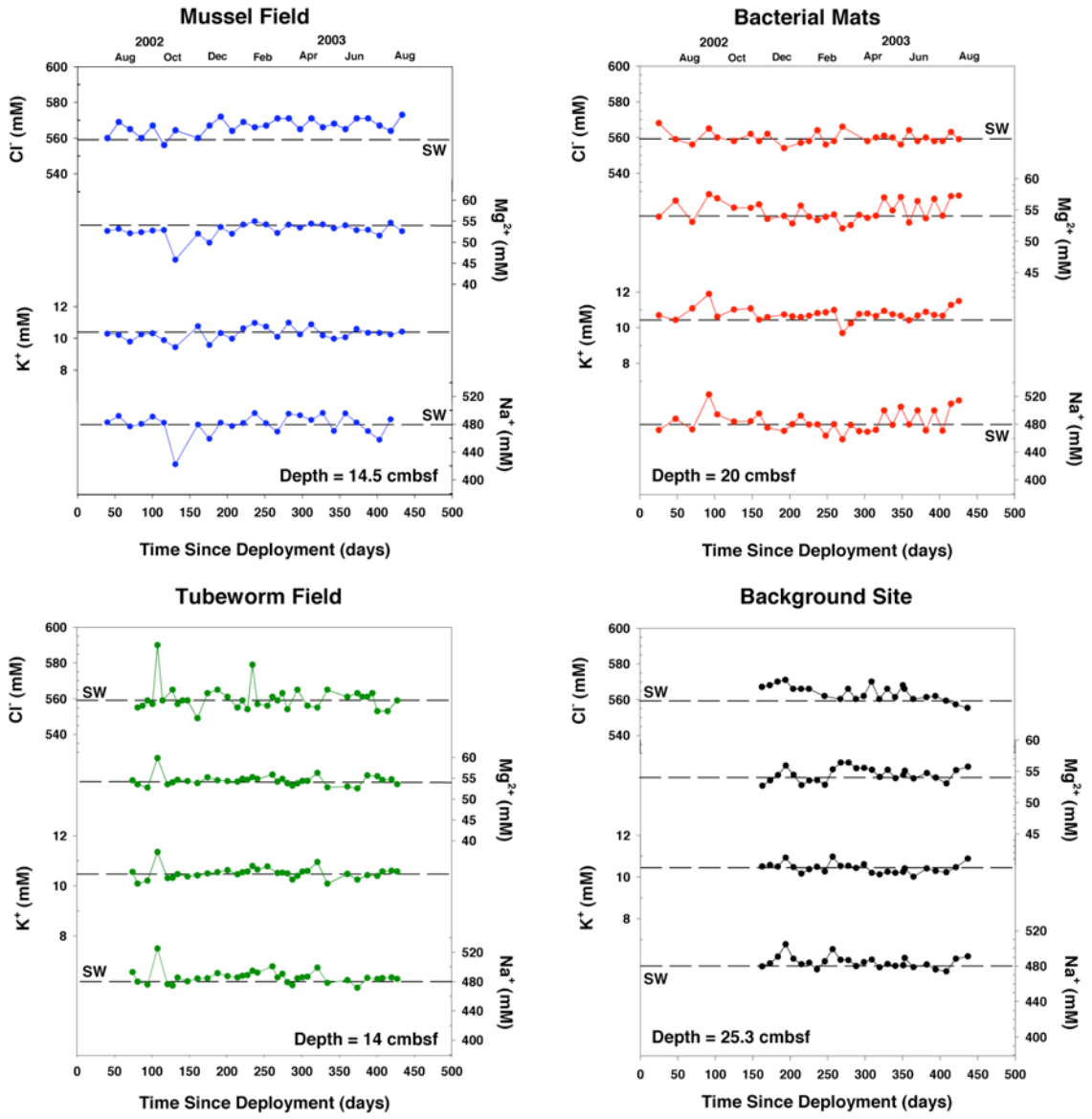

Figure 4.10 Plots of Mg^{2+}, K^{+}, and SO_4^{2-} versus time since deployment for each of the MOSQUITOs. Depth of the Ti sampling capillaries are presented at the bottom of each plot.

Table 4.1 Range in fluid flow rates and net flow distance, integration of the fluid flow rate over time curve, during the two hydrological periods discussed in Section 6. The last column is the net flow distance over the 430-day deployment period.

MOSQUITO	Flow Rate Range (cm/yr)	Net Flow Distance Day 0-130 (cm)	Net Flow Distance Day 130-430 (cm)	Net Flow Distance Over Deployment Period (cm)
Mussel Field	- 63 to 32	-6.33	+0.937	-5.39
Tubeworm Field	- 161 to 273	-17.1	+2.87	-14.2
Bacterial Mats	-130 to 96	-39.7	+29.9	-9.85
Background Site	-145 to 70	+24.9	-9.82	+15.1

Table 4.2 Average upward fluid flow rates between 130 and 410 days (second period) in the mussel field tubeworm field, and bacterial mats. Estimated avg. flow rates at the background site over the deployment period and focused gas vents during the first 130 days (first period). Estimated methane fluxes at each of the mound sub-environments and a focused gas vents (right column).

Sub-environment	Avg. Upward Advection (cm/yr)	CH_4 Flux (mol/m^2yr)
Mussel Field	**1.1**	**0.89**
Tubeworm Field	**3.5**	**2.8**
Bacterial Mats	**36**	**29**
Background Site	**13**	**11**
CH_4 Vent	**$4.8 \cdot 10^7$**	**$3.9 \cdot 10^7$**

Table 4.3 Estimated methane fluxes extrapolated to areas occupied by components of the Bush Hill chemosynthetic community identified during a laser line-scan survey of Green Canyon 185 (MacDonald et al., 2003).

Community Component	Area (m^2)	CH_4 (mol/yr)
Seep Mussels	**71.9**[a]	**64**
Tubeworms	**116**[a]	**325**
Gas Vents (1% of gas hydrate outcrops)	**0.119**	**$4.6 \cdot 10^6$**
Bacterial Mats and Background Settings	**27,450**	**$5.5 \cdot 10^5$**
Total	**27,650**[a]	**$5.2 \cdot 10^6$**

[a]Data from MacDonald et al. (2003). Gas hydrate outcrops occupy an area of 11.9 m^2 at Bush Hill (MacDonald et al., 2003).

References

Baetsle, L.H., 1969. Migration of radionuclides in porous media, in: Duhamel, A.M.F. (Ed.), Progress in Nuclear Energy XII, Health Physics. Pelargonium Press, Elmsford, N.Y., pp. 707-730.

Boudreau, B.P., 1996. The diffusive tortuosity of fine-grained unlithified sediments. Geochim. et Cosmochim. Acta. 60, 3139-3142.

Brewer, P.G., 1999. Gas hydrates and global climatic change, in: Gas Hydrates, Challenges for the Future, Annals, N.Y. Acad. Sci.. 912, 195-199.

Brooks, J.M., Kennicutt II, M.C., Fay, R.R., MacDonald, T.J., Sassen, R., 1984. Thermogenic gas hydrates in the Gulf of Mexico. Science. 225, 409-411.

Chen, D.F., Cathles III, L.M., 2003. A kinetic model for the pattern and amounts of hydrate precipitated from a gas steam: application to the Bush Hill vent site, Green Canyon Block 185, Gulf of Mexico. J. Geophys. Res. 108 (B1), 2058, doi:10.1029/2001JB001597.

Cook, D., D'Onfro, P, 1991. Jolliet Field thrust fault structure and stratigraphy, Green Canyon block 184, offshore Louisiana. Trans. Gulf Coast Assoc. Geol. Soc. 41, 100-121.

Denman, K.L., G. Brasseur, A. Chidthaisong, P. Ciais, P.M. Cox, R.E. Dickinson, D. Hauglustaine, C. Heinze, E. Holland, D. Jacob, U. Lohmann, S Ramachandran, P.L. da Silva Dias, S.C. Wofsy and X. Zhang, 2007. Couplings Between Changes in the Climate System and Biogeochemistry. In: Climate Change 2007: The Physical Science Basis. Contribution of Working Group I to the Fourth Assessment Report of the Intergovernmental Panel on Climate Change [Solomon, S., D. Qin, M. Manning, Z. Chen, M. Marquis, K.B. Averyt, M.Tignor and H.L. Miller (eds.)]. Cambridge University Press, Cambridge, United Kingdom and New York, NY, USA, pp. 67.

Dickens, G.R., Castillo, M.M., Walker, J.C.G., 1997. A blast of gas in the latest Paleocene: simulating first-order effects of massive dissocation of oceanic methane hydrate. Geology. 25, 259-262.

Dillon, W.P., Danforth, W.W., Hutchinson, D.R., Drury, R.M., Taylor, M.H., Booth, J.S., 1998. Evidence for faulting related to dissociation of gas hydrate and release of methane from the southeastern United States, Gas Hydrates: Relevance to World Margin Stability and Climatic Change, in: Henriet, P.P., Mienert, J. (Eds.), Geol. Soc. Lond. Spec. Pub. 137, 293-302.

Dimitrov, L.I., 2003. Mud volcanoes – a significant source of atmospheric methane. GeoMarine Lett. 23, 155-161.

Flemings, P.B., Liu, X., Winters, W.J., 2003. Critical pressure and multiphase flow in Blake Ridge gas hydrates. Geology 31, 1057-1060.

Formolo, M.J., Lyons, T.W., Zhang, C., Kelley, C., Sassen, R., Horita, J., Cole, D.R. 2004. Quantifying carbon sources in the formation of authigenic carbonates at gas hydrate sites in the Gulf of Mexico. Chem. Geol. 205, 253-264.

Goñi, M.A., Ruttenberg, K.C., Eglinton, T.I., 1998. A reassessment of the sources and importance of land-derived organic matter in surface sediments from the Gulf of Mexico. Geochim. et Cosmochim. Acta 62(18), 3055-3075.

Handa, Y.P., 1990. Effect of hydrostatic pressure and salinity on the stability of gas hydrates. J. Pys. Chem. 94, 2652-2657.

Hesslein, R.H., 1976. An in situ sampler for close interval pore water studies, Limn. and Ocean. 20, 912-914.

Ingebritsen, S.E., Sanford, W.E., 1998. Groundwater in Geologic Processes. Cambridge University Press, Cambridge, 341 pp.

Iverson, N., Jörgensen, B.B., 1993. Diffusion coefficients of sulfate and methane in marine sediments: Influence of porosity. Geochim. et Cosmochim. Acta. 57, 571-578.

Jannasch, H.W., Wheat, C.G., Plant, J., Kastner, M., Stakes, D., 2004. Continuous chemical monitoring with osmotically pumped water samplers: OsmoSampler design and applications. Limn. and Ocean. Methods. 2, 102-113.

Joye, S.B., Boetius, A., Orcutt, B.N., Montoya, J.P., Schulz, H.N., Erickson, M.J., Lugo, S.K., 2004. The anaerobic oxidation of methane and sulfate reduction in sediments from Gulf of Mexico cold seeps. Chem. Geol. 205, 219-238.

Kastner, M., Stonecipher, S.A., 1979. Zeolites in pelagic sediments of the Atlantic, Pacific, and Indian oceans. *In* Natural Zeolites: Occurrence, Properties, and Use. L.B. Sand, F.A. Mumpton (eds) Pergamon Press, Elmsford, New York, p 199-220.

Kastner, M., Jannasch, H., Weinstein, Y., Martin, J., 2000. A new sampler for monitoring fluid and chemical fluxes in hydrologically active submarine environments. OCEANS 2000 MTS/IEEE Conference, Providence RI, Conference Proceedings, 109-112.

Kastner, M., Solem, C., Bartlett, D., MacDonald, I., Valentine, D., 2003. The extent of CH_4 emission and oxidation in thermogenic and biogenic gas hydrate. EOS Trans. AGU 84(46) Fall Meet. Suppl., Abstract OS42B-07.

Kennet, J.P., Cannariato, K.G., Hendy, I.L., Behl, R.J., 2000. Carbon isotope evidence for methane hydrate instability during quaternary interstadials. Science. 288, 128-133.

Kennicutt II, M.C., Brooks, J.M., Brigidare, R.R., Denoux, G.J., 1988. Gulf of Mexico hydrocarbon seep communities I. Regional distribution of hydrocarbon seepage and associated fauna. Deep Sea Res. Part A. 36, 1639-1651.

King, S.L., Froelich, P.N., Jahnke, R.A., 2000. Early diagenesis of germanium in sediments of the Antarctic South Atlantic: In search of the missing Ge sink. Geochim. et Cosmochim. Acta 64, 1375-1390.

Kvenvolden, K.A., 1999. Potential effects of gas hydrate on human welfare. Proc. Nat. Ac. Sci. 96, 3420-3426.

Kvenvolden, K.A., Rogers, B.W., 2005. Gaia's breath – global methane exhalations. Mar. Petr. Geology. 22, 579-590.

Leifer, I., MacDonald, I., 2003. Dynamics of the gas flux from shallow gas hydrate deposits: interaction between oily hydrate bubbles and the oceanic environment. Earth Planet. Sci. Lett. 210, 411-424.

MacDonald, G., 1990. Role of methane clathrates on past and future climate. Climate Change. 16, 247-281.

MacDonald, I.R., Guinasso Jr., N.L., Sassen, R., Brooks, J.M., Lee, L., Scott, K.T., 1994. Gas hydrate that breaches the seafloor on the continental slope of the Gulf of Mexico. Geology. 22, 699-702.

MacDonald, I.R., Leifer, I., Sassen, R., Stine, P., Mitchell, R., Guinasso J.R., N., 2002. Transfer of hydrocarbons from natural seeps to the water column and atmosphere. Geofluids. 2, 95-107.

MacDonald, I.R., Sager, W.W., Peccini, M.B., 2003. Gas hydrate and chemosynthetic biota in mounded bathymetry at mid-slope hydrocarbon seeps; northern Gulf of Mexico. Mar. Geol. 198, 133-158.

MacDonald, I.R., Bender, L.C., Vardaro, M., Bernard, B., Brooks, J.M., 2005. Thermal and visual time-series at a seafloor gas hydrate deposit on the Gulf of Mexico slope. Earth Planet. Sci. Lett. 233, 45-59.

Milikov, A.V., Sassen, R., 2003. Two-dimensional modeling of gas hydrate decomposition in the northwestern Gulf of Mexico: significance to global change assessment. Global and Planet. Change 36, 31-46.

Milikov, A.V., Claypool, G.E., Lee, Y-J., Xu, W., Dickens, G.R., Borowski, W.S., 2003. In situ methane concentrations at Hydrate Ridge, offshore Oregon: New constraints on the global gas hydrate inventory from an active margin Geology. 31, 833-836.

Mitchell, R., MacDonald, I.R., Kvenvolden, K.A., 2000. Estimates of total hydrocarbon seepage into the Gulf of Mexico based on satellite remote sensing images, Conf Proc 2000 Ocean Sciences Meet, San Antonio, TX, AGU, Abstract OS41I-02.

Nunn, J.A., 1996. Buoyancy-driven propagation of isolated fluid-filled fractures: Implications for fluid transport in the Gulf of Mexico geopressured sediments. J. Geophys. Res., 101, 2963-2970.

Roberts, H.H., Cook, D.J., Sheedlo, M.K., 1992. Hydrocarbon seeps of the Louisiana continental slope: seismic amplitude signature and seafloor response. Gulf Coast Assoc. Geol. Soc. Trans. 42, 349-361.

Roberts, H.H., Aharon, P., 1994. Hydrocarbon-derived buildups of the northern Gulf of Mexico: a review of submersible investigations. Geo. Mar. Lett. 14, 134-148.

Roberts, H.H., Carney, R., 1997. Evidence of episodic fluid, gas, and sediment venting on the northern Gulf of Mexico slope. Econ. Geol. 92, 863-879.

Roberts, H.H., 2001. Fluid and gas expulsion on the northern Gulf of Mexico continental slope: mud-prone to mineral-prone responses, in: Paull, C.K., Dillon, W.P. (Eds.), Natural Gas Hydrates: Occurrences, Distribution, and Detection, Geophysical Monograph 124, Am. Geophys. Un., Washington, DC, pp. 145-161.

Sabatini, D.A., Austin, T.A., 1991. Characteristics of rhodamine WT and fluorescein as adsorbing ground-water tracers. Ground Water 29, 341-349.

Sabatini, D.A., 2000. Sorption and intraparticle diffusion of fluorescent dyes with consolidated aquifer media. Ground Water 38, 651-656.

Sassen, R., MacDonald, I.R., Requejo, A.G., Guinasso, N.L., Kenicutt II, M.C., Sweet, S.T., Brooks, J.M., 1994. Organic geochemistry of sediments from chemosynthetic communities, Gulf of Mexico slope. Geo. Mar. Lett. 14, 110-119.

Sassen, R., Joye, S., Sweet, S.T., deFreitas, D.A., Milikov, A.V., MacDonald, I.R., 1999. Thermogenic gas hydrates and hydrocarbon gases in complex chemosynthetic communities, Gulf of Mexico continental slope. Org. Geochem. 30, 485-497.

Sassen, R., Losh, S.L., Cathles III, L., Roberts, H.H., Whelan, J.K., Milikov, A.V., Sweet, S.T., DeFreitas, D.A.,, 2001. Massive vein-filling gas hydrate: relation to ongoing gas migration from the deep subsurface of the Gulf of Mexico. Mar. Pet. Geol. 18, 551-560.

Sassen, R., Roberts, H.H., Carney, R., Milikov, A.V., DeFreitas, D.A., Lanoil, B., Zhang, C., 2004. Free hydrocarbon gas, gas hydrate, and authigenic minerals in chemosynthetic communities of the northern Gulf of Mexico slope: relation to microbial processes. Chem. Geol. 205, 195-217.

Shipley, T.H., Houston, M.H., Buffler, R.T., Richard, T., Shaub, F.J., McMillen, K.J., Ladd, J.W., Worzel, J.L., 1979. Seismic evidence for widespread possible gas hydrate horizons on continental slopes and rises. Bull. Am. Assoc. Pet. Geol. 62, 2204-2213.

Sloan Jr., E.D., 1998. Clathrate Hydrates of Natural Gases, 2nd ed., Marcel Dekker, New York.

Solomon, E., Kastner, M, MacDonald, I., 2006. Methane fluxes to the atmosphere from perennial hydrocarbon plumes in the northern Gulf of Mexico, EOS Trans. AGU Fall Meet. Suppl., Abstract B32A-02.

Sorey, M.L., Grant, M.A., Bradford, E., 1980. Nonlinear effects in two-phase flow to wells in geothermal reservoirs. Water Resour. Res. 16, 767-777.

Tishchenko, P., Hensen, C., Wallmann, K., Wong, C.S., 2005. Calculation of the stability and solubility of methane hydrate in seawater. Chem. Geol. 219, 37-52.

Tryon, M.D., Brown, K.M., Torres, M.E., Trehu, A.M., McManus, J., Collier, R.W., 1999. Measurements of transience and downward fluid flow near episodic methane vents, Hydrate Ridge, Cascadia. Geology 27, 1075-1078.

Tryon, M.D., Brown, K.M., Torres, M.E., 2002. Fluid and chemical flux in and out of sediments hosting methane hydrate deposits on Hydrate Ridge, Or, II: hydrological processes. Earth Planet. Sci. Let. 201, 541-557.

Vardaro, M., MacDonald, I.R., Bender, L.C., Guinasso Jr., N.L., 2005. Dynamic process observed at a gas hydrate outcropping on the continental slope of the Gulf of Mexico. Geo-Mar. Let. 26, 6-15.

Wilke, C.R., Chang, P., 1955. Correlation of diffusion coefficients in dilute solutions. AICHE Journal. 1(2), 264-270.

Zatsepina, O.Y., Buffet, B.A., 1998. Thermodynamic conditions for the study of gas hydrate in the seafloor. J. Geophys. Res. 103, 24,127-24,139.

Chapter 5

Methane Flux to the Atmosphere from Perennial Hydrocarbon Plumes in the Gulf of Mexico

5.1 Abstract

Methane is an important trace gas in the atmosphere playing a significant role in greenhouse warming and ozone destruction. The global CH_4 source strength is relatively well known (Denman et al., 2007), but the methane flux from individual sources is poorly constrained. Although marine geological sources may be significant (Dimitrov, 2003; Etiope and Klusman, 2002; Judd, 2004; Kvenvolden and Rogers, 2005), most remain poorly quantified and are not included in the atmospheric CH_4 budget (Denman et al., 2007). Here we report ~500 m CH_4 concentration and isotopic depth profiles collected from a research submersible above seafloor perennial hydrocarbon plumes in the northern Gulf of Mexico. We show that surface water CH_4 concentrations above perennial hydrocarbon plumes are up to 2,000 times supersaturated. We quantify diffusive CH_4 fluxes to the atmosphere from individual plumes that are 3-4 orders of magnitude greater than previously reported from the deepwater marine environment (Holmes et al., 2000; Owens et al., 1991; Reeburgh et al., 1991; Tilbrook and Karl, 1995; Yoshida et al., 2004). Oil lines the gas bubbles inhibiting aerobic methane oxidation in the water column, and diffusive methane fluxes to the atmosphere range from 641 to 16,397 $\mu mol\ m^{-2}\ d^{-1}$. Extrapolation over the Gulf of Mexico continental shelf and slope indicates that these perennial hydrocarbon plumes emit at least 0.1 to 2.3 Tg $CH_4\ yr^{-1}$. This estimated Gulf of Mexico methane flux is ~35% of the estimated global oceanic flux (Houweling et al., 2000; Wuebbles and Hayhoe, 2002) and ~50% of the global mud volcano flux (Dimitrov, 2003). These results suggest that estimates of the CH_4 flux from the global ocean and mud volcanoes

are too low, and indicate submarine hydrocarbon seeps are significant sources of ^{14}C-dead ("fossil") methane to the atmosphere.

5.2 Background

The northern Gulf of Mexico (GOM) is a prolific hydrocarbon province where rapid migration of oil, gases, and brines from deep subsurface petroleum reservoirs occurs through faults generated by active salt tectonics (Cook and D'Onfro, 1991; Kennicutt et al, 1998; Roberts and Carney, 1997). The focused expulsion of hydrocarbons is manifested at the seafloor by gas vents, oil seeps, gas hydrates (Figure 5.1a), chemosynthetic biological communities, brine pools, and mud volcanoes (De Beukelaer, 2003; MacDonald et al., 1994; Roberts and Carney, 1997; Sassen et al, 1994). Hydrocarbon gas is emitted as plumes of bubbles from focused gas vents within larger hydrocarbon seep sites. The bubble plumes are visible throughout the water column on acoustic profiles and echo-sounder records (De Beukelaer et al., 2003; Roberts, 2001), and the bubbles are commonly coated with a thin layer of oil (Leifer and MacDonald, 2003). Upon reaching the sea surface, this oil forms targets (Fig. 5.1b) that are easily detected by satellite remote sensing methods such as synthetic aperture radar (SAR). SAR imagery of the northwestern GOM slope has revealed ~350 perennial oil slicks associated with hydrocarbon plumes (De Beukelaer et al., 2003; MacDonald et al., 1993; MacDonald et al., 2002; MacDonald et al., 2005). This is a minimum estimate that does not include the non-oily plumes in the northern Gulf of Mexico.

The atmospheric methane flux from six perennial hydrocarbon plumes was quantified at three GOM seep sites. The three seep sites occur at depths of ~550-600 m (Fig. 5.1c), and are representative of a variety of seafloor features and seepage processes in the Gulf of Mexico. Sites GC 185 and GC 234 (lease block numbers) are fault related seeps containing gas hydrate outcrops that breach the seafloor. Perennial bubble plumes and drops of oil escape from numerous gas vents adjacent to the gas hydrate outcrops. GB 425 is a mud volcano at a depth of ~600 m. Hydrocarbons are discharged in a steady stream in its center, and the gas bubbles do not appear to have an oily coating (Leifer and MacDonald, 2003).

Traditional hydrocasts that sample water column CH_4 concentrations over seeps have difficulty targeting the relatively narrow hydrocarbon plumes that meander through the water column, thus typically fail in sampling the seafloor source. During two research expeditions in 2002 and 2003, six bubble plumes were sampled by a novel plume experiment in which water column samples were collected from a research submersible from within the bubble plume while ascending from the seafloor seeps to the sea-surface. Navigation through the water column was based on visual identification of gas bubbles, assuring only the center of the plumes were sampled. Water column samples collected by submersible and traditional hydrocasts were analyzed for C_1-C_3 concentrations, $\delta^{13}C$-CH_4, and $\delta^{13}C$ of the dissolved inorganic carbon (DIC) to estimate the magnitude of aerobic CH_4 oxidation in the water column and the diffusive methane flux from the mixed layer to the atmosphere above the plumes.

5.3 Methods - C_1-C_3, δ^{13}C-CH_4, and δ^{13}C-DIC Analyses

Plume experiment water column samples were collected by the *Johnson Sea-Link* research submersible and the CTDs were deployed from the *R/V Seaward Johnson*, both operated by Harbor Branch, during two research expeditions in 2002 and 2003. C_1-C_3 hydrocarbons were analyzed on a gas chromatograph equipped with a flame ionization detector (GC 14A, Shimadzu Corp.). The C_1-C_3 compounds were resolved with isothermal 60^{o}C runs using UHP N_2 as a carrier gas through a 3.658 m by 0.318 cm packed column (*n*-octane Res-Sil C). Standard errors were $\pm$ 3% for methane and ethane and $\pm$ 4% for propane. δ^{13}C-CH_4 isotopic analyses were performed on a Finnigan MAT 252 mass spectrometer with a GC1 interface with a standard deviation of $\pm$ 0.6‰. δ^{13}C-DIC was measured on a ThermoFinnigan Delta XP Plus stable isotope ratio mass spectrometer with a standard deviation of $\pm$ 0.1‰. Stable isotope compositions are expressed in δ (‰) = 10^3 (($R_{sample}/R_{standard}$)-1), where R is $^{13}C/^{12}C$ and standards refer to Vienna Peedee belemnite (VPDB).

5.4 Results and Discussion

Anaerobic oxidation of methane (AOM) is an important CH_4 removal process in diffusion-dominated sediment systems (Boetius et al., 2000), where most to all of the methane is consumed before it reaches the overlying water column (D'Hondt et al., 2002). At advective hydrocarbon seeps, like those presented in this study, methane advection rates are greater than AOM rates, and significant quantities can enter the

ocean system. Based on δ^{13}C-DIC analyses of pore fluids (Solomon et al., submitted) and radiotracer techniques (Joye et al., 2004; Roberts et al., 2007) at GC 185 and 234, marine and terrestrial organic matter and oil oxidation are the dominant SO_4^{2-} removal processes in the sediments, and there is negligible AOM. Thus, most of the CH_4 advecting from depth enters the overlying water column. The rate of methane discharge ranges from 1.5-3.5 cm^3 s^{-1} at steady vents (Leifer and MacDonald, 2003; Solomon et al., submitted) to 22.0 cm^3 s^{-1} at pulsing vents at GC 185 (Leifer and MacDonald, 2003).

As a result of the negligible AOM in the sediments and the intense CH_4 discharge at focused vents, bottom water sampled by the plume experiments exhibits extremely high CH_4 concentrations ranging from 124 nM above the mud volcano (GB 425) to 13,660 nM at GC 185 (Figure 5.2b). Hydrocast samples were obtained from within and adjacent to the bubble plumes and at background sites >400 m from the plumes. Bottom water methane concentrations in these samples were only ~12% of those measured in the plume experiments (Fig. 5.2a).

Methane concentrations in the plumes decrease by 80-99% from the seafloor to 350 m water depth (Fig. 5.2a,b). At GC 185 and 234, CTD samples from background sites exhibit slightly elevated CH_4 concentrations (~20 nM, Fig 5.2a,e) within this depth interval, indicating that a portion of the methane lost from the plumes is due to horizontal mixing by currents. Between 350 and 60 m, plume experiment CH_4 concentrations are rather constant, then increase near the sea surface to concentrations as high as 1,609 nM (Fig. 5.2c,d). The exceptionally high surface water CH_4

concentrations are observed in both the oily and non-oily plumes and coincide with the oceanic mixed layer, where CH_4 is free to exchange with the atmosphere.

Methane concentration depth profiles alone do not provide information on the role of CH_4 oxidation versus physical processes in methane loss during transit through the water column. Changes in $\delta^{13}C$-CH_4, however, are an unambiguous indicator of the occurrence and extent of CH_4 oxidation. The $\delta^{13}C$ of bottom water CH_4 ranges from -54.38 to -44.71‰, indicating that the methane is primarily thermogenic in origin (Fig. 5.3 a,b). As methane ascends through the water column and is aerobically oxidized, the residual CH_4 becomes isotopically enriched in ^{13}C ($CH_4 + 2O_2 \rightarrow CO_2 + 2H_2O$) with an isotopic fractionation factor (α) of ~1.025 (Kinnaman et al., 2007; Reeburgh, 2003). There is either no change or a slight increase in $\delta^{13}C$-CH_4 from the seafloor to the sea surface in plumes sampled by submersible, but there is an 18‰ enrichment in one of the CTD casts (Fig. 5.33a,b).

A simple Rayleigh distillation model was applied to compute the amount of CH_4 oxidized in water column samples collected within the plumes by submersible and samples collected away from the plumes by hydrocasts. It was assumed that the methane discharge at the seafloor vents is constant and the plumes behave as isotopically-closed systems, where changes between bottom water and water column $\delta^{13}C$-CH_4 isotope ratios are only the result of CH_4 oxidation. With these assumptions, the magnitude of aerobic CH_4 oxidation and resulting $\delta^{13}C$ of the CO_2 produced is computed by

$$\delta^{13}C_{CH4} = (\delta^{13}C_{CH4}{}^{o} + 10^3)f^{1/\alpha - 1} - 10^3 \qquad \text{(Eq. 5.1)}$$

$$\delta^{13}C_{CO2} = 1/\alpha(\delta^{13}C_{CH4}{}^{o} + 10^{3})f^{1/\alpha -1} - 10^{3} \qquad \text{(Eq. 5.2)}$$

where $\delta^{13}C_{CH4}{}^{o}$ is the bottom water methane carbon isotope ratio (equivalent to the vent input ratio), α is the fractionation factor (1.025), and f is the fraction of the bottom water CH_4 remaining. The results of these calculations show that only 0 to 16% of the plume CH_4 sampled by submersible is oxidized in the water column (Table 5.1). The thin layer of oil coating the gas bubbles inhibits methane oxidation during ascent. Thus, physical processes such as bubble dissolution and mixing account for 84-100% of the methane lost from the bubble plumes. Using the same model for the CTD casts, up to 51% of the methane is oxidized away from the focused bubble plumes (Table 5.1). This indicates that as the bubbles dissolve and are advected away from the plumes, the CH_4 is more effectively oxidized.

The bubble plumes are constantly being replenished by intense methane discharge at focused gas vents, and the $\delta^{13}C$-CH_4 measured in the bubble plumes may not accurately reflect the amount of CH_4 oxidized over time. The water column $\delta^{13}C$-DIC, however, provides a record of the amount of isotopically-light CO_2 added to the DIC pool by CH_4 oxidation over longer time periods ($CH_4 + 2O_2 \rightarrow CO_2 + 2H_2O$). The $\delta^{13}C$-DIC from three of the hydrocarbon plumes is presented in Figure 5.4. In general, the $\delta^{13}C$-DIC values within the plumes are approximately seawater value. Bottom waters above the main gas vent at GC 185, however, show a clear signature of depleted $\delta^{13}C$-DIC of -3.2‰, clearly indicating long-term CH_4 oxidation immediately above the gas vent. A closed system calculation that uses a bottom water $\delta^{13}C$-DIC value of 0.59‰, an isotopic fractionation factor of 1.025, and a bottom water DIC concentration

of 2050 μM, requires the oxidation of 117 μM of methane to produce the observed δ^{13}C-DIC of -3.2‰. Using the estimated CH_4 flux at the main gas vent at GC 185 of 1.5 cm^3 s^{-1} or 4092 mol yr^{-1} (Solomon et al., submitted), provides a CH_4 oxidation rate of 5.5 mol yr^{-1} or 0.13% of the methane emitted at the seafloor vent.

The negligible to minor methane oxidation in both the oily hydrocarbon plumes at GC 185 and 234 and non-oily plume at GB 425, results in the very high mixed-layer methane concentrations despite the significant loss of CH_4 by physical processes. The mixed-layer depth in the northern GOM averages 15 m in the summer and 75 m in the winter. The summer mixed layer methane concentrations range from 28-954 times saturation, and the winter concentrations range from 28 to 2,040 times saturation (Table 5.1).

From the summer and winter mixed layer plume CH_4 concentrations, diffusive methane fluxes to the atmosphere were computed using the diffusive exchange equation

$$\text{Flux} = K_{avg}(C_{plume} - C_{eq}) \qquad \text{(Eq. 5.3)}$$

where K_{avg} is the gas transfer coefficient at the average wind speed and C_{eq} is the seawater CH_4 concentration in equilibrium with air at ambient conditions (Yamamoto et al., 1976). The gas transfer coefficient for the diffusive flux equation was computed using the empirical relationship presented in Wanninkhof (1992).

$$K_{avg} = 0.39u^2_{avg}\,(Sc/660)^{-0.5} \qquad \text{(Eq. 5.4)}$$

where u_{avg} is the average wind speed at 10 m above the sea surface and Sc is the Schmidt number, which is the kinematic viscosity of *in situ* seawater divided by the diffusion coefficient of CH_4 in seawater. The average wind speed during 2002 and 2003 at the three focus sites was obtained from the National Data Buoy Center Stations

42038 and 42041 (see: http://www.ndbc.noaa.gov/). Station 42038 is located 15 km from the GB 425 mud volcano, and measured an average wind speed of 5.63 m s^{-1} during 2002 and 2003. Station 42041 is 100 km from GC185 and 75 km from GC 234 with an average wind speed of 5.84 m s^{-1} from 2002 to 2003. From these wind speeds, the estimated value for K_{avg} is 15.4 cm hr^{-1} at GB 425 and 16.47 cm hr^{-1} at GC 185 and GC 234.

The diffusive flux from the plume experiments range from 183 to 16,397 μmol m^{-2} d^{-1}, and the flux from the background sites range from -2.36 to 32 μmol m^{-2} d^{-1} (Table 5.1). The diffusive CH_4 fluxes from the bubble plumes exceed previous estimates from various oceanic settings by 3 to 4 orders of magnitude, i.e. Pacific Ocean open water (0.9-3.5 μmol m^{-2} d^{-1}; Tilbrook and Karl, 1995), the subtropical North Pacific (~1.6 μmol m^{-2} d^{-1}, Holmes et al., 2000), Sargasso Sea (4.4 μmol m^{-2} d^{-1}; Holmes et al., 2000), Sea of Okhotsk (1.5-63 μmol m^{-2} d^{-1}; Yoshida et al., 2004), and Arabian Sea (4.6-13.9 μmol m^{-2} d^{-1}; Owens et al, 1991).

The perennial hydrocarbon plume distribution is fairly well characterized in the northern GOM, offshore Louisiana. Based on SAR imagery (De Beukelaer et al., 2003; MacDonald et al., 1993; 2002; 2005), this relatively small area (only 1-3.5% of the total GOM surface area) contains ~350 seeps originating at water depths from 200 to 2000 m, each containing 6-12 individual hydrocarbon plumes (MacDonald et al., 1993;2005; De Beukelaer, 2003). The sea surface footprint of individual bubble plumes is ~100 m in diameter (MacDonald et al., 2002), and wind-driven currents carry the surface oil slicks over distances of several kilometers (MacDonald et al., 1993; 2002; De Beukelaer, 2003). Due to these surface currents, water column CH_4 advected into the

mixed layer disperses over distances greater than the bubble footprint. The footprint of CH_4 supersaturated water at each bubble plume is ~500 m. Assuming each of the 350 seeps contain an average of 9 perennial bubble plumes, ~1.8% or 690 km^2 of the sea surface offshore Louisiana is CH_4 supersaturated. Extrapolating the highest diffusive CH_4 flux calculated for the 6 plumes of this study to the 690 km^2 area, yields a diffusive flux of ~66 Gg CH_4 yr^{-1}. This is a minimum estimate that does not include the advective flux of gas bubbles across the sea surface or the diffusive flux of CH_4 from non-oily plumes such as that at GB 425. The non-oily plumes may be equally as abundant as the oily plumes (De Beukelaer et al., 2003), suggesting the diffusive flux from this relatively small area of the GOM may be as high as 132 Gg CH_4 yr^{-1}.

The perennial plume distribution in other regions of the GOM is not well constrained. The GOM shelf and slope represents a 630,000 km^2 area. Assuming the area covered by perennial hydrocarbon plumes offshore Louisiana (~1.8%) is representative of the GOM continental shelf and slope, the extrapolated diffusive CH_4 flux from the entire GOM shelf and slope ranges from 0.1 to 2.3 Tg CH_4 yr^{-1}. This extrapolated GOM flux is considered conservative because it is a diffusive flux estimate based on the number of deep-water plumes offshore Louisiana. There are likely 2-3 orders of magnitude more seeps at shallower depths (<200 m) along the GOM continental shelf and slope. For example, the “Serendipity Gas Seep Area” offshore southern Texas contains an estimated 19,000 seeps in water depths between 60 and 230 m, and a 2,350 km^2 area offshore Florida contains an estimated 8,600 seeps originating at water depths ranging from 50 to 200 m (Hovland et al., 1993). Gas bubbles emitted at these shallow seeps have a shorter transit distance to the mixed layer, thus are less

affected by dissolution and oxidation in the water column enabling more efficient transfer of CH_4 to the atmosphere. Nevertheless, the estimated diffusive flux out of the GOM is ~50% of the global mud volcano flux (Dimitrov, 2003), ~60% of the North Siberia thaw lake flux (Walter et al., 2006), and 15-60% of the estimated global oceanic methane flux (Houweling et al., 2000; Wuebbles and Hayhoe, 2002).

5.5 Implications for the Global Methane Budget

It is generally assumed that the ^{14}C-depleted ("fossil") CH_4 in the atmosphere is attributed to anthropogenic fossil fuel related CH_4 sources such as coal mining and the gas/oil industry. The results of the novel plume sampling method employed in this study shows that a considerable flux of fossil CH_4 is emitted from natural seafloor seeps in the GOM. It is very likely that detailed plume sampling at other petroleum basins such as the Persian Gulf, Caspian Sea, Sea of Okhotsk, West African Margin, North Sea, and north Slope of Alaska would yield similar CH_4 fluxes. The global submarine CH_4 seep flux combined with other estimates of geologically-sourced emissions such as mud volcanoes (5 Tg yr^{-1}; Dimitrov, 2003), geothermal fields (~3 Tg yr^{-1}; Lacroix, 1993), microseepage from soil (~7 Tg yr^{-1}; Etiope and Klusman, 2002), and arc volcanoes (~4 Tg yr^{-1}; Lacroix, 1993), could conservatively exceed 25 Tg CH_4 yr^{-1}. A flux of 25 Tg yr^{-1} is ~55% of the estimated flux from coal mining and ~45% of the flux from the gas/oil industry (Denman et al., 2007). Thus, geologically-sourced CH_4 is likely a significant source of fossil methane to the atmosphere that should be considered in the global methane budget. A more extensive measurement program of deep-water

submarine seeps would improve estimates of the natural CH_4 input from the oceans, and better constrain anthropogenic inputs and their contribution to global climate change.

5.6 Acknowledgements

We thank the crewmembers and pilots of the *R/V Seaward Johnson* and *Johnson Sea-Link* for their support in meeting the objectives of the 2002 and 2003 dive programs. We thank D. Valentine for use of his laboratory for the C_1-C_3 hydrocarbon analyses, and F. Kinnaman, B. Deck, R. Solem, and T. Rust for technical assistance. We greatly appreciate the shipboard assistance from G. Robertson and the numerous UCSD and Texas A&M students during the 2002 and 2003 research expeditions.

5.7 Chapter Acknowledgement

Chapter 5, in full, is the material as submitted to *Nature*: Solomon, E.A., Kastner, M., and MacDonald, I.R., 2007. Methane flux to the atmosphere from perennial hydrocarbon plumes in the Gulf of Mexico. *Nature*.

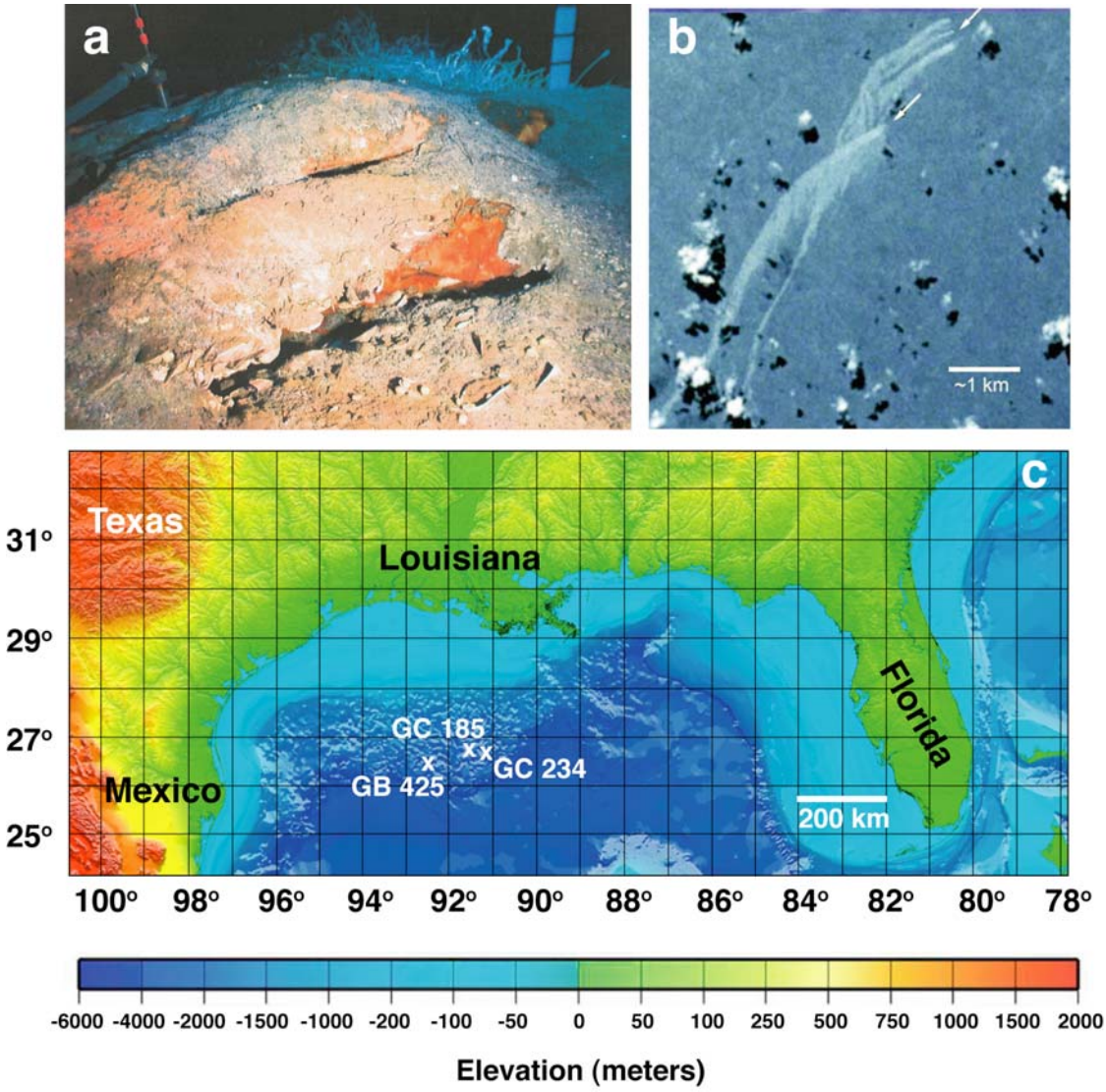

Figure 5.1 Manifestations of prolific hydrocarbon flux in the northern Gulf of Mexico. a, Seafloor gas hydrate outcrop at GC 185. Chemosynthetic mussels occupy the flanks of the outcrop in the foreground and tubeworms are present in the background. The gas hydrate outcrop is ~2.5 m wide and 60 cm high. Perennial hydrocarbon bubble plumes are emitted to the water column adjacent to the outcrop. **b,** Photograph from space shuttle showing sun-glint from the sea surface footprint of perennial hydrocarbon plumes. Figure from MacDonald et al. (2002). **c,** Bathymetric map of the northern Gulf of Mexico showing the locations of the three hydrocarbon seep sites examined in this study. Bathymetry from the NOAA National Geophysical Data Center.

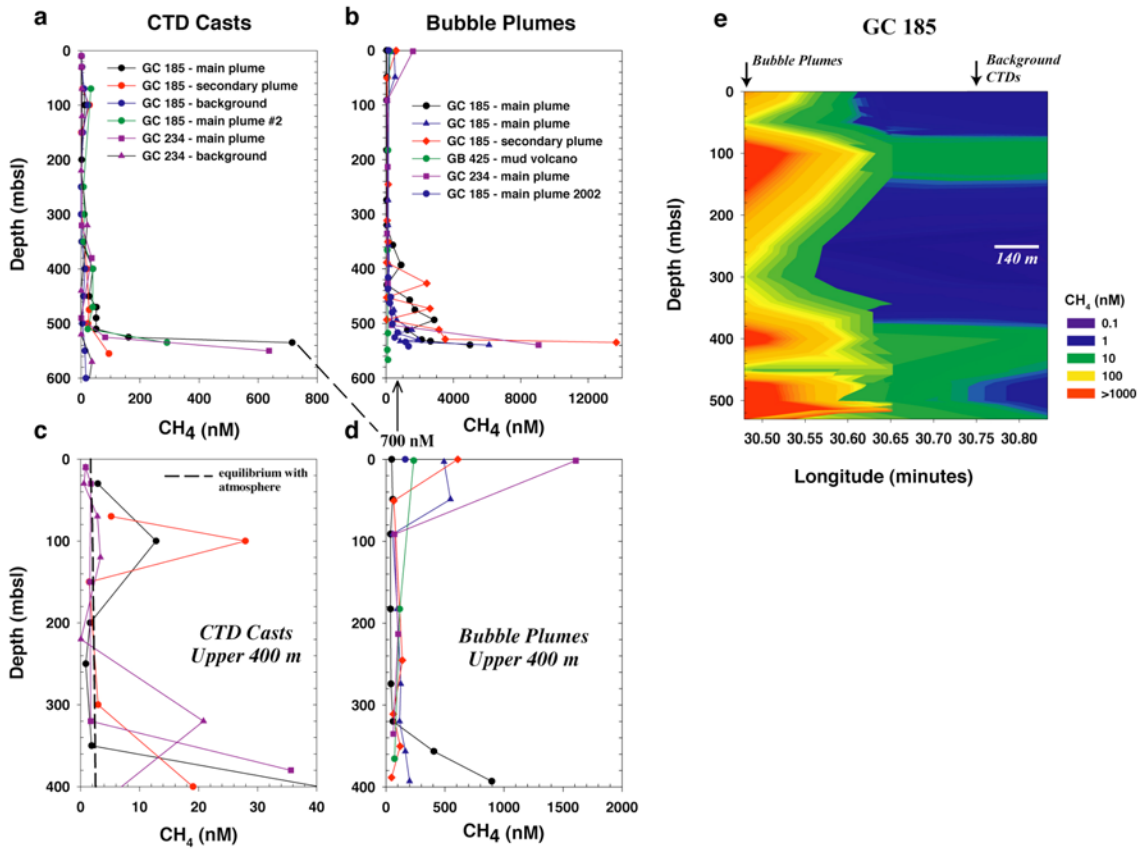

Figure 5.2 Methane concentration-depth profiles from the plume experiments and CTD casts. a, Water column CH_4 concentrations from traditional CTD casts. **b,** Water column CH_4 concentrations from the plume experiments. Note the concentration scale is expanded with respect to (**a**). **c,** CTD cast methane concentrations in the upper 400 m of the water column. **d,** Bubble plume CH_4 concentrations in the upper 400 m. **e,** Two-dimensional contour plot of the water column CH_4 distribution at GC 185.

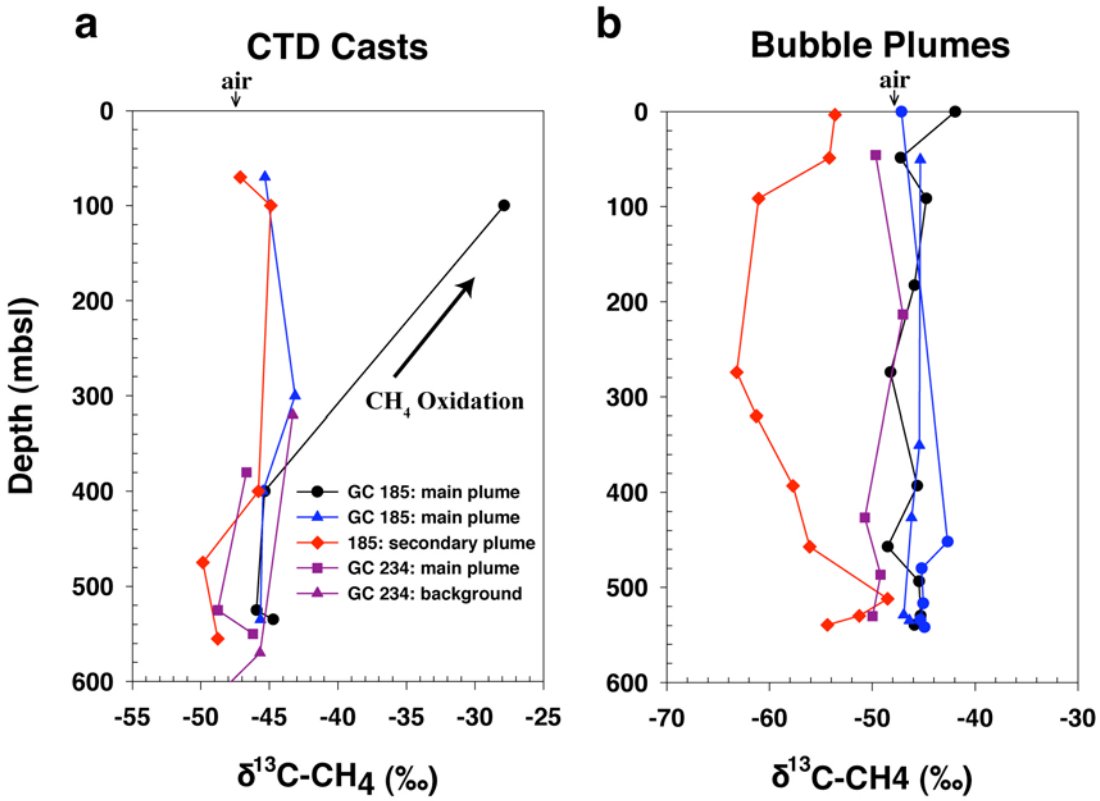

Figure 5.3 Water column δ^{13}C-CH_4 profiles from plume experiments and CTD casts. a, Water column δ^{13}C-CH_4 from CTD casts. An increase in δ^{13}C-CH_4 from the seafloor to sea surface indicates aerobic methane oxidation. **b,** δ^{13}C-CH_4 depth profiles from plume experiments showing only minor aerobic methane oxidation within the water column.

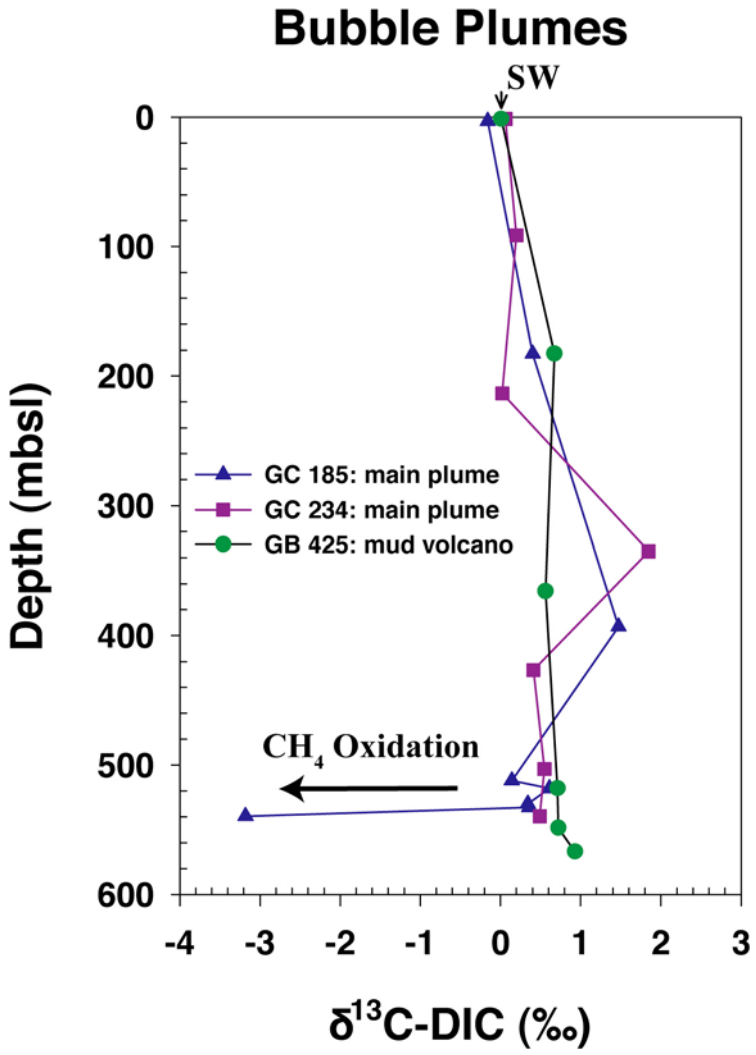

Figure 5.4 Water column δ^{13}C-DIC profiles from plume experiments. A depletion in δ^{13}C-DIC from seawater value reflects aerobic methane oxidation.

Table 5.1 Water column CH_4 oxidation and mixed layer diffusive methane flux to the atmosphere

Plume Experiments	Summer Mixed Layer CH_4 (nM)	Winter Mixed Layer CH_4 (nM)	Times Saturation[a]	% Oxidized[b]	Summer Flux (μmol CH_4 m^{-2} d^{-1})	Winter Flux (μmol CH_4 m^{-2} d^{-1})
Bush Hill Main Plume	48.1	57.1	28-30	16	183	221
Bush Hill Main Plume	492	546	288	3	1936	2151
Bush Hill Secondary Plume	608	4151	354-2024	5	2396	16,397
GB 425 - Mud Volcano	236	236	137	-	866	866
GC234 - Main Plume	1609	1609	954	1	6352	6352
Bush Hill Main Plume 2002	164	164	96	0	641	641
CTDs						
Bush Hill Main Plume	2.92	12.8	1.5-6.3	51	4.87	44.7
Bush Hill Main Plume	0.760	33.2	0.40-16	1	-3.71	124
Bush Hill Secondary Plume	2.10	5.20	1.2-2.7	7	1.58	13.9
Bush Hill Background	1.13	9.84	0.66-4.9	-	-2.36	32.0
Bush Hill Background	1.71	6.02	1.0-3.0	-	0.046	17.1
GC234 - Main Plume	1.75	352	1.0-179	-	0.204	1384
GC 234 - Background	0.880	2.86	0.52-1.5	-	-3.23	4.59

[a]Times saturated computed from the observed concentration of CH_4 divided by the CH_4 in seawater equilibrated with ambient air at *in situ* conditions (Yamamoto et al., 1976). Average CH_4 in air = 1.77403 ppmv (Denman et al., 2007). [b]Water column $\delta^{13}C$-CH_4 profiles that lacked adequate density were not used to compute % oxidation and are indicated with a dash.

References

Boetius, A., *et al.* Microscopic identification of a microbial consortium apparently mediating anaerobic methane oxidation above marine gas hydrates. *Nature* **407**, 623-626 (2000).

Cook, D., & D'Onfro, P. Joliet Field thrust fault structure and statigraphy, Green Canyon Block 184, offshore Louisiana. *Trans. Gulf Coast Assoc. Geol. Soc.* **41**, 100-121 (1991).

D'Hondt, S., Rutherford, S., & Spivack, A.J. Metabolic activity of subsurface life in deep-sea sediments. *Science* **295**, 2067-2070 (2002).

De Beukelaer, S.M. Remote sensing analysis of natural oil and gas seeps on the continental slope of the northern Gulf of Mexico. [MSc. Thesis]: College Station, Texas A&M University, 128 p. (2003).

De Beukelaer, S.M., MacDonald, I.R., Guinnasso Jr., N.L., & Murray, J.A. Distinct side-scan sonar, RADARSAT SAR, and acoustic profiler signatures of gas and oil seeps on the Gulf of Mexico slope. *Geo-Mar Lett.* **23**, 177-186 (2003).

Denman, K.L. *et al.* Couplings Between Changes in the Climate System and Biogeochemistry. In: Climate Change 2007: The Physical Science Basis. Contribution of Working Group I to the Fourth Assessment Report of the Intergovernmental Panel on Climate Change [Solomon, S.D. *et al.* (eds.)]. Cambridge University Press, Cambridge, UK and New York, NY, USA, pp. 67.

Dimitrov, L.I. Mud volcanoes – a significant source of atmospheric methane. *Geo-Marine Let.* **23**, 155-161 (2003).

Etiope, G., & Klusman, R.W. Geologic emissions of methane to the atmosphere. *Chemosphere* **49**, 777-789 (2002).

Holmes, M.E., Sansone, F.J. Rust, T.M., & Popp, B.N. Methane production, consumption, and air-sea exchange in the open ocean: An evaluation based on carbon isotopic ratios. *Global Biogeochem. Cycles* **14**, 1-10 (2000).

Houweling, S., Dentener, F., & Lelieveld, J. Simulation of preindustrial atmospheric methane to constrain the global source strength of wetlands. *J. Geophys. Res.* **105**, 17243-17255 (2000).

Hovland, M., Judd, A.G., & Burke Jr., R.A. The global flux of methane from shallow submarine sediments. *Chemosphere* **26**, 559-578 (1993).

Joye, S.B., et al. The anaerobic oxidation of methane and sulfate reduction in sediments from Gulf of Mexico cold seeps. *Chem. Geol.* **205**, 219-238 (2004).

Judd, A.G. Natural seabed gas seeps as sources of atmospheric methane. *Evnv. Geol.* **46**, 988-996 (2004).

Kennicutt II, M.C., Brooks, J.M., & Denoux, G.J. Leakage of deep, reservoired petroleum to the near surface of the Gulf of Mexico continental slope. *Mar. Chem.* **24**, 39-59 (1988).

Kinnaman, F.S., Valentine, D.L., & Tyler, S.C. Carbon and hydrogen isotope fractionation associated with the aerobic microbial oxidation of methane, ethane, propane and butane. *Geochim. et Cosmochim. Acta* **71,** 271-283 (2007).

Kvenvolden, K.A., & Rogers, B.W. Gaia's breath – global methane exhalations. *Marine Petr. Geol.* **22**, 579-590 (2005).

Lacroix, A.V. unaccounted sources of fossil and isotopically-enriched methane and their contribution to the emissions inventory: a review and synthesis. *Chemosphere* **26**, 507-558 (1993).

Leifer, I., & MacDonald, I. Dynamics of the gas flux from shallow gas hydrate deposits: interaction between oily hydrate bubbles and the oceanic environment. *Earth Planet. Sci. Let.* **210**, 411-424 (2003).

Leifer, I., & MacDonald, I. Dynamics of the gas flux from shallow gas hydrate deposits: interaction between oily hydrate bubbles and the oceanic environment. *Earth Planet. Sci. Let.* **210**, 411-424 (2003).

MacDonald, I.R. *et al.* Transfer of hydrocarbons from natural seeps to the water column and atmosphere. *Geofluids* **2**, 95-107 (2002).

MacDonald, I.R., *et al.* Gas hydrate that breaches the seafloor on the continental slope of the Gulf of Mexico. *Geology* **22**, 699-702 (1994).

MacDonald, I.R., *et al.* Natural oil slicks in the Gulf of Mexico visible from space. *J. Geophys. Res.* **98**, 16,351-16,364 (1993).

MacDonald, I.R., Kastner, M., Leifer, I.. Estimates of natural hydrocarbon flux in the Gulf of Mexico basin from remote sensing data. *EGU General Assembly Proceedings*, Abstract EGU-05-A-09970 (2005).

Owens, N.J.P., Law, C.S., Mantoura, R.F.C., Burkill, P.H., & Llewellyn, C.A. Methane flux to the atmosphere from the Arabian Sea. *Nature* **354**, 293-296 (1991).

Reeburgh, W.S. Global methane biogeochemistry. In: *Treatise on Geochemistry* vol. 4 (ed. Keeling, R.F.) 65-89 (Elsevier-Pergamon, Oxford, 2003).

Reeburgh, W.S., *et al.* Black Sea methane geochemistry. *Deep-Sea Res.* **38**, S1189-S1210 (1991).

Roberts, H., et al. *Alvin* explores the deep northern Gulf of Mexico slope. *Eos* **88(35)**, 341-342 (2007).

Roberts, H.H. Fluid and gas expulsion on the northern Gulf of Mexico continental slope: mud-prone to mineral-prone responses. In *Natural Gas Hydrates: Occurrences, Distribution, and Detection* (eds. Paull, C.K., & Dillon, W.P.) 145-161 (Geophysical Monograph 124, AGU, Washington, DC, 2001).

Roberts, H.H., & Carney, R. Evidence of episodic fluid, gas, and sediment venting on the northern Gulf of Mexico slope. *Econ. Geol.* **92**, 863-879 (1997).

Sassen, R., *et al.* Organic geochemistry of sediments from chemosynthetic communities, Gulf of Mexico slope. *Geo-Mar. Lett.* **14**, 110-119 (1994).

Solomon, E.A., Kastner, M., Jannasch, H., Robertson, G., & Weinstein, Y. *in revision*. Dynamic fluid flow and chemical fluxes associated with a seafloor gas hydrate deposit on the northern Gulf of Mexico slope. *Earth Planet. Sci. Let.* MS. Ref. No. EPSL-D-07-00484 (2007).

Tilbrook, B.D., & Karl, D.M. Methane sources, distributions and sinks from California coastal waters to the oligotrophic North Pacific gyre. *Mar. Chem.* **49**, 51-64 (1995).

Walter, K.M., Zimov, S.A., Chanton, J.P., Verbyla, D., Chapin III, F.S. Methane bubbling from Siberian thaw lakes as a positive feedback to climate warming. *Nature* **443**, 71-75 (2006).

Wanninkhof, R. Relationship between wind speed and gas exchange over the ocean. *J. Geophys. Res.* **97**, 7373-7382 (1992).

Wuebbles, D.J., & Hayhoe, K. Atmospheric methane and global change. *Earth Sci. Rev.* **57**, 177-210 (2002).

Yamamoto, S., Alcauskas, J.B., & Crozier, T.E. Solubility of methane in distilled water and seawater. *J. Chem. Eng. Data* **21**, 78-80 (1976).

Yoshida, O., Inoue, Y., Watanabe, S., Noriki, S., Wakatsuchi, M. Methane in the western part of the Sea of Okhotsk in 1998-2000. *J. Geophys. Res.* **109**, C09S12, doi:10.1029/2003JC001910 (2004).

Chapter 6

Summary and Implications

This dissertation has focused on long-term hydrogeochemical monitoring at two distinct hydrogeological settings that are important for understanding tectonic processes and global fluid and geochemical fluxes. In general, the research presented in this dissertation shows how time-series measurements of fluid flow and chemistry can be used to constrain the relationships between fluid flow and tectonic processes, two-phase fluid flow in gas-rich settings, geochemical fluxes and global mass balances, gas hydrate dynamics, and CH_4 fluxes to the atmosphere from submarine hydrocarbon seeps.

6.1 Hydrogeochemistry of the Costa Rica Subduction Zone

The long-term continuous monitoring of fluid flow rates and chemistry in CORKed boreholes at the Costa Rica margin, in concert with the long-term pressure record (Davis and Villinger, 2006), has enabled us to address the role of the upper igneous basement as a subduction zone fluid flow pathway and the hydrologic responses to episodic strain along the décollement. Radiogenic $^{87}Sr/^{86}Sr$ ratios along with elevated Li concentrations sampled by the OsmoSamplers in the basement at Site 1253, ~0.2 km from the deformation front, strongly argue for a subduction zone component in the fluid sampled. A simple mixing calculation, presented in Chapter 2, shows that 10% of the fluid sampled originates from the consolidating sediment section and/or the prism in the forearc, suggesting there is efficient fluid flow along the permeable basement, potentially extending to depths >10 km, near the up-dip limit of the seismogenic zone. This observation has important implications for models of subduction zone hydrogeology and deformation. The upper igneous basement has

traditionally been considered a no-flow boundary in these models (e.g. Ge and Screaton, 2005; Saffer and Bekins, 1999; Screaton and Saffer, 2005; Spinelli et al., 2006). The results of our study show that the basement should be included, and has a permeability ranging from 10^{-8} to 10^{-11} m^2 (depending on whether it is sills or flows), which is much greater than in the underthrust sediments or the décollement and out-of-sequence thrust faults in the prism. Adding the basement as a permeable pathway would act to relieve modeled pore pressures at the depth of the aseismic to seismic transition and limits the amount of fluid that can flow along the décollement. Collectively, this would decrease estimated pore pressure ratios along the plate boundary and increase the effective stress, decrease estimates of the décollement permeability, and increase estimates of geochemical fluxes out of subduction zones by adding another pathway with higher flow rates. There is evidence that the upper basement is highly permeable in other regions as well (e.g. Fisher, 1998; Fisher and Becker, 2000; Fisher et al., 2003), and is likely an important flow pathway at all subduction zones.

Three transients in fluid flow rates were observed along the décollement at Site 1255, two of which coincide with recorded step-wise increases in formation pressure. The two correlated transients are the result of aseismic slip events on the subduction thrust. The increase in flow rates during these events precedes the increase in pressure by a few days, consistent with the formation experiencing compression during an up-dip propagating dislocation. Both of the flow rate/pressure transients are coincident with on-shore strain episodes observed during a GPS monitoring experiment onshore from the CORK sites at the Nicoya Peninsula (Protti et al., 2004). These onshore events reflect slow slip events that propagated down-dip over the course of three weeks. The

flow rate transients suggest a mirrored dislocation propagated up-dip at the same rate and at the same time, suggesting both slip events ruptured through the seismogenic zone with no detectable earthquakes. In the case of the May 2003 slip event, pressure remained elevated after the observed onset of the dislocation, indicating slip terminated before reaching the trench "loading" the formation in the vicinity of Site 1255. These observations are unique because offshore deformational events are difficult to detect using traditional monitoring techniques (e.g. onshore GPS monitoring), and indicate that they relieve stress along some locations of the décollement while loading neighboring regions of the prism. The results show that the seismogenic zone is far from static during interseismic periods with variations in the stress-strain fields occurring at intra-annual to iner-annual time scales. The third transient in flow rates occurred over a period of 7 months, exhibiting a higher degree of flow variability and sustained elevated flow rates. This period preceded two large subduction zone earthquakes, a M_w 7.1 earthqauke off central Nicaragua and an M_w 6.0 earthquake just south of the Nicoya Peninsula, raising the possibility that the third transient may be a precursor to these large earthquakes. The recovery of the downhole instrumentation during the next CORK servicing expedition will shed light on the possible relationship between the transient flow and these seismic events. Collectively, the nature and temporal behavior of strain and the associated hydrological response during these slow slip events may provide an analog for their response prior to and during larger subduction zone earthquakes.

Large ion lithophile elements and other fluid-soluble elements are enriched in subducted sediments (e.g. K, Rb, Cs, Ca, Sr, Ba, B). These elements are also enriched

in arc volcanics. The output fluxes typically match the sediment input fluxes to the subduction zone, and, using a box-model mass balance approach, have been used to estimate the amount of subducted sediment recycled to the volcanic arc in subduction zones (e.g. Plank and Langmuir, 1993). Results from these mass balance calculations indicate that 20-30% of the subducted sediments are recycled to the arc, with the remainder continuing down to the deep mantle (Plank and Langmuir, 1997). These estimates are based on the incoming reference sediment section seaward of the trench. In Chapter 3, I presented the results of detailed analyses of pore fluid and sediment Ba concentrations from a transect of ODP sites across the Middle America Trench, providing some constraints on the shallow cycling of fluid soluble elements in the forearc of subduction zones. I showed that a considerable amount of barite is dissolved in the forearc as pore fluid SO_4^{2-} becomes depleted. This shallow dissolution of barite accounts for a loss of 60% of the sedimentary Ba originally present in the incoming sediment section seaward of the trench. This process is not unique to the Costa Rica subduction zone, and greatly reduces previous estimates of the Ba input flux to the depths of magma generation based solely on reference sections. The shallow loss of other elements used to infer a sediment component in arc magmas may also occur in the forearc, decreasing their input sediment flux as well. For example, the concentrations of Li, Rb, Cs, and B are highly enriched in fluids sampled along the décollement and thrust faults in a variety of subduction zones (Chan and Kastner, 2000; Fryer et al., 1999; Grevemeyer et al., 2004; Hensen et al., 2004; Martin et al., 1996), and are interpreted to originate from fluid-sediment reactions at temperature >100 ^{o}C. Thus, collectively, these data indicate that there is significant cycling of fluid-soluble elements

in the shallow forearc of subduction zones, impacting their delivery to greater depths in the subduction zone. The large decrease in sedimentary Ba by barite dissolution suggests that estimates of the global sediment contribution to the arc volcanoes based on Ba should be reevaluated, and likely need to be revised upwards.

6.2 Northern Gulf of Mexico Hydrocarbon Province and Gas Hydrate Stability

The northern Gulf of Mexico is a prolific hydrocarbon basin where the rapid migration of oil, gases, and brines from deep subsurface petroleum reservoirs occurs through faults generated by active salt tectonics. The focused expulsion of hydrocarbons is manifested at the seafloor by focused gas vents, oil seeps, gas hydrates, chemosynthetic biological communities, and mud volcanoes. It has been known that the gas emitted at some of these seeps transits through the entire 500-2000 m water column (De Beukelaer et al., 2003; Roberts, 2001; MacDonald et al., 2002), but the flux of CH_4 into the water column and to the atmosphere has been previously unknown. The data from the long-term continuous monitoring of seafloor fluid flow and chemical fluxes and the results of the detailed sampling of water column hydrocarbon plumes by submersible, provide constraints on the dynamic stability of seafloor gas hydrate deposits, methane fluxes to the water column, and CH_4 fluxes to the atmosphere from submarine hydrocarbon seeps.

Previous seafloor photographic observations indicated that the morphology of the gas hydrate mound at Bush Hill can alter significantly from year to year, with lobes intermittently breaking off, releasing methane and exposing fresh gas hydrate. Furthermore, spontaneous gas expulsion episodes at vents around the mound were

recorded when bottom water temperatures exceeded 8 ^{o}C. (MacDonald et al., 1994). These results indicated that the gas hydrate mounds are an unstable component of the seep environment, but it was unclear as to what was controlling the instability. Based on these observations, four MOSQUITOs were deployed adjacent to the gas hydrate mound for 15-months to determine how dynamic subsurface fluid flow and temperature act together to influence gas hydrate stability and to estimate the associated methane fluxes into the water column. The results show that fluid flow in these gas-rich hydrological setting is highly variable and complex as a result of two-phase flow processes. The flow rates ranged from -161 to 273 cm/yr, highlighting that both strong upward and downward fluid flow can occur at these sites. The continuous record of fluid chemistry shows that the gas hydrate mound was stable over the 1.5 yr continuous monitoring period, and gas hydrate continuously formed despite the variable thermal regime.

We observed long periods of downward fluid flow adjacent to focused gas vents (up to four months) that are related to local sub-pressure resulting from focused gas ebullition through faults and fractures due to gas overpressure at depth. We also observed high frequency variations in the fluid flow field that were likely due to temporal changes in the sediment permeability and 3-D fluid flow field as a result of active gas hydrate formation, authigenic carbonate precipitation, and the presence of free gas within the pore space. The long periods of negative flow (up to four months) observed at the gas hydrate mound at Bush Hill have not been observed before, likely because there are no other long-term records (>3 months) at Bush Hill or other gas-rich settings. This significant downward flow, less than a meter from focused gas vents

attests to the heterogeneous nature of fluid flow in gas-rich hydrological settings. The long periods of downflow must have a profound impact on the local benthic biological communities. During these periods, the seep fauna are effectively "cut-off" from essential nutrients such as H_2S and CH_4.

Overall, these observations suggest the gas hydrate mound receives an ample supply of CH_4 by high-volume focused gas venting followed by a more diffuse intergranular flow to keep the hydrates within the stability field. The results indicate that the Bush Hill gas hydrate deposit is presently stable despite the variable bottom water temperature and hydrological regime, and suggests instability will only occur if temperatures increase above ~16.5 ^{o}C or subsurface gas venting ceases. This should be the case for other shallow Structure II gas hydrate deposits in other margins as well (e.g. Barkley Canyon, Cascadia Margin), and suggests gas hydrate deposits may be more stable than previously thought, and that stability in the present marine regime is mainly a function of hydrocarbon supply. Thus, unless bottom water temperatures increase dramatically (~10 ^{o}C), the Structure II gas hydrates outcropping at the seafloor in the northern Gulf of Mexico will be stable until subsurface methane discharge decreases. The rapid increase in the flux of gas bubbles at vents adjacent to the gas hydrate mound due to 1 ^{o}C temperature changes (MacDonald et al., 1994; Roberts et al., 2001) may simply be the manifestation of the abrupt methane pulsing events due to repeated decreases in sediment permeability caused by gas hydrate precipitation and authigenic carbonate precipitation.

Another interesting result of the long-term MOSQUITO deployment and pore fluid sampling is that the δ^{13}C-DIC in the push cores and peepers varied between -5.2

and -23.9‰, suggesting little to no SO_4^{2-} reduction by anaerobic oxidation of methane (AOM). Instead, the $\delta^{13}C$-DIC values in the push cores and peepers indicate that the majority of electrons for sulfate reduction are supplied by the oxidation of terrestrial organic matter, seeping non-methane hydrocarbons, and/or oil. Thus, most to all of the methane advecting along focused faults and fractures to the seafloor, not used in gas hydrate precipitation, makes it into the water column at these sites. Based on this observation, I estimate a seafloor methane flux at Bush Hill of ~$5 \bullet 10^6$ mol/yr. Extrapolating this flux to the estimated area covered by focused gas vents in the northern Gulf of Mexico yields a integrated seafloor flux of ~1.5 Tg CH_4/yr. This is a considerable flux coming out of a relatively small area of the seafloor, and it is ~20% of the Black Sea basin-wide CH_4 flux to the water column (Kessler et al., 2006).

To estimate the amount of this methane lost to aerobic methane oxidation in the water column and by physical processes (such as mixing), and to quantify the methane fluxes to the atmosphere we collected a series of water column profiles by a novel plume experiment in which samples were collected from a research submersible from within focused bubble plumes while ascending from the seafloor seeps to the sea-surface. Traditional hydrocasts that sample water column CH_4 concentrations over seeps have difficulty targeting the relatively narrow hydrocarbon plumes that meander through the water column, thus typically fail in sampling the seafloor source. Bottom water sampled by the plume experiments exhibits extremely high CH_4 concentrations ranging from 124 nM above the mud volcano (GB 425) to 13,660 nM at GC 185. Estimated diffusive CH_4 fluxes to the atmosphere from individual plumes are 3-4 orders of magnitude greater than previously reported from the deepwater marine environment.

Oil lines the gas bubbles inhibiting aerobic methane oxidation in the water column to 0-16% of the methane emitted from the focused vents. Oil does not line the gas bubbles at all of the seep sites in the Gulf of Mexico, yet the surface waters at these sites are also supersaturated, indicating that aerobic methane oxidation in the water column is also inhibited by the high bubble flux at these sites. The estimated diffusive methane fluxes to the atmosphere range from 641 to 16,397 μmol m^{-2} d^{-1}. This is a minimum estimate that does not include the advective flux of gas bubbles across the sea surface. Extrapolation over the Gulf of Mexico continental shelf and slope indicates that these perennial hydrocarbon plumes emit at least 0.1 to 2.3 Tg CH_4 yr^{-1}. This is a minimum estimate based on the number of seeps offshore Louisiana, and does not take into account the gas seeps at water depths less than 200 m. There are likely 2-3 orders of magnitude more seeps at shallower depths (<200 m) along the GOM continental shelf and slope. Nevertheless, this estimated Gulf of Mexico methane flux is ~35% of the estimated global oceanic flux (Houweling et al., 2000; Wuebbles and Hayhoe, 2002) and ~50% of the global mud volcano flux (Dimitrov, 2003). These results suggest that estimates of the CH_4 flux from the global ocean and mud volcanoes are too low, and indicate submarine hydrocarbon seeps are significant sources of methane to the atmosphere.

It is generally assumed that the ^{14}C-depleted ("fossil") CH_4 in the atmosphere is attributed to anthropogenic fossil fuel related CH_4 sources such as coal mining and the gas/oil industry. The results of the novel plume sampling method employed in this study shows that a considerable flux of fossil CH_4 is emitted from natural seafloor seeps in the Gulf of Mexico. It is very likely that detailed plume sampling at other petroleum

basins such as the Persian Gulf, Caspian Sea, Sea of Okhotsk, West African Margin, North Sea, and north Slope of Alaska would yield similar CH_4 fluxes. The global submarine CH_4 seep flux combined with other estimates of geologically-sourced emissions such as mud volcanoes (5 Tg yr^{-1}; Dimitrov, 2003), geothermal fields (~3 Tg yr^{-1}; Lacroix, 1993), microseepage from soil (~7 Tg yr^{-1}; Etiope and Klusman, 2002), and arc volcanoes (~4 Tg yr^{-1}; Lacroix, 1993), could conservatively exceed 25 Tg CH_4 yr^{-1}. A flux of 25 Tg yr^{-1} is ~55% of the estimated flux from coal mining and ~45% of the flux from the gas/oil industry (Denman et al., 2007). Thus, geologically-sourced CH_4 is likely a significant source of fossil methane to the atmosphere that should be considered in the global methane budget. A more extensive measurement program of deep-water submarine seeps would improve estimates of the natural CH_4 input from the oceans, and better constrain anthropogenic inputs and their contribution to global climate change.

References

Chan, L.H., Kastner, M., 2000. Lithium isotopic compositions of pore fluids and sediments in the Costa Rica subduction zone: implications for fluid processes and sediment contribution to the arc volcanoes. Earth Planet. Sci. Lett. 183, 275-290.

Davis, E. E., Villinger, H.W., 2006. Transient formation fluid pressures and temperatures in the Costa Rica forearc prism and subducting oceanic basement: CORK monitoring at ODP Sites 1253 and 1255. Earth. Planet. Sci. Lett. 245, 232-244.

De Beukelaer, S.M., MacDonald, I.R., Guinnasso Jr., N.L., & Murray, J.A., 2003. Distinct side-scan sonar, RADARSAT SAR, and acoustic profiler signatures of gas and oil seeps on the Gulf of Mexico slope. Geo-Mar Lett. 23, 177-186.

Denman, K.L. *et al.* Couplings Between Changes in the Climate System and Biogeochemistry. In: Climate Change 2007: The Physical Science Basis. Contribution of Working Group I to the Fourth Assessment Report of the Intergovernmental Panel on

Climate Change [Solomon, S.D. *et al.* (eds.)]. Cambridge University Press, Cambridge, UK and New York, NY, USA, pp. 67.

Dimitrov, L.I., 2003. Mud volcanoes – a significant source of atmospheric methane. Geo-Marine Let. 23, 155-161.

Etiope, G., & Klusman, R.W., 2002. Geologic emissions of methane to the atmosphere. Chemosphere 49, 777-789.

Fisher, A.T., 1998. Permeability within basaltic oceanic crust. Rev. Geophys. 36, 143-182.

Fisher, A.T., Becker, K., 2000. Channelized fluid flow in oceanic crust reconciles heat-flow permeability data. Nature 403, 71-74.

Fisher, A.T., Davis, E.E., Hutnak, M., Spiess, V., Zuhlsdorff, L., Cherkaoui, A., Christiansen, L., Edwards, K., MacDonald, R., Villinger, H., Mottl, M.J., Wheat, C.G., Becker, K., 2003. Hydrothermal recharge and discharge across 50 km guided by seamounts on a young ridge flank. Nature 421, 618-621.

Fryer, P., Wheat, C.G., Mottl, M.J., 1999. Mariana blueschist mud volcanism: Implications for conditions within the subduction zone. Geology 27, 103-106

Ge, S., Screaton, E., 2005. Modeling seismically induced deformation and fluid flow in the Nankai subduction zone. Geophys. Res. Lett. 32, doi:10.1029/2005GL023473.

Grevemeyer, I., Kopf, A.J., Fekete, N., Kaul, N., Villinger, H.W., Heesemann, M., Wallmann, K., Spiel, V., Gennerich, HH., Muller, M., Weinbre, W., 2004. Fluid flow through active mud dome Mound Culebra offshore Nicoya Peninsula, Costa Rica: Evidence from heat flow surveying. Mar. Geol. 207, 145-157.

Hensen, C., Wallman, K., Schmidt, M., Ranero, C.R., Suess, E., 2004. Fluid expulsion related to mud extrusion off Costa Rica-A window to the subducting slab. Geology 32, 201-204.

Houweling, S., Dentener, F., Lelieveld, J., 2000. Simulation of preindustrial atmospheric methane to constrain the global source strength of wetlands. J. Geophys. Res. 105, 17243-17255.

Kessler, J.D., Reeburgh, W.S., Southon, J., Seifert, R., Michaelis, W., Tyler, S.C., 2006. Basin-wide estimates of the input of methane from seeps and clathrates to the Black Sea. Earth Planet. Sci. Lett. 243, 366-375.

Lacroix, A.V., 1993. Unaccounted sources of fossil and isotopically-enriched methane and their contribution to the emissions inventory: a review and synthesis. Chemosphere 26, 507-558.

MacDonald, I.R. *et al.*, 2002. Transfer of hydrocarbons from natural seeps to the water column and atmosphere. Geofluids 2, 95-107.

MacDonald, I.R., *et al.*, 1994. Gas hydrate that breaches the seafloor on the continental slope of the Gulf of Mexico. Geology 22, 699-702.

Martin, J.B., Kastner, M., Henry, P., Le Pichon, X, Lallement, S., 1996. Chemical and isotopic evidence for sources of fluids in a mud volcano field seaward of the Barbados accretionary wedge, J. Geophys. Res., 101, 20325-20346, 10.1029/96JB00140.

Plank, T., Langmuir, C.H., 1993. Tracing trace elements from sediment input to volcanic output at subduction zones. Nature 362, 739-743.

Plank, T., Langmuir, C.H., 1997. Sediment recycling at subduction zones: the ins and outs of arc volcanoes. ODP's Greatest Hits, p. 24.

Protti, M., Gonzalez T., Kato, T., Iinuma, T., Miyazaki, S., Obana, K., Kaneda, Y., LaFemina, P., Dixon, T., Schwartz, S., 2004. A creep event on the shallow interface of the Nicoya Peninsula, Costa Rica seismogenic zone. EOS, Trans. Am. Geophys. Union, Fall Meet. Program Abstr. 85, F1378.

Roberts, H.H., 2001. Fluid and gas expulsion on the northern Gulf of Mexico continental slope: mud-prone to mineral-prone responses. In *Natural Gas Hydrates: Occurrences, Distribution, and Detection*, Paull, C.K., & Dillon, W.P. (Eds.), Geophysical Monograph 124, AGU, Washington, DC, 145-161.

Saffer, D.M., Bekins, B.A., 1999. Fluid budgets at convergent plate margins: Implications for the extent and duration of fault-zone dilation. Geology 27(12), 1095-1098.

Screaton, E.J., Saffer, D.M., 2005. Fluid expulsion and overpressure development during initial subduction at the Costa Rica convergent margin. Earth Planet. Sci. Lett. 233, 361-374.

Spinelli, G.A., Saffer, D.M., Underwood, M.B., 2006. Hydrogeologic responses to three-dimensional temperature variability, Costa Rica subduction margin. J. Geophys. Res. 111, B04403, doi:10.1029/2004JB003436.

Wuebbles, D.J., Hayhoe, K., 2002. Atmospheric methane and global change. Earth Sci. Rev. 57, 177-210.